Conformal Phased Array for DISTURB

W. Bouwmeester

Technische Universiteit Delft

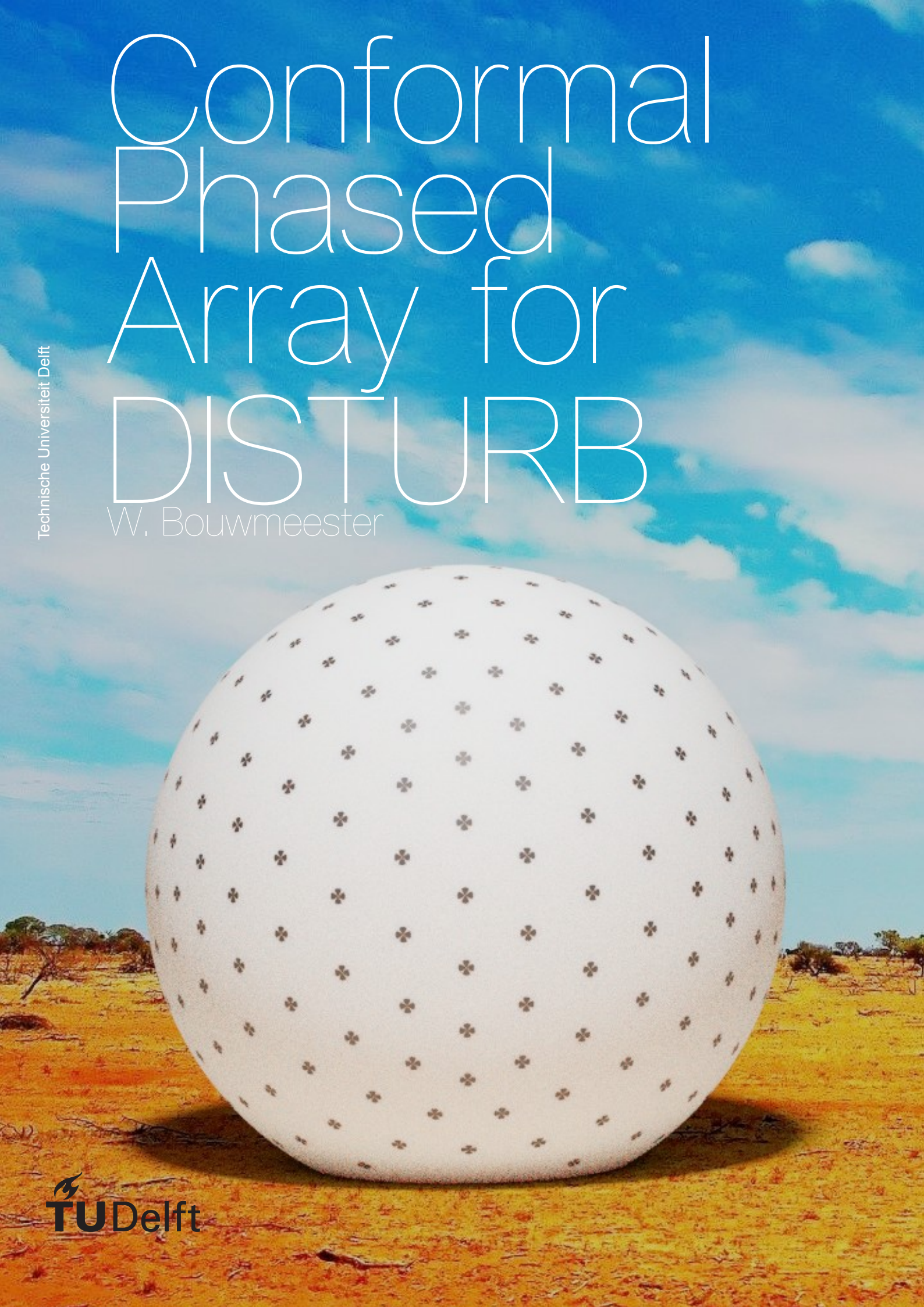

TU Delft

Conformal Phased Array for DISTURB

by

W. Bouwmeester

to obtain the degree of Master of Science
at the Delft University of Technology,
to be defended publicly on Thursday January 30, 2020 at 10:00 AM.

Student number:	4300807	
Project duration:	June 1, 2019 – February 1, 2020	
Thesis committee:	Prof. DSc. A. Yarovoy,	TU Delft, supervisor
	Dr. A. Endo,	TU Delft
	Dr. D. S. Prinsloo,	ASTRON

TU Delft

Preface

It is a well known wisdom that solving one problem creates another. In fact, often solving one problem creates multiple other problems. This is something I did not really believe at first but since completing this thesis project, I have been convinced of the contrary. For me, this also resulted in extra proof that time is both man's most valuable resource and also its worst enemy.

Heit en mem, ik wol jimme hiel graach betanke foar jimme stipe troch myn studintetiid hinne. Ik tink dat ik feilich kin sizze dat it sûnder jimme net sa goed slagge soe wêze as it is.

W. Bouwmeester
Delft, January 2020

Abstract

Mankind becomes ever more reliant on wireless technology like mobile communications, navigation and radar. This development has resulted in more sensitive receivers, but this increased sensitivity also has increased the susceptibility of these receivers to interference from external sources. One of these sources that is known to disrupt terrestrial communications is the Sun.

The DISTURB project aims to provide the means to observe and study interference phenomena generated by the Sun between frequencies of 10 MHz and 3 GHz. Furthermore, DISTURB stations should provide the ability to observe the Sun from sunrise to sunset, at any location in the world and thus require full hemispherical coverage.

This master thesis project is concerned with the design of a conformal phased array antenna for a novel application in radio astronomy. The goal of this project is to provide an initial conformal array design that is able to provide full hemispherical coverage in the 1500 MHz to 3 GHz band of the DISTURB project.

A quasi-spherical array of radius 1.55 metres and with 343 crossed modified bow-tie antenna elements, distributed using a novel geodesic topology, is proposed and found to satisfy DISTURB requirements in the frequency range of 1.3 to 3 GHz. Hence, the designed array is found to achieve a fractional bandwidth of 79% and therefore even exceeds the initial design goal.

Finally, the designed array is compared to a parabolic reflector antenna, resulting in an insight in the complexity of a conformal phased array antenna design and the advantages and disadvantages such a conformal phased array antenna may bring to the DISTURB project.

Contents

1 Introduction

This chapter aims to provide background on the research project as well as introducing the research problem, approach and the final research objective. Next to this, this chapter will also provide an overview of the current state-of-the-art related to this thesis' subject and the novel aspects of this thesis work. Finally, an outline of the thesis is provided.

1.1. Background of the Research

As time progressed, man has become more and more dependent on technology. This has resulted in society becoming increasingly reliant on wireless technologies such as, amongst others, wireless communication, radar and navigation to name but a few. In order to improve the reliability and capability of wireless services, a continuous effort is put into advancing the sensitivity and efficiency of wireless systems. However, this makes wireless equipment also more sensitive to interference from numerous external sources. One particularly strong source that is known to disrupt communication and navigational services is the Sun.

Just like society has seen progressive use of wireless electronics, so have armed forces all around the world. It should even be mentioned that most of the technologies like radar and the global positioning system were developed for military applications in the first place. As electronic tools and more advanced weaponry became more prevalent, also electronic countermeasures have found widespread use. These electronic countermeasures range from jamming wireless communication systems to tricking radars into seeing false targets. This has lead to the desire of knowing whether interference is related to space weather or generated by a potential adversary.

Space weather refers to the electromagnetic conditions in space near Earth. Space weather includes for example factors like solar wind speeds, magnetic field strengths and energetic particle levels. These factors are mostly controlled by the Sun and therefore, the Sun is the prime object with regards to determining whether interference is man-made or related to space weather. [1]

Interference related to space weather may for example occur in power grids. Power grids nowadays are large interconnected systems that are sensitive to large-scale electric fields. A disturbance in these fields can be caused by a disturbance in solar wind pressure that may compress the Earth's magnetic field. This field may subsequently induce large currents on power grids leading to potential black-outs. [1]

The Sun can also effect satellites. This can for example happen due to charged particles resulting from solar flares or coronal mass ejections impacting on microelectronics [2]. These charged particles can cause bits in the memory of a satellite to flip, with a worst case scenario of rendering a satellite inoperable due to a critical change of the satellite's programming.

1.2. Research Problem

In order to gain a better understanding of radiation emitted by the Sun and the interference that it causes, a new solar monitoring aperture array concept has been proposed by the Netherlands Institute for Radio Astronomy, abbreviated ASTRON. This project has been code-named DISTURB which is an acronym

for Disturbance-detection by Intelligent Solar radio Telescope of (Un)perturbed Radio frequency Bands. The primary purpose of this project is to continuously observe the Sun at frequencies ranging from 10 MHz to 3 GHz as many wireless services such as communications and navigation operate within this band. Aperture array technology for radio astronomy has already been demonstrated in the frequency range from 10 MHz to 1500 MHz by arrays such as LOFAR [3] and EMBRACE [4]. Therefore, a phased antenna array design, operating between 1500 and 3000 MHz, is desired to realise the full potential of DISTURB.

Next to the 2:1 operational bandwidth requirement, the antenna array must be able to look at the Sun at any time of day, at any location in the world. Hence, the array should provide full upper hemispherical coverage. Conventional planar arrays suffer from the fact that the beam widens the more the beam is steered away from broadside and towards the horizon. This is due to a decreasing effective aperture because of projection effect (i.e. the area of a planar array when looking at it from the side is much smaller than when looking at it from the top) [5].

1.3. Research Objective

The main objective of this study is to provide a conceptual design of an antenna array that meets the requirements listed in section 1.3.1 as well as possible. This research project is mainly set up to provide a feasibility study for the final design used for the 1500 MHz to 3000 MHz frequency range of DISTURB.

1.3.1. Requirements

The main requirements for system are as follows.

- *The half-power beam width of the array must be larger than 2 degrees over the operational frequency range, for any scan angle in the upper hemisphere*. Even though the Sun itself has an angular size of about 0.5 degrees, its corona is larger than that. Since a spectrogram needs to be taken of the Sun including the corona and other phenomena such as solar flare loops, the half-power beam width needs to be at least 2 degrees. Also, with a minimum of 2 degrees, the pointing of the beam also can be less precise, which may reduce complexity of beam steering and phase shifters involved. Phase shifters are often implemented in a discrete way and therefore beams can only be steered in steps of for example 1 degree. The finer the steering step required, the more complex the phase-shifters and beam-forming network and hence, the more expensive the array.
- *The half-power beam width of the array must be smaller than 15 degrees over the operational frequency range, for any scan angle in the upper hemisphere*. It is intended to calibrate the antenna array using celestial sources. This can be reasonably done if the half-power beam width is smaller than 15 degrees. If the HPBW would be larger than 15 degrees, multiple strong sources may be within the beam and disturb the calibration process.
- *The operational frequency range of the array must at least cover 1500 MHz to 3000 MHz*. As mentioned before, the DISTURB project aims to observe the Sun at frequencies between 10 MHz and 3 GHz. As the lower part of the band could potentially be covered by antenna arrays like LOFAR, an antenna array that is able to cover the higher part of the band is considered in this thesis project.
- *The array must be able to receive both polarisations*. Since sunlight is not polarised in a single way, i.e. may consists both out of circular and linear polarised light, both of two orthogonal polarisations need to be observed. Also, the polarisation of the solar emissions may reveal interesting information about observed phenomena.
- *The noise temperature of the antenna array must not exceed 100 K*. The Sun is a very strong signal source. Therefore, ultra low noise temperatures are not critical and a sensitivity of one solar flux unit would already be sufficient. However, in order to improve observations and potentially use the array to observe other astronomical objects, a receiver noise temperature of 100 K is required.
- *The array must not contain any movable parts*. The DISTURB project needs to provide 24/7 observation capability of the Sun and therefore the down-time needs to be kept as close as possible

to 0%. Movable parts wear out over time and thus are a source of failure. This risk can be mitigated by regular maintenance. However, DISTURB stations may be deployed at very remote locations to make sure at least one station sees the Sun at any time. Dispatching maintenance crews and equipment to these remote locations can be very costly and therefore performing regular maintenance may be too expensive.

Furthermore, the desires of the ASTRON research personnel for the system are as follows.

1. *The array should be able to cover as much of the 10 MHz - 3000 MHz band as possible*. Even though the lower part of the frequency band of interest for DISTURB can be covered with arrays like LOFAR, it is desirable that much of this range can be covered using one antenna system. This reduces the need for the deployment of multiple different antenna systems at one DISTURB station, thus potentially reducing project cost tremendously.

2. *The shape of the main beam should be as circular as possible over all hemispherical scan angles*. If the shape of the beam is not circular, an observed signal from a target may change as the Earth rotates. To reduce this effect and simplify observations, it is desired that the beam is as circular as possible.

3. *The array should have as little as possible total antenna elements to reduce costs of the array*. Each antenna element requires its own components like connectors, amplifiers, phase-shifters to name a few and complicate signal processing. These components add costs as does processing power. Hence, to keep costs down, it is desirable to have as little elements as possible.

4. *The array should have as little as possible enabled antenna elements*. The radio-frequency (RF) front-end electronics can potentially be switched off to save on power consumption. Since providing power to remote DISTURB stations probably requires custom infrastructure as it cannot be simply connected to the grid, power generation is likely a significant factor in the costs of a station. If the power requirements are kept to a minimum, less expensive power generation equipment can potentially be used. This could leads to costs savings.

1.4. Overview of State-of-the-art

The ability to achieve hemispherical coverage with a phased array is subject that has been of interest for a long time. Already written in 1965, [6] considers the problem of determining the optimal number of faces a phased array should have to achieve hemispherical scan coverage. In current literature, most papers that deal with achieving hemispherical coverage, take one of three approaches. The first approach is extending the scan range of an planar array, the second approach is by making use of dielectric lenses and the third is by using conformal arrays. These three approaches will be covered in the following subsections.

1.4.1. Wide-Angle Scanning Planar Arrays

In recent years, there has been extensive research effort into extending the wide-angle scanning capabilities of planar arrays. One of the key applications that drives this research is providing broadband mobile terminals for satellite communications [7–9]. These terminals are for example of interest to the aeronautical sector to provide more elaborate in-flight entertainment on airliners [7].

Increasing the wide-angle scanning of a planar array can be achieved in a number of ways. The array described in [10], on which the antenna array from [7] is based, makes use of a connected array antenna where the mutual coupling is exploited to extend the scanning range. The final array is able to scan to 60° from zenith in a frequency range from 10.7 GHz to 14.5 GHz [7].

In contrast, in [11] a wide-angle scanning planar array is constructed out of antenna elements with quasi-hemispherical radiation patterns that are combined with grounded decoupling cavities to reduce mutual coupling. The final array of 16 by 16 active elements achieves a scan range of $\pm 77°$ with a gain variation of less than 5 dB [11].

Another approach to wide-angle scanning is by making use of reconfigurable antenna arrays. One of the earliest examples of this is a phased array antenna consisting of waveguide elements that are shorted when scanning to the endfire direction. In this way the array transforms into a corrugated surface wave antenna and a narrow beam towards endfire can be achieved [12].

In [13], pattern reconfigurable antenna elements are used to extend the scanning range. The array consists out of microstrip yagi antennas that can be reconfigured using PIN diodes as switches. Another way to reconfigure the element radiation pattern is by using an antenna design that has different radiation patterns based on the field mode present in the feed of the antenna [14]. Next to this, a multi-scale array concept which uses separate antenna elements for different bands can be used to extend the scanning range of the array [15].

Also, the scanning range for an array can be extended by optimising beamforming algorithms, for example by exploiting the position of the nulls in the radiation pattern [16].

1.4.2. Dielectric lenses

An alternative way to obtain good hemispherical scanning is to make use of dielectrics. Using dielectrics, lenses can be made that shape or deflect the beam generated by a phased array feed to achieve hemispherical scanning.

One way of obtaining hemispherical coverage using dielectric lenses is by making use of a Luneburg lens. This is a spherical lens that has a relative permittivity that varies along the radius of the lens [17]. A Luneburg lens has the adventageous property that, due to its symmetry, the beam shape is independent of the scan angle [18]. Such a Luneburg lens has been considered for use in the Square Kilometre Array [19]. To save some material costs on the Luneburg lens, also a hemispherical lens with a ground plane underneath the lens can be used [20]. However, this requires a mechanically movable feed if hemispherical scanning is desired [21].

Another solution is by using a dielectric lens on top of a planar array as a beam deflector [22]. This deflector lens can have several shapes, ranging from pyramidal to spherical lenses and faceted designs [22–24].

1.4.3. Conformal Arrays

Lastly, the hemispherical coverage problem can also be solved by using a conformal antenna array. A conformal antenna array is defined by the IEEE as an antenna or an antenna array that conforms to a surface whose shape is determined by considerations other than electromagnetic; for example, aerodynamic or hydrodynamic. However, in common usage, the term conformal array is applicable to any array that has some three-dimensional shape, either smooth or faceted [25]. By this definition, although the term conformal array is not mentioned, [6] is one of the earliest examples of using a conformal array to achieve hemispherical coverage.

The structure proposed in [6] comprises four faces, each carrying a phased array that covers a sector of 55°, which is optimal from an minimum antenna element point of view. Furthermore, [6] mentions the optimal number of faces is strongly dependent on the requirements of the final array. This work has later been extended by [26] and revisited in [27]. The final conclusion of the two last mentioned papers is that for their application, an array with four faces is optimal for both volume and horizon scanning considering the revised criteria. Another paper that considers the optimisation of the number of facets an array should have is [28]. Next to optimising the number of facets required, [28] describes a way to optimise the elevation angles the facets should have in order to reduce the maximum required scan angle per subarray. Furthermore, [28] states that among the pyramidal frusta class of shapes, a frustum with six or seven facets requires the least elements. This design has been put in practice by [29], in which the design of a pyramidal frustum with seven facets is described. Each facet contains a subarray with seven stacked patch antennas, with a final resulting gain exceeding 10 dBi within 86.6% of the full upper hemisphere [29].

A more sophisticated faceted shape is presented in [30]. This array consist out of multiple different angled facets: facets perpendicular to the ground, parallel to the ground and facets at an angle to close the shape. The gain variation over the upper hemisphere is less than 2 dB for an array with 17 faces [30]. This provides the hemispherical scanning capability required for telemetry, tracking and command of satellites [30]. Next to this, [30] also describes a beamforming algorithm which is able to place a null at the location of an interference source.

Besides shapes with facets, also continuous/smooth shapes can be used for arrays to provide hemispherical coverage. One of the first examples of this is [31] in which an array of open ended waveguides is placed on a cone. In the case of [31], the conical shape is not specifically selected because of the radiation requirements, but because of aerodynamic reasons as the array is designed for use as a nose cone for guided missiles. Another example of a conical array, that does use its shape

for electromagnetic purposes, is presented in [32]. This array consists out of 24 subarrays of 6 patch antennas each that are placed on a conical frustum. The array is able to achieve coverage between 0° to 62.3° in elevation and 360° in azimuth with a gain variation of 0.15 dB [32].

Another example that does utilise its shape for electromagnetic purposes, is the GPS antenna design in [33]. A spherical cap shape is used to provide a better signal to noise and interference ratio for GPS satellites at low elevation. Similarly, [34] also presents an conformal antenna array based on a spherical cap for GPS purposes. However, instead of making the antenna elements conform to the surface, the spherical cap is locally flattened so that a number of flat circular facets are created. Each flattened facet carries a patch antenna. It is found that this array is indeed able to provide good gain over the complete hemisphere and also is resonant in multiple frequency bands so that multiple satellite navigation constellations can be supported [34].

Instead of spherical cap shaped antenna, full spherical antenna arrays can be used. The spherical array in [35] is designed for use on a satellite. Spherical arrays have the potential to provide wide-angle scanning capability with near constant directivity which makes it very interesting for satellites in low-earth orbit [35]. In [36], the problem of determining the best element radiation pattern for use in this array is considered. It is concluded that an element with a cosine squared pattern is the most desirable and this antenna element is subsequently realised with a quasi-tapered helix antenna [36]. Furthermore, a beamforming algorithm based on evolutionary techniques that could be used for this type of spherical array is presented in [37]. Two other examples of spherical arrays are presented in [38]. Firstly, a spherical array with monopole antenna elements is presented. However, it is found that beamforming is very difficult since the monopoles have a radiation pattern that is distributed in a band [38]. To make beamforming simpler, [38] presents a spherical array consisting of horn antennas. It is found that this array is able to provide good uniform coverage of the upper hemisphere with a gain variation 3 dB in the lower end of its frequency band and 6 dB in the upper part of its frequency band [38]. Instead of a full sphere, [39] describes a hemispherical array. This array is designed for satellite ground station applications, in which it is desirable to have higher gain near the horizon [39]. This hemispherical array, with a radius of approximately 57.8λ and 82177 antenna elements, is able to achieve a maximum gain of 46 dBi, which can be reduced by disabling elements if required [39].

Next to purely facet based and smooth shapes, there are also arrays that are faceted approximations of smooth shapes. A prime example of this is the geodesic sphere phased array antenna described in [40]. This array is a sphere that has been approximated by an icosahedron, with each of the facets housing a subarray. This array has practically the same gain for every scan direction [40]. Also in [41], a faceted approximation of a hemisphere is used with each facet carrying a microstrip patch antenna. This array does not make use of phase shifters or circulators but instead only enables the patch antenna which is facing the scan direction the best [41]. This has the potential to reduce the costs of the array [41].

1.5. Research Approach

Although wide-angle scanning capability of planar arrays is increasing slowly, full hemispherical coverage has not been achieved yet. The array from [10] is designed to scan up to angles of 60°, but to cover the full upper hemisphere, minor mechanical scanning is still required [10]. Next to this, planar arrays suffer from projection effects which makes the antenna gain decrease by $\cos^{\alpha} \theta_s$ when scanning towards the horizon, where θ_s is the scan angle measured from broadside [5].

Dielectric lenses also provide a possible solution to the hemispherical coverage problem, however lenses have two important drawbacks. Firstly, lenses are generally large in terms of wavelength which make them bulky in the frequency range required for DISTURB and makes them more applicable at millimetre wave frequencies [42]. Secondly, dielectric lenses may be very difficult to manufacture, especially in the case of a Luneburg lens where the dielectric constant needs to vary with radius within the lens [43].

Alternatively, by designing an antenna array that conforms to a certain shape, the projection effect can be circumvented. The shape of the beam is controlled by the shape of the conformal array and therefore the shape of the array can be designed in such a way that scan-invariant patterns can be achieved [44]. The fact that gain variation is minimal with scan direction is confirmed by the results mentioned in section 1.4. As listed in section 1.3.1, this is the most important requirement. Next to this, because conformal arrays can be designed in such a way that the whole upper hemisphere can

be covered, such arrays also do not require any movable parts.

The before mentioned disadvantages of lenses and planar arrays and the advantages of conformal arrays lead to the conclusion that conformal arrays provide the most potential to fulfil the requirements for DISTURB. Therefore, this thesis seeks to achieve the research objective by means of a conformal array.

Firstly, the advantages and disadvantages of certain conformal array geometries are studied. From this comparison, the most advantageous shape is selected and an antenna element is designed for use in the selected array. Lastly, a complete analysis of the array, including active element patterns and therefore mutual coupling, is performed to find out of if the final array complies to or even exceeds the requirements in section 1.3.1.

1.6. Novelty

Traditionally, radio astronomy has been conducted by means of large reflector antennas or other large antenna such as the Holmdel horn antenna used by Penzias and Wilson to discover the cosmic microwave background [45]. As technology progressed, also phased array antennas designed for radio astronomy like LOFAR and EMBRACE were commissioned. However, all of these arrays are planar.

For the first time, a novel application of conformal arrays in radio astronomy is investigated in this thesis project.

By using a method of analysis based on isotropic active element patterns, a significant reduction of computational resources is achieved allowing for a novel comparison far-field properties of numerous different array configurations.

The configurations considered include spherical arrays with new concepts for element topologies. The first is a novel topology where the element positions are based on the vertices of a geodesic dome. The second novel topology is based on a new application of the HEALPix grid which has originally been developed for creating maps of spherical surfaces as alternative to for example a Mercator projection which can introduce unacceptable distortion. For example, HEALPix is used to create maps of cosmic microwave background radiation.

1.7. Thesis Outline

This first chapter of the thesis gives a description of the research problem, the approach and the final research objective. Next to this, this chapter also provides an overview of the current state-of-the-art for large scan range phased arrays and the novelties of this thesis project.

The second chapter of the thesis gives a general introduction to conformal arrays and their theory of operation. Furthermore, chapter 2 describes how the conformal arrays are analysed and how the radiation patterns are calculated for a given array geometry.

The third chapter deals with the three dimensional shape of the conformal array and the distribution of the elements on said three dimensional shape. The performance of the different conformal array configurations will be discussed on compliance with the requirements given in section 1.3.1. A trade-off will be made and the most optimal configuration is selected. This configuration is then used in the following chapters of the thesis.

Chapter 4 deals with the antenna element design to be used in the conformal array selected in chapter 3.

The performance of the completed array is evaluated in chapter 5. Besides this, the conformal array performance is compared to that of a parabolic reflector antenna.

Chapter 6 gives a conclusion on the achieved results. In addition, recommendations for further research are made.

2

Conformal Array Analysis

This chapter deals with the analysis of generic conformal arrays. It will describe the theory of operation of conformal arrays and analysis of radiation patterns of conformal arrays. For the details regarding implementation of this analysis in MATLAB, the reader is referred to appendix A.

2.1. Reference System

Throughout this thesis, the reference system from figure 2.1 is used. The system features an ordinary right handed Cartesian coordinate system. Next to this, also a spherical coordinate system is used. In this system, the angle θ is measured from the z-axis and the angle ϕ from the x-axis. In some cases, the z-axis is also referred to as zenith.

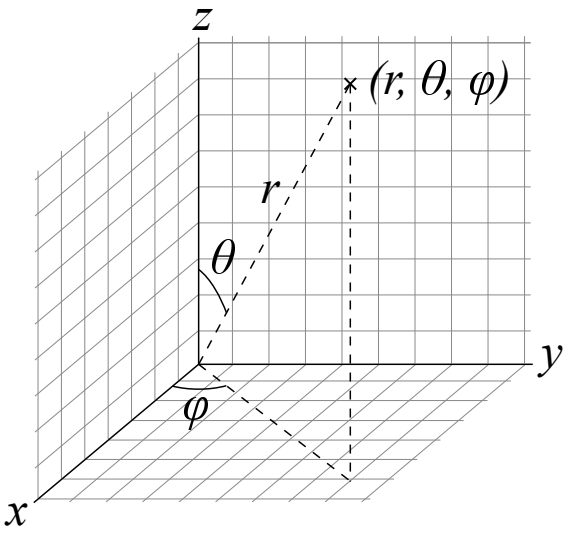

Figure 2.1: The reference system used in this thesis. [46]

2.2. Operation Theory of Conformal Arrays

A conformal array has a few important differences with respect to ordinary planar arrays. Firstly, when scanning to a particular direction, some elements may become obscured by the array itself due to its three dimensional shape. This can be seen in figure 2.2 which displays an array with a hemispherical shape. Only part of all of its elements is visible as the rest of the points is obscured and subsequently left out of the plot.

Secondly, in a planar array, generally the broadside direction of all elements are oriented in the same direction. However, in a conformal array, the antenna element broadside directions are generally oriented in multiple different directions. This can also be seen in figure 2.2. In this figure, the element

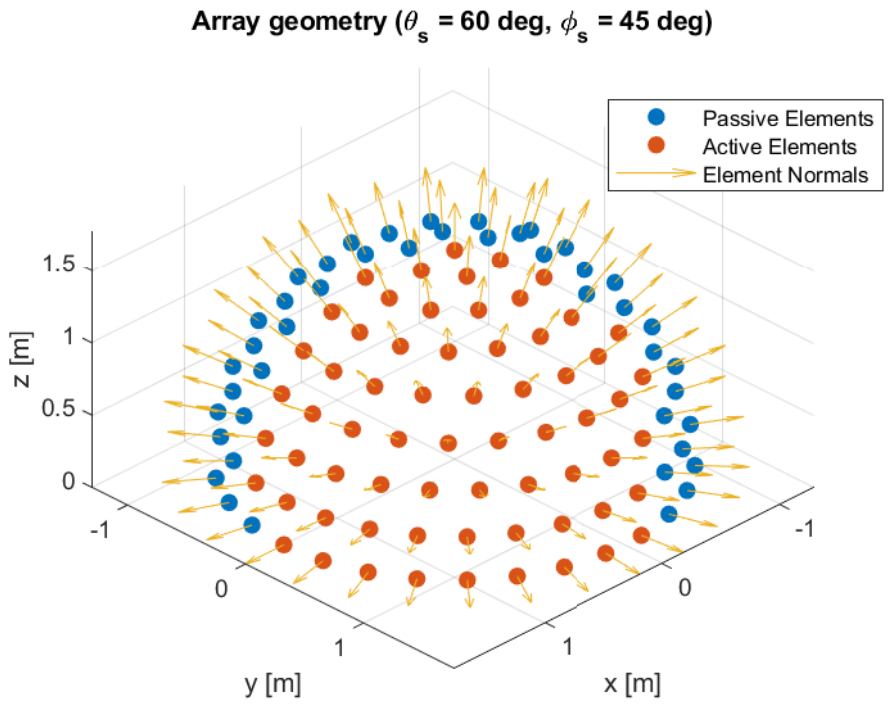

Figure 2.2: An conformal array with the active elements indicated with red circles for a maximum scan angle of 60° and a scan angle of θ_s of 60° and ϕ_s of 45°.

broadside directions are indicated by the element normal vectors, since the elements are all placed normal to the surface of the conformal array. Because the orientations of the antenna elements are different, the scan angle for each element is a different angle in its local coordinate system. Since the radiation patterns of real antennas are non-isotropic and dependent on angle, effectively an amplitude taper is generated. Such an amplitude taper causes the main beam to broaden [47].

In order to deal with these problems, only the elements that can see the scan angle within a certain maximum angle from their broadside directions are activated. This angle is indicated by the (local) maximum scan angle. Throughout this thesis, this angle is set to 60°, since this scan angle is generally considered to be achievable without too much difference in radiation intensity between the active antenna elements.

2.3. Analysis of Conformal Array Radiation Patterns

In order to find an expression for the electric far-field of a (conformal) array, the first step is to derive the electric far-field radiated by an antenna element in the array. This can be done by using the Green's functions. We recall that a Green's function is the impulse response of an elementary current. Therefore, performing a convolution of an arbitrary element i represented by an equivalent electric current $\vec{J}_i^{eq}$ and an equivalent magnetic current $\vec{M}_i^{eq}$ and the appropriate Green's functions as shown in equation 2.1 gives the field radiated by the i-th element $\vec{E}_i$ [48]. It should further be noted that $\vec{r}$ is the vector to the observation location and the vector $\vec{r}'$ indicates the location of the equivalent current sources.

$$\vec{E}_i(\vec{r}) = \iiint_{V'} \underline{\underline{\mathbf{G}}}_{fs}^{E,J}(\vec{r}-\vec{r}')\,\vec{J}_i^{eq}(\vec{r}')\,d\vec{r}' + \iiint_{V'} \underline{\underline{\mathbf{G}}}_{fs}^{E,M}(\vec{r}-\vec{r}')\,\vec{M}_i^{eq}(\vec{r}')\,d\vec{r}' \tag{2.1}$$

The Green's functions are represented using dyadic functions, their full forms are given in equation 2.2 and 2.3 [48].

$$\underline{\underline{\mathbf{G}}}_{fs}^{E,J}(\vec{r}-\vec{r}') = -j\frac{\zeta}{k}\begin{bmatrix} k^2+\frac{\partial^2}{\partial x^2} & \frac{\partial^2}{\partial x\partial y} & \frac{\partial^2}{\partial x\partial z} \\ \frac{\partial^2}{\partial x\partial y} & k^2+\frac{\partial^2}{\partial y^2} & \frac{\partial^2}{\partial y\partial z} \\ \frac{\partial^2}{\partial x\partial z} & \frac{\partial^2}{\partial y\partial z} & k^2+\frac{\partial^2}{\partial z^2} \end{bmatrix}\frac{e^{-jk|\vec{r}-\vec{r}'|}}{4\pi|\vec{r}-\vec{r}'|} \tag{2.2}$$

$$\underline{\underline{\mathbf{G}}}_{fs}^{E,M}(\vec{r}-\vec{r}') = -\begin{bmatrix} 0 & -\frac{\partial}{\partial z} & \frac{\partial}{\partial y} \\ \frac{\partial}{\partial z} & 0 & -\frac{\partial}{\partial x} \\ -\frac{\partial}{\partial y} & \frac{\partial}{\partial x} & 0 \end{bmatrix}\frac{e^{-jk|\vec{r}-\vec{r}'|}}{4\pi|\vec{r}-\vec{r}'|} \tag{2.3}$$

In equations 2.2 and 2.3 the free space impedance is represented by ζ and the wave vector k can be found using equation 2.4.

$$k = \frac{2\pi f}{c} = \frac{2\pi}{\lambda} \tag{2.4}$$

These dyadic expressions can also be written in a simpler form, first we introduce the scalar Green's function $G_0(\vec{r})$ defined in equation 2.5.

$$G_0(\vec{r}-\vec{r}') = \frac{e^{-jk|\vec{r}-\vec{r}'|}}{4\pi|\vec{r}-\vec{r}'|} \tag{2.5}$$

By introducing the $\nabla\nabla$ operator, which can be read as the multiplication of the gradient operator as column vector with the gradient as row vector, equation 2.6 is found. In this equation $\underline{\underline{\mathbf{I}}}$ is an identity matrix as dyad.

$$\vec{E}_i(\vec{r}) = \iiint_{V'} -j\omega\mu\left(\underline{\underline{\mathbf{I}}}+\frac{1}{k^2}\nabla\nabla\right)G_0(\vec{r}-\vec{r}')\,\vec{J}_i^{eq}(\vec{r}')\,d\vec{r}' - \iiint_{V'}\left(\nabla\times\underline{\underline{\mathbf{I}}}\right)G_0(\vec{r}-\vec{r}')\,\vec{M}_i^{eq}(\vec{r}')\,d\vec{r}' \tag{2.6}$$

Equation 2.6 is valid everywhere in the near- and far-fields but is not easily solvable since the equation still contains derivatives. However, by making some approximations to limit the scope of equation 2.6 to the far-field, equation 2.6 loses its derivatives. First we introduce the vector $\vec{R}$ which is equal to $\vec{r}-\vec{r}'$. This can be alternatively written as $R\hat{R}$, with $R = |\vec{R}|$. In the same manner, $\vec{r}$ can be written as $r\hat{r}$ and $\vec{r}'$ as $r'\hat{r}'$ with $r = |\vec{r}|$ and $r' = |\vec{r}'|$. Because the observation point is in the far-field, $r \gg r'$ and because of this, $\hat{R} \approx \hat{r}$. Using this in equation 2.6, we find equation 2.7.

$$\vec{E}_i(\vec{r}) = \iiint_{V'} -j\omega\mu\left(\underline{\underline{\mathbf{I}}}+\frac{1}{k^2}\nabla\nabla\right)G_0\left(\vec{R}\right)\vec{J}_i^{eq}(\vec{r}')\,d\vec{r}' - \iiint_{V'}\left(\nabla\times\underline{\underline{\mathbf{I}}}\right)G_0\left(\vec{R}\right)\vec{M}_i^{eq}(\vec{r}')\,d\vec{r}' \tag{2.7}$$

The gradient of the scalar Green's function in radial coordinates can be found as shown in equation 2.8 [48].

$$\nabla G_0(\vec{R}) = -(j+\frac{1}{kr})kG_0(\vec{R})\hat{R} \tag{2.8}$$

If the assumption $R \gg \frac{1}{k}$ is made, the curl and $\nabla\nabla$ operators change to vector operations as displayed in equation 2.7. This is because the $\frac{1}{r}$ term becomes negligible and therefore the gradient of the scalar Green's function is approximately equal to a multiplication of the scalar Green's function with $-jk\hat{R}$. This results in an expression for the far-field with the radiative Green's functions as shown in equation 2.9.

$$\vec{E}_i^{FF}(\vec{r}) = -j\omega\mu\iiint_{V'}\left(\underline{\underline{\mathbf{I}}}-\hat{R}\hat{R}\right)G_0(\vec{r}-\vec{r}')\,\vec{J}_i^{eq}(\vec{r}')\,d\vec{r}' + jk\iiint_{V'}\left(\hat{R}\times\underline{\underline{\mathbf{I}}}\right)G_0(\vec{r}-\vec{r}')\,\vec{M}_i^{eq}(\vec{r}')\,d\vec{r}' \tag{2.9}$$

Secondly, because the observation point is far away compared to the vector pointing to the source integration points, it can be said that the vector from the origin to the observation point is parallel to the vector from the integration point to the observation point. Therefore, $\hat{R} \approx \hat{r}$. Since $\hat{R}$ is no longer a function of the integration variable $\hat{r}'$, it can be taken out of the integral resulting in equation 2.10.

$$\vec{E}_i^{FF}(\vec{r}) = -j\omega\mu\left(\underline{\underline{\mathbf{I}}}-\hat{r}\hat{r}\right)\iiint_{V'}G_0(\vec{r}-\vec{r}')\,\vec{J}_i^{eq}(\vec{r}')\,d\vec{r}' + jk\left(\hat{r}\times\underline{\underline{\mathbf{I}}}\right)\iiint_{V'}G_0(\vec{r}-\vec{r}')\,\vec{M}_i^{eq}(\vec{r}')\,d\vec{r}' \tag{2.10}$$

Now we notice the denominator of the scalar Green's function as shown in equation 2.5. When considering the far-field, $\vec{r} \gg \vec{r}'$ due to the fact that $\hat{r}'$ is very small in comparison to $\hat{r}$. Therefore, the denominator of equation 2.5 can be approximated by $4\pi r$, where r is the distance to the observation point. Therefore, the denominator of the scalar Green's function is no longer dependent on $\vec{r}'$ and thus also can be taken outside of the integrals. This leads to equation 2.11.

$$\vec{E}_i^{FF}(\vec{r}) = -\frac{j\omega\mu}{4\pi r}\left(\underline{\underline{\mathbf{I}}} - \hat{r}\hat{r}\right)\iiint_{V'} e^{-jk|\vec{r}-\vec{r}'|}\vec{J}_i^{eq}(\vec{r}')\,d\vec{r}' + \frac{jk}{4\pi r}\left(\hat{r}\times\underline{\underline{\mathbf{I}}}\right)\iiint_{V'} e^{-jk|\vec{r}-\vec{r}'|}\vec{M}_i^{eq}(\vec{r}')\,d\vec{r}' \tag{2.11}$$

Next, we consider the exponential phase term in the integral. This term cannot be easily approximated by r since the difference with $|\vec{r}-\vec{r}'|$ may still be comparable to the wavelength λ. If this is the case, a significant phase shift can occur that leads to wrong results. To eliminate this possibility, a more elaborate approximation is required. To derive this approximation, we first consider equation 2.12 [49].

$$\begin{aligned}|\vec{r}-\vec{r}'| &= \sqrt{(r_x^2+r_y^2+r_z^2)+(r_x'^2+r_y'^2+r_z'^2)-2(r_xr_x'+r_yr_y'+r_zr_z')}\\ &= \sqrt{r^2+r'^2+2(\vec{r}\cdot\vec{r}')}\\ &= r\sqrt{1+\frac{r'^2}{r^2}+2\frac{r'}{r}(\hat{r}\cdot\hat{r}')}\end{aligned} \tag{2.12}$$

We notice that 2.12 is of the form $r\sqrt{1+x}$ with $x = \frac{r'^2}{r^2}+2\frac{r'}{r}(\hat{r}\cdot\hat{r}')$. The $\sqrt{1+x}$ term can be approximated by its Taylor series of which we consider the first three terms. This results in equation 2.13.

$$\begin{aligned}|\vec{r}-\vec{r}'| &= r\sqrt{1+x}\\ &\approx r\left(1+\frac{1}{2}x-\frac{1}{8}x^2\right)\\ &\approx r\left(1-\frac{r'}{r}(\hat{r}\cdot\hat{r}')+\frac{1}{2}\left(\frac{r'}{r}\right)^2\left(1-(\hat{r}\cdot\hat{r}')^2\right)+\frac{1}{2}\left(\frac{r'}{r}\right)^3(\hat{r}\cdot\hat{r}')-\frac{1}{8}\left(\frac{r'}{r}\right)^4\right)\end{aligned} \tag{2.13}$$

Since $r \gg r'$ in the far-field, the $r\left(1-\frac{r'}{r}(\hat{r}\cdot\hat{r}')\right)$ part is dominant in equation 2.13. Because this dominant term is the result of only the first order term of the Taylor series expansion of $\sqrt{1+x}$ and the higher order terms of the expansion result only in terms that vanish in the far-field, the final approximation in equation 2.14 is found.

$$|\vec{r}-\vec{r}'| \approx r - r'(\hat{r}\cdot\hat{r}') \tag{2.14}$$

Now phase error ϕ_{error} of this approximation is calculated. This is shown in equation 2.15 [49].

$$\phi_{error} = k\Big(|\vec{r}-\vec{r}'| - \big(r - r'(\hat{r}\cdot\hat{r}')\big)\Big) \tag{2.15}$$

Since 2.14 is effectively the dominant term of the Taylor series expansion of $|\vec{r}-\vec{r}'|$, the phase error is basically the non-dominant terms of the expansion multiplied by k. Since we are considering the far-field and therefore $r \gg r'$, the phase error is by approximation equivalent to the next-dominant term multiplied by k as shown in equation 2.16.

$$\phi_{error} \approx \frac{kr'^2}{2r}\left(1-(\hat{r}'\hat{r})^2\right) \tag{2.16}$$

The phase error is largest in the case when $\vec{r}' = \vec{r}'_{max}$ and $\hat{r}'$ and $\hat{r}$ are orthogonal to each other. In this case the dot product of $\hat{r}$ and $\hat{r}'$ is 0. $\vec{r}'_{max}$ indicates the largest dimension of the source. Therefore, the worst case phase error is given by approximation 2.17.

$$\phi_{error,worst} \approx \frac{k}{2}\frac{r'^2_{max}}{r} \approx \frac{\pi}{\lambda}\frac{r'^2_{max}}{r} \tag{2.17}$$

Now that an approximation for the phase error is known, it is now possible to assign an upper bound on this error and calculate the region for which approximation 2.14 is valid. Using a value of $\frac{\pi}{8}$ for this upper bound of the phase error leads to equation 2.18.

$$\begin{aligned} \phi_{error,worst} &\leq \frac{\pi}{8} \\ \frac{\pi}{\lambda}\frac{r'^2_{max}}{r} &\leq \frac{\pi}{8} \\ r &\geq \frac{8r'^2_{max}}{\lambda} \end{aligned} \tag{2.18}$$

When condition 2.18 is met, the observation point is located in the Fraunhofer region and in this region approximation 2.14 is valid [49]. Using this approximation allows for taking out the r-dependency of the exponential term and leads to equation 2.19.

$$\vec{E}_i^{FF}(\vec{r}) = -j\omega\mu\frac{e^{-jkr}}{4\pi r}\left(\underline{\underline{\mathbf{I}}} - \hat{r}\hat{r}\right)\iiint_{V'} e^{jk\vec{r}'\hat{r}}\vec{J}_i^{eq}(\vec{r}')\,d\vec{r}' + jk\frac{e^{-jkr}}{4\pi r}\left(\hat{r}\times\underline{\underline{\mathbf{I}}}\right)\iiint_{V'} e^{jk\vec{r}'\hat{r}}\vec{M}_i^{eq}(\vec{r}')\,d\vec{r}' \tag{2.19}$$

Introducing the wave vector $\vec{k} = k\hat{r}$ finally results in equation 2.20.

$$\vec{E}_i^{FF}(\vec{r}) = -j\omega\mu\frac{e^{-jkr}}{4\pi r}\left(\underline{\underline{\mathbf{I}}} - \hat{r}\hat{r}\right)\iiint_{V'} e^{j\vec{k}\vec{r}'}\vec{J}_i^{eq}(\vec{r}')\,d\vec{r}' + jk\frac{e^{-jkr}}{4\pi r}\left(\hat{r}\times\underline{\underline{\mathbf{I}}}\right)\iiint_{V'} e^{j\vec{k}\vec{r}'}\vec{M}_i^{eq}(\vec{r}')\,d\vec{r}' \tag{2.20}$$

We recall that this derivation is valid under the conditions that $r \gg \frac{1}{k}$, $r \gg r'_{max}$ and $r \geq \frac{8r'^2_{max}}{\lambda}$. This is clearly the case for solar observation at 10 MHz, since at this frequency $k = 0.21$, $\lambda = 30$ metre and the distance to the Sun is 149.6 million kilometres. In order for the Sun to be outside of the Fraunhofer region, the array should be more than 748 km wide.

Subsequently, we look at what happens when the source is translated to a certain position in 3D space, indicated by $\vec{p}_i$. This can be done by replacing the argument $\vec{r}'$ of the electric and magnetic current distributions in equation 2.20 by $\vec{r}' - \vec{p}_i$. This results in equation 2.21.

$$\begin{aligned} \vec{E}_{i,trans}^{FF}(\vec{r}) = &-j\omega\mu\frac{e^{-jkr}}{4\pi r}\left(\underline{\underline{\mathbf{I}}} - \hat{r}\hat{r}\right)\iiint_{V'} e^{j\vec{k}\vec{r}'}\vec{J}_i^{eq}(\vec{r}' - \vec{p}_i)\,d\vec{r}' + \\ &jk\frac{e^{-jkr}}{4\pi r}\left(\hat{r}\times\underline{\underline{\mathbf{I}}}\right)\iiint_{V'} e^{j\vec{k}\vec{r}'}\vec{M}_i^{eq}(\vec{r}' - \vec{p}_i)\,d\vec{r}' \end{aligned} \tag{2.21}$$

Applying a substitution of $\vec{r}'' = \vec{r}' - \vec{p}_i$ yields equation 2.22.

$$\begin{aligned} \vec{E}_{i,trans}^{FF}(\vec{r}) = &-j\omega\mu\frac{e^{-jkr}}{4\pi r}\left(\underline{\underline{\mathbf{I}}} - \hat{r}\hat{r}\right)\iiint_{V''} e^{j\vec{k}\vec{r}''+\vec{p}_i}\vec{J}_i^{eq}(\vec{r}'')\,d\vec{r}'' + \\ &jk\frac{e^{-jkr}}{4\pi r}\left(\hat{r}\times\underline{\underline{\mathbf{I}}}\right)\iiint_{V''} e^{j\vec{k}\vec{r}''+\vec{p}_i}\vec{M}_i^{eq}(\vec{r}'')\,d\vec{r}'' \end{aligned} \tag{2.22}$$

Now we take out the $e^{j\vec{k}\vec{p}_i}$ term, resulting in equation 2.23.

$$\begin{aligned} \vec{E}_{i,trans}^{FF}(\vec{r}) = &e^{j\vec{k}\vec{p}_i}\left(-j\omega\mu\frac{e^{-jkr}}{4\pi r}\left(\underline{\underline{\mathbf{I}}} - \hat{r}\hat{r}\right)\iiint_{V''} e^{j\vec{k}\vec{r}''+\vec{p}_i}\vec{J}_i^{eq}(\vec{r}'')\,d\vec{r}'' + \right. \\ &\left. jk\frac{e^{-jkr}}{4\pi r}\left(\hat{r}\times\underline{\underline{\mathbf{I}}}\right)\iiint_{V''} e^{j\vec{k}\vec{r}''+\vec{p}_i}\vec{M}_i^{eq}(\vec{r}'')\,d\vec{r}''\right) \end{aligned} \tag{2.23}$$

Lastly, we notice that because the domain of the integrals have translated with the same amount as $\vec{r}'$ itself, the integrals are the same as the untranslated integrals. This finally results in equation 2.24, which shows that a translation of the source corresponds with multiplication of $e^{j\vec{k}\vec{p}_i}$ with the original untranslated field.

$$\vec{E}_{i,trans}^{FF}(\vec{r}) = e^{j\vec{k}\vec{p}_i}\vec{E}_i^{FF}(\vec{r}) \tag{2.24}$$

Next, the field for a number of sources is derived. Because of the superposition principle, the fields of all sources can be added together to find the total field. However, when sources are placed in the vicinity of each other, the sources start to influence each other by means of mutual coupling. This mutual coupling influences the equivalent magnetic and electric current sources. Therefore, $\vec{E}_i^{FF}(\vec{r})$ in equation 2.24 is the active element pattern (AEP) of the i-th element which includes mutual coupling and thus should not be confused with the field that the source radiates when no other sources are present. By using superposition, the total field of a total number N antenna elements can thus be found using equation 2.25, where $\vec{E}_i^{FF}(\vec{r})$ is the AEP of the i-th element.

$$\vec{E}_{tot}^{FF}(\vec{r}) = \sum_{i=1}^{N} \vec{E}_i^{FF}(\vec{r}) e^{j\vec{k}\vec{p}_i} \tag{2.25}$$

To control the radiation pattern of the array, the active element pattern of the elements can be modified by multiplying them with factor $A_i e^{j\beta_i}$. This multiplication factor can be implemented by an attenuation and a phase shift of the received fields by the elements. This results in equation 2.26.

$$\vec{E}_{tot}^{FF}(\vec{r}) = \sum_{i=1}^{N} A_i e^{j\beta_i} \vec{E}_i^{FF}(\vec{r}) e^{j\vec{k}\vec{p}_i} = \sum_{i=1}^{N} A_i \vec{E}_i^{FF}(\vec{r}) e^{j\left(\vec{k}\vec{p}_i + \beta_i\right)} \tag{2.26}$$

The term e^{jx} has a maximum real value of 1, which occurs at $x = 0$. Therefore, when $\left(\vec{k}\vec{p}_i + \beta_i\right)$ in equation 2.26 equals 0 for every element at the same observation angle, all the active element patterns of the antenna elements will sum without attenuation of the exponent and maximum field strength is achieved. As shown in equation 2.27, $\vec{k}$ is a function of the observation angle θ and ϕ.

$$\vec{k} = k\hat{r} = \begin{bmatrix} k\sin(\theta)\cos(\phi) \\ k\sin(\theta)\sin(\phi) \\ k\cos(\theta) \end{bmatrix} \begin{bmatrix} \hat{x} \\ \hat{y} \\ \hat{z} \end{bmatrix} \tag{2.27}$$

Therefore, the phase compensation factor for each element β_i can be set according to equation 2.28 so that the field strength is maximum at a scan angle of θ_s and ϕ_s. By varying θ_s and ϕ_s, the main beam of the array can therefore effectively be steered. In equation 2.28, x_i, y_i and z_i indicate the location of the i-th element.

$$\beta_i = -\vec{k}(\theta_s, \phi_s)\vec{p}_i = -\begin{bmatrix} k\sin(\theta_s)\cos(\phi_s) \\ k\sin(\theta_s)\sin(\phi_s) \\ k\cos(\theta_s) \end{bmatrix} \cdot \begin{bmatrix} x_i \\ y_i \\ z_i \end{bmatrix} \tag{2.28}$$

The amplitude factor A_i in equation 2.26 can be used to enable or disable elements in the array by setting A_i to 1 or 0 respectively. Alternatively, A_i can also be used to apply a taper to the array. This taper can for example be exploited to reduce side lobes at the cost of a wider main beam.

Equation 2.26 is closely related to the array factor. Namely, if the active element patterns are isotropic, the equation represents the array factor. To demonstrate this, the array factor of a planar array is derived from equation 2.26. If the antenna elements are distributed in a rectangular pattern with M elements with an inter-element spacing of d_x along $\hat{x}$ and N elements with a spacing of d_y along $\hat{y}$ and a z-coordinate of 0, the location of the m,n-th element is defined by equation 2.29.

$$\vec{p}_i = \begin{bmatrix} (m-1)d_x \\ (n-1)d_y \\ 0 \end{bmatrix} \tag{2.29}$$

Using this position vector in accordance with the fact the $\hat{x}$ and $\hat{y}$ positions are not dependent on each other, equation 2.30 is found.

$$AF = \sum_{n=1}^{N} A_{n1} \left(\sum_{m=1}^{M} A_{m1} e^{j(m-1)(kd_x \sin\theta\cos\phi + \beta_x)} \right) e^{j(n-1)\left(kd_y \sin\theta\sin\phi + \beta_y\right)} \tag{2.30}$$

This equation is effectively the same as found in [50], thus demonstrating the relation to the array factor.

Finally, the power radiated as function of observation angle is derived. In the far-field, the electric and magnetic fields are related as shown in equation 2.31.

$$\vec{H}^{FF}(\vec{r}) = \frac{1}{\zeta}\hat{r} \times \vec{E}^{FF}(\vec{r}) \tag{2.31}$$

The power that is radiated in a certain direction can be found by using the Poynting vector. The time averaged Poynting vector for electromagnetic radiation is defined in equation 2.32, where H^* is the complex conjugate of H.

$$S = \frac{1}{2}\vec{E} \times \vec{H}^* \tag{2.32}$$

Substituting equation 2.31 in equation 2.32 leads to equation 2.33, in which ζ is the free space impedance.

$$\begin{aligned} S^{FF} &= \vec{E}^{FF} \times \left(\frac{1}{\zeta}\hat{r} \times \vec{E}^{FF}\right)^* \\ &= \frac{1}{2\zeta}|\vec{E}^{FF}|^2\hat{r} \end{aligned} \tag{2.33}$$

Therefore, the normalised radiated power from a generic conformal array is given by equation 2.34 and normalised in decibels in equation 2.35.

$$S^{FF}_{norm}(\theta,\phi) = \frac{|\vec{E}^{FF}_{tot}(\vec{r})|^2}{\max(|\vec{E}^{FF}_{tot}(\vec{r})|^2)} \tag{2.34}$$

$$S^{FF}_{norm,dB}(\theta,\phi) = 20\log\left(\frac{|\vec{E}^{FF}_{tot}(\vec{r})|}{\max(|\vec{E}^{FF}_{tot}(\vec{r})|)}\right) \tag{2.35}$$

From these equations, the half-power beam width can simply be found by looking at the the angles below and above the scan angle where the beam pattern first reaches a value of $\frac{1}{2}$ in equation 2.34 or -3 dB in equation 2.35. The difference between these angles is the half-power beam width.

2.4. Conclusions on Analysis

This chapter presented how conformal arrays are operated throughout this thesis project. Namely, antenna elements are enabled when the angle between the scan direction vector and the antenna normal vector is less than 60°.

Based on the active elements, the radiation pattern of the conformal array can be calculated by using superposition of the active element patterns of the antenna elements. By applying a phase shift per element depending on its location, the fields of the elements can be made to sum in phase at a specific scan angle. Hence, by this means, the beam can be steered.

In the next chapter, this method of analysis is used in accordance with isotropic active element patters allowing for far faster computations of the far-fields of conformal array configurations. This enables the computation of far-fields over scan angle for many different configurations instead of a only a few. In this way a novel comparison can be performed between many different array configurations on their half-power beam widths so that best configuration for application in DISTURB can be selected. Besides this, fast computation of far-fields also allow for determining general characteristics of conformal phased array radiation patterns.

3

Comparative Analysis of Conformal Array Configurations

This chapter describes how a suitable array configuration for application in the DISTURB project is selected. An array configuration is a combination of an array geometry and topology. The array geometry refers to the three-dimensional shape of the array and the array topology refers to the way elements are distributed on the array geometry. First, a few general characteristics of conformal array radiation patterns will be presented. Thereafter, numerous conformal array configurations are analysed. Finally, a novel comparison of these configurations is performed and the most beneficial array configuration is selected. The selected configuration is also the configuration that is used throughout the rest of this thesis.

3.1. General Radiation Pattern Characteristics of Conformal Arrays

This section provides insight into some properties of the behaviour of radiation patterns of conformal arrays. In order to make fair comparisons between several configurations, isotropic radiation patterns are used even though isotropic radiators do not exist in reality. By using isotropic radiation patterns, no accidental amplitude taper is generated by the mechanism explained in section 2.2 which may increase the HPBW. In this way, array configurations can be purely compared on a basis of array factor. Next to this, isotropic patterns also simplify the computational load, since the radiation patterns of the elements do not have to be taken into account.

3.1.1. Half-Power Beam Width versus Frequency

First, the behaviour of the HPBW versus frequency is investigated. The array displayed in figure 3.1 is scanned to an angle of $\theta_s = 0°$ and $\phi_s = 0°$ and the radiation pattern is evaluated at frequencies of 1500 MHz, 2250 MHz and 3000 MHz. The $\phi = 0°$ cuts are shown in figure 3.2.

As seen from this figure, the beam width at 1500 MHz is approximately 6 degrees, at 2250 MHz 4 degrees and at 3000 MHz 3 degrees. In free space, 1500 MHz corresponds to a wavelength of 20 centimetres, 2250 MHz corresponds to 13.3 centimetres and 3000 MHz to 10 centimetres. It is noticed that the wavelength at 1500 MHz is twice as long as the wavelength at 3000 MHz and the HPBW is also twice as large, as can be seen in figure 3.2. The same is true for 2250 MHz, at which the frequency is 1.3 times the wavelength at 3000 MHz and also the HPBW is 1.3 times as large. Therefore, the equation 3.1 follows.

$$HPBW \propto \lambda \propto \frac{1}{f} \tag{3.1}$$

Combining this equation with the requirements on half-power beam width from section 1.3.1, a maximum possible operating frequency range can be found. At 3000 MHz the HPBW is minimum and should have a value of 2 degrees. Since the maximum acceptable HPBW is 15 degrees, it can be found that HPBW can grow by a factor of $\frac{15°}{2°} = 7.5$. Therefore, the lowest possible operating frequency can

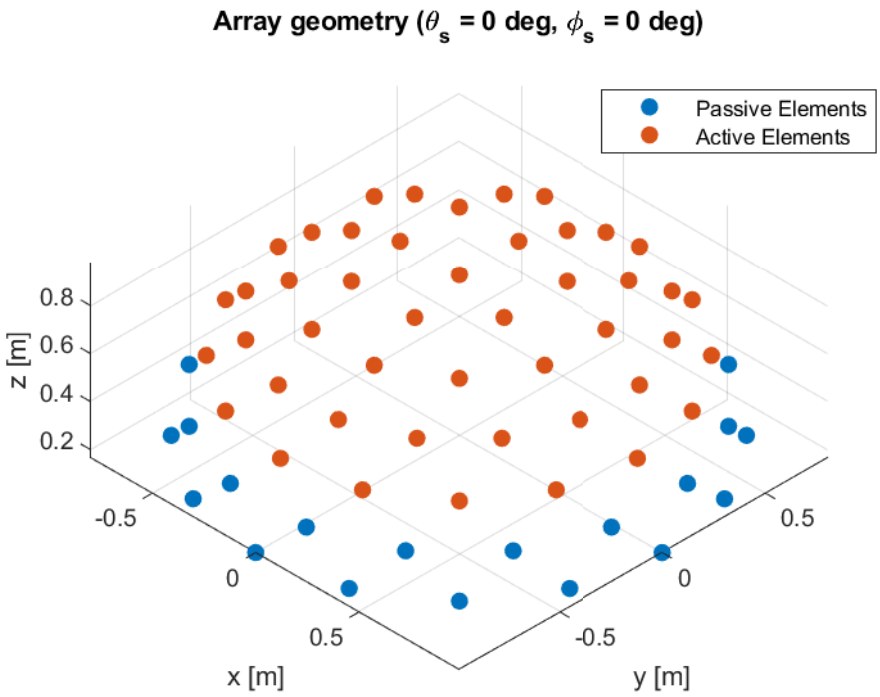

Figure 3.1: The array geometry used for the beam width comparison in figure 3.2.

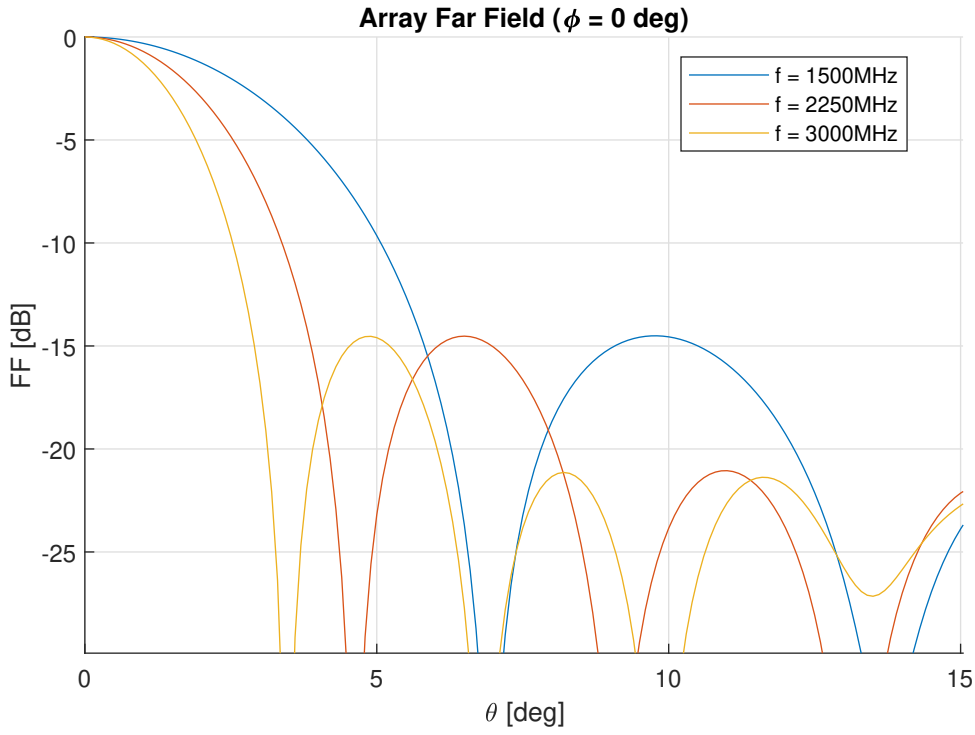

Figure 3.2: Comparison of beam widths at 1500, 2250 and 3000 MHz for the array geometry displayed in figure 3.1.

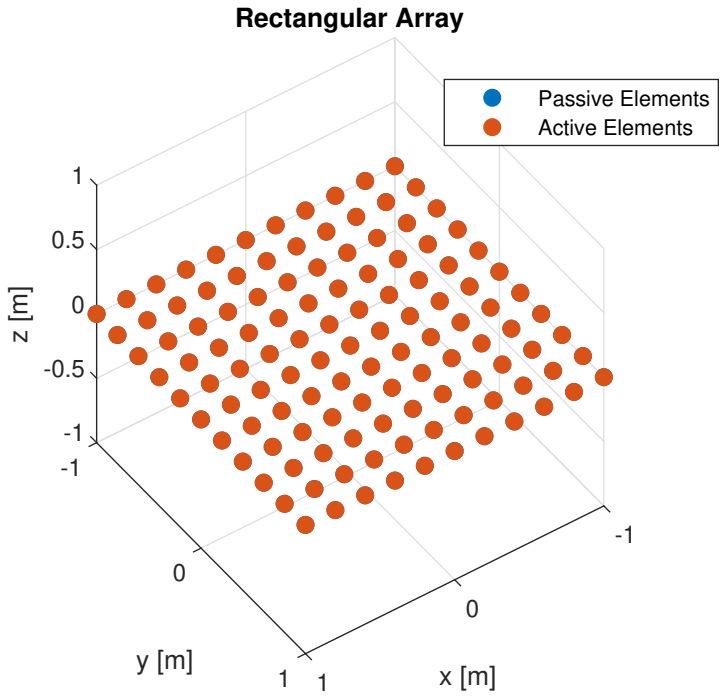

Figure 3.3: Periodic rectangular array used for generating the radiation patterns in figure 3.4.

be found by dividing 3000 MHz by 7.5, resulting in 400 MHz. Thus, the maximum possible operating frequency range spans from 400 MHz to 3000 MHz.

3.1.2. Grating Lobes in Conformal Arrays

In conformal arrays, grating lobes do not manifest themselves in the way that they do in regular planar arrays. In planar arrays with a sparse element spacing, i.e. an element spacing large in comparison with the wavelength, grating lobes tend to also sum in phase at observation angles other than the scan direction. This leads to the radiation pattern reaching the same value as the main beam at undesired angles. This in turn results in the fact that signals from a not-of-interest source located in some other direction are picked up with the same strength as the signals from the source of interest, thus potentially causing severe interference.

The fact that regular periodic planar arrays do suffer from grating lobes and conformal arrays do not can be understood as follows. Assume a periodic planar array, i.e. a rectangular array that consists of eleven elements in along $\hat{x}$ and eleven elements along $\hat{y}$ with an element spacing of 20 centimetres as displayed in figure 3.3. The corresponding radiation patterns at 1500 and 3000 MHz are displayed in figure 3.4. From this radiation pattern it can be seen that at 1500 MHz, there is no grating lobe. This is as expected since no grating lobe should appear for a scan angle of $\theta_s = 0°$ when the element spacing is lower or equal to one λ. However, at 3000 MHz, a grating lobe can be noticed at $\theta = 30°$ since the element spacing is 2λ at this frequency.

Next, this rectangular array is projected on a hemisphere with a radius of $\sqrt{2}$ metre, resulting in the array configuration displayed in 3.5. This breaks the periodicity along $\hat{z}$ and results in the grating lobes disappearing and re-emerging as side lobes, as can be seen in figure 3.6. To conclude, as long as conformal arrays do not have any periodicity along all three axis, which for most conformal arrays is true as their elements are projected on 3D shapes, they do not suffer from grating lobes. However, this suppression of grating lobes may come at the price of an increased side lobe level as high side lobes may originate from grating lobes. This origination results from the fact that the irregularity along $\hat{z}$ may be negligible locally.

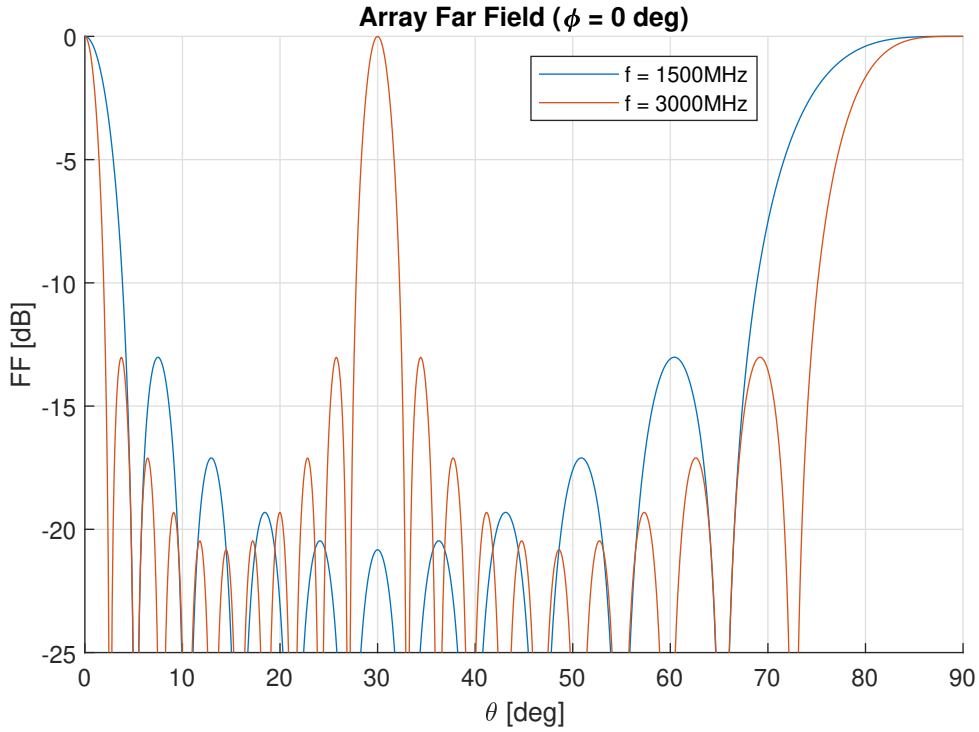

Figure 3.4: Comparison of the radiation patterns at 1500 and 3000 MHz for the array geometry displayed in figure 3.3.

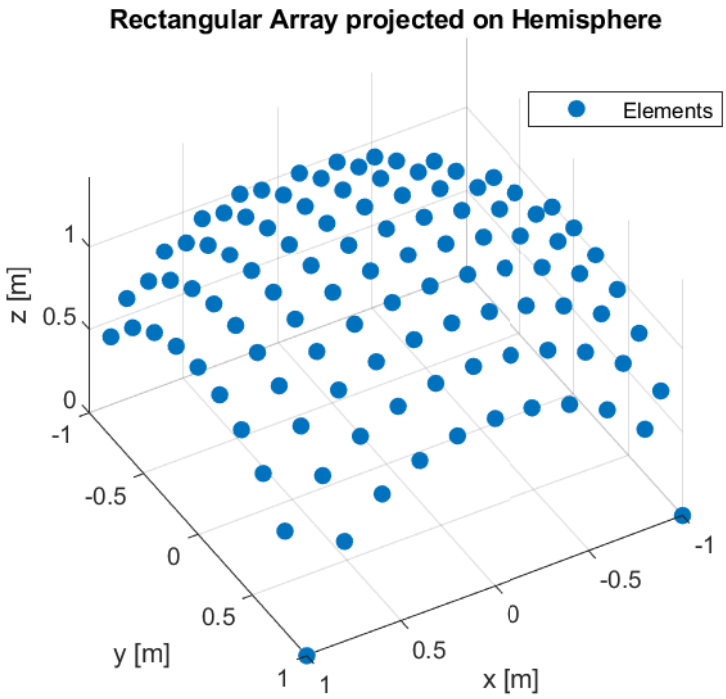

Figure 3.5: Periodic rectangular array of figure 3.3 projected on a hemisphere with a radius of $\sqrt{2}$.

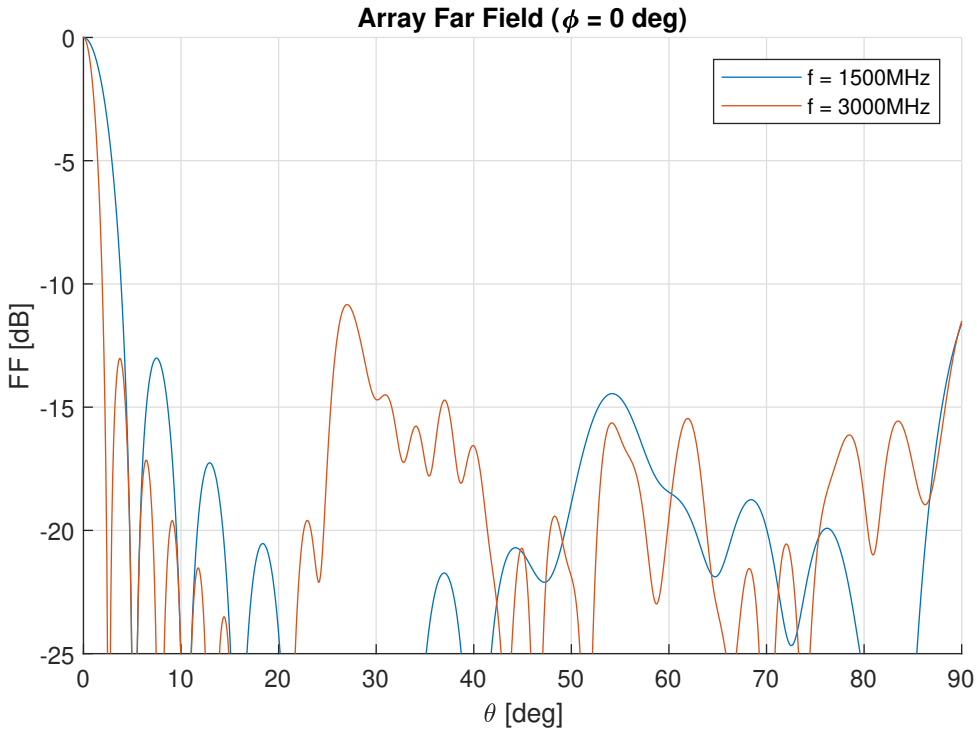

Figure 3.6: Comparison of the radiation patterns at 1500 and 3000 MHz for the array geometry displayed in figure 3.5.

3.1.3. Array Topology

Lastly, the effects of array topology, i.e. the way the antenna elements are distributed on the array geometry, are discussed. First, the effect of the density of the antenna elements is discussed and secondly the effect of the lattice or pattern in which the elements are distributed is investigated.

As seen from section 3.1.2, most conformal arrays do not suffer from grating lobes. However, the side lobe levels of these conformal arrays can be significantly large. These increased side lobe levels may still be caused by large inter-element spacing resulting in side lobes reminiscent of grating lobes. The side lobe level may therefore potentially be reduced by increasing the density of an array topology, just as with increasing the density of a planar array increases the upper frequency at which no grating lobes are present. The radiation patterns in figure 3.7 belong to an array configuration as displayed in 3.5, but with an inter-element spacing of 10 centimetres instead of 20 centimetres before projection. Also, the outer dimensions of this array still span 2 metre, similar to the array from figure 3.5, thus it can be said that the element density of the array has been increased. From figure 3.7, it can be seen that the side lobe level indeed has decreased significantly compared to the side lobe level in figure 3.5. Another advantage of an increased-density topology is that it may be possible to apply more sophisticated amplitude tapers which could reduce the side lobe level even further. However, the effect of mutual coupling becomes more severe.

Subsequently, the effect of array topology on HPBW is investigated. For this, the radiation patterns and beam widths over scan angle are computed for three arrays with a hemispherical geometry and different topologies. These topologies are the so-called arclength topology (figure 3.8a), the novel geodesic topology (figure 3.8b) and the novel HEALPix topology (figure 3.8c). These three topologies strive to distribute points as evenly as possible on a spherical geometry. The way in which these topologies are generated is elaborated upon in section 3.2.

In figure 3.9, a comparison of the beam widths is presented. As can be seen, the beam widths of the topologies are about equal. However, there is a small difference at scan angles near the horizon with the arclength topology having a small advantage. This is explained by the fact that the effective aperture is a bit larger due to some elements just being within 60 degrees from the scan angle whereas in the other topologies, those elements are just outside. As the element density increases, this advantage disappears. Therefore, it can be concluded that the topology has no significant influence on the beam

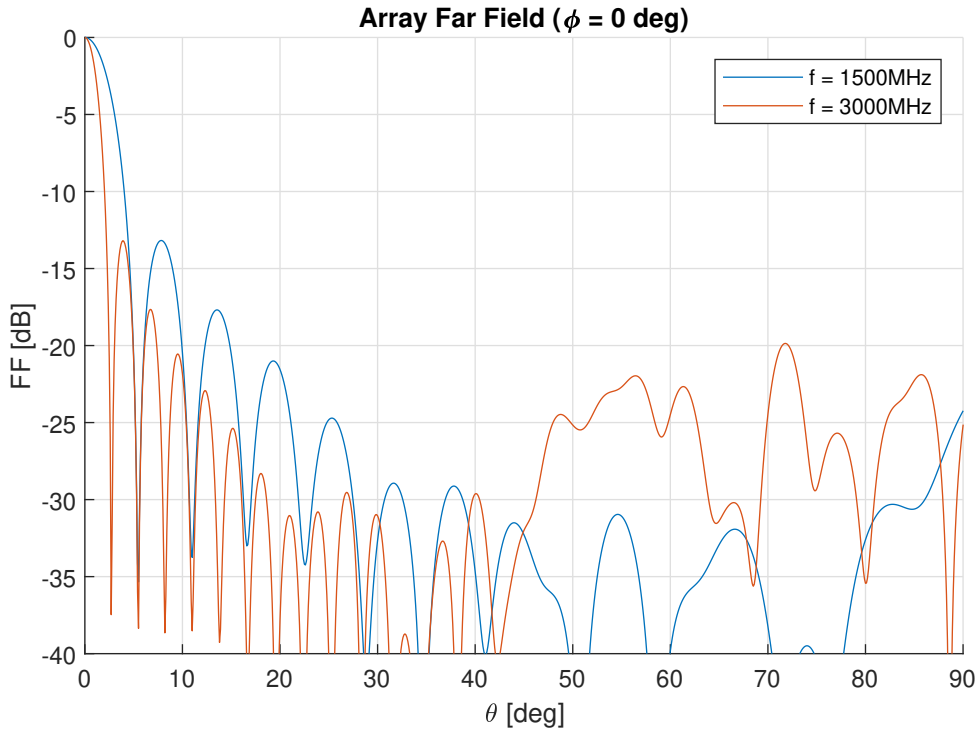

Figure 3.7: Radiation patterns at 1500 and 3000 MHz for an array configuration similar to the one from figure 3.5 but with an inter-element spacing of 10 instead of 20 centimetres before projection on a hemisphere.

width.

Finally, the effect of topology on side lobe level is investigated when the elements are placed densely. This is done by comparing two spherical arrays with the two novel geodesic and HEALPix topolgies of the same size and the about the same number of elements. Both arrays have a radius of 0.5 metres. The generated geodesic array has 812 elements and the HEALPix array has 768 elements. The number of elements cannot be exactly the same for both configurations as the HEALPix and geodesic grids cannot exist out of an arbitrary amount of elements, this is further elaborated upon in section 3.2.12. Plots of the arrays for scanning to zenith are shown in figures 3.10a and 3.10b. A comparison of the radiation patterns cuts at which the side lobe levels are highest for these two topologies is shown in figure 3.11. From this figure, it can be seen that the side lobe levels are about -13.60 and -15.05 dB respectively for the geodesic and HEALPix spherical arrays. As expected, the half-power beam widths are the same for both arrays as they have the same diameter.

Besides scanning to zenith, also a scan angle of $\theta_s = 90°$ and $\phi_s = 30°$ is considered. Figures 3.12a and 3.12b show what the active apertures of both array topologies look like at this scan angle. Figure 3.13 shows a comparison of the critical far-field cuts at which the side lobe level is maximum for these two arrays for said scan angle. This figure shows that the side lobe level of the geodesic array in this case is -15.62 dB while that of the HEALPix array is -14.62 dB.

Figures 3.11 and 3.13 show that when scanning to zenith, the HEALPix topology performs better and when scanning to $\theta_s = 90°$ and $\phi_s = 30°$, the geodesic topology has a lower side lobe level. Therefore, it can be concluded that the topology of the array has influence on the side lobe levels and that the side lobe level is dependent on the scan angle as element lattices in the active aperture are varying with scan angle.

As there are no requirements in 1.3.1 on side lobe levels, this factor is not taken into consideration in the following sections.

3.2. Analysis of Conformal Array Configurations

As geometries of conformal arrays can have almost any three-dimensional shape, the possibilities are infinite. Therefore, not every possible array configuration can be considered and thus it is hard to

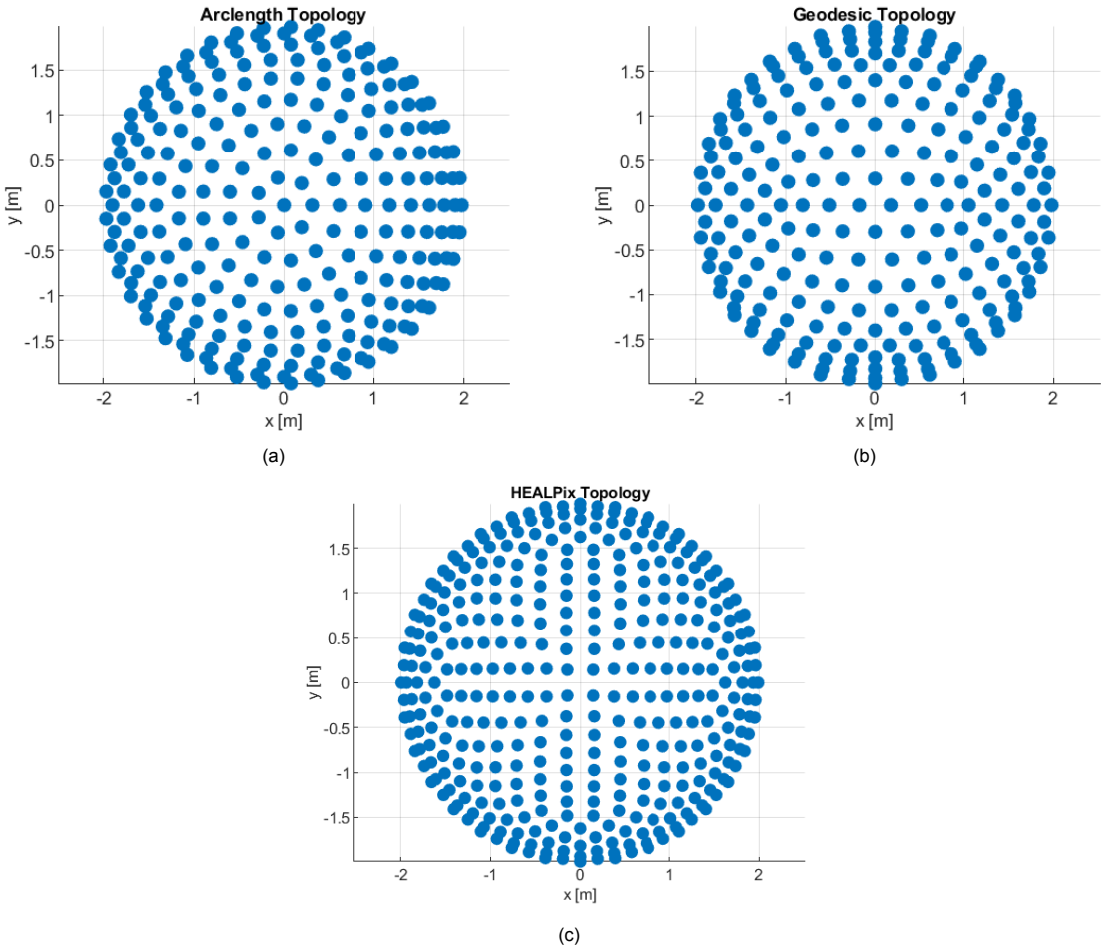

Figure 3.8: (a) The arclength topology (b) The geodesic topology (c) the HEALPix topology.

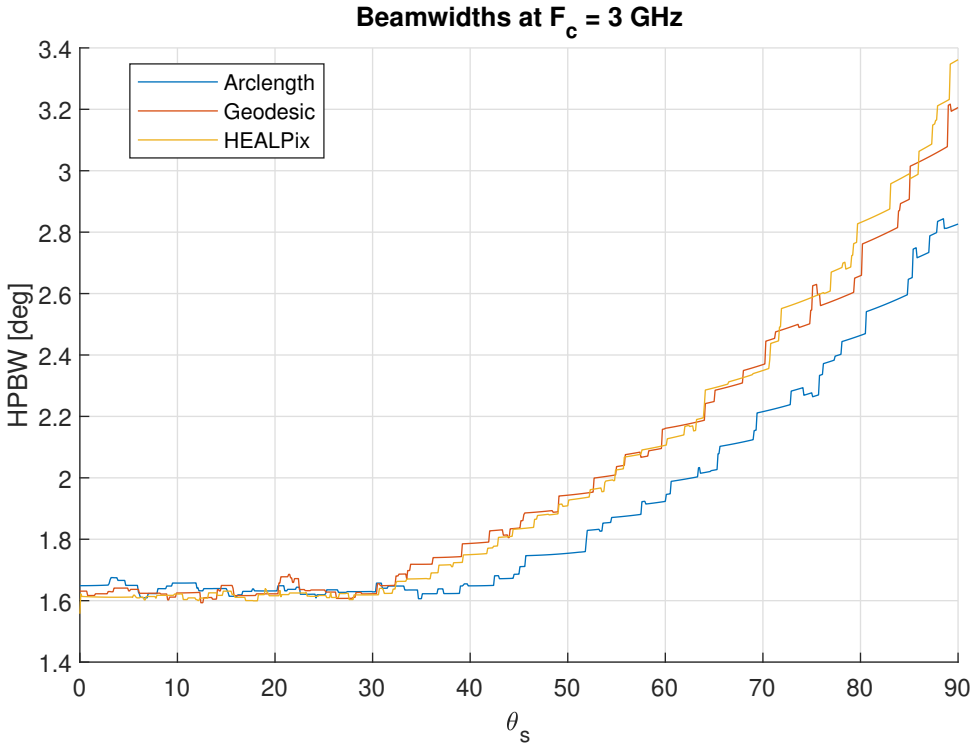

Figure 3.9: Comparison of the HPBW for several array topologies as function of scan angle.

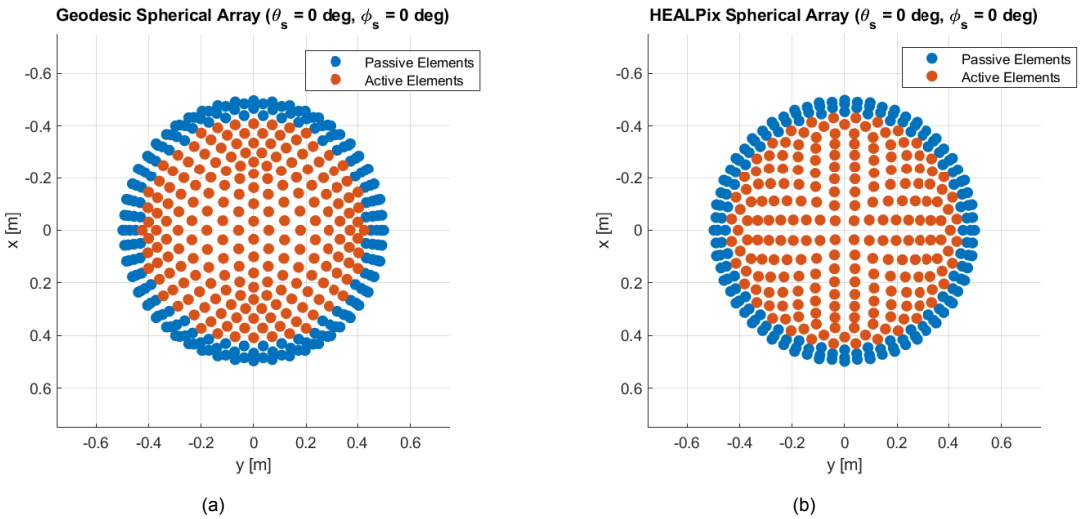

(a) (b)

Figure 3.10: The geodesic (a) and the HEALPix (b) spherical arrays of radius 0.5 metres and 812 and 768 elements respectively when scanning to zenith.

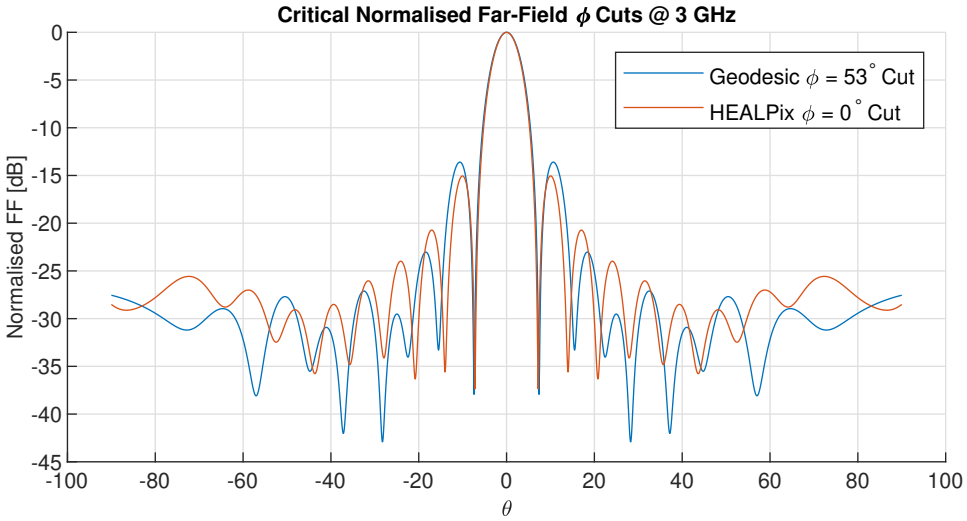

Figure 3.11: Comparison of the radiation pattern cuts at which the side lobe level is maximum for the geodesic and HEALPix spherical array topologies when scanning to zenith.

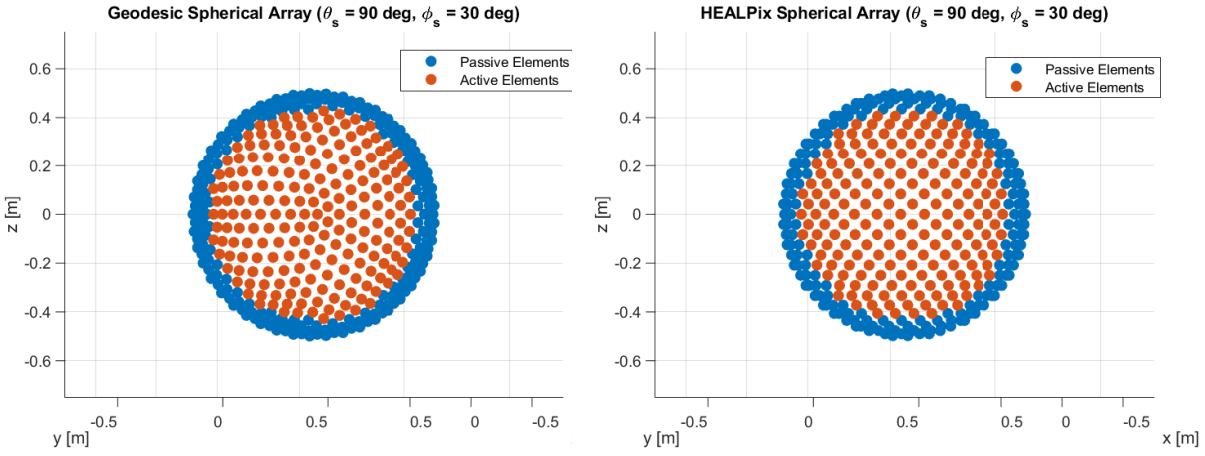

(a) (b)

Figure 3.12: The geodesic (a) and the HEALPix (b) spherical arrays of radius 0.5 metres and 812 and 768 elements respectively when scanning to $\theta_s = 90^\circ$ and $\phi_s = 30^\circ$.

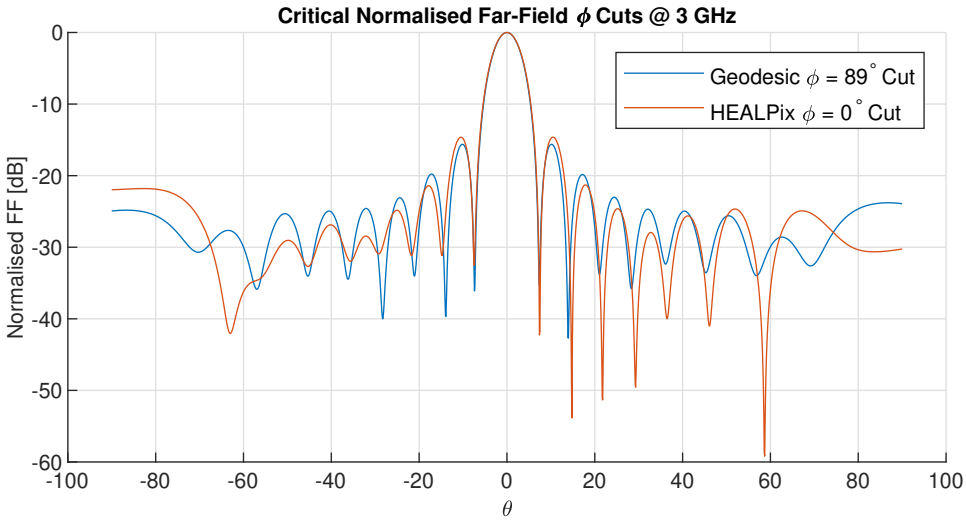

Figure 3.13: Comparison of the radiation pattern cuts at which the side lobe level is maximum for the geodesic and HEALPix spherical array topologies when scanning to $\theta_s = 90°$ and $\phi_s = 30°$.

say whether or not a specific array configuration is the global optimum. Nevertheless, a considerable amount of different configurations have been analysed, of which the most important are presented in this section.

Just as described in section 3.1, isotropic radiation patterns are used to make fair comparisons and quick computations, enabling a novel comparison of all of these configurations regarding their properties for application in the DISTURB project. Next to using isotropic radiation patterns for fair comparisons, also the element density is set to be about the same for every configuration. The element spacing is selected to be about 0.3 metres. With an inter-element spacing of this amount, the number of antenna elements is not extremely large and therefore computational loads are within reasonable limits. Next to computational limitations, an inter-element spacing of 0.3 metres, 1.5λ at 1.5 GHz, also results in less severe mutual coupling between the elements which decreases the difference between array factor analysis performed in this section and full wave solutions.

Using the results from section 3.1, the reader can tune the array configuration to his or her needs. For example, if the side-lobe level is found to be too high, the reader could elect to increase the element density in his or her design.

3.2.1. Comparison Criteria

In this section, the array configurations are rated on several aspects which follow from the requirements listed in section 1.3.1.

The first and most important aspect is the maximum operational bandwidth, which results from the HPBW. The maximum operational bandwidth can be calculated by first finding the maximum HPBW at 3 GHz which is dependent on scan angle. Using this found maximum beam width $HPBW_{max}$, the operational bandwidth can be calculated using equation 3.2.

$$BW_{operational} = \left(1 - \frac{HPBW_{max}}{15°}\right) \cdot 3\ GHz \tag{3.2}$$

Since the operational bandwidth is the most important performance characteristic of an array for DISTURB, all array geometries in subsequent sections are tuned in such a way that their minimum HPBW is just above 2 degrees while their maximum HPBW is kept as low as possible.

Secondly, to provide a figure of merit for the shape of the main beam which should be as circular as possible, the eccentricity e of the beam is calculated. The higher the eccentricity, the more elliptical the shape of the main beam. The eccentricity of the beam is found by using equation 3.3.

$$e = \sqrt{1 - \frac{HPBW_{min}^2}{HPBW_{max}^2}} \tag{3.3}$$

As the shape of the active aperture of a conformal array can change depending on scan angle, so can the shape of the main beam. Therefore, the maximum value of the eccentricity over all scan angles is used to compare the different array configurations with each other.

Thirdly, the surface areas of the various array geometries are given. These areas provide an indication of the total number of elements that are needed to populate the array which is independent of the element density. For example, given two arrays with the same element density, the array with the least surface area will have the least elements. The surface area is used instead of the total number of elements because for most configurations in this thesis, the element density cannot be set to an exact value but is approximated based on parameters provided to the configuration generation functions.

Lastly, the fraction of active elements N_{active} and total elements N_{total} multiplied by the array surface area A is used to provide an indication of the total active elements. This yields effectively a value for the active aperture area. In equation form, the active aperture is given by equation 3.4.

$$A_{active} = \frac{N_{active}}{N_{total}} A \tag{3.4}$$

The active aperture is dependent on scan angle and therefore the maximum value of this active aperture is provided as to present the largest amount of elements that are active at the same time.

3.2.2. Hemispherical Array - Arclength Topology

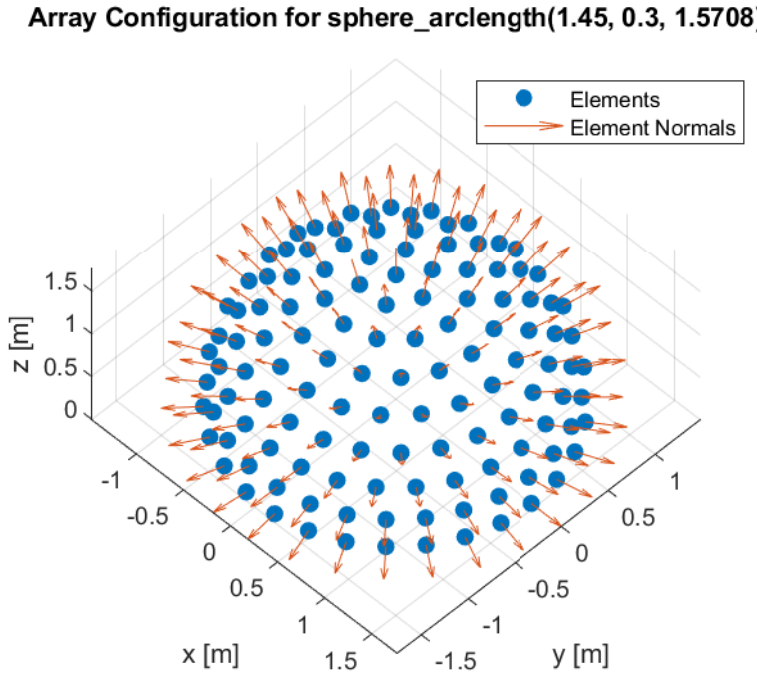

Figure 3.14: The hemispherical array geometry with an arclength topology of radius 1.45 m and an element spacing of 0.3 m.

The first geometry that springs to mind for providing hemispherical coverage, is a hemisphere. Thus, this is also the first geometry that is considered. The hemispherical array configuration can be generated using `sphere_arclength(R, arclength, theta_max)`. The `R` argument indicates the radius of the spherical array which is set to 1.45 metres and `arclength` indicates the topology dimension parameter which is set to 0.3 metre and is further explained in the next paragraph. Lastly, `theta_max` indicates the maximum angle of θ for which elements are present. The elements that have a θ-coordinate larger than this value, are removed. Thus, by specifying `theta_max` to be $\frac{\pi}{2}$, a hemispherical array is generated. A plot of the resulting configuration is shown in figure 3.14.

This particular configuration uses the so called arclength topology. This topology is generated in the following way. First, the number of rings parallel to the xy-plane, which are comparable to the parallels on a globe indicating latitude, is calculated. This number is found by dividing the arclength along the sphere from its north pole to the xy-plane by the topology density parameter. This density parameter is set to 0.3 metres to achieve an inter element spacing of about 30 centimetres. The result from the division is rounded to the nearest integer. Now that the number of parallels is known, the radius of each parallel can be found. Next, the circumference of each parallel is calculated and divided by the dimension parameter. In a similar manner as with the parallels, the result of the division is rounded to find the number of elements per parallel. Finally, the parallels are populated with elements starting from $\phi = 0°$. This means that first set of elements are located on the $\phi = 0°$ meridian. However, for any other meridian, not all parallels will necessarily have an element at said meridian. This causes array configurations with arclength topology to be asymmetric. This can be seen from figure 3.8a, where at $\phi = 0°$ all parallels have an element but only a few parallels have an element at $\phi = 180°$.

Figure 3.15 shows a plot of the minimum and maximum half-power beam widths as function of various scan angles. Since the shape of the beam can be elliptical, the minimum and maximum HPBW at a particular scan angle can differ. The minimum HPBW is found to be 2.08 degrees and the maximum HPBW is found to be 3.93 degrees. Thus, the minimum HPBW is larger than 2 degrees for every scan angle and therefore satisfies the requirement on minimum HPBW. It can also be seen that the maximum HPBW grows as the beam is pointed more and more towards the horizon while the minimum HPBW stays approximately the same. This can be explained as follows. As the beam is scanned towards the

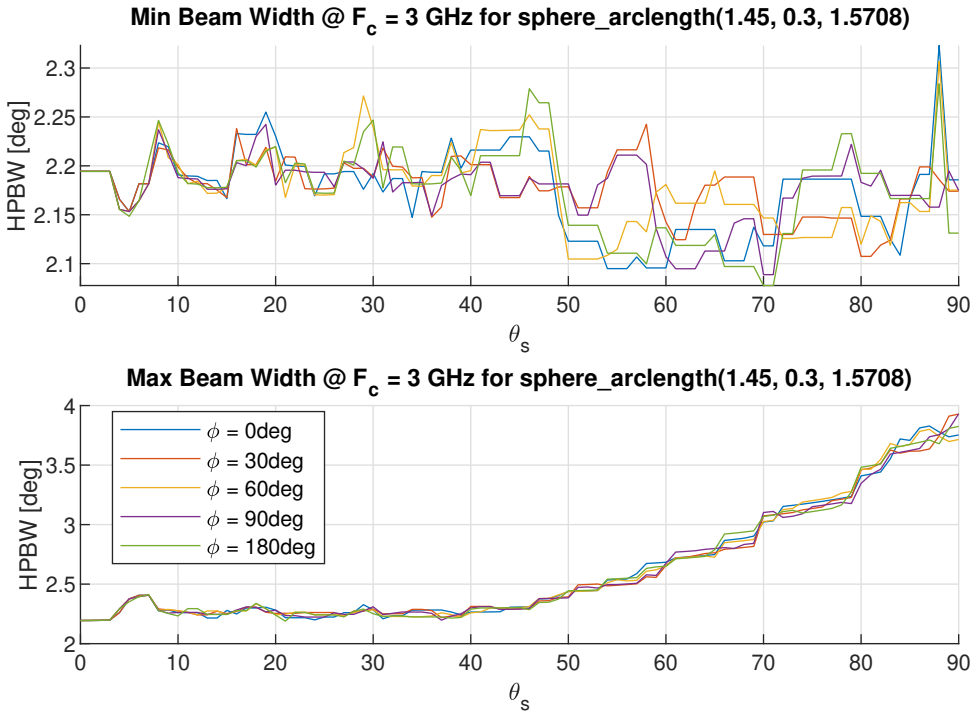

Figure 3.15: HPBW of the hemispherical array with an arclength topology as function of θ_s and ϕ_s.

horizon, the active aperture reduces as less and less elements have an angle of less than 60 degrees between their normal vector and the scan direction. The shape of the active aperture therefore changes from a circular shape to half a circle when scanning towards the horizon as demonstrated in figure 3.16. However, the minimum HPBW remains approximately the same since the active aperture along the $\hat{\phi}$ direction is approximately the same as it is when scanning towards zenith.

Figure 3.17 shows a plot of the eccentricity of the beam shape as function of scan angle. This result agrees with the observations made in figure 3.18, where it can be seen that the active aperture is larger along the y-axis than along the z-axis. The maximum eccentricity is found to be 0.84.

The surface area of spherical array can simply be calculated using equation 3.5, where θ_{max} is specified by `theta_max`.

$$\begin{aligned} A &= \int_0^{2\pi} \int_0^{\theta_{max}} R^2 \sin\theta d\theta d\phi \\ &= 2\pi R^2 \left(1 - \cos\theta_{max}\right) \end{aligned} \tag{3.5}$$

Using this equation with $\theta_{max} = \frac{\pi}{2}$ results in a surface area of 13.21 m^2. Furthermore, figure 3.18 shows a plot of the active aperture area of the hemispherical array. This plot shows that the active aperture area decreases when θ_s increases, which agrees with the explanation given in the previous paragraphs.

Table 3.1 provides an overview of the comparison criteria given in section 3.2.1.

Table 3.1: Comparison criteria of the hemispherical array.

$BW_{operational}$ $[MHz]$	e_{max}	A $[m^2]$	$A_{active,max}$ $[m^2]$
2214	0.83	13.21	6.37

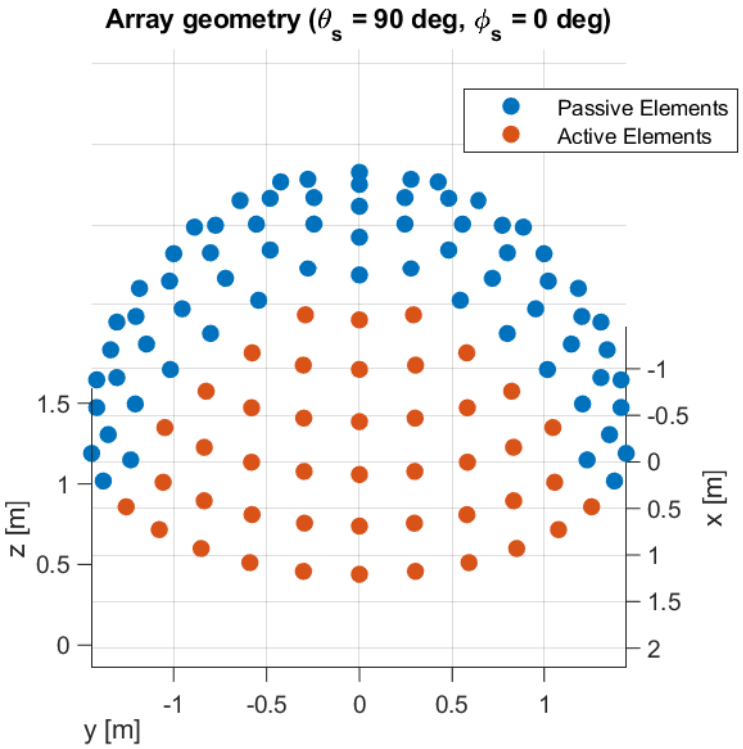

Figure 3.16: Active aperture of the hemispherical array for a scan angle of $\theta_s = 90°$ and $\phi_s = 0°$.

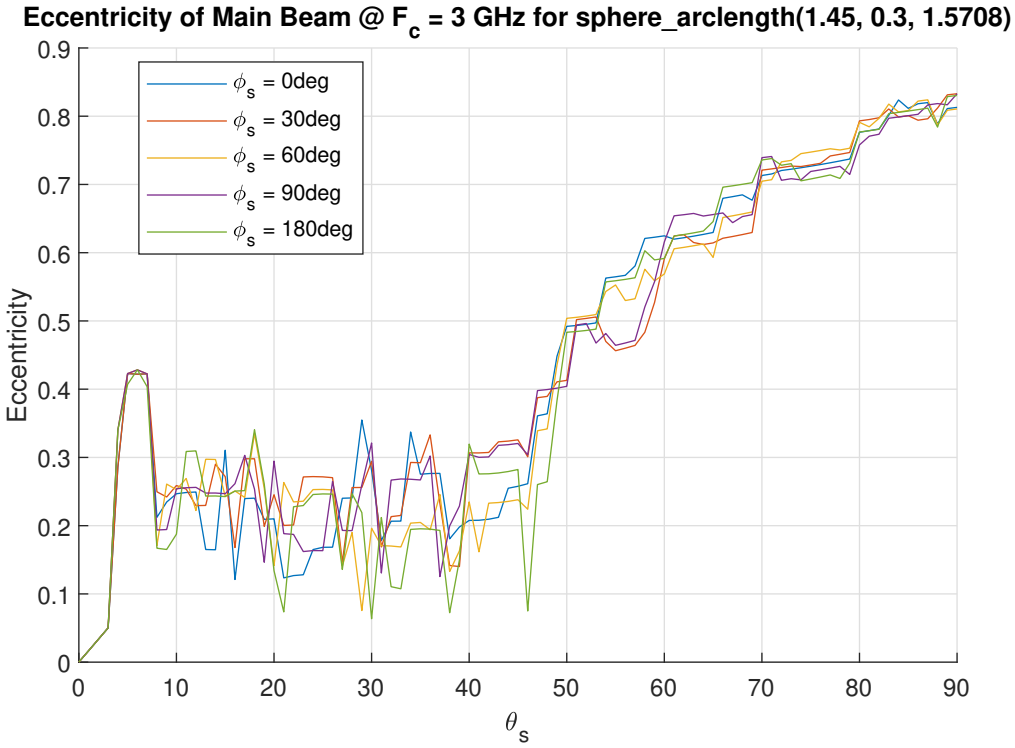

Figure 3.17: Eccentricity of the main beam versus scan angle for the hemispherical array configuration.

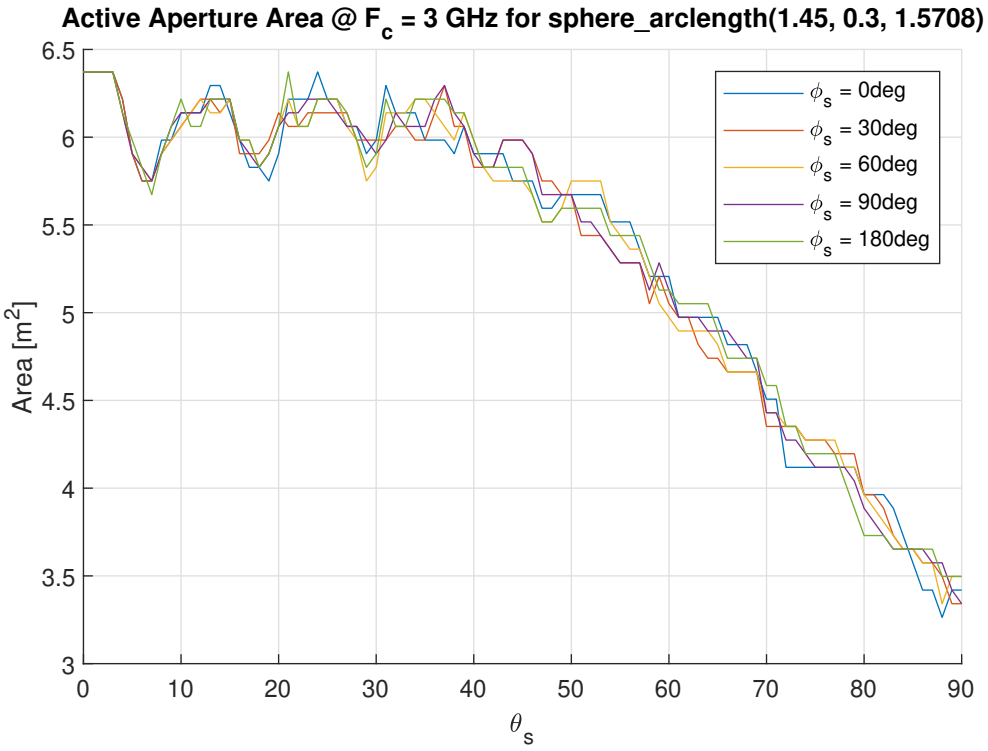

Figure 3.18: Active aperture area of the hemispherical array as function of scan angle.

3.2.3. Quasi-Spherical Array - Arclength Topology

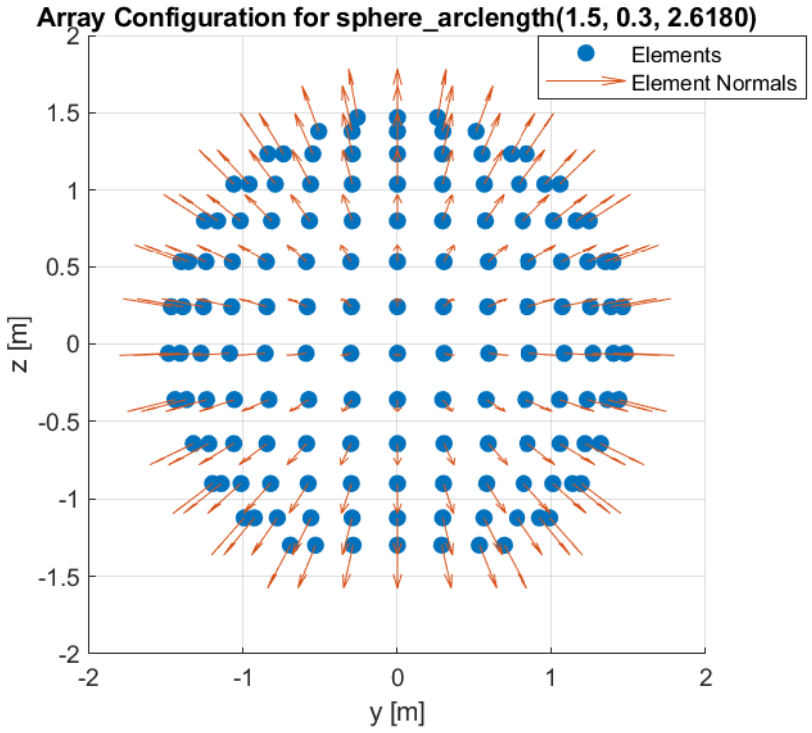

Figure 3.19: The quasi-spherical array geometry with an arclength topology of radius 1.5 m and an element spacing of 0.3 m.

As shown in section 3.2.2, the hemispherical array suffers from a reduction in active aperture area when scanning towards the horizon. This results in a number of unwanted effects such as an increase in maximum HPBW and a more elliptical beam shape.

In order to solve this problem, the hemisphere can be extended so that the active aperture is not limited to the upper half of the sphere. Since the maximum scan angle θ_s is 90° and the fact that elements are activated when the scan direction is within 60° of their normal vectors, it can be concluded that the `theta_max` parameter should be set to $90° + 60° = 150°$ thus forming a quasi-spherical shape. When θ_{max} is 150°, the active aperture will remain approximately the same and becomes independent of scan angle. Alternatively, this array configuration can be understood as a spherical array of which the elements that are never active for all scan angles from zenith to horizon have been removed.

The quasi-spherical array can be generated using the `sphere_arclength(R, arclength, theta_max)` function with `R` set to 1.5 metres, `arclength` set to 0.3 metres and `theta_max` set to 2.6180. The resulting configuration is displayed in figure 3.19. The minimum and maximum HPBW resulting from this configuration are plotted in figure 3.20.

Since the active aperture is more constant, the eccentricity is also more constant. Also, since the aperture has a shape that is approximately circular over the whole scan range, the eccentricity is in general lower than the eccentricity of the hemispherical array. A plot of the eccentricity is displayed in figure 3.21.

The surface area of the array can be found in the same way as with the hemispherical array by using equation 3.5. This results in a surface area of 26.38 m^2. A plot of the active aperture size is shown in figure 3.22. A summary of the comparison criteria is shown in table 3.2.

Table 3.2: Comparison criteria of the quasi-spherical array.

$BW_{operational}$ $[MHz]$	e_{max}	A $[m^2]$	$A_{active,max}$ $[m^2]$
2547	0.43	26.38	7.68

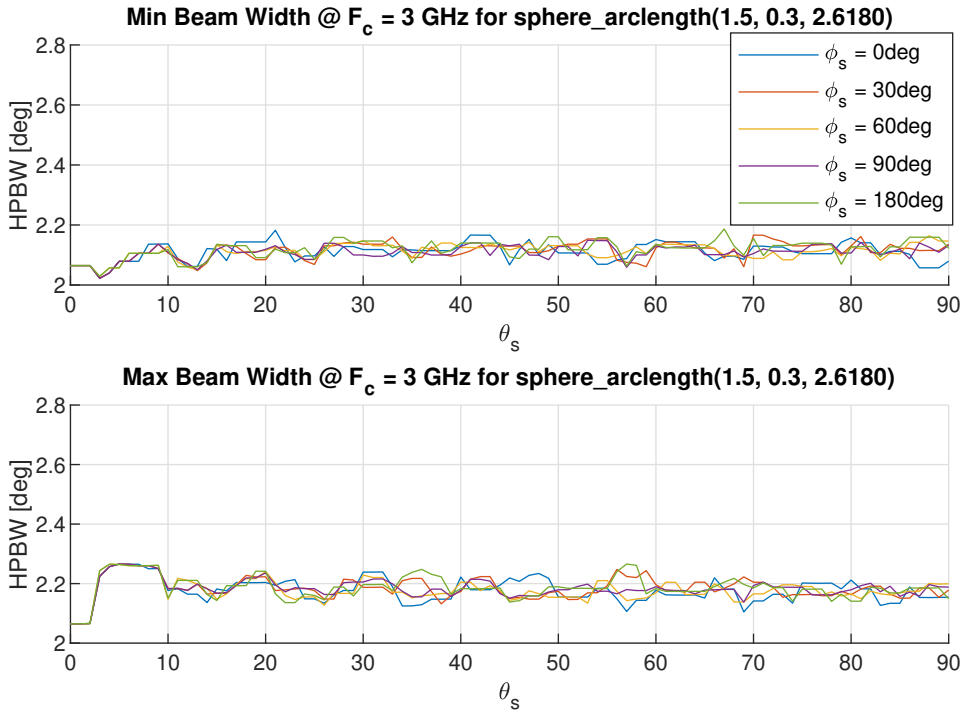

Figure 3.20: Beam width for the quasi-spherical array with an arclength topology as function of θ_s and ϕ_s.

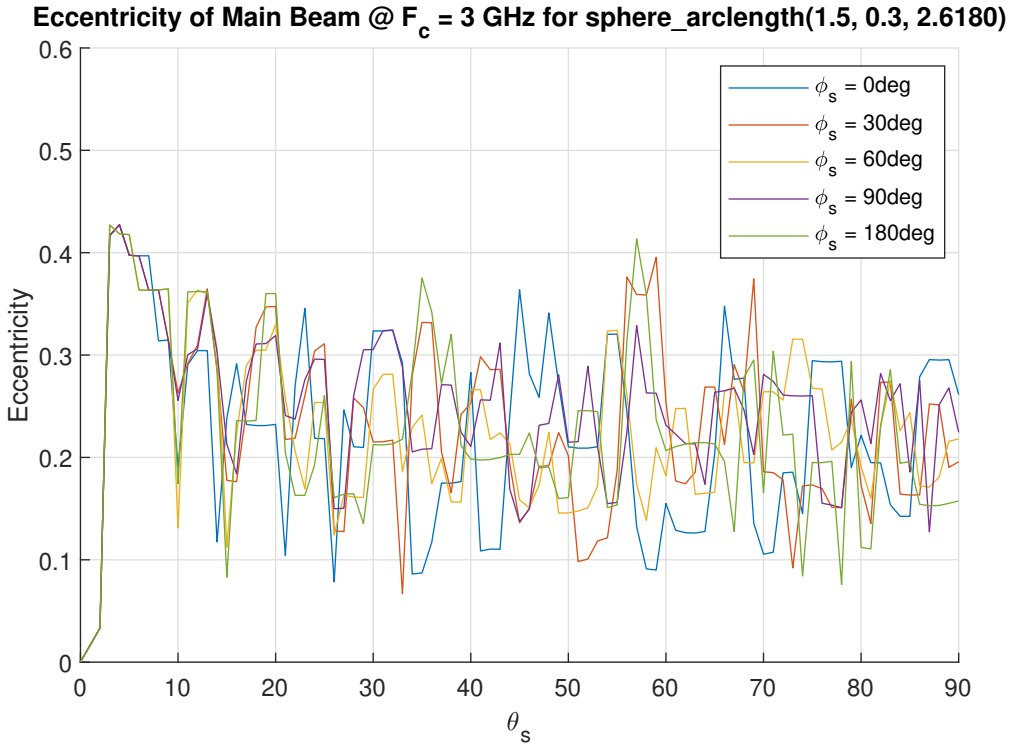

Figure 3.21: Eccentricity of the main beam versus scan angle for the quasi-spherical array configuration.

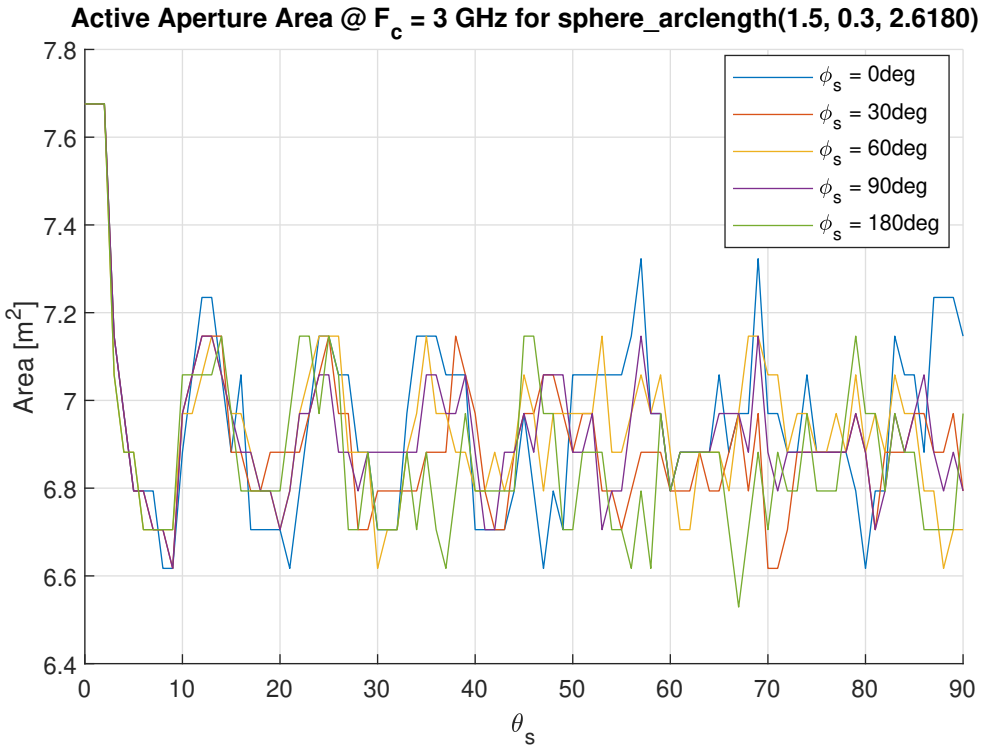

Figure 3.22: Active aperture area of the quasi-spherical array as function of scan angle.

3.2.4. Conical Array - Arclength Topology

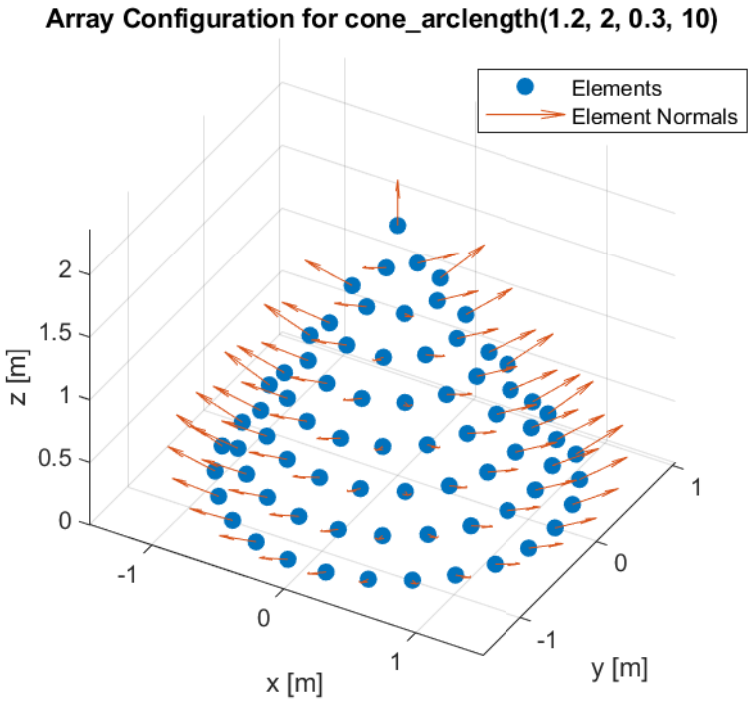

Figure 3.23: The conical array geometry with an arclength topology of radius 1.2 m, a height of 2 m and an element spacing of 0.3 m.

Besides spherical geometries, a conical array configuration is also of interest. A cone could potentially provide hemispherical coverage whilst having a smaller surface area than a spherical geometry.

The function `cone_arclength(R, H, arclength, z_max)` generates a conical geometry with an arclength topology. In this function, `R` represents the radius at the base of the cone, `H` the height of the cone, `arclength` the topology parameter and `z_max` the height at which the cone is truncated. By setting `z_max` to some value that is larger than `H`, a full cone is created.

Similar to the generation of the hemispherical geometry, first the number of parallels is calculated. Next, the circumference of each parallel is calculated and the number of points that fit on the respective parallels is found by dividing and rounding the before mentioned circumferences by the topology parameter.

A conical array with a radius of 1.2 metres and a height of 2 metres is found to maximise operational bandwidth and is plotted in figure 3.23. The resulting half-power beam width over the hemispherical scan range at 3 GHz is shown in figure 3.24. From this figure can be concluded that in the transition region from zenith to about 5 degrees from zenith the active aperture is reducing quickly due to fact that the elements at the backside of the array are now pointing away from the scan direction.

Figure 3.26 shows the eccentricity of the beam shape. It can be seen that the beam shape becomes significantly elliptic in the transition region. This is because the elements at the backside of the array become inactive and the active aperture forms approximately half a circle when seen from above. When θ_s is increased, the cone is effectively seen more from the side. At an angle of approximately 30° to 45° of θ_s, depending on ϕ_s, the projection of the active aperture of the cone in the vertical direction is about the same as the projection in the horizontal direction, as illustrated in figure 3.25. This decreases the ellipticity and makes the beam more circular.

The surface area of the conical array configuration can be computed using equation 3.6.

$$A = \pi R \sqrt{R^2 + H^2} \tag{3.6}$$

The total area of the cone is found to be 8.79 m^2. Figure 3.27 shows the active aperture versus scan angle of the conical array. It can be seen that the conical array has very little surface area compared

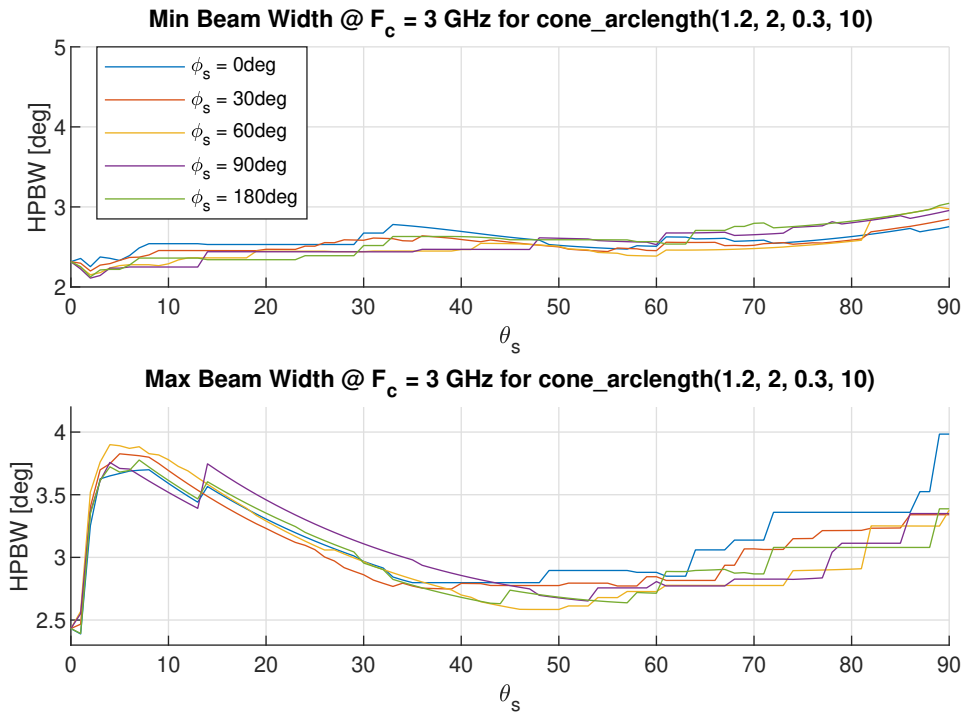

Figure 3.24: Beam width for a conical array with an arclength topology as function of θ_s and ϕ_s.

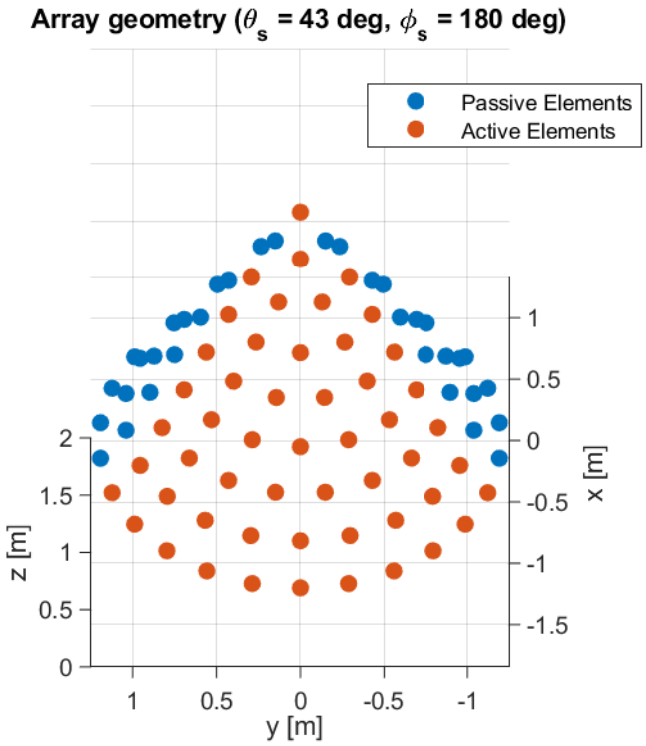

Figure 3.25: Active aperture of the conical array for a scan direction of $\theta_s = 43°$ and $\phi_s = 180°$.

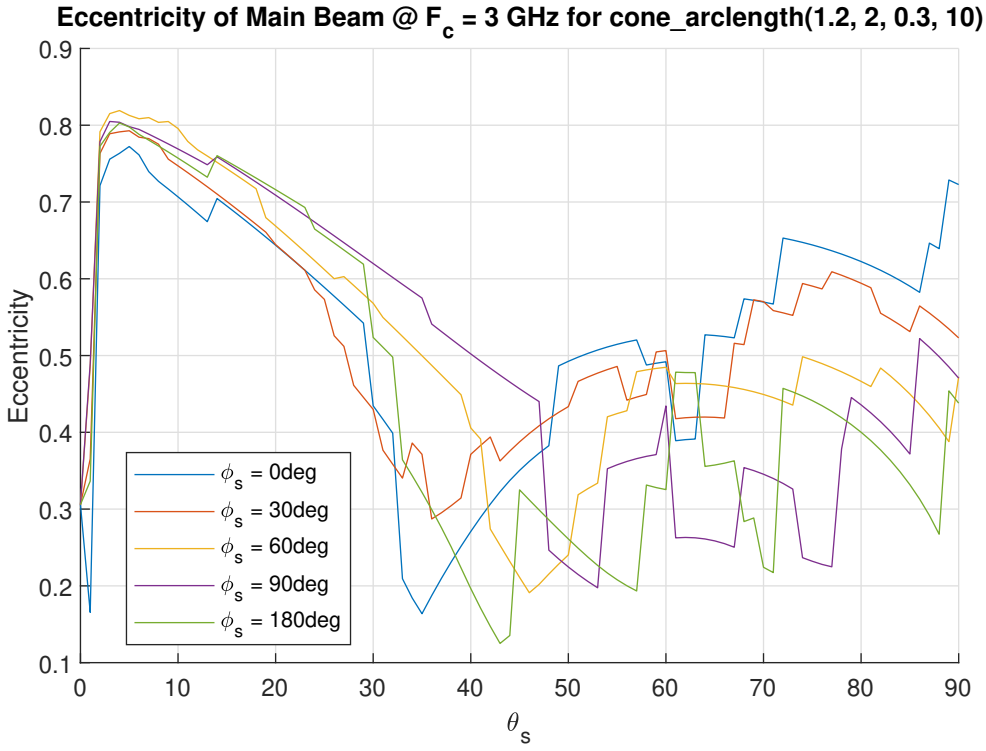

Figure 3.26: Eccentricity of the main beam versus scan angle for the conical array configuration.

to the spherical geometries and therefore the amount of antenna elements is much smaller. However, the maximum active aperture of the cone is equal to the surface area of the cone since all elements are within 60° when scanning to zenith. This results in the maximum active aperture area of the cone to even exceed the maximum active aperture areas of both spherical geometries.

Table 3.3 provides a summary of the comparison criteria of the conical array.

Table 3.3: Comparison criteria of the conical array.

$BW_{operational}$ $[MHz]$	e_{max}	A $[m^2]$	$A_{active,max}$ $[m^2]$
2203	0.82	8.79	8.79

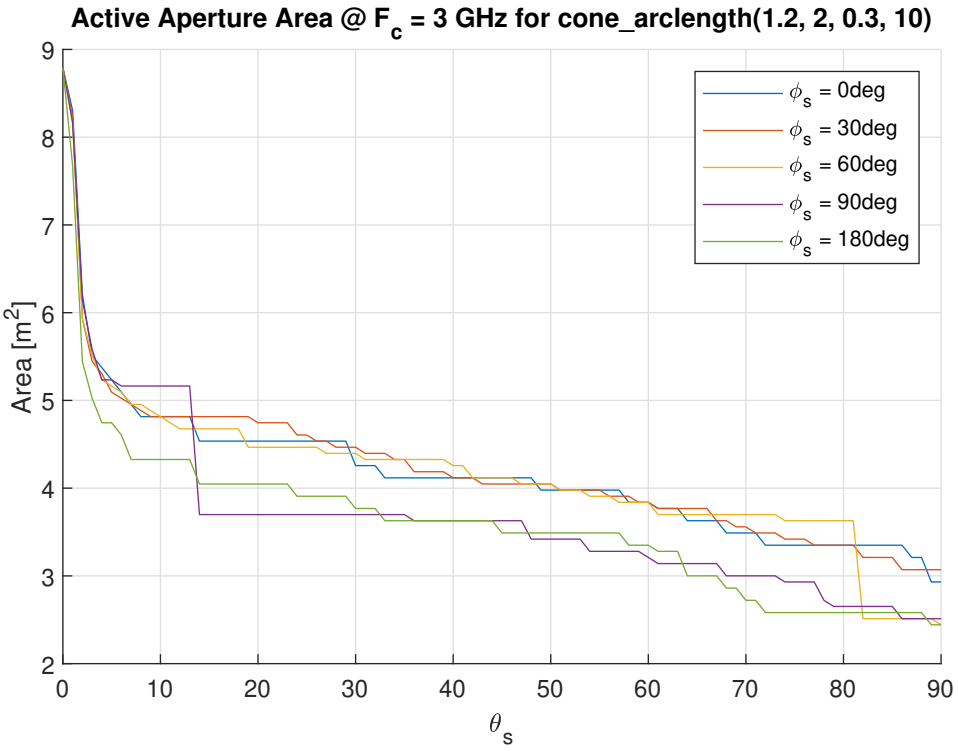

Figure 3.27: Active aperture area of the conical array as function of scan angle.

3.2.5. Cylindrical Array - Arclength Topology

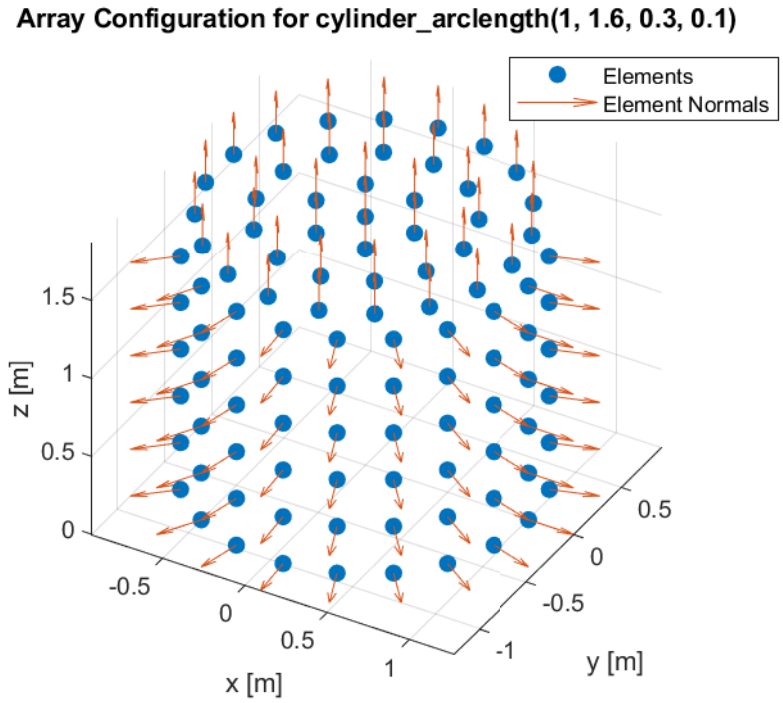

Figure 3.28: The cylindrical array geometry with an arclength topology with a radius of 1 m, a height of 1.6 m, an element spacing of 0.3 m and a keep-out distance of 0.1 m.

The conical geometry can be extended to a cylindrical array. A cylinder has no doubly-curved surfaces, which results in more possibilities to distribute a regular grid on the array.

The cylindrical arclength configuration can be generated using the `cylinder_arclength(R, H, arclength, d_edge)` function. Here `R` represents the radius of the cylinder, `H` the height of the cylinder, `arclength` the topology distribution parameter and `d_edge` is the keep-out distance from the edges of the cylinder where no elements are to be placed. The generation of this configuration comprises two steps. The first step is to generate the elements on the side of the cylinder. This is done by using the generation function used for the cone arclength configuration, but with a height set to a large number such as 1 km. All elements above the height parameter of the cone are removed.

The second part of the array configuration creation is to generate the elements on the top of the cylinder. First the number of rings fitting on this cap is calculated by dividing the radius minus the keep-out distance of the cylinder by the topology parameter. Subsequently, the circumference of each circle is calculated and the amount of points fitting on each of the circles is found. Lastly, the points are distributed on the circles in such a way that all circles have an element on the positive x-axis.

Figure 3.28 shows a cylindrical array with a height of 1 metre and a radius of 1.6 metres. The HPBW for this configuration is shown in figure 3.29. Just as with the cone, a steep transition occurs at certain scan angles. In the case of the cylinder, this transition happens at a θ_s of 30°. This can be explained by the fact that the elements on the side of the cylinder are suddenly within 60° from the scan direction as their normal vectors are parallel to the xy-plane. This sudden increase in aperture reduces the HPBW significantly. A similar transition but in opposite direction happens at 60°. Here the top side of the cylinder becomes inactive, thus reducing the active aperture.

The ellipticity of the beam over scan angle is displayed in figure 3.30. The beam starts out circular, but becomes gradually more elliptical up to 30° from zenith as the side becomes active. This results in the effective aperture becoming rectangular of shape, thus increasing the eccentricity. The same thing in reverse happens at 60° as the top of the cylinder becomes inactive.

The area of the cylinder can be found using equation 3.7.

$$A = \pi R^2 + 2\pi RH \tag{3.7}$$

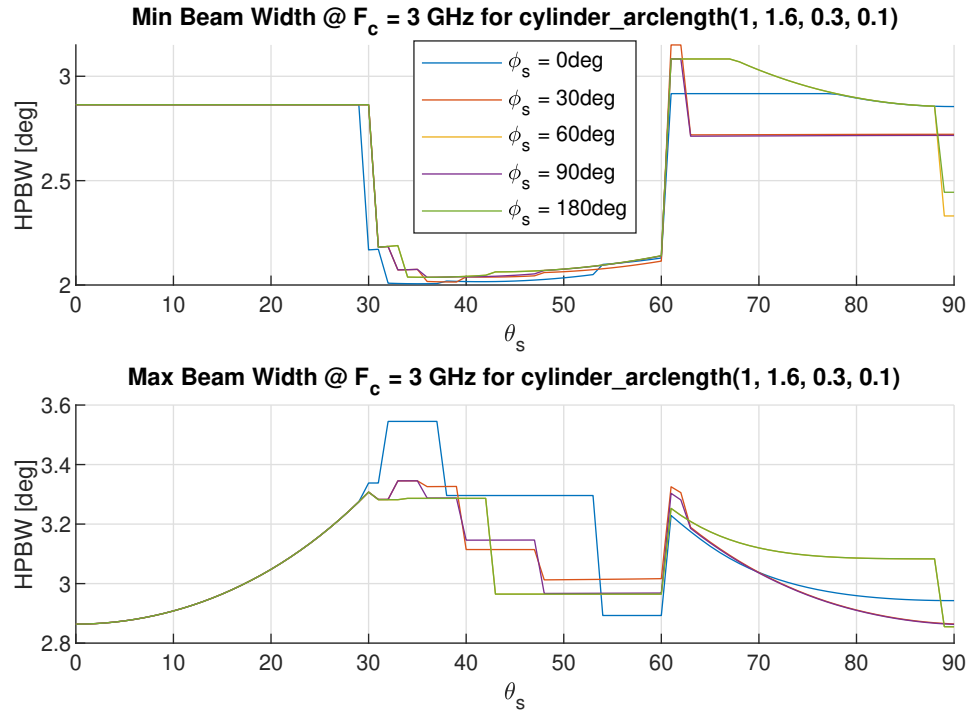

Figure 3.29: Beam width for a cylindrical array with an arclength topology as function of θ_s and ϕ_s.

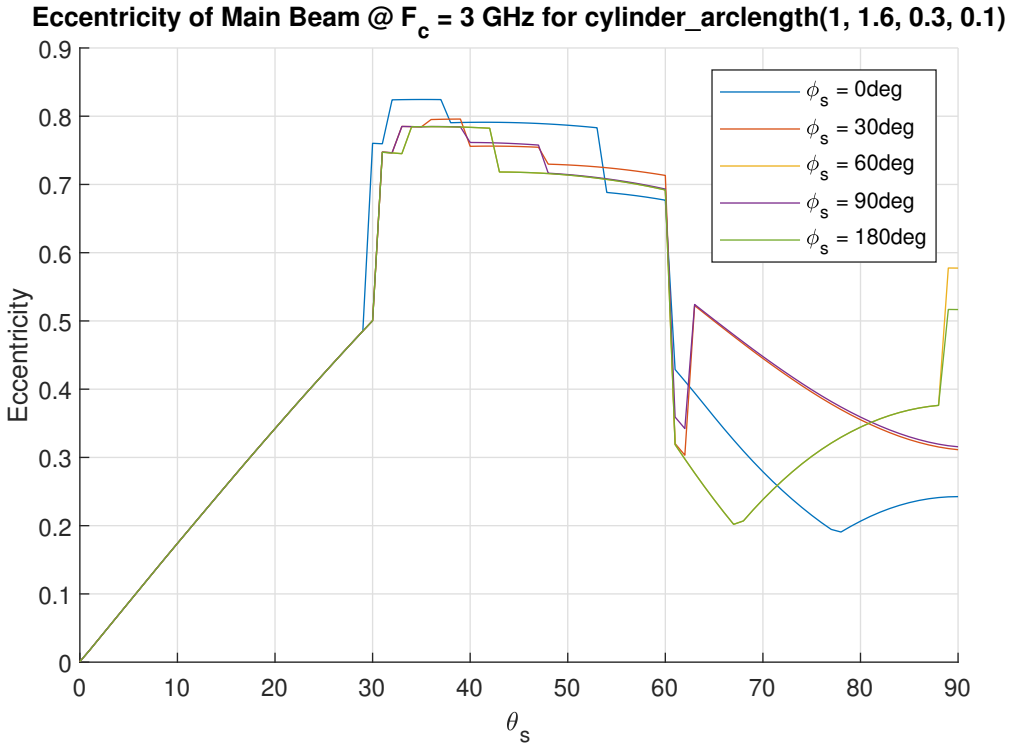

Figure 3.30: Eccentricity of the main beam versus scan angle for the cylindrical configuration.

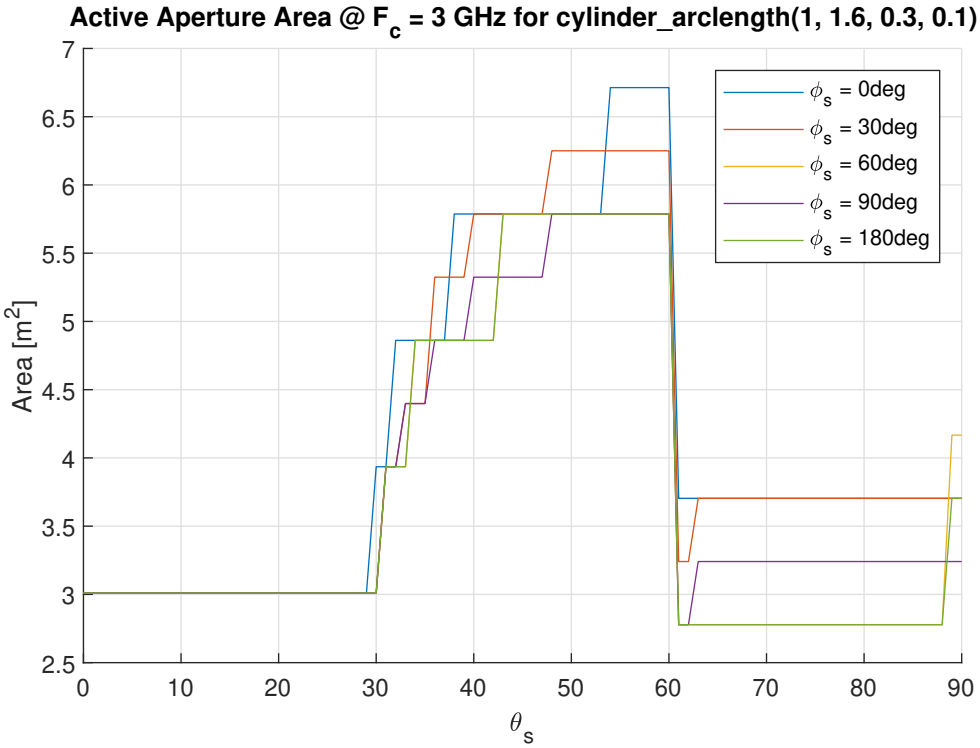

Figure 3.31: Active aperture area of the cylindrical array as function of scan angle.

The total area of the cylinder is 13.19 m^2. A plot of the active aperture area is shown in figure 3.31. This figure is in line with the previous conclusion by showing that the active aperture is significantly larger in the region for θ_s between 30° and 60°.

Lastly, table 3.4 provides an overview of the comparison criteria.

Table 3.4: Comparison criteria of the cylindrical array.

$BW_{operational}$ $[MHz]$	e_{max}	A $[m^2]$	$A_{active,max}$ $[m^2]$
2291	0.82	13.19	6.71

3.2.6. Ellipsoidal Array - Arclength Topology

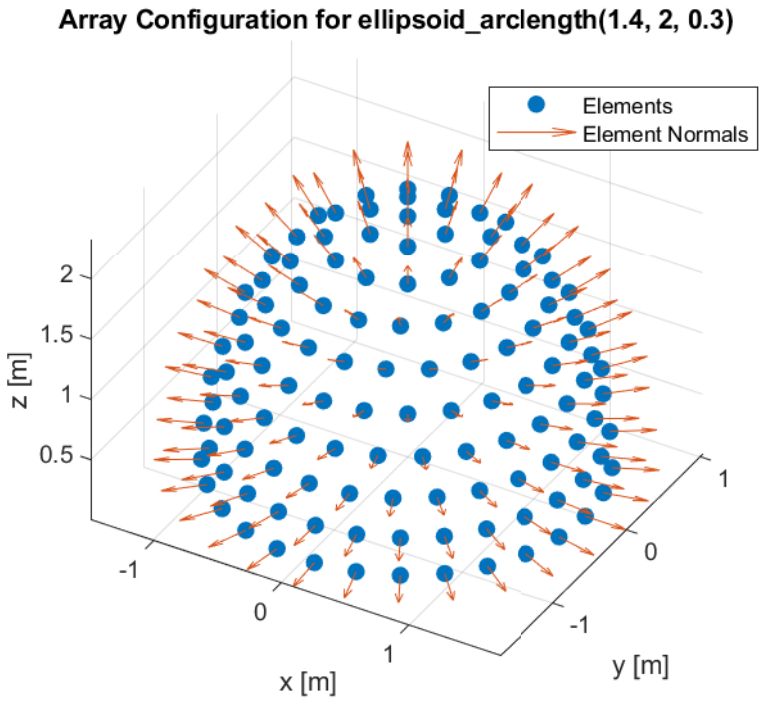

Figure 3.32: The ellipsoidal array geometry with an arclength topology and a radius of 1.4 m, a height of 2 m and an element spacing of 0.3 m.

A half-ellipsoidal array geometry may be able to provide a compromise between a cylinder, cone and sphere. Since it is desirable that the array has the same beam properties independent of scan angle, the parameters of the ellipsoidal geometry are set in such a way that it becomes rotationally symmetric. This type of ellipsoid is also called a spheroid. It should be noted that if the track of the Sun at a certain geographic position of the array location is known, a true ellipsoidal instead of spheroidal geometry could be utilised to provide better beam properties when scanning on-track of the Sun than off-track. A spheroid can be defined by a radius and a height and an array with this geometry can be created using the function `ellipsoid_arclength(R, H, arclength)`. Here `H` specifies the height of the ellipsoid and `R` the radius at the base of the ellipsoid.

The calculation of the arclength along the $\hat{\theta}$ direction of an ellipsoid is more involved than for a sphere or a cone. The arclength is given by equation 3.8. In this equation $E(m)$ is the complete elliptic integral of the second kind with the parameter m.

$$l = RE(1 - H^2/R^2) \tag{3.8}$$

The z-coordinates for which the parallels are spaced at equal arclength from each other is not easily solved analytically. Therefore, this is done in a numerical fashion instead.

It is found that an ellipsoidal array with a height of 2 metres and a width of 1.4 metres yields the best results regarding operational bandwidth. The configuration is displayed in figure 3.32. The HPBW for this configuration is displayed in figure 3.33. A plot of the eccentricity is shown in figure 3.34.

The area of the ellipsoid can be found by a complex expression involving elliptic integrals of the first and second kind [51]. However, since the ellipsoidal geometry that is considered is also a half-spheroid, the surface area can be found using equation 3.9 if $H > R$ and equation 3.10 if $H < R$, adapted from

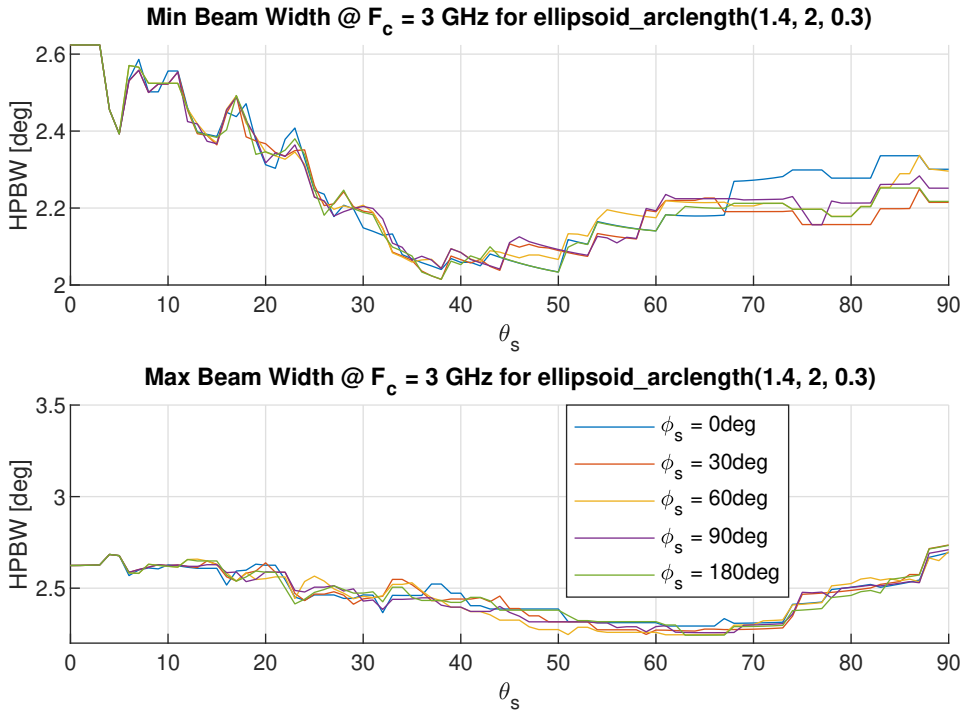

Figure 3.33: Beam width for an ellipsoidal array with an arclength topology as function of θ_s and ϕ_s.

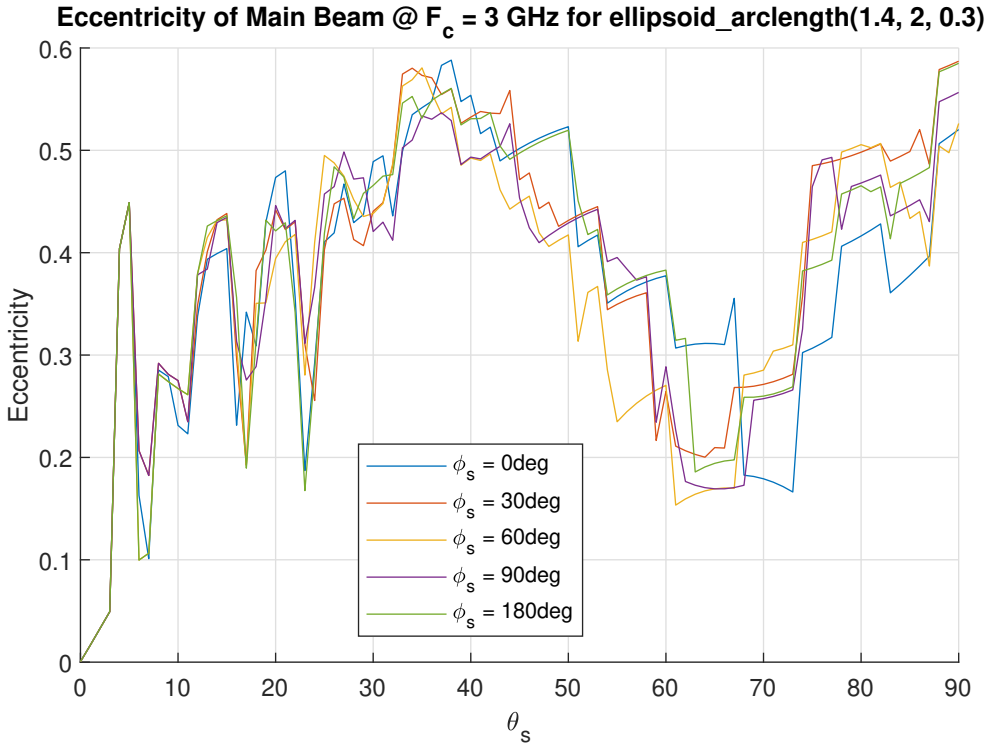

Figure 3.34: Eccentricity of the main beam versus scan angle for the ellipsoidal array configuration.

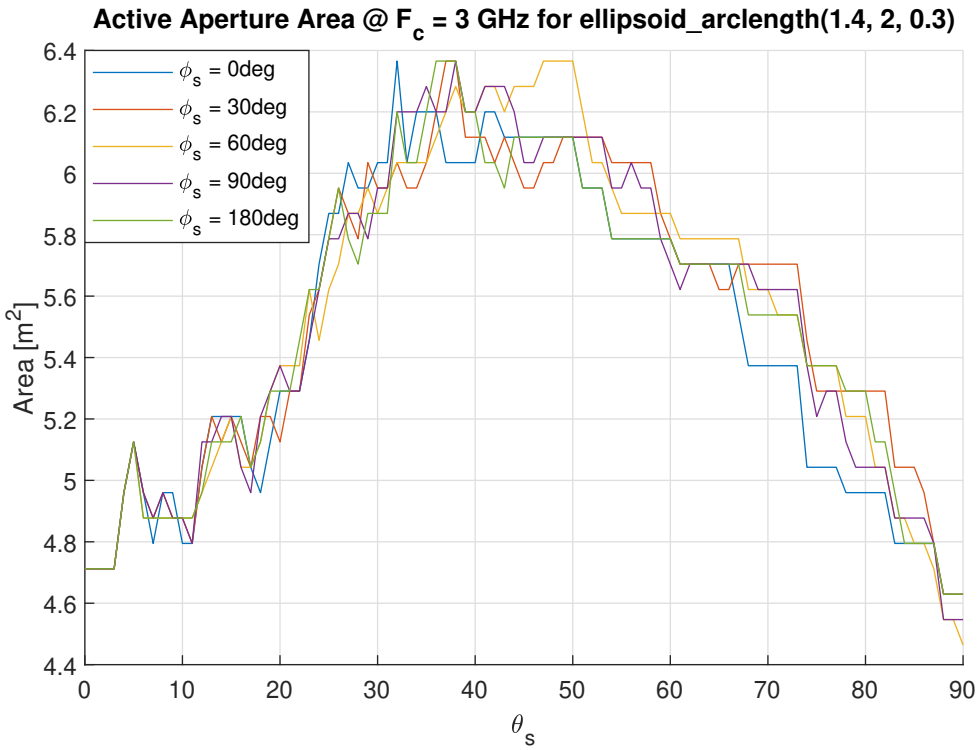

Figure 3.35: Active aperture area of the ellipsoidal configuration as function of scan angle.

[52] and [53] respectively.

$$A = \pi R^2 + \frac{\pi R H^2}{\sqrt{H^2 - R^2}} \arcsin\left(\frac{\sqrt{H^2 - R^2}}{H}\right) \tag{3.9}$$

$$A = \pi R^2 - \frac{j\pi R H^2}{\sqrt{R^2 - H^2}} \arccos\left(\frac{R}{H}\right) \tag{3.10}$$

The total area of the ellipsoidal configuration is found to be 15.95 m^2. The active aperture area of the array is displayed in figure 3.35.

As seen from figures 3.33 to 3.35, the ellipsoidal geometry seems to eliminate the sudden large shifts in active aperture area that occur for the conical and cylindrical configurations. This reduces the large variation in HPBW. The comparison criteria of the ellipsoidal array are shown in table 3.5.

Table 3.5: Comparison criteria of the ellipsoidal array.

$BW_{operational}$ $[MHz]$	e_{max}	A $[m^2]$	$A_{active,max}$ $[m^2]$
2453	0.59	15.95	6.37

3.2.7. Faceted Conical Array

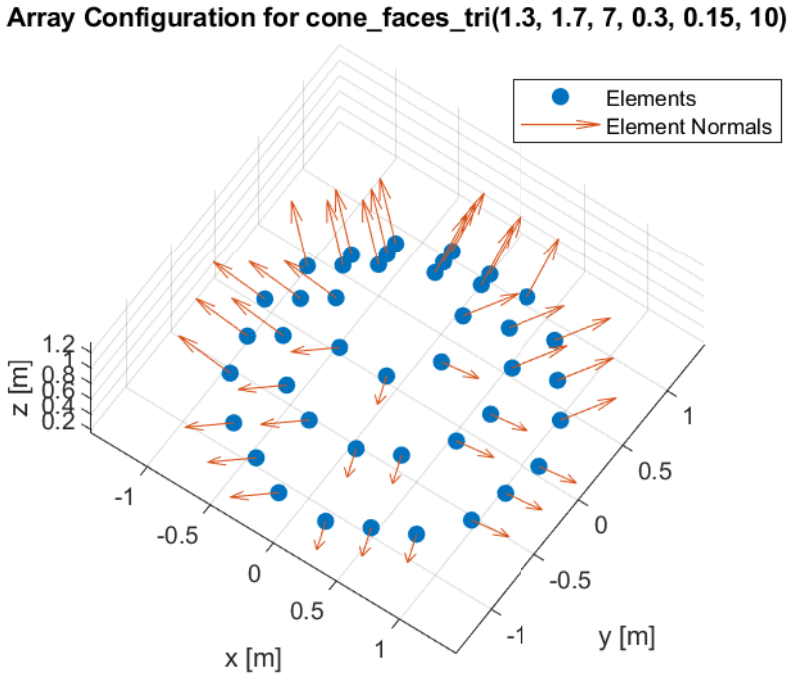

Figure 3.36: The faceted conical array with 7 facets, a radius of 1.3 m, a height of 1.7 m, an element spacing of 0.3 m and a keep-out distance of 0.15 m.

All previously considered geometries are more or less of continuous nature. This means that they all exist out of single and/or doubly curved surfaces. However, these curved surfaces may not be easily manufacturable and obtaining regular distributions of elements on these geometries is non-trivial.

Therefore, faceted versions of previously considered shapes may be of interest. The first of the faceted geometries that is investigated, is the faceted cone. The faceted cone can be generated using the MATLAB function `cone_faces_tri(R, H, N_faces, dx, d_edge, z_max)`. Here, the radius `R` is the largest distance from the centre of the cone to the corner of a face on the xy-plane. As with the regular cone, `H` indicates the height, `d_edge` the keep-out distance and `z_max` the height for which all elements above said height should be removed. The `N_faces` argument determines the number of faces the cone should be consisting of. For example, when `N_faces` is set to 3, a tetrahedron is generated and when set to 4, a pyramid is created. Lastly, `dx` determines the spacing of the elements parallel to the xy-plane. The elements are distributed in such a way that they are parallel to the edges of the triangular facets of the faceted cone and thus results in a triangular grid.

A faceted conical array with 7 facets, a radius of 1.3 metres and a height of 1.7 metres is shown in figure 3.36. Also, `d_edge` is set to 0.15 metres and `dx` is set to 0.3 metres. The HPBW for this configuration is shown in figure 3.37. The eccentricity is shown in figure 3.38.

The total area of the faceted cone can be found by calculating the area of one facet, which is a triangle, and multiplying that by the number of facets. The total area of the faceted conical array in this section is calculated to be 8.15 m^2. Figure 3.39 shows the active aperture area of the faceted conical array. As is the case with the regular conical array, at a scan angle of $\theta_s = 0°$ all elements are active. Furthermore, the angles at which facets become active can clearly be seen. Each step in figure 3.39 represents a facet that is switched off, revealing that for some angles of ϕ_s three facets are active and at others two. This is due to the fact that when the ϕ_s angle coincides with one of the edges of the array, only two facets are able to see the scan direction while when scanning head on to a facet, the two neighbouring faces are also able to see the scan direction.

A summary of the comparison criteria is shown in table 3.6.

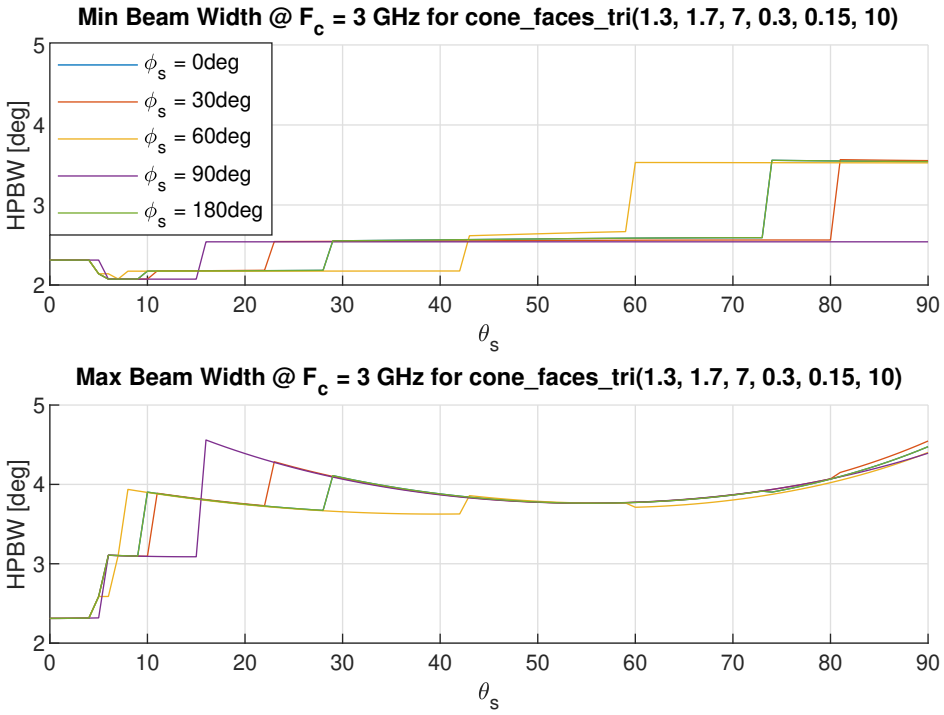

Figure 3.37: Beam width for an faceted conical array as function of θ_s and ϕ_s.

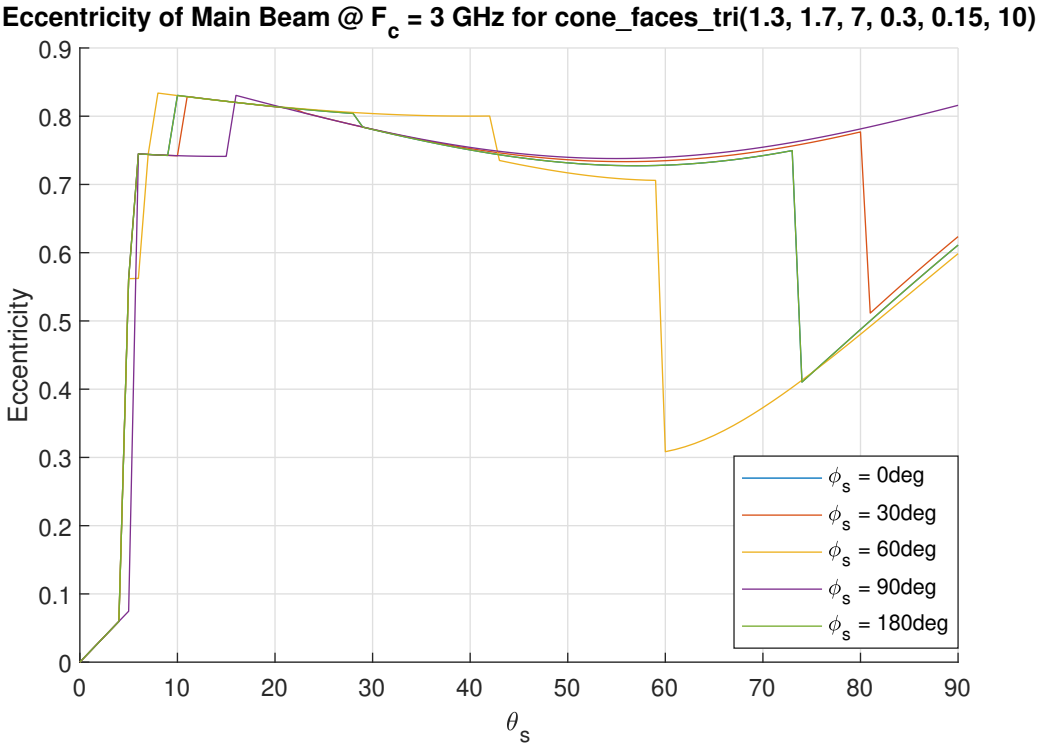

Figure 3.38: Eccentricity of the main beam versus scan angle for the faceted conical array.

Table 3.6: Comparison criteria of the faceted conical array.

$BW_{operational}$ $[MHz]$	e_{max}	A $[m^2]$	$A_{active,max}$ $[m^2]$
2088	0.83	8.15	8.15

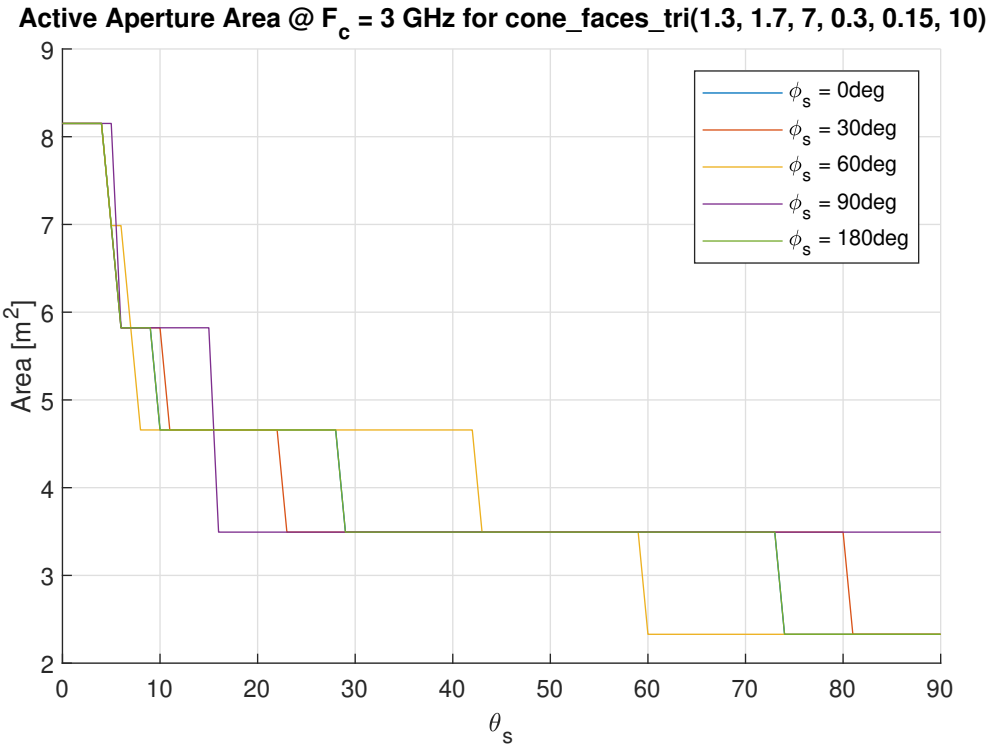

Figure 3.39: Active aperture area of the faceted conical array as function of scan angle.

3.2.8. Faceted Cylindrical Array

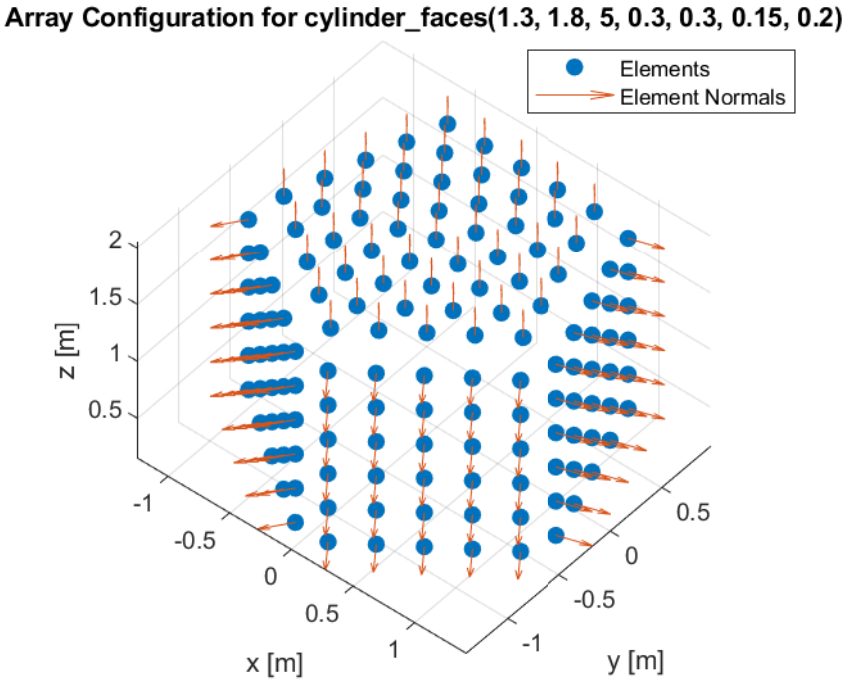

Figure 3.40: The faceted cylindrical array with 5 facets with a radius of 1.3 m, a height of 1.8 m, an element spacing of 0.3 m, a keep-out distance of 0.15 m on the sides and 0.2 metres on the top.

Another configuration that is easily transformed to its faceted counterpart, is the cylinder. This faceted cylindrical configuration can be generated using the function `cylinder_faces(R, H, N_faces, dx, dy, d_edge, d_edge_cap)`. The parameters for which the configuration is found to perform best in terms of bandwidth is a radius of 1.3 metres, a height of 1.8 metres and 5 facets. The `dx` and `dy` arguments, which represent the spacing of the elements when orthogonal to the facets, are both set to 0.3 metres. The keep-out for the elements on the side facets of the cylinder, represented by `d_edge` is set to 0.15 metres and the keep-out for the elements on top of the cylinder is specified to be 0.2 metres and is specified using the `d_edge_cap` argument. The resulting configuration is shown in figure 3.40. A plot of the beam width versus scan angle is shown in figure 3.41. The eccentricity is shown in figure 3.42.

As with the faceted conical array, the surface area of the cylindrical array is calculated by adding the areas of all individual facets. The total area of the cylindrical array is found to be 17.77 m^2. A plot of the active area is shown in figure 3.43. As with the faceted conical array, here also the discrete steps of facets switching off can be seen.

Finally, table 3.7 provides an overview of the comparison criteria for the faceted cylindrical array.

Table 3.7: Comparison criteria of the faceted cylindrical array.

$BW_{operational}$ $[MHz]$	e_{max}	A $[m^2]$	$A_{active,max}$ $[m^2]$
2253	0.78	17.77	10.63

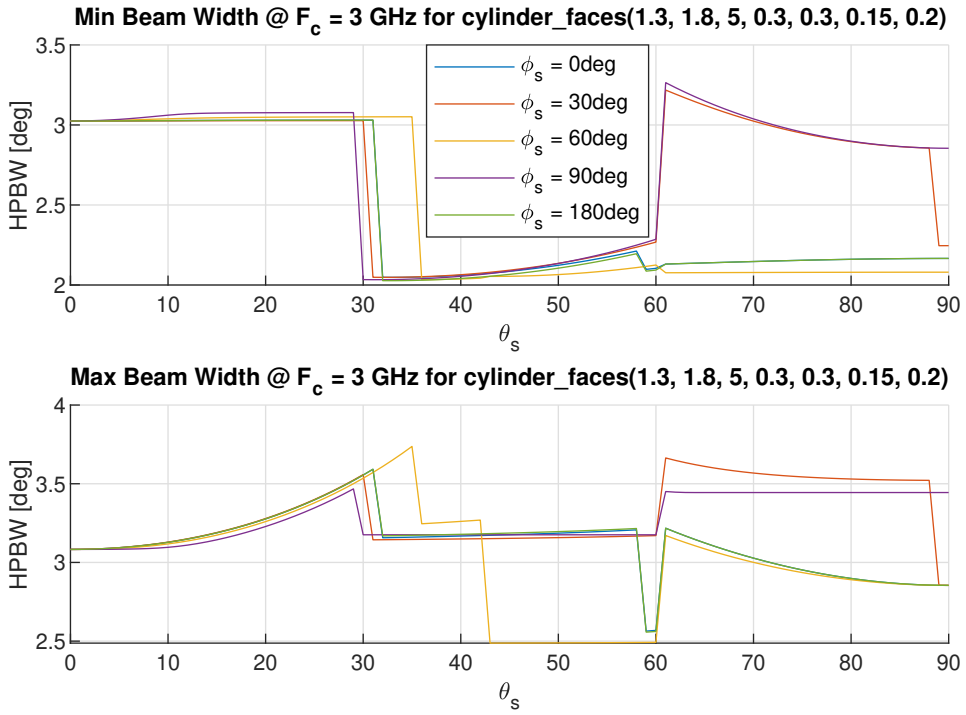

Figure 3.41: Beam width for an faceted cylindrical array as function of θ_s and ϕ_s.

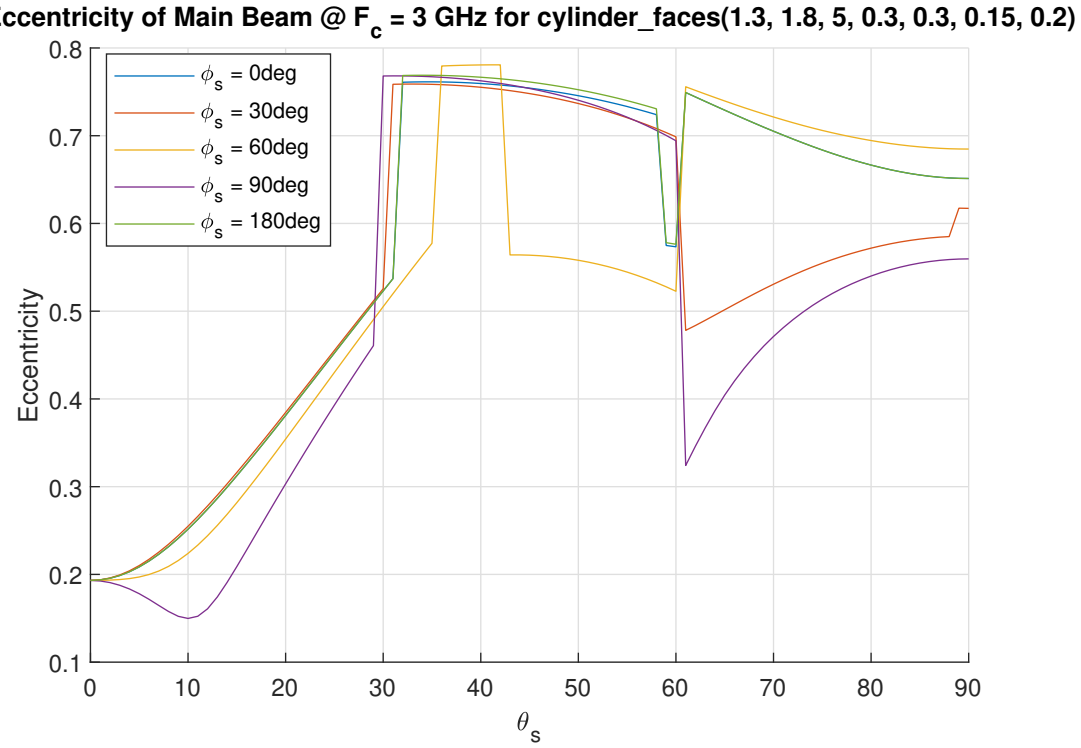

Figure 3.42: Eccentricity of the main beam versus scan angle for the faceted cylindrical array.

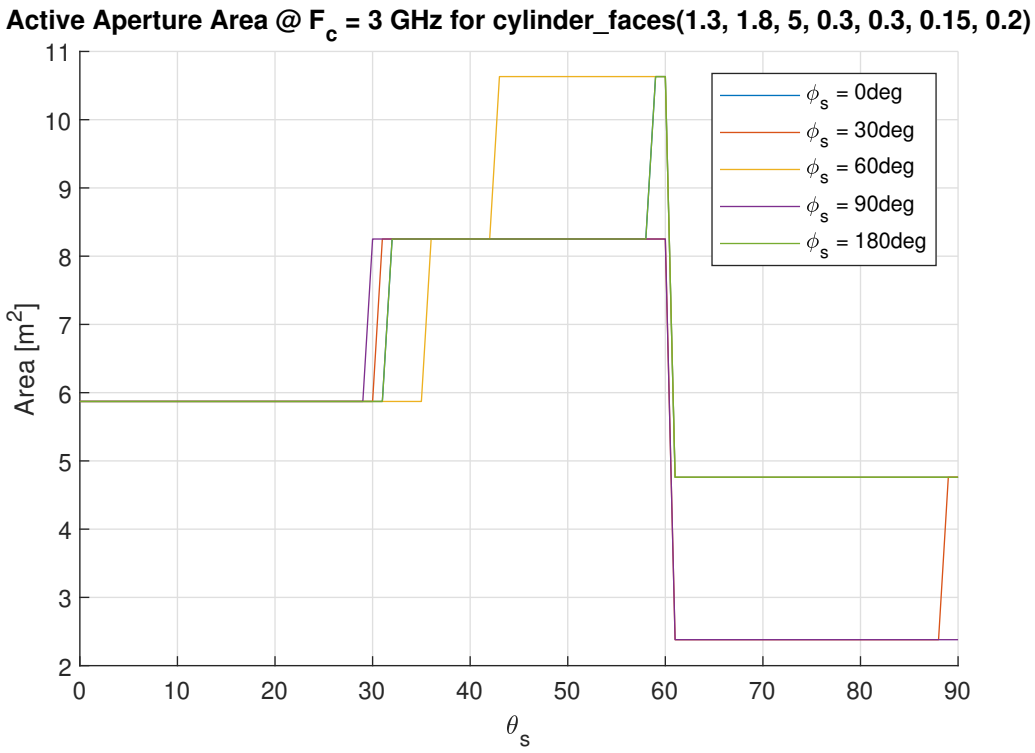

Figure 3.43: Active aperture area of the faceted cylindrical array as function of scan angle.

3.2.9. Faceted Quasi-Spherical Array - 2 Subdivisions

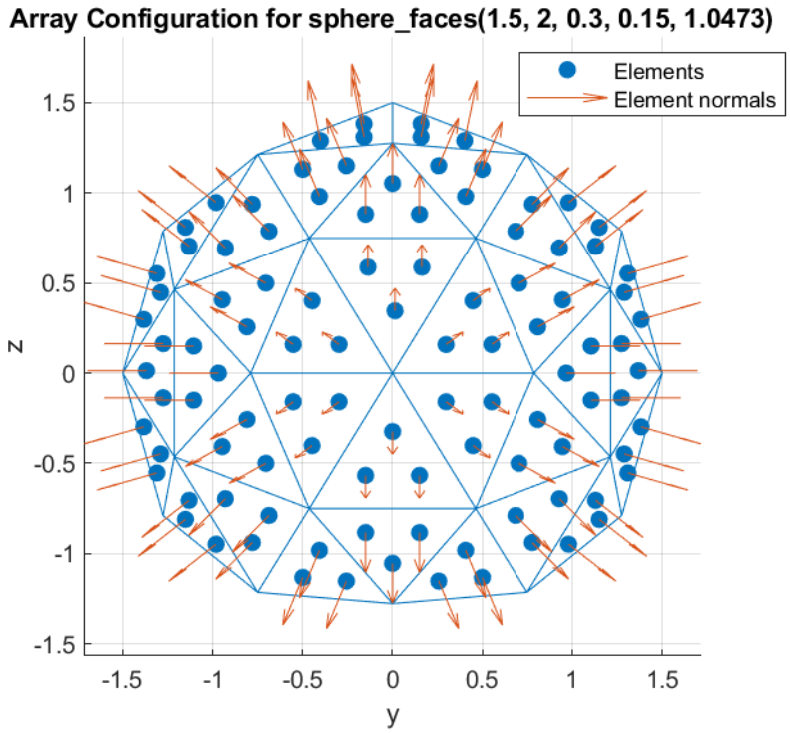

Figure 3.44: The faceted quasi-spherical array with 2 subdivisions and a radius of 1.5 m, an element spacing of 0.3 m and a keep-out distance of 0.15 m.

In contrast to the cone and the cylinder, the sphere is not easily translated to a faceted design. There only exist 5 solids that represent faceted spheres which consist out of the same facets. This group of geometries is called the Platonic solids. Two of these shapes are for example the dodecahedron consisting out of 12 facets, where the facets are pentagrams and another example is the icosahedron, which has 20 triangular facets.

In order to improve the approximation of a sphere by its faceted counterpart, one would like to increase the number of facets. However, by doing this, one has to use differently shaped facets. Generating a faceted sphere is implemented by subdividing the facets of an icosahedron into smaller triangles using a number of specified subdivisions. For example, each edge of a facet can be divided into two and drawing lines between the newly split points results in the facet now consisting of four triangles as shown in figure 3.45. Instead of 2 subdivisions, an arbitrary number of divisions can be done. For example, specifying 3 subdivisions, would result in dividing the edges of the triangle in three, ultimately dividing each original facets into 9 equilateral triangles. Subsequently, all the subdivided triangles are projected onto a sphere of radius `R`. Unfortunately, this projection breaks the congruency of the triangles. The resulting shape is a geodesic polyhedron. Lastly, all facets are populated with elements in a triangular lattice.

A faceted quasi-spherical configuration can be generated using the method described above by the function `sphere_faces(R, N_sub, d_x, d_edge, element_max_angle)`. Here, `R` is used to specify the radius, `N_sub` the number of subdivisions, `dx` the spacing between the elements along the base edge of the triangles, `d_edge` the keep-out distance from the edges of the facets and `element_max_angle` specifies the maximum scan angle of the elements which is used to remove the facets with elements that are not able to see any scan angle in the upper hemisphere. It is found that a 2-subdivision faceted sphere with a radius of 1.5 metres, an element spacing of 0.3 metres and a keep-out of 0.15 metres gives maximum bandwidth for said configuration type. A plot of the configuration is shown in figure 3.44. Using these parameters results in a configuration that has 3 antenna elements per facet. The HPBW is plotted in figure 3.46.

Figure 3.46 shows that the HPBW is relatively constant but the variation is a bit more in comparison

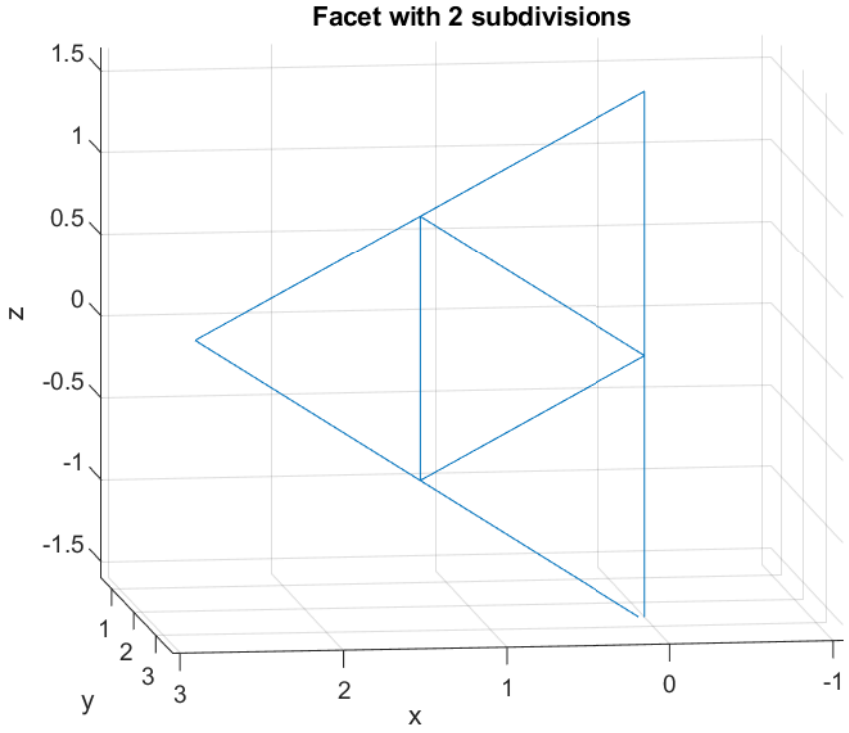

Figure 3.45: Subdivided triangular facet of an icosahedron.

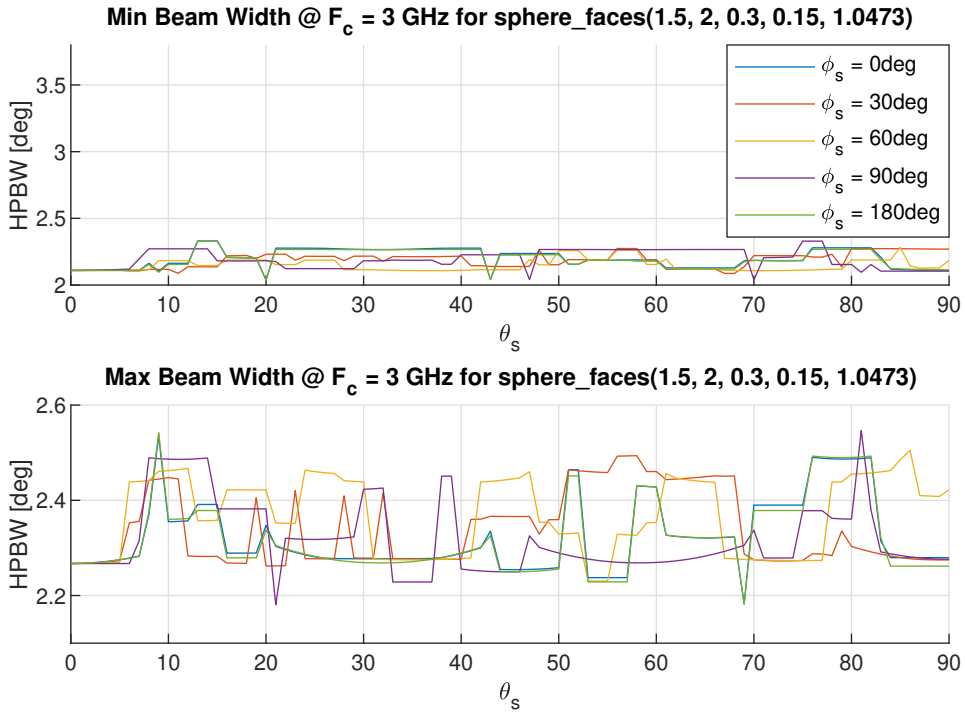

Figure 3.46: Beam width for a faceted quasi-spherical array with 2 subdivisions as function of θ_s and ϕ_s.

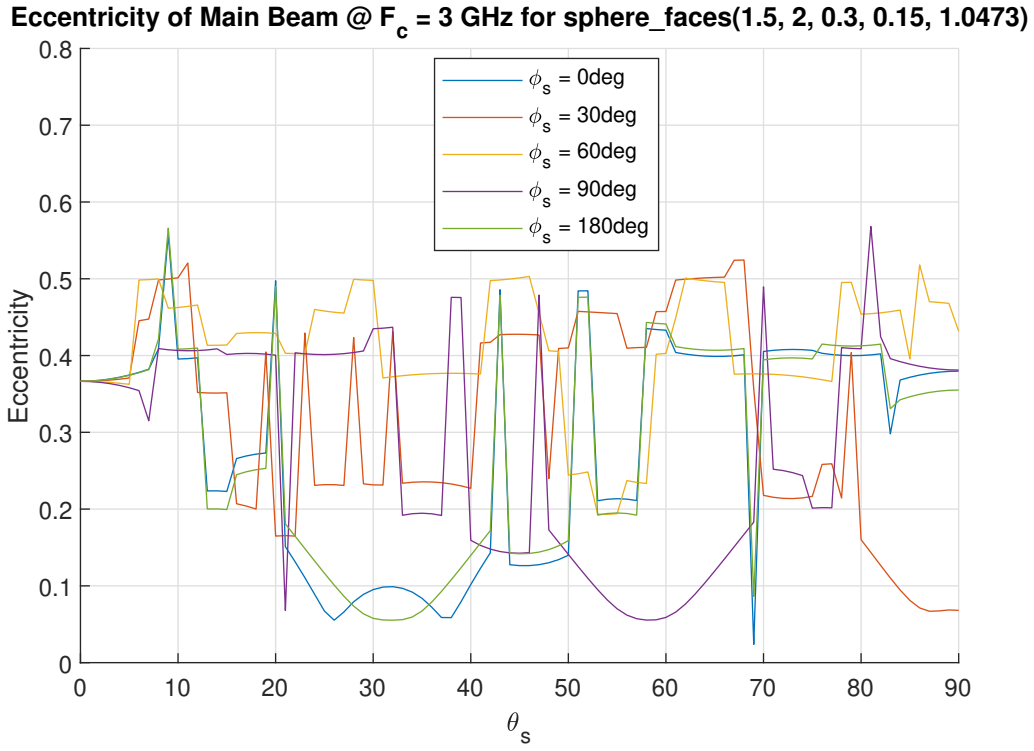

Figure 3.47: Eccentricity of the main beam versus scan angle for the 2-subdivision faceted quasi-spherical array.

to the continuous quasi-spherical configuration. The eccentricity is displayed in figure 3.47. Figure 3.47 shows that also the eccentricity is relatively good but a bit worse than for the continuous case.

The total area of the array is calculated by calculating the area of each triangular facet and summing all these facet areas. This results in an area of 24.25 m^2. A plot of the active aperture is shown in figure 3.48. It can be seen from this figure that even though the HPBW and eccentricity are less optimal, the active aperture area of faceted version is smaller compared to the continuous quasi-spherical configuration. This means that a potential reduction in active elements and thus power consumption can be achieved. Table 3.8 shows the comparison criteria for the 2-subdivision quasi-spherical array.

Table 3.8: Comparison criteria of the 2-subdivision faceted quasi-spherical array.

$BW_{operational}$ $[MHz]$	e_{max}	A $[m^2]$	$A_{active,max}$ $[m^2]$
2491	0.57	24.25	7.21

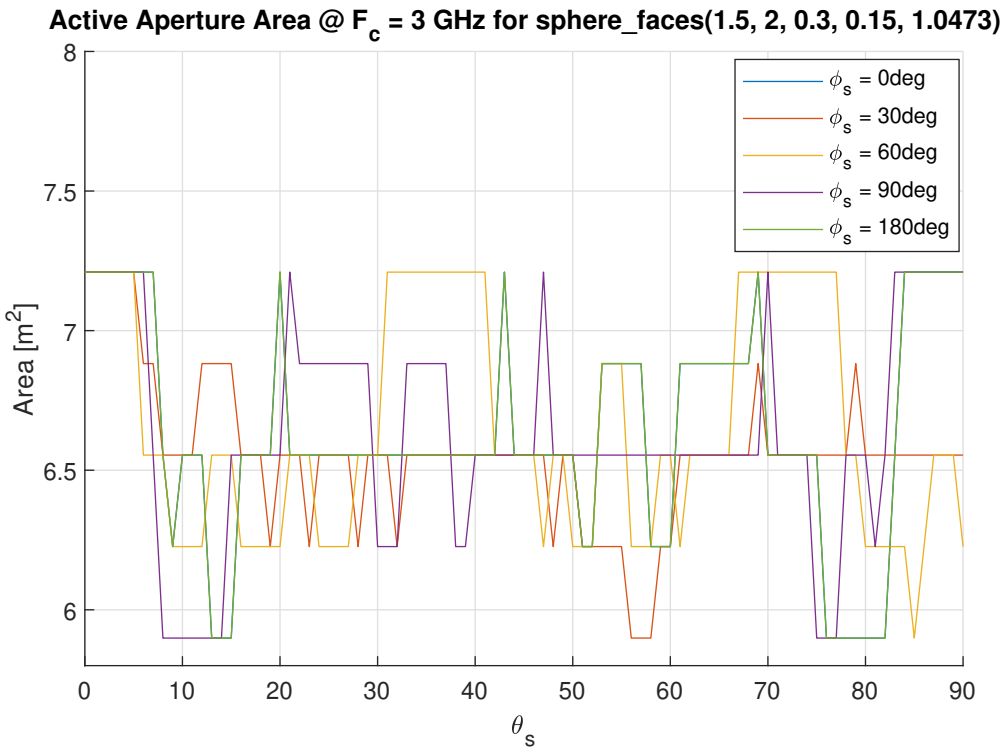

Figure 3.48: Active aperture area of the 2-subdivision faceted quasi-spherical configuration as function of scan angle.

3.2.10. Faceted Quasi-Spherical Array - 4 Subdivisions

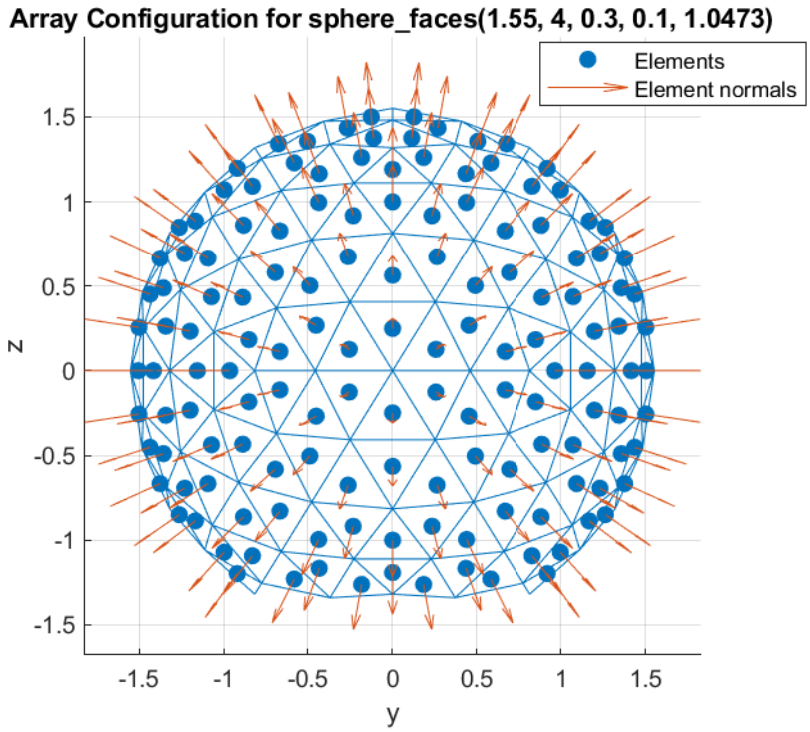

Figure 3.49: The 4-subdivision faceted quasi-spherical array with a radius of 1.55 m, an element spacing of 0.3 m and a keep-out distance of 0.1 m.

As mentioned in the previous section, the performance of the 2-subdivision faceted quasi-spherical configuration is a bit worse than the continuous quasi-spherical array. An increase in the number of facets increases the approximation of the continuous quasi-spherical array at the cost of less elements per facets which may result in more complex beamforming networks as less elements have the same normal vectors. Also, as the number of facets increases, the facets may become too small to house a suitable antenna element.

The dimensions of the 4-subdivision quasi-spherical array that are found to be ideal is a configuration with a radius of 1.55 metres and a keep-out distance of 0.1 metres. The configuration is displayed in figure 3.49. The HPBW for this configuration is shown in figure 3.50. From this figure can be seen that the HPBW is closer compared to the 2-subdivision version to the non-faceted quasi-spherical array and is even able to exceed its performance. This is likely due to the fact that the radius of the faceted quasi-spherical array could be made a bit larger before the the minimum HPBW would drop below 2 degrees.

A plot of the eccentricity is shown in figure 3.51. This figure also shows that the eccentricity is better than the continuous version of the quasi-spherical array. This could be because the topology of the elements is symmetrical along more axis than the arclength topology used for the regular quasi-spherical array.

The active aperture area is found to be 27.36 m^2. A plot of the active aperture area is shown in figure 3.52. From this plot can be observed that the variation in the active aperture area is about the same for both the continuous and faceted versions (except for the large variation for the continuous quasi-spherical array for $\theta_s < 3°$) even though the total area of the faceted array is larger. The comparison criteria are shown in table 3.9.

Table 3.9: Comparison criteria of the 4-subdivision faceted quasi-spherical array.

$BW_{operational}$ $[MHz]$	e_{max}	A $[m^2]$	$A_{active,max}$ $[m^2]$
2562	0.36	27.36	7.77

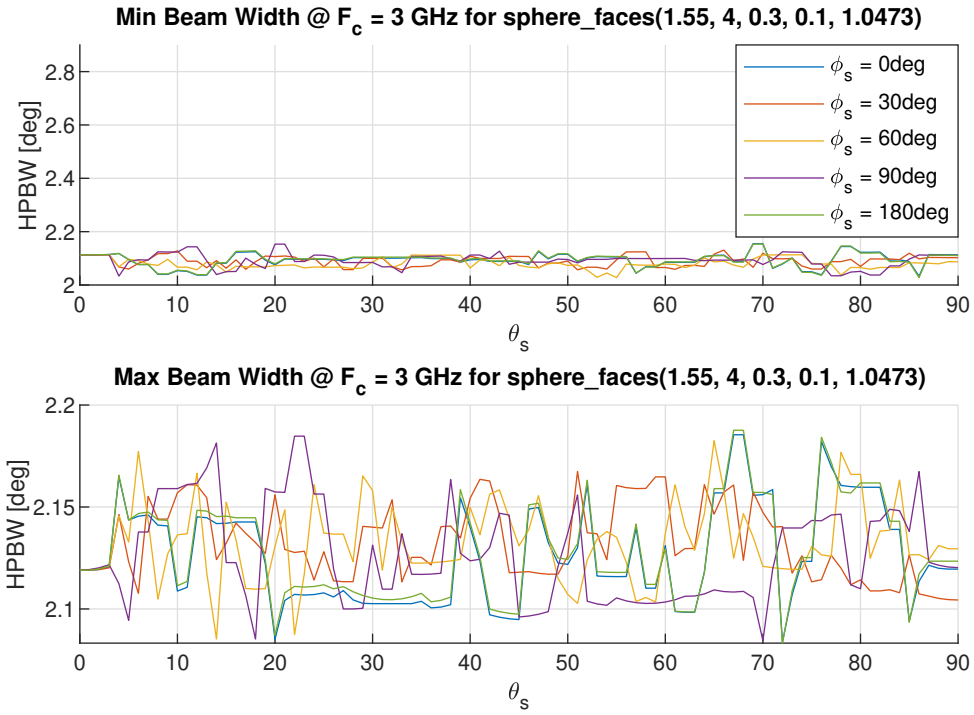

Figure 3.50: Beam width for a faceted quasi-spherical array with 4 subdivisions as function of θ_s and ϕ_s.

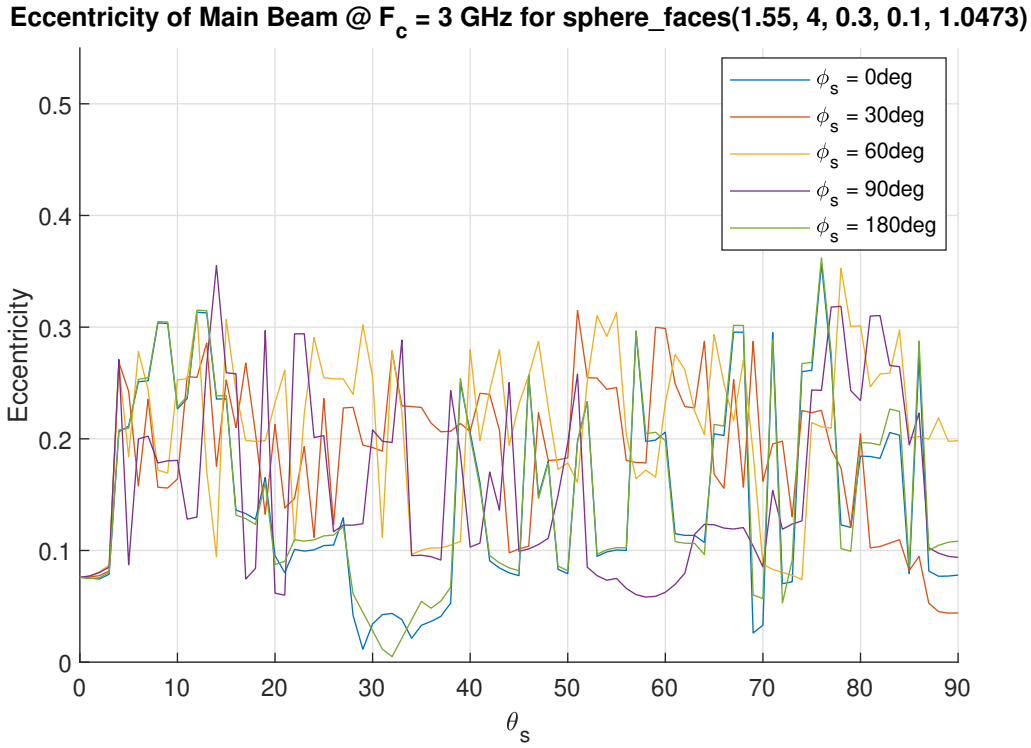

Figure 3.51: Eccentricity of the main beam versus scan angle for the 4-subdivision faceted quasi-spherical configuration.

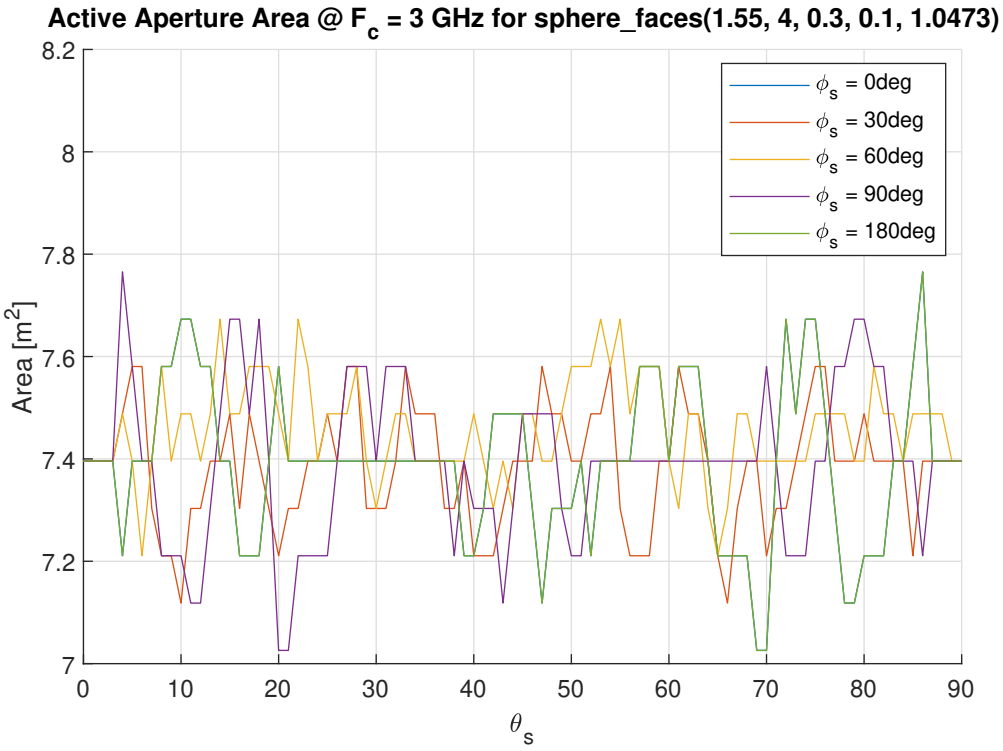

Figure 3.52: Active aperture area of the 4-subdivision faceted quasi-spherical array as function of scan angle.

3.2.11. Quasi-Spherical Array - Geodesic Topology

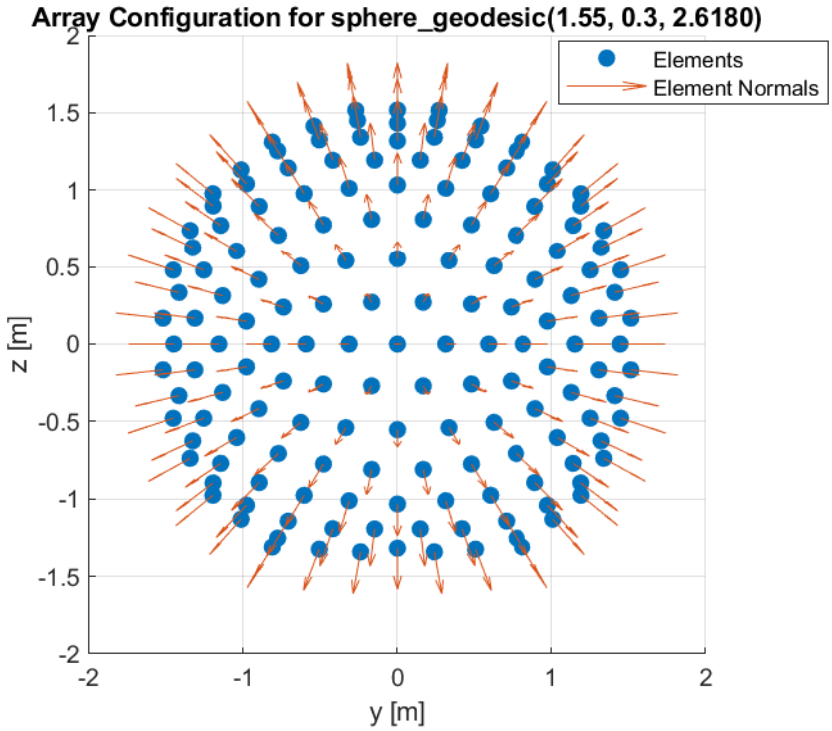

Figure 3.53: The quasi-spherical array with a geodesic topology, a radius of 1.55 m and an element spacing of 0.3 m.

A preliminary comparison between the array configurations shows that the quasi-spherical configurations, continuous and faceted, seem to outperform other configurations regarding the two most important comparison criteria, namely operational bandwidth and eccentricity.

As suggested by the results obtained for the 4-subdivision quasi-spherical array and the results of section 3.1.3, the topology of the elements could have a minor impact on the performance. Therefore, two other variations on topology for the continuous quasi-spherical configuration are investigated.

Inspired by the results of the 4-subdivision quasi-spherical array which outperforms the continuous quasi-spherical array regarding bandwidth, the first novel topology has been developed. This topology is named the geodesic topology. The geodesic topology shares a lot of similarities with the faceted quasi-spherical arrays. The difference is that instead of distributing elements on the facets, the vertices of the facets are used as element locations instead. An array with quasi-spherical geometry and geodesic topology can be created using the function `sphere_geodesic(R, d, theta_max)`. Here, `R` sets the radius of the sphere and `d` the desired spacing between the elements. The `theta_max` argument indicates the elements that should be removed, just as with the quasi-spherical array with arclength topology.

The number of subdivisions is calculated first by projecting an edge of the original icosahedral on a sphere of the radius set by `R` and calculating the length of the resulting line. The found length is then divided by the length set by `d` and rounded to the nearest integer. The resulting number is the number of subdivisions.

It is found that the radius of the geodesic-topology quasi-spherical configuration with an element spacing of 0.3 metres for which the beam properties are best is 1.55 metres. Figure 3.53 displays this configuration. The HPBW for before mentioned novel configuration is displayed in figure 3.54 and the eccentricity is plotted in figure 3.55.

As with the other continuous spherical geometries, the surface area of the array can be found using equation 3.5, resulting in a total area of 28.17 m^2. A plot of the active aperture area is shown in figure 3.56. Finally, an overview of the comparison criteria for the configuration is given in table 3.10.

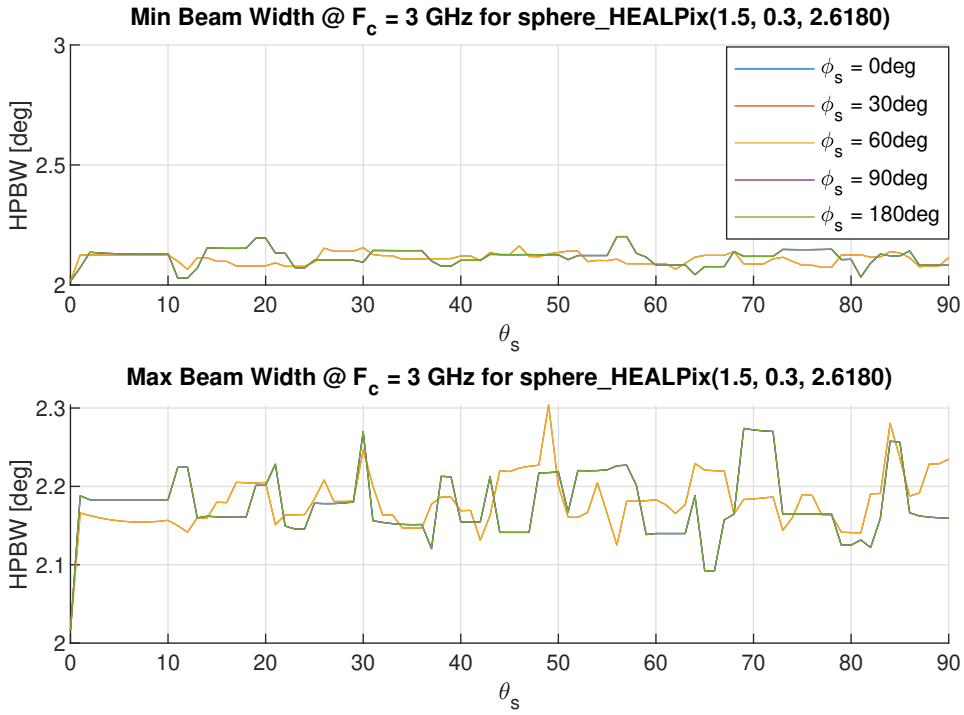

Figure 3.54: Beam width for a quasi-spherical array with a geodesic topology as function of θ_s and ϕ_s.

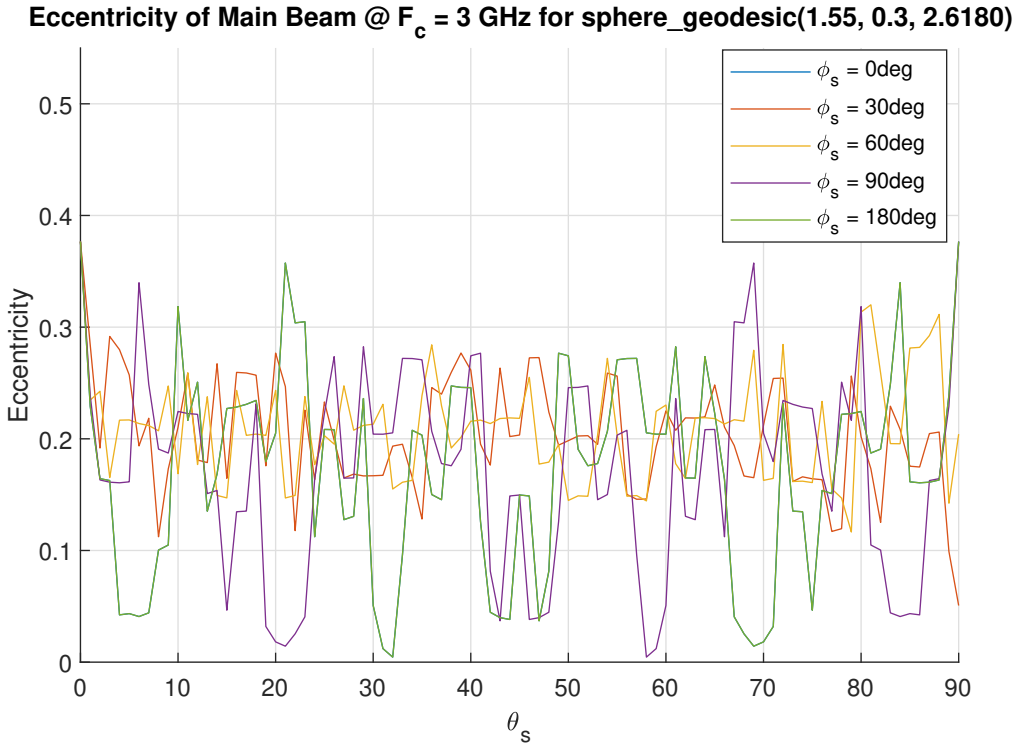

Figure 3.55: Eccentricity of the main beam versus scan angle for the quasi-spherical array with geodesic topology.

Table 3.10: Comparison criteria of the quasi-spherical array with geodesic topology.

$BW_{operational}$ $[MHz]$	e_{max}	A $[m^2]$	$A_{active,max}$ $[m^2]$
2564	0.38	28.17	7.72

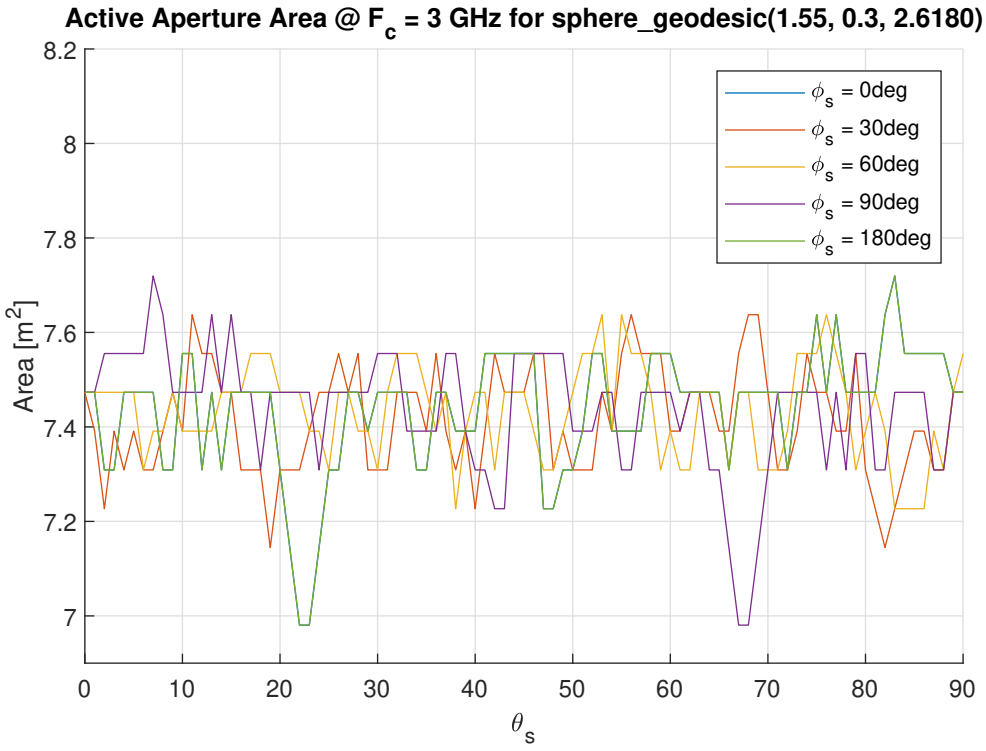

Figure 3.56: Active aperture area of the quasi-spherical array with geodesic topology as function of scan angle.

3.2.12. Quasi-Spherical Array - HEALPix Topology

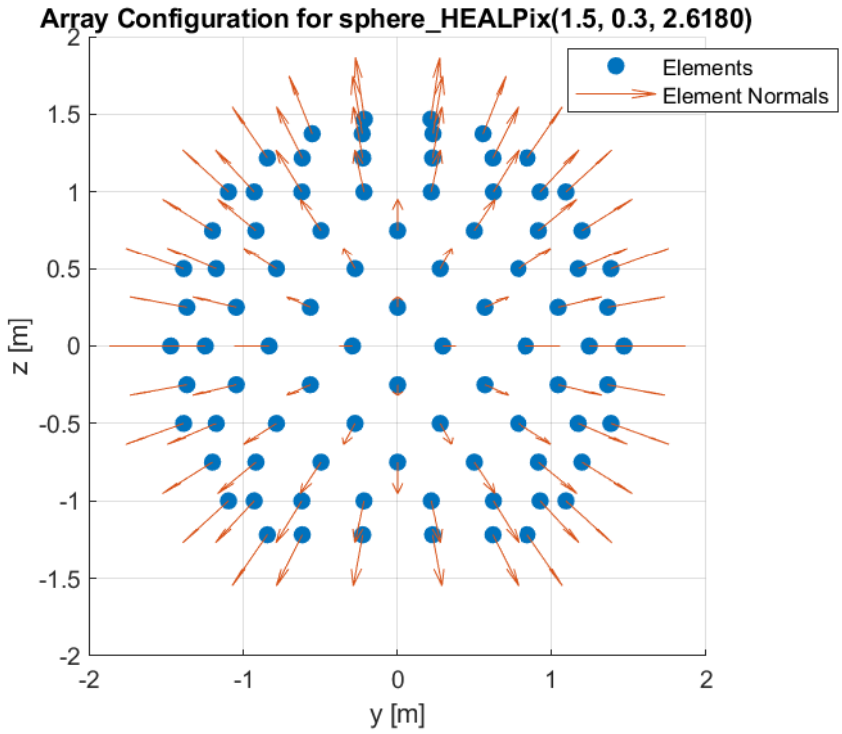

Figure 3.57: The quasi-spherical array with the HEALPix topology, a radius of 1.5 m and an element spacing of 0.3 m.

The other novel variation of topology for the quasi-spherical geometry is the so-called Hierarchical Equal Area isoLatitude Pixelisation (HEALPix) topology which is based on the HEALPix method of pixelisation of data on a sphere. HEALPix has originally been developed for analysis of data from cosmic microwave background experiments. [54]

The HEALPix algorithm distributes pixels on a sphere in such a way that each pixel comprises the same area as the other elements. However, the centre points of the pixels can also be interpreted as element locations, thus giving rise to a novel array topology.

A quasi-spherical array with the HEALPix topology can be generated using the function `sphere_HEALPix(R, arclength, theta_max)`. In this function, `R` indicates the radius of the sphere, `arclength` the desired spacing between the elements and `theta_max` the angle of θ for which elements beyond said angle should be removed. The HEALPix grid itself is generated using the MEALPix framework, which is a MATLAB version of the HEALPix software [55].

Unfortunately, HEALPix grids cannot comprise any arbitrary amount of points but need to consist of a number of points following equation 3.11 where N is an integer greater than zero [56].

$$N_{points} = 12 \cdot N^4 \tag{3.11}$$

This is also true to a certain degree for the arclength and geodesic topologies, however the number of points is much more flexible than in the HEALPix topology where the number of points needs to grow by the fourth power. The number of points used in the HEALPix topology is selected in such a way that the spacing between the elements is as close as possible to the value specified by the `arclength` argument. The resulting configuration for a quasi-spherical array with a HEALPix topology of radius 1.5 meter is shown in figure 3.57. The HPBW for this configuration is shown in figure 3.58.

The eccentricity of the array is shown in figure 3.59.

The area of the array is calculated in the same way as for the other topologies. As expected, this results in the same area as for the quasi-spherical array with arclength topology, namely 26.38 m^2. The active aperture area is shown in figure 3.60.

It is interesting that figures 3.58 to 3.60 only seem to show only two different lines. One of the two lines is formed by $\phi_s = 0°$, $\phi_s = 90°$ and $\phi_s = 180°$ which are overlapping. The other line is formed by

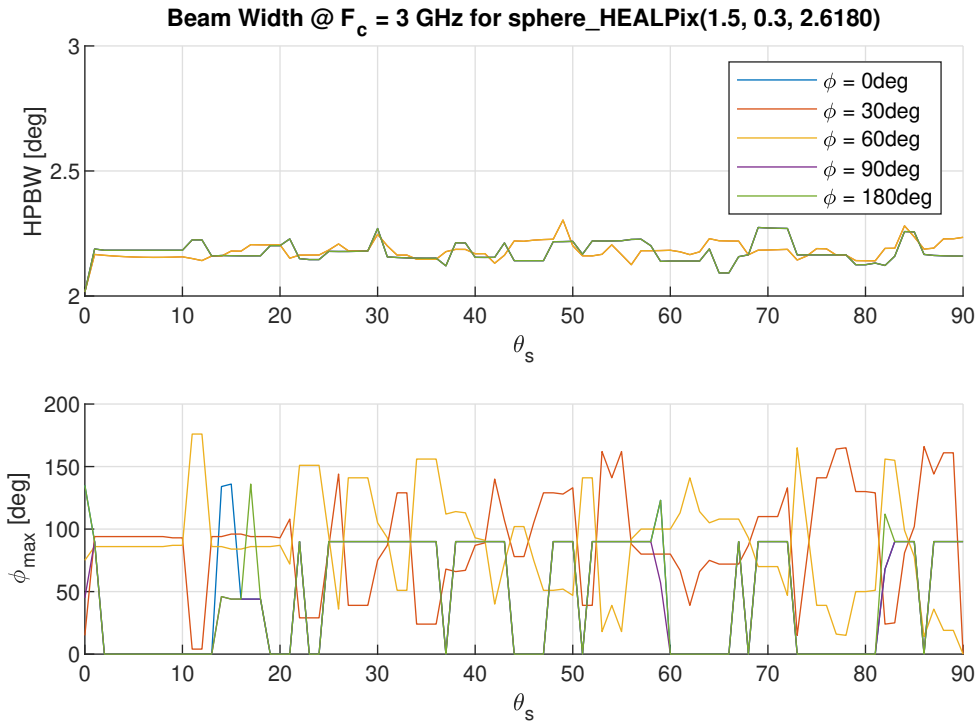

Figure 3.58: Beam width for a quasi-spherical array with a HEALPix topology as function of θ_s and ϕ_s.

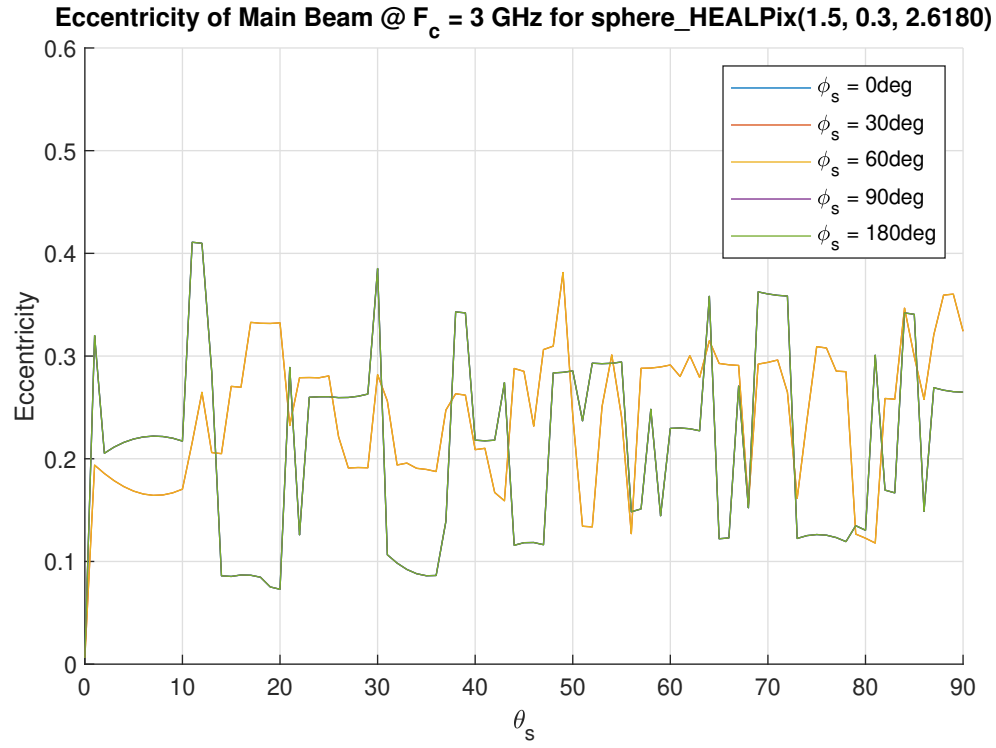

Figure 3.59: Eccentricity of the main beam versus scan angle for the quasi-spherical array with HEALPix topology.

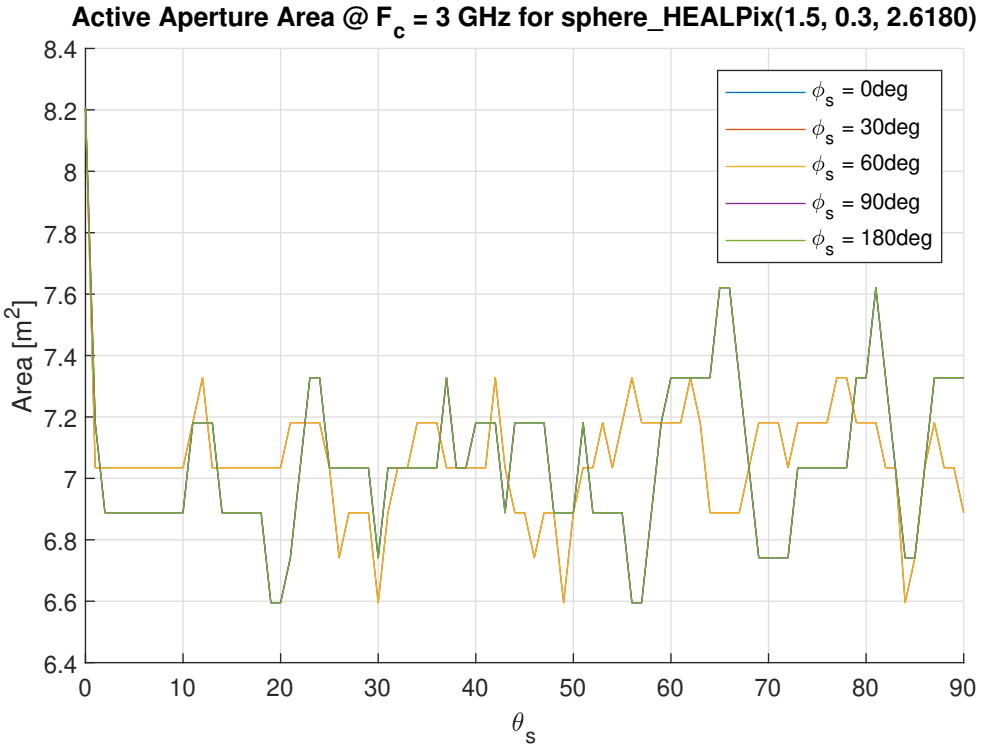

Figure 3.60: Active aperture area versus scan angle for the quasi-spherical array with HEALPix topology.

the set of angles consisting of $\phi_s = 30°$, $\phi_s = 60°$. This overlapping is a result of the HEALPix topology being highly symmetric.

To conclude, the comparison criteria for this configuration are displayed in table 3.11.

Table 3.11: Comparison criteria of the quasi-spherical array with HEALPix topology.

$BW_{operational}$ $[MHz]$	e_{max}	A $[m^2]$	$A_{active,max}$ $[m^2]$
2539	0.41	26.38	8.21

3.3. Trade-off of Conformal Array Configurations

In the previous section, numerous array configurations have been analysed. Subsequently, for the first time, this much data can now be used for a novel comparison in order to select the array configuration that is most suitable for application in DISTURB.

As described in section 3.2.1, the performance characteristics of interest of the arrays in order of importance are the operational bandwidth, ellipticity of the beam, the total surface area and the active aperture area. The comparison criteria as shown in the tables of the previous section, are compiled in table 3.12.

Table 3.12: Compilation of the comparison criteria for the analysed arrays.

Configuration	$BW_{operational}$ $[MHz]$	e_{max}	A $[m^2]$	$A_{active,max}$ $[m^2]$
Hemisphere	2214	0.83	13.21	6.37
Quasi-sphere	2547	0.43	26.38	7.68
Cone	2203	0.82	8.79	8.79
Cylinder	2291	0.82	13.19	6.71
Ellipsoid	2453	0.59	15.95	**6.37**
Faceted Cone	2088	0.83	**8.15**	8.15
Faceted Cylinder	2253	0.78	17.77	10.63
Faceted Quasi-sphere (2 subdivisions)	2491	0.57	24.25	7.21
Faceted Quasi-sphere (4 subdivisions)	2562	**0.36**	27.36	7.77
Geodesic quasi-sphere	**2564**	0.38	28.17	7.72
HEALPix quasi-sphere	2539	0.41	26.38	8.21

In this table, the best values for each criterion are printed in bold face. As can be seen from the table, the quasi-spherical configuration with geodesic topology has the largest theoretical operational bandwidth. However, the HEALPix quasi-spherical, faceted quasi-spherical with 4-subdivisions and the arclength quasi-spherical configurations are not far off.

Considering the eccentricity, the faceted quasi-spherical configuration with 4 subdivisions is the best but as with the operational bandwidth, the other continuous quasi-spherical configuration are quite close.

Table 3.12 also shows that the faceted conical array has the least amount of surface area, but also has the worst operational bandwidth. The ellipsoidal configuration has the least active aperture area but relatively good eccentricity and operational bandwidth.

Since operational bandwidth and eccentricity are more important than the other criteria, it becomes clear that a quasi-spherical array geometry is the best choice. As the novel geodesic topology scores better on bandwidth and eccentricity than the other continuous quasi-spherical arrays, the HEALPix and arclength topologies can be eliminated especially since the differences in total and active surface areas are not that large. Also, since the HEALPix topology has a number of elements following equation 3.11, it is also less flexible regarding element density than the geodesic topology.

Now that the HEALPix and arclength topologies have been eliminated, the choice remains between the 4-subdivision faceted and geodesic quasi-spherical arrays. From a practical standpoint, a faceted array may be easier to manufacture. However, the larger the number of subdivisions, the number of unique facets increases as well, thereby reducing the manufacturability benefit. Also regarding the fact that a full-wave analysis is to be performed on the array configurations, a faceted quasi-spherical array is geometrically more complex. Therefore, it is harder to set-up this configuration in numerical EM analysis software, thus requiring a larger investment of time.

This results in the fact that the quasi-spherical array configuration with geodesic topology is selected as the best configuration to proceed with because of the interest of time and because the manufacturing benefit is reduced at 4 subdivisions.

Lastly, it should be mentioned that if the surface area of the array had been a more important consideration, the ellipsoidal configuration would be best. This is due to the fact that operational bandwidth and eccentricity are quite good in comparison with the configurations that have a similar or smaller surface area. Therefore, the ellipsoidal array seems to provide the best eccentricity and operational bandwidth per antenna element.

3.4. Conclusions on Array Configuration

Using isotropic patterns for the active element patterns, a great reduction in required computational resources is achieved. This allowed for an analysis of numerous array configurations to determine their relation on general radiation pattern characteristics over scan angle and frequency. Here, the array configuration comprises the geometry of an array, i.e. three-dimensional shape, and topology, i.e. the antenna element lattice.

It has been shown that the HPBW is inversely proportional to the frequency. Furthermore, it has been demonstrated by the novel comparison that conformal arrays do not suffer from grating lobes in the classical sense due to this class of array generally not having periodicity along the z-direction. However, these grating lobes appear as very strong side lobes. Also, it is concluded that the topology of the array has no significant impact on the HPBW but has significant effect on side lobe levels when the antenna elements are placed densely.

By using isotropic element patterns, for the first time many different array configurations could be compared for their radiation patterns properties regarding operational bandwidth and beam eccentricity over scan angle. In combination with the total array surface area and active aperture area, it is concluded from this novel comparison that a quasi-spherical array with a novel geodesic topology with a radius of 1.55 metres and a 0.3 metre-element spacing, resulting in an array with 343 elements, is most beneficial for the DISTURB project. This configuration has a theoretical operational bandwidth of 2564 MHz, a maximum beam eccentricity of 0.38, a surface area of 28.17 square metres and a maximum active aperture area of 7.72 square metres.

In the next chapter, an element for this array is designed to achieve an ultimate performance that is as close as possible to the theoretical maximum bandwidth computed in this chapter.

4

Antenna Element Design

This chapter presents the design of the antenna element to be used in the conformal array configuration selected in chapter 3. Firstly, the properties of the ideal antenna for application in the quasi-spherical conformal phased array are discussed. Subsequently, a number of potential antenna element designs are investigated. Lastly, the most beneficial antenna element is selected in a trade-off.

4.1. Ideal Antenna Element Properties

In order to be able to select the most suitable antenna element for use in the conformal phased array, it is important to know what the properties of an ideal antenna element for this application should be.

For the DISTURB project, three antenna properties in particular are of importance. These are the radiation pattern, the input impedance and the polarisation characteristics. The relevance and ideal characteristics of these properties will be elaborated on in the following sections.

Since the antenna array considered in this thesis should be able to operate from 1.5 to 3 GHz, the complexity of the design of the antenna element is increased. Namely, all the mentioned antenna properties should be acceptable over the whole operational bandwidth of the array and if possible, even exceed the 2:1 bandwidth requirement.

4.1.1. Radiation Pattern

From section 2.3, it is recalled that the active element radiation pattern of an antenna element is of great importance when an element is used in an array configuration. Namely, the array radiation pattern is the active element pattern multiplied by the array factor. Therefore, if one or multiple elements have no radiation in the direction of an angle within the scan range, then the array radiation pattern pattern of the array will also have a reduced amount of radiation toward that direction. Using the fact that reciprocity holds, this also means that the antenna array will receive less radiation from that particular direction. If all elements happen to have no radiation into a particular direction, the antenna array as a whole will also not have any emissions towards that direction. This is also known as scan blindness as the array is effectively blind when scanning in the direction at which scan blindness occurs. Avoiding reduced gain and scan blindness is obviously key as the array needs to be able to observe the Sun at all times when it is above the horizon. If the array would have insufficient capability to scan towards certain directions, this needs to be compensated for by adding antenna arrays with another orientation, thus adding significantly to the cost of the project.

As described in section 2.2, an element is active when a scan direction is within 60° from the element normal vector. Therefore, it can be concluded that the antenna elements themselves do not need to radiate any energy at angles beyond 60° from their normals. Furthermore, it is desirable that the radiation patterns of the elements within 60° from their normal vector are as uniform as possible. This is to not accidentally introduce an amplitude taper. Even though a taper may benefit the array radiation pattern, this taper is different for each scan angle and therefore it is best that an accidental amplitude taper is avoided.

The fact that an element shall only have radiation for angles of θ below 60° and that the radiation pattern should be uniform in this range, leads to the conclusion that the ideal active element pattern

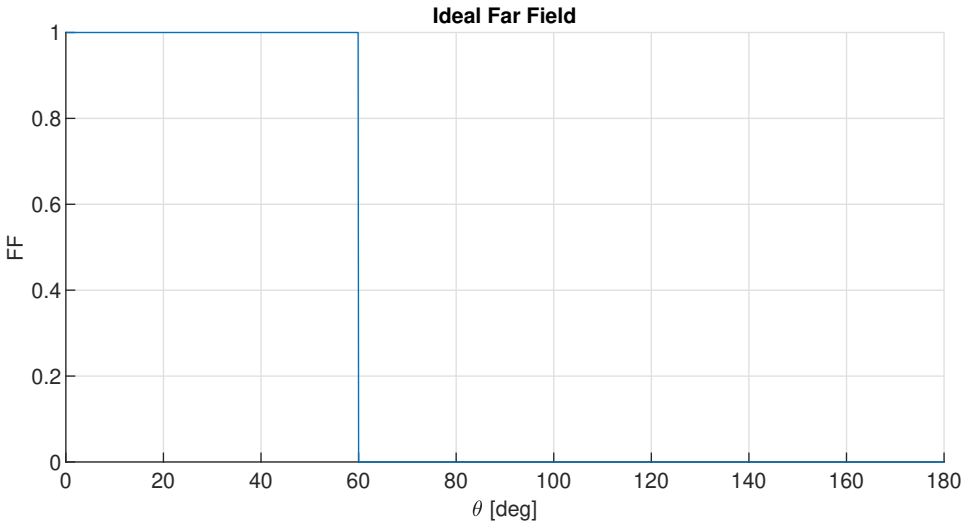

Figure 4.1: The ϕ cut of the element radiation pattern for an ideal antenna element in the conformal array.

should follow equation 4.1, where θ is in degrees and $H(x)$ is the Heaviside step function.

$$\vec{E}^{ff}(\theta, \phi) = H(60 - \theta) \tag{4.1}$$

Figure 4.1 shows equation 4.1 in a graphical way. Alternatively, figure 4.2 shows the ideal radiation pattern in a three dimensional fashion.

Unfortunately, this ideal pattern cannot exist in reality since it has a clear discontinuity at a θ angle of 60 degrees. However the ideal pattern gives a guideline to what the active element pattern of an element should look like. The more the final element radiation pattern approaches the ideal pattern, the better the final radiation pattern of the antenna array will be.

4.1.2. Input Impedance

For antenna systems used for astronomical observation purposes, the noise figure is usually of great importance. As the intended observation target of DISTURB is the Sun, which is a very strong signal source, the requirement on noise temperature is not as stringent as may be the case for other high-end astronomy systems. The requirements from section 1.3.1 place a requirement on the maximum receiver noise temperature, which is not to exceed 100 K. This maximum receiver noise temperature places in turn a requirement on the input impedance of the antenna element which is dependent on the used RF front-end components. The total noise factor of a cascade of RF components can be calculated using equation 4.2 [57].

$$F = F_1 + \frac{F_2 - 1}{G_1} + \frac{F_3 - 1}{G_1 G_2} + \cdots + \frac{F_i - 1}{G_1 G_2 \cdots G_{i-1}} \tag{4.2}$$

This equation shows that the first component in the cascade is the most important since the noise of the subsequent components is divided by the gain of the first component. Therefore, if the first component is a low noise amplifier (LNA) with sufficient gain, the noise caused by the components following the LNA can be neglected.

As demonstrated by equation 4.2, the noise factor of the receiver is dependent on the specific LNA that is used. Since the front-end RF printed circuit board design and component selection is outside the scope of this thesis project, a LNA recommended by ASTRON is used. This LNA is the SAV-541+ from Finicircuits [58].

The receiver noise factor can be calculated by equation 4.3 [59]. In this equation, F_{min} is the minimum noise factor of the LNA, r_n is the normalised noise resistance, Γ_{opt} is the optimum noise reflection coefficient of the LNA and S_{11} is the reflection coefficient of the antenna.

$$F = F_{min} + 4r_n \frac{|S_{11} - \Gamma_{opt}|^2}{(1 - |S_{11}|^2)\,|1 + \Gamma_{opt}|^2} \tag{4.3}$$

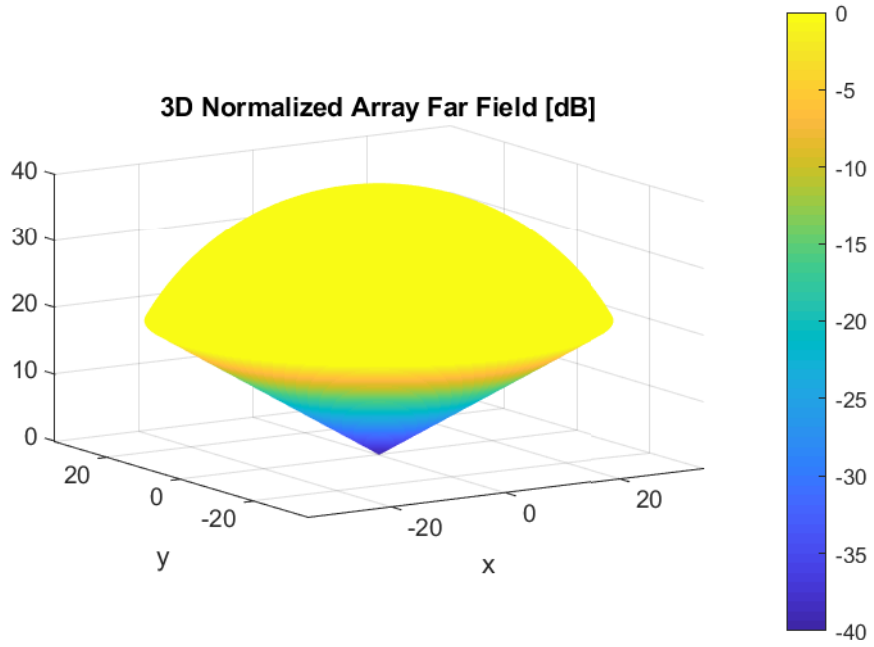

Figure 4.2: Three-dimensional plot of the ideal radiation pattern.

The noise factor can be easily converted to noise temperature using equation 4.4. In this equation, T_0 is the reference temperature which is 290 K.

$$T_n = (F - 1)T_0 \tag{4.4}$$

Equation 4.3 shows that the noise factor is equal to the minimum noise factor when the reflection coefficient of the antenna is equal to the optimum noise reflection coefficient of the LNA. Equation 4.3 also shows that if there is a mismatch between the optimum noise reflection coefficient and the antenna reflection coefficient, the severity of the increase in noise factor is determined by the normalised equivalent noise resistance.

Using some algebraic manipulation, so-called noise circles can be found from equation 4.3. These circles indicate the values of the antenna reflection coefficient for which the noise factor is equal to a set value. The centre of the noise circle O_N can be found using equation 4.6 and the radius R_N can be found using equation 4.7. In both equations, N is defined in equation 4.5, which has been adapted from [60].

$$N = \frac{F - F_{min}}{4r_n}|1 + \Gamma_{opt}|^2 \tag{4.5}$$

$$O_N = \frac{\Gamma_{opt}}{1 + N} \tag{4.6}$$

$$R_N = \frac{1}{1 + N}\sqrt{N^2 + N - N|\Gamma_{opt}|^2} \tag{4.7}$$

From equation 4.4, the maximum noise factor can be calculated from the requirement in section 1.3.1 and is found to be 1.34. Subsequently, this noise factor can be used to set requirements on S_{11} by equations 4.6 and 4.7. Since the noise parameters of the LNA are frequency dependent, so are the noise circles. A few of them have been plotted in figure 4.3. As long as the reflection coefficient of the antenna is within the noise circle at the corresponding frequency for all frequencies, the noise requirement is met.

The Smith chart from figure 4.3 has a reference impedance Z_0 of 50 Ω and is valid for the case when the LNA is connected in a single-ended manner. The single-ended configuration has a balun connected

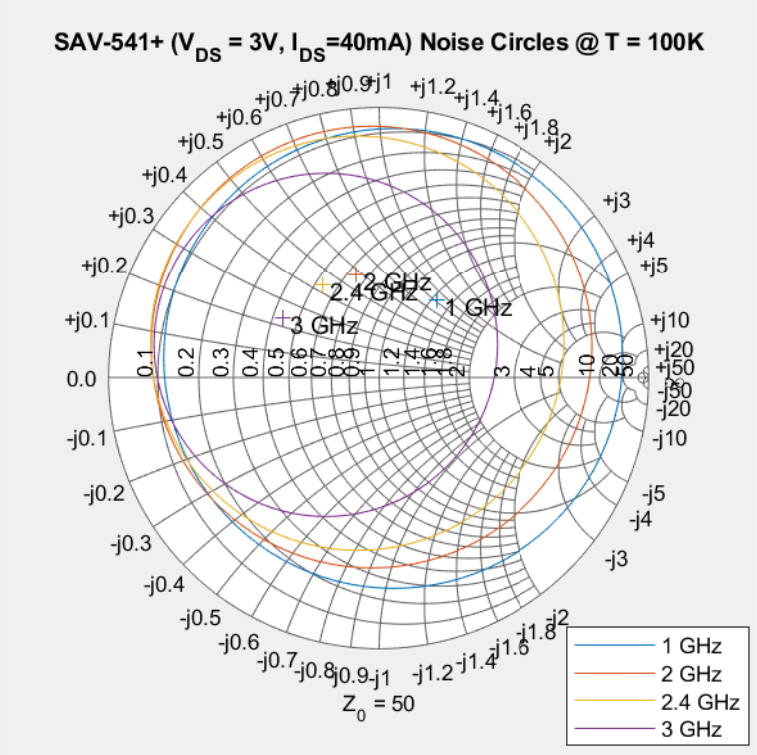

Figure 4.3: Smith chart plot of the noise circles for the SAV-541+ that is biased for minimum noise figure.

directly to the antenna to transform the differential output of both dipole arms to one ground-referenced transmission line. This line is subsequently connected to the input of a LNA which is in turn connected to a matched load. This load could be another amplifier, a mixer, ADC and so on.

Instead of using a single-ended configuration, also a differential connection scheme can be considered. In this scheme, both arms of a dipole-like antenna are each connected to an individual LNA. The outputs of the LNA can then be connected to more differential RF components or transformed to a single-ended output by using a balun.

The differential configuration has the nice property that the characteristic impedance of the system is multiplied by a factor of two [61]. Furthermore, under the condition of a differential system with same signal path gains, the noise properties are the same for the single-ended and differential configurations and the noise circles and optimum noise reflection coefficients remain the same [62]. Therefore, antenna elements with a larger input impedance can be used without noise-increasing matching networks. Besides this potential benefit in input impedance, also the first component in the RF-chain is the LNA in contrast to the single-ended case, where the first component is a balun. Thus, in the single-ended configuration the balun may add a non-negligible amount of noise due to loss which directly translates to noise figure whereas this is not occurring in the differential case.

In the ideal scenario, the antenna is perfectly matched to the optimum noise reflection coefficient. The optimum noise reflection coefficient can subsequently be used to calculate the ideal input impedance of the antenna elements in single-ended and differential configurations using equation 4.8. In this equation, Z_0 is the characteristic impedance which in the single-ended case is 50Ω and in the differential case 100Ω. The resulting input impedances are shown in figure 4.4.

$$Z_{antenna} = \frac{\Gamma_{opt} + 1}{1 - \Gamma_{opt}} Z_0 \tag{4.8}$$

4.1.3. Polarisation

The requirements in section 1.3.1 state that the antenna should be able to receive signal from the Sun independent of polarisation. This can be achieved in two ways. The first of which is using an antenna element that is sensitive to two orthogonal components of polarisation. This could for example be the θ

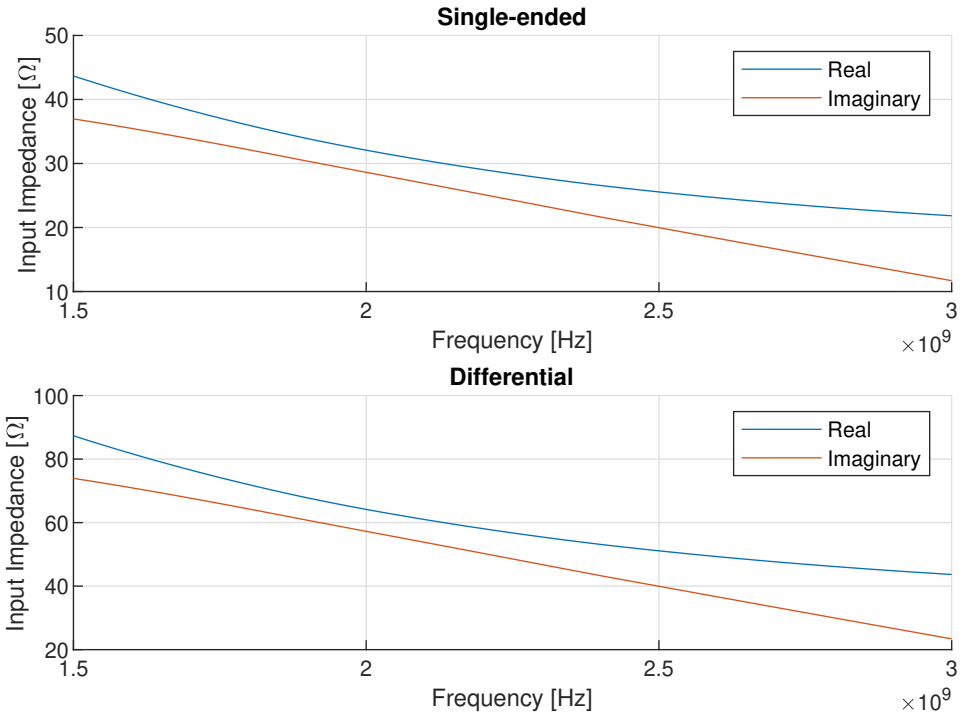

Figure 4.4: Ideal antenna input impedance for single-ended and differential LNA configurations for the SAV-541+ at minimum noise factor biasing conditions.

and ϕ components, horizontal- and vertical-polarisation in the Ludwig-III reference system or left- and right-hand circular polarisation. Alternatively, an antenna element could also be constructed out of two sub-elements of which one is sensitive to one component of the polarisation and the other to the other component.

The second option is preferable, since this approach allows the conformal antenna array also to be utilised as a polarimeter. This comes at a cost of a doubling of the required RF front-end electronics. However, the way that the emissions of the Sun are polarised may provide interesting data [63] and is found to outweigh this disadvantage.

In order for an antenna element to be used as polarimeter effectively, the antenna must be as sensitive as possible to one of the orthogonal polarisation directions and reject the other. If this is not the case, the output of one sub-element may become contaminated with signal which is polarised in the other direction and therefore the estimation of the polarisation of the measured signal may contain a significant error.

This leads to the conclusion that the isolation between the two orthogonal directions should be at least more than 0 dB as below that value the cross-polarised component is stronger than the co-polarised one. In the ideal case, the ratio of co- and cross-polarised components is infinite.

4.2. Comparative Study of Antenna Element Designs

The next step is to find an antenna element that approximates the ideal properties listed in the previous section as well as possible. To this end, a number of antenna elements are evaluated and tuned for the DISTURB frequency range using Computer Simulation Technology Studio Suite 2017, CST for short.

Since the element density of the chosen array configuration is quite sparse, the radiation patterns, impedances and polarisation properties of the elements in isolation should not differ much from their active element properties. Therefore, the isolated element properties already provide a good indication of the performance of the antenna when used in the geodesic quasi-spherical array configuration. Analysing the elements in isolation allows for a grand reduction in required computational resources compared to performing full-wave analysis of the entire array.

4.2.1. Crossed Bow-Tie Antenna

A half-wavelength dipole possesses good qualities regarding polarisation. However, the half-wave dipole is a very narrow band antenna. A dipole-like configuration that is able to achieve wide bandwidth is the biconical antenna [64]. Here, both antenna arms are cones instead of wires. If these conical arms are extended to infinity, the input impedance of the biconical antenna is independent of frequency and can be controlled by the cone apex angle [64]. This makes that the bandwidth of the biconical antenna is effectively infinite.

As a true biconical antenna is practically impossible to manufacture due to the infinite nature of the cones, approximations can be made by using finite cones. In order for this approximation to provide reasonable performance, the cones should be made long in terms of wavelength. Since these cones may still be impractical and expensive to manufacture, this approximated biconical antenna can be reduced to a planar slice along the length of the cones. This results in the bow-tie antenna.

The radiation pattern of a bow-tie antenna is close to that of a half-wavelength dipole. However, as stated in section 4.1, radiation towards angles of θ of more than 60° is undesired. To help with this, a ground plane is placed underneath the antenna. After a number of iterations, a bow-tie antenna with a radius of 4 centimetres, a flare angle of 80 degrees and a distance to the ground plane of 3.3 centimetres is found to perform best. The resulting receiver noise temperature is shown in figure 4.5. This figure shows that the antenna element is able to provide a noise temperature lower than 100 K in the band ranging from about 0.9 GHz to 3 GHz.

By using another bow-tie antenna, rotated by 90°, and overlaying that with the original bow-tie antenna, an antenna element is created that is capable of polarimetry. A picture of this antenna is shown in figure 4.6.

Unfortunately, due to the small gap between the two sub-elements, the sub-elements seem to couple with each other and change the impedance behaviour. This results in the antenna causing the receiver to have a noise temperature above 100 K, as shown in figure 4.7. Therefore, the crossed bow-tie antenna does not adhere to the specifications. Performing a parametric study of the crossed bow-tie antenna improved the receiver noise temperature but unfortunately, the antenna still could not comply with the specifications.

In order to deal with these problems, other antenna designs are considered. One of these designs is a planar dipole antenna which consists out of two ellipses [65]. Antennas of this design can cover almost two octaves and are well matched to 50Ω [65]. This impedance is about the same as the real part of the ideal impedance for the differential LNA configuration. However, the downside of this design is that the elements cannot be rotated by 90° and overlaid with each other, since they will intersect and thus cause a short.

Therefore, in order to emulate the ellipticity of the dipole elements, exponential tapers are used instead. The lines emanating from the centre of the antenna are defined by an exponential function

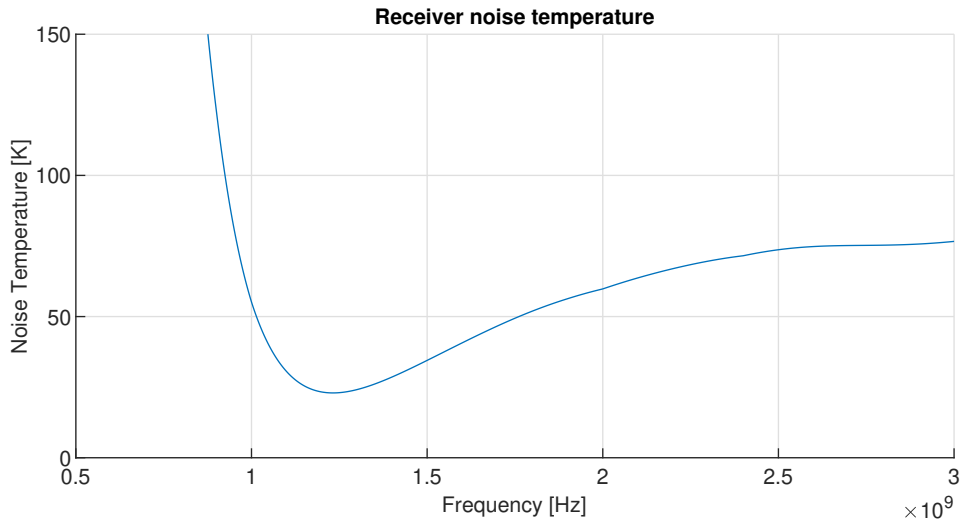

Figure 4.5: The receiver noise temperature for a bow-tie antenna connected to a SAV-541+ LNA.

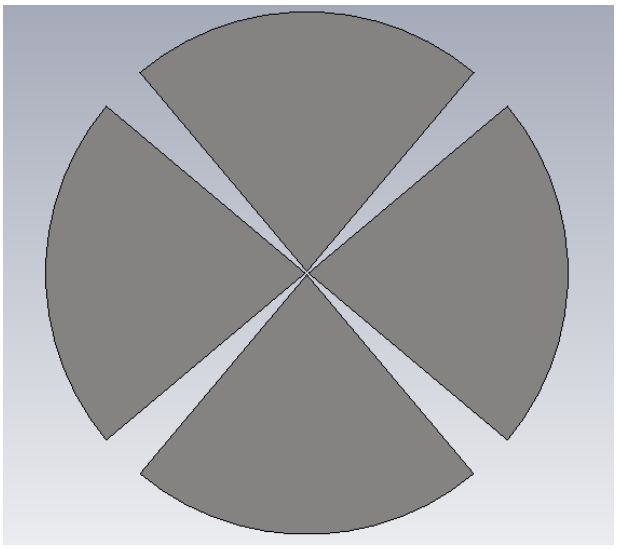

Figure 4.6: Illustration of the crossed bow-tie antenna.

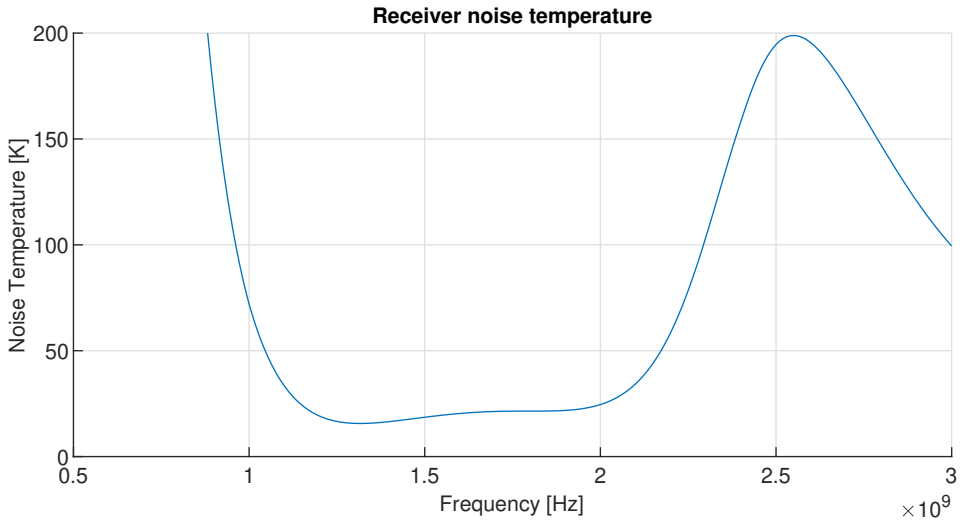

Figure 4.7: The receiver noise temperature for a crossed bow-tie antenna connected to a SAV-541+ LNA.

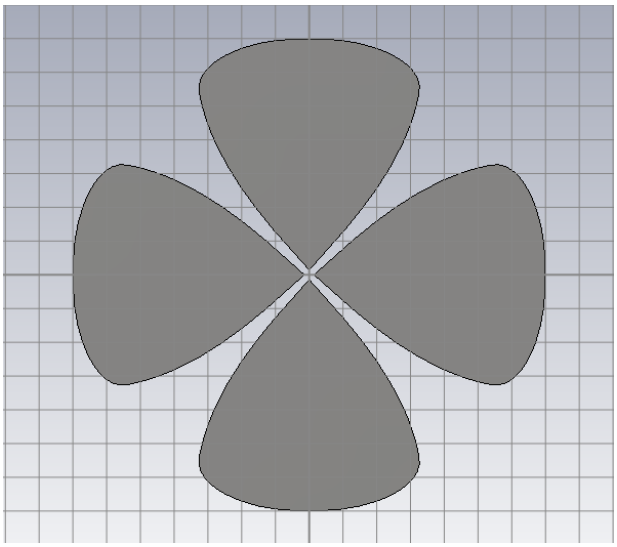

Figure 4.8: Illustration of the crossed modified bow-tie antenna.

of the form Ae^{bx} with x indicating the x-coordinate, which is copied, translated and rotated to form the edges of the dipole flares. To be more specific, A is 0.5 millimetres and b is 90.27 metres. The flares are completed using a spline which is defined in such a way that its derivative is as identical as possible in the connecting points with the exponential taper. The completed antenna is shown in figure 4.8. This antenna has a diameter of about 7 centimetres and is placed 3.3 centimetres above a ground plane.

The HPBW of the sub-element itself in the H-plane is almost 60° at 3 GHz as can be seen from figure 4.9. The beam width for higher frequencies is wider, this is ascribed to the fact that the antenna becomes longer than half a wavelength at 3 GHz and thus the beam is split. This figure also shows that the beam is much narrower in the E-plane with a HPBW close to 25°. This is expected as a dipole antenna also shows narrower beam-width in the E-plane than in the H-plane, where it is omnidirectional. The radiation pattern of both sub-elements is the same, but rotated since the antenna looks the same as seen from the port of the first sub-element as from the port of the second sub-element.

The receiver noise temperature of the modified bow-tie antenna is shown in figure 4.10. Due to symmetry, both sub-elements have the same impedances. Therefore, the noise temperature is also the same.

Lastly, the cross-polarisation isolation X_{pol} achieved by this antenna at 1.5 GHz is shown in figure 4.11. This cross-polarisation isolation is calculated using equation 4.9.

$$X_{pol} = \left| \frac{E_{co}}{E_{cross}} \right| \tag{4.9}$$

It is found that the minimum value of the cross-polarisation isolation in the region of θ between 0° and 60° is about 4.7 dB. This occurs at a frequency of 1.5 GHz for large angles of θ.

4.2.2. Open-Ended Square Waveguide

Instead of a planar element, one can also consider three-dimensional antennas. One of the first antennas that comes to mind is a horn antenna. However, the flare of the horn antenna expands the waveguide and increases the aperture of the antenna. This increases gain, which is undesirable given the broad characteristics of the ideal far field. The simple solution to combat this effect is by leaving out the horn altogether and use an open-ended waveguide as antenna element as was done with some examples of early phased array antennas [12].

Since the antenna element should be capable of receiving both polarisations of the electric field with the same properties, the waveguide should be of square shape. Using equation 4.10 [66], which gives the cut-off frequency $f_{c_{mn}}$ of the TE$_{mn}$ mode, the dimensions of the waveguide can be determined.

$$f_{c_{mn}} = \frac{1}{2\pi\sqrt{\mu\epsilon}} \sqrt{\left(\frac{m\pi}{a}\right)^2 + \left(\frac{n\pi}{b}\right)^2} \tag{4.10}$$

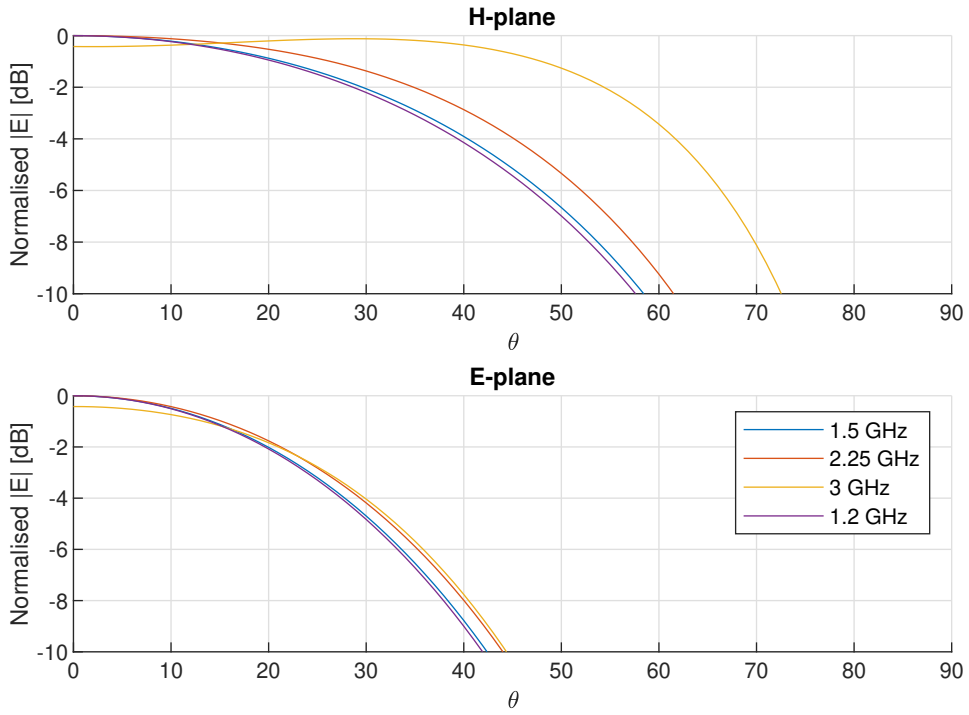

Figure 4.9: Normalised far field of the crossed modified bow-tie antenna in the E- and H-planes for several frequencies.

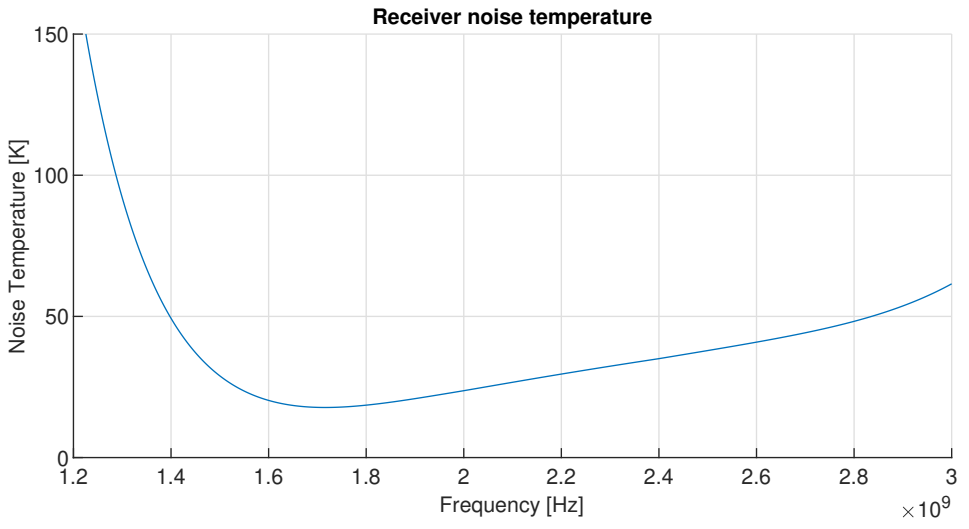

Figure 4.10: Receiver noise temperature for the crossed modified bow-tie antenna with a SAV-541+ LNA.

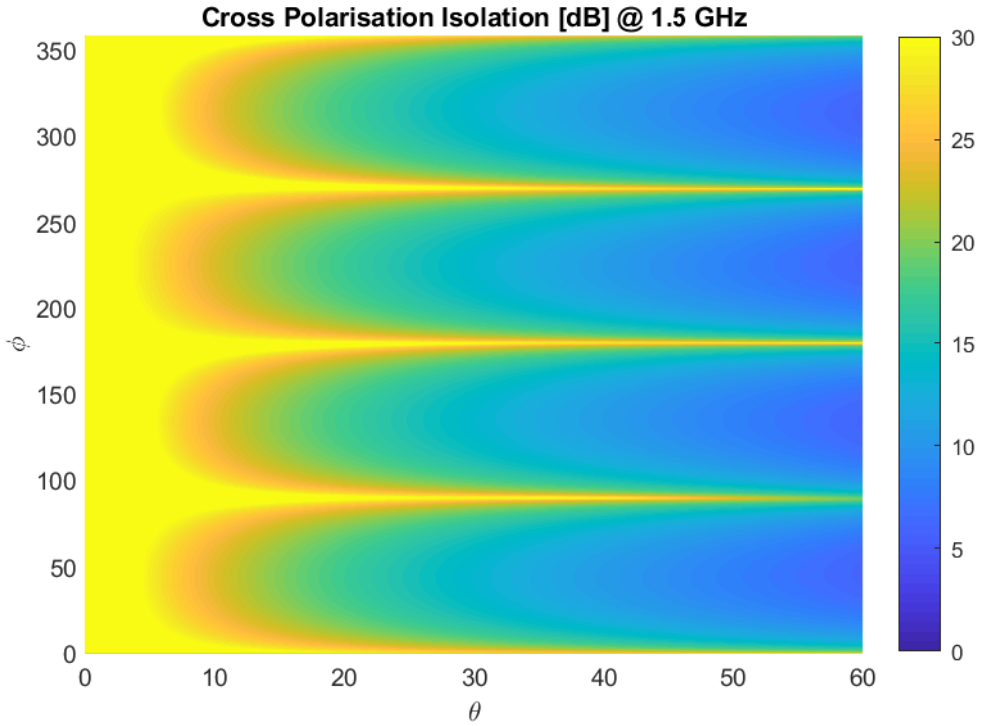

Figure 4.11: Cross-polarisation isolation in dB of the crossed modified bow-tie antenna at 3 GHz.

In this equation a is the width of the waveguide and b is the height of the waveguide.

It is desired that only the fundamental mode is propagating in the waveguide, since this mode gives good radiation patterns. Therefore, the cut-off frequency of the TE_{10} mode should be 1.5 GHz. Using $m = 1$ and $n = 0$ and 1.5 GHz as cut-off frequency, a is calculated to be 10 centimetres, which is half a wavelength at that frequency. Because of the fact that the waveguide is square, b is equal to a and it can be seen that the orthogonally polarised mode TE_{01} unsurprisingly has the same cut-off frequency.

Now the first non-fundamental modes are considered. Theoretically, these are the TE_{11} and TM_{11} modes. The cut-off frequency of the transverse magnetic modes can also be found using equation 4.10. Since the width and the height of the waveguide is the same, these two modes have the same cut-off frequency. This frequency is calculated to be about 2.12 GHz. Next to these two modes, the TE_{20} and TE_{02} modes have a cut-off frequency of 3 GHz, which is also within the operational frequency range.

To confirm the presented theory, a square waveguide of 10 by 10 centimetres fed with a waveguide port is modelled in CST. The cut-off frequencies of the fundamental modes are found to be 1.50 GHz, 2.12 GHz for the TE_{11} and TM_{11} modes and 3.00 GHz for the TE_{20} and TE_{02} modes. This is in line with the theoretical predictions. Some far field cuts of the different modes are shown in figure 4.12.

This figure shows that the fundamental modes have a maximum at $\theta = 0°$, however, the other modes go to zero at said angle. This means that these modes will suffer from scan blindness and potentially distort the overall radiation pattern.

Even if the unwanted modes can be suppressed, it can be seen that the HPBW of the fundamental modes is significantly smaller than for the modified bow-tie antenna. This could potentially be solved by using an open-ended waveguide that is filled with a dielectric as it allows for reducing the aperture size. However, dielectrics introduce losses which reduce noise performance.

Figure 4.13 shows the cross-polarisation isolation for the waveguide. This figure shows an isolation which is comparable to or even worse than the cross-polarisation isolation of the modified bow-tie antenna.

As shown, the far field properties are less optimal than the far field properties of the crossed modified bow-tie antenna and the non-fundamental modes may limit bandwidth significantly. Therefore, creating a feeding structure for the square open-ended waveguide antenna and investigating the radiation

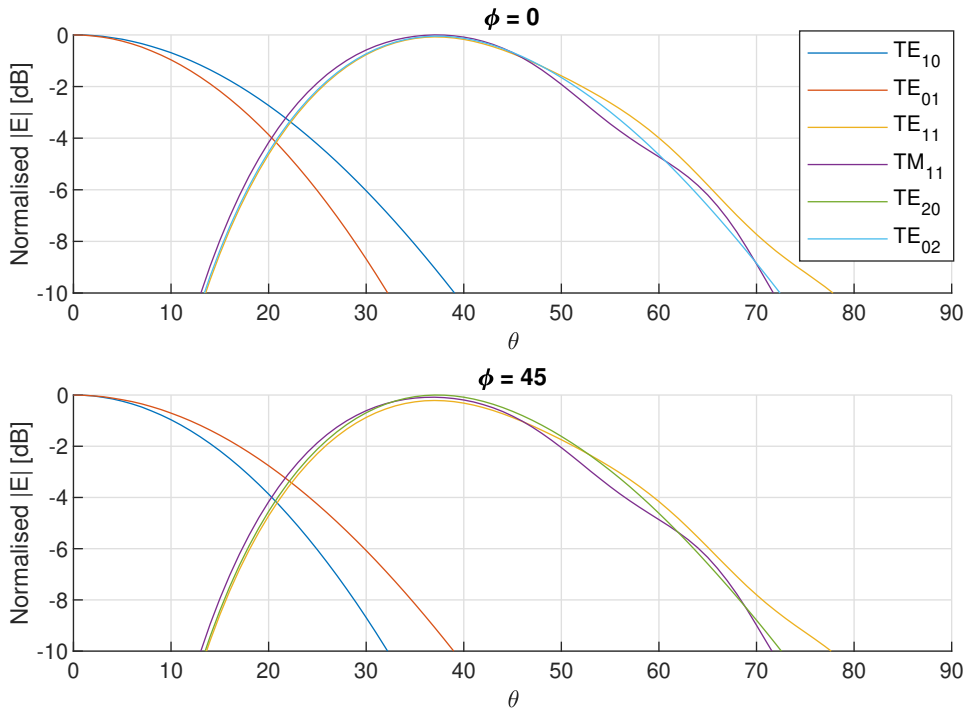

Figure 4.12: Normalised far field cuts for the six propagating modes in the open-ended square waveguide at 3 GHz.

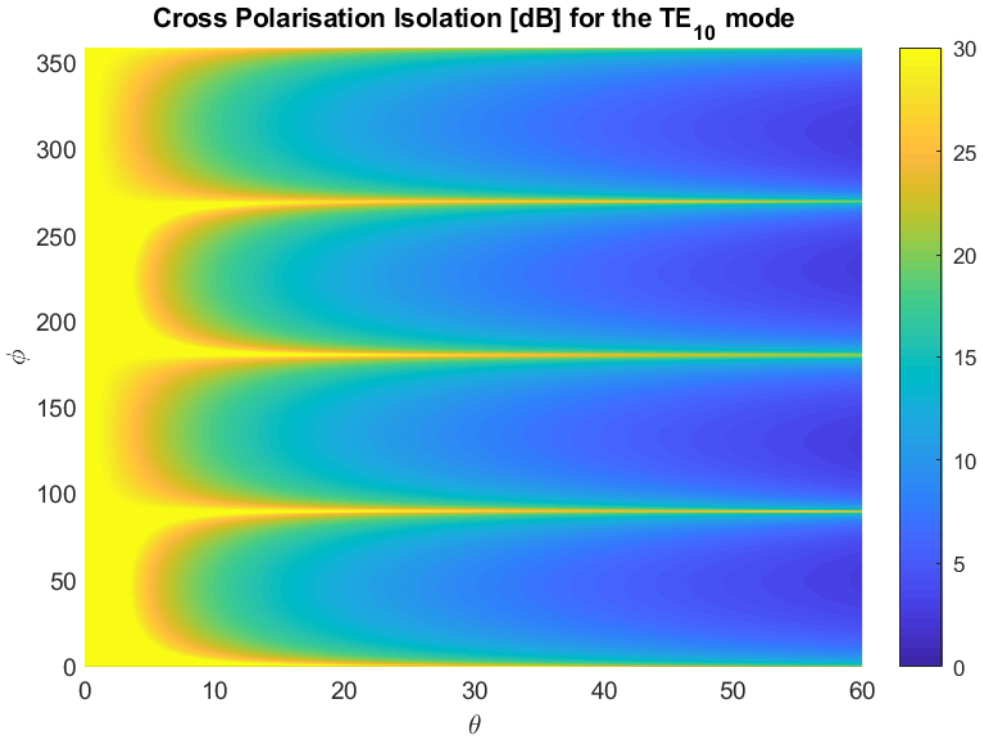

Figure 4.13: Cross-polarisation isolation in dB of the square open-ended waveguide antenna.

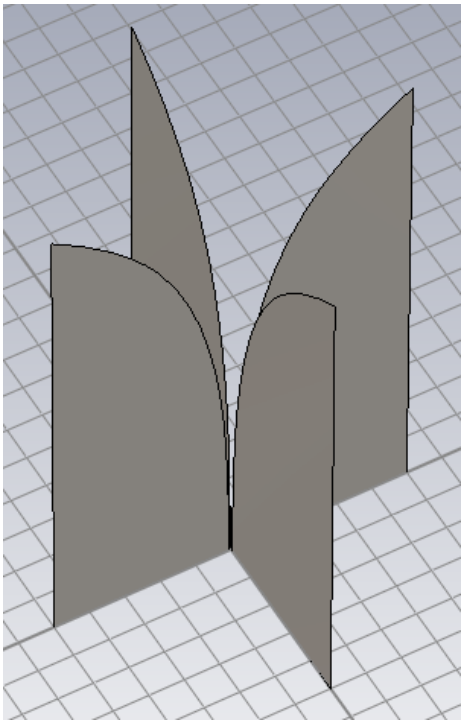

Figure 4.14: Illustration of the crossed tapered slot antenna.

pattern improvement with the use of dielectrics are not further pursued.

4.2.3. Crossed Tapered Slot Antennas

Inspired by EMBRACE [4], a tapered slot antenna (TSA) may also satisfy the requirements. The tapered slot antenna, also known as a Vivaldi antenna, is a planar antenna in which a slot has been cut out. The shape of this slot is defined by a function of the form Ae^{bz} where z indicates the position along z and A and b are geometry parameters. The TSA can have impedance bandwidths of up to 10:1 [67]. Since the TSA is linearly polarised, it can be used in a crossed configuration as with the crossed modified bow-tie antenna so it can be operated as a polarimeter.

The sub-elements of the crossed tapered slot antenna are 30 centimetres high and have a width of 20 centimetres. The feed gap is dimensioned to be 2 millimetres. Using these dimensions, the A and b parameters of the exponential taper can be found. Parameter A is calculated to be 1 millimetre and b is about 15.35. In order for the antenna to not pick up interference generated by the RF front-end electronics and to shield the electronics from external interference, the tapered slot antenna is backed by a ground plane at a distance of 2 centimetres from the base of the TSA. A picture of the resulting crossed tapered slot antenna is shown in figure 4.14.

Subsequently, the receiver noise temperature is evaluated. The result is displayed in figure 4.15. As can be seen, the crossed TSA is able to comfortably comply to the specification on receiver noise temperature.

A number of cuts of the radiation patterns have been plotted in figure 4.16. It can be seen that the HPBW in the H-plane ($\phi = 0°$) is larger than in the E-plane ($\phi = 90°$). However, there is quite some variation in the beam within their half-power beam width regions at some frequencies which may impact the array beam shape adversely. Also, the beam width in the E-plane is quite narrow.

Figure 4.17 shows the cross polarisation isolation at the frequency at which it is best, namely 2.25 GHz. It can be seen that for small angles of θ the cross-polarisation isolation shows about the same behaviour as the crossed modified bow-tie. However, for scan angles above 30° in θ, the cross-polarisation isolation drops below 0 dB, meaning that the cross-polarised component is received stronger than the co-polarised component, which is undesirable.

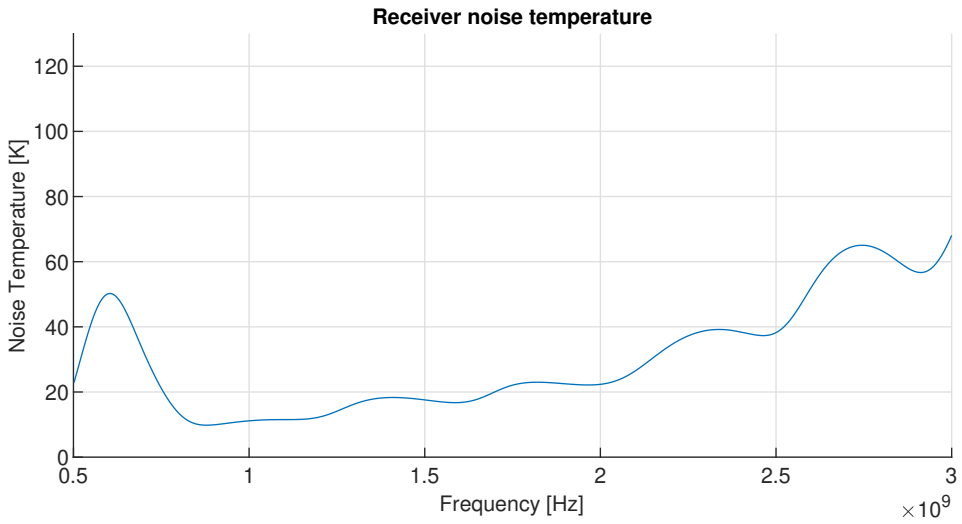

Figure 4.15: Receiver noise temperature for the crossed TSA with a SAV-541+ LNA.

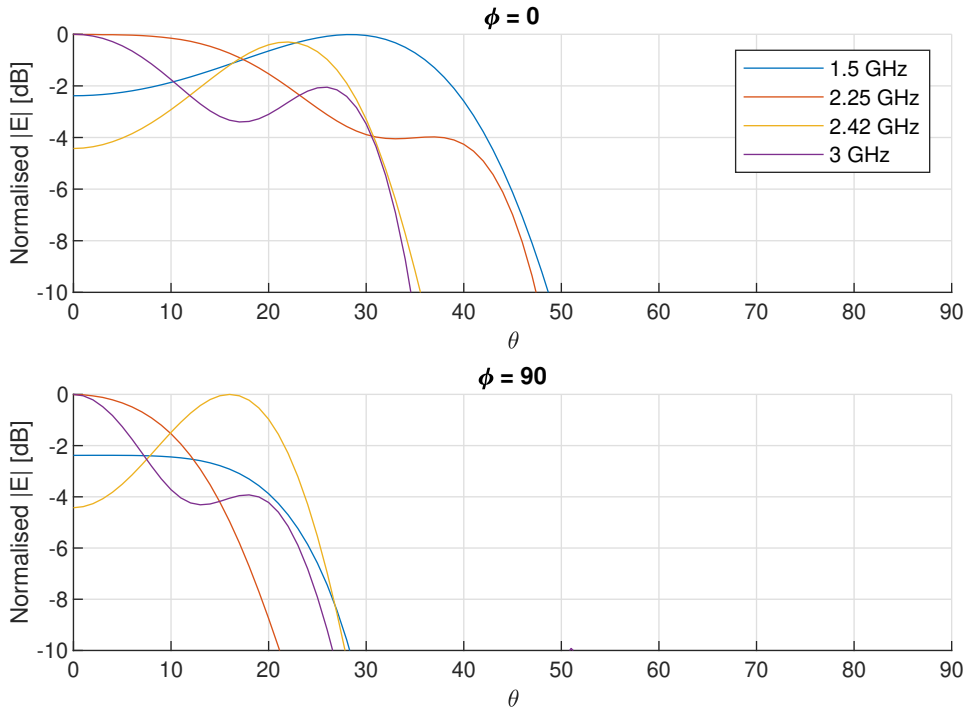

Figure 4.16: Normalised far field cuts for the crossed tapered slot antenna at several frequencies.

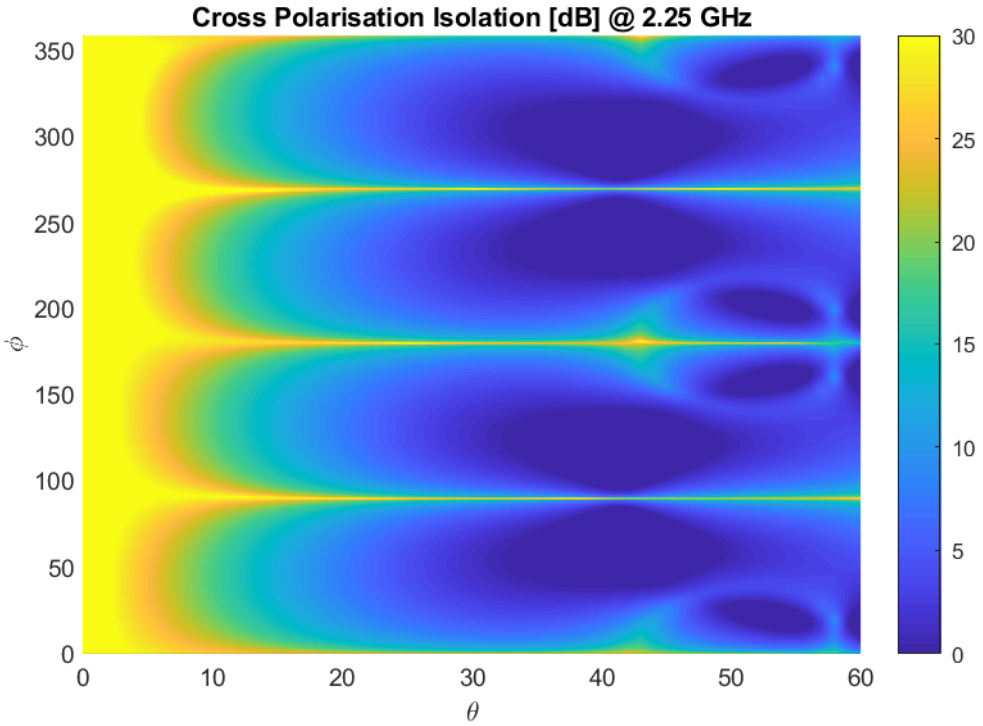

Figure 4.17: Cross-polarisation isolation in dB of the crossed TSA at a frequency of 2.25 GHz.

4.2.4. Self-Complementary Planar Log-Periodic Antenna

A very interesting class of antennas is the class of self-complementary antennas. Self-complementary antennas are antennas of which the metallised geometry has the same shape as the slots in between the metallised components. True self-complementary antennas have the remarkable property that their impedances are independent of frequency [68]. However, true self-complementary antennas are infinitely large. Therefore, in practice the self-complementary antennas are of course finite and thus approximations, just as with the bow-tie antenna.

The self-complementary property can be combined with a 4-arm planar log-periodic antenna as done in [69]. This may allow the antenna to start operating as a regular log-periodic antenna if the self-complementary approximation is not holding due to for example the antenna being electrically too short.

The base parameters that define the geometry of the self-complementary planar log-periodic antenna are shown in figure 4.18. In order to create the log-periodic nature of the antenna, the tooth defined by radii R_1 and R_2 is scaled by a factor k. This is repeated N_{rep} times to create all teeth. In order for the antenna to be self-complementary, the angle β should be equal to $90 - \alpha$. Furthermore, R_{feed} indicates the radius of the feed gap.

The implemented antenna is shown in figure 4.19. This antenna has a feed radius of 0.5 millimetres, R_1 is 2 millimetres, R_2 is 2.2 millimetres, the repetition factor k is set to 1.2 and the number of repetitions N_{rep} is 21, resulting in 44 teeth per arm. The angle α is set to 15°.

Figure 4.20 shows that the impedance of the self-complementary log-periodic antenna is indeed very stable, but starts to vary a lot as the frequency becomes low. Since it is matched relatively well to the optimum noise reflection coefficient, also the receiver noise temperature is well-behaved as shown in figure 4.21.

However, the self-complementary planar log-periodic antenna is sensitive to radiation from both front and backside. This is not desirable since the antenna may pick up spurious signals generated by the RF front-end electronics. Therefore, the antenna needs to be backed by a ground plane. Unfortunately, adding the ground plane breaks the self-complementary property of the antenna and makes it operate with a dominant log-periodic characteristic. This can partly be mitigated by increasing the distance between the antenna and the ground plane. However, increasing this distance also results

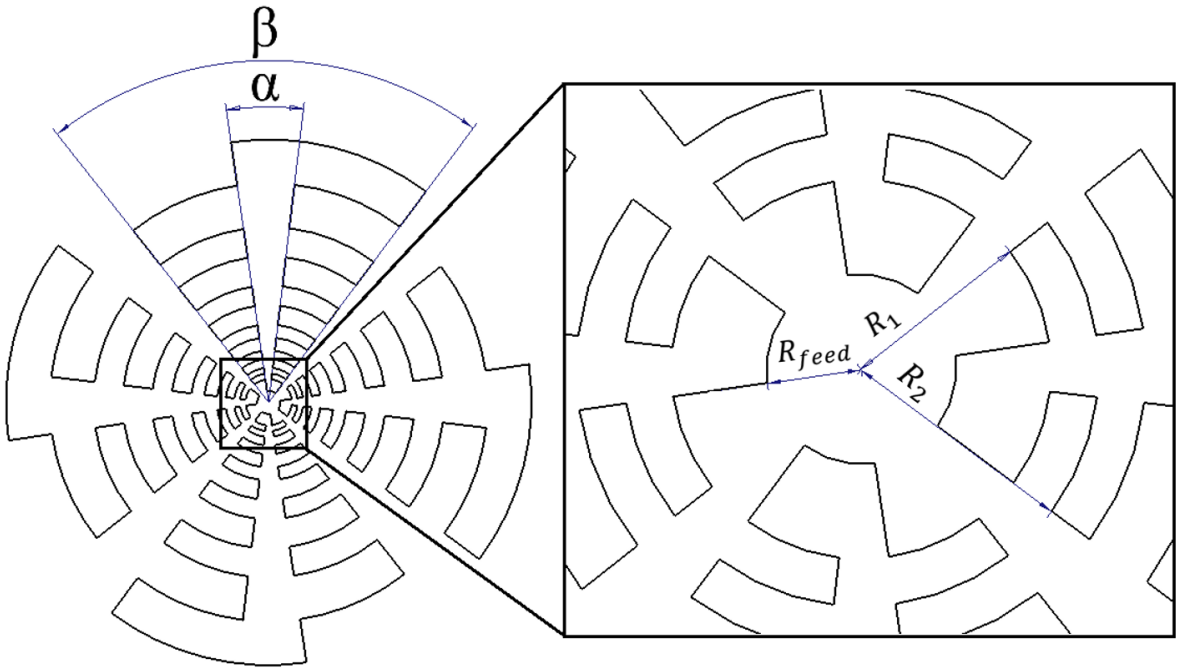

Figure 4.18: Dimensions of the self-complementary planar log-periodic antenna.

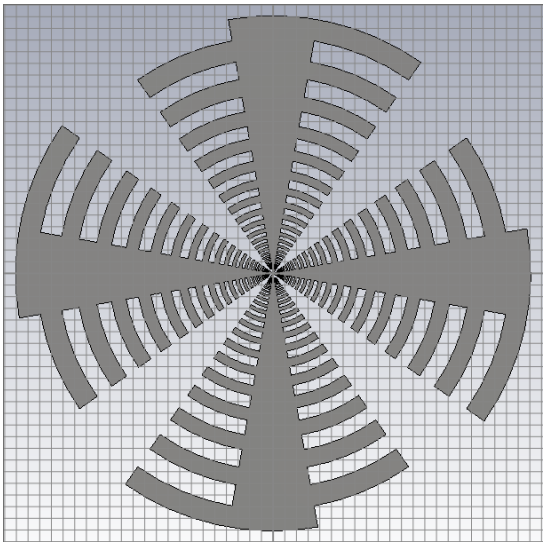

Figure 4.19: Illustration of the self-complementary planar log-periodic antenna.

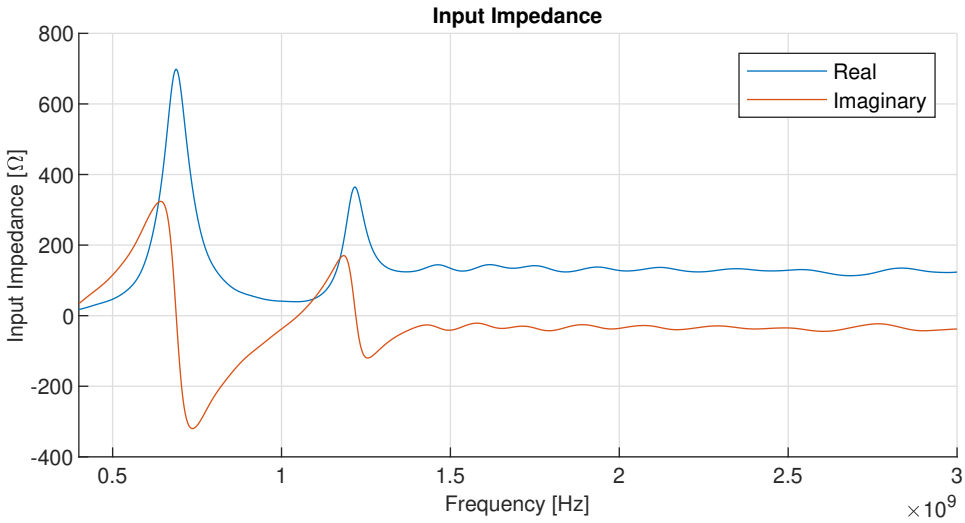

Figure 4.20: Input impedance of the self-complementary planar log-periodic antenna.

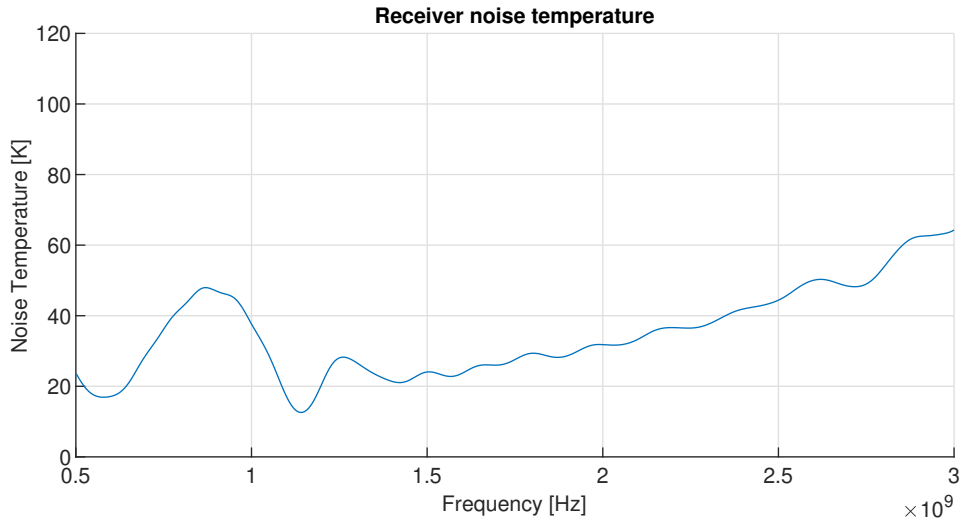

Figure 4.21: Receiver noise temperature for the self-complementary planar log-periodic antenna with a SAV-541+ LNA.

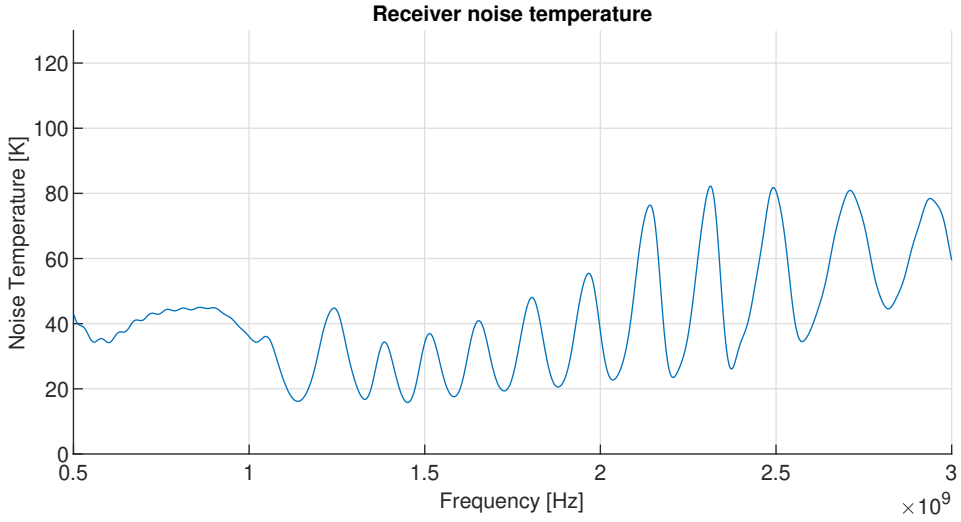

Figure 4.22: Receiver noise temperature for the self-complementary planar log-periodic antenna with a ground plane at 7 centimetres and a SAV-541+ LNA.

in the fact that the radiation that is directly incident on the antenna starts destructively interfering with the radiation scattered from the ground plane. This causes the radiation patterns of the antenna to be sub-optimal as gain reductions can now appear in the scan range. It is found that by using a ground plane at a distance of 7 centimetres away from the antenna is able to just keep the receiver noise temperature below 100 K.

Another option to mitigate the disadvantageous effect of the ground plane on impedance and beam width is by using a RF absorber between the antenna and the ground plane. When the absorber absorbs sufficiently, no radiation is reflected from the ground plane and therefore the antenna has effectively the same properties as without ground plane. The big downside of this is that this absorber will increase the noise temperature of the antenna and therefore this option has not been taken in consideration.

Some cuts of the radiation pattern are shown in figure 4.23. As mentioned, destructive interference occurs which negatively impacts the radiation patterns. Furthermore, since the antenna is not symmetrical, the radiation patterns of the antenna are also asymmetrical in contrast to the crossed TSA and the crossed modified bow-tie antenna. From figure 4.23 it can also be seen that for a number of frequencies, the main beam is not even directed towards zenith, i.e. the radiation pattern is not 0 dB at $\theta = 90°$ as the patterns have been normalised at each frequency with respect to all angles of θ and ϕ.

A plot of the cross-polarisation isolation is shown in figure 4.24. It can be seen that the cross-polarisation isolation of the planar log-periodic antenna is low. This is probably due to the surface currents running partly along the teeth and partly along the main beam of the antenna. Since these directions are orthogonal, this likely lowers the cross-polarisation isolation significantly. Also, as with the crossed TSA, the cross-polarisation drops below 0 dB at certain angles.

4.3. Antenna Element Trade-off

In the previous section a number of antenna elements have been investigated. Now, the antenna elements are compared on their receiver noise temperature, radiation patterns and cross-polarisation isolation. This is done in a mostly qualitative manner as defining figures of merit for each property would be quite involved.

As previously mentioned, due to the bandwidth-limiting multi-mode propagation of the open-ended square waveguide, this antenna is not taken into consideration as the other elements are able to cover larger bandwidth.

Table 4.1 lists the antenna elements and their properties. The receiver noise temperature is rated + + if it is lower than 100 K over the whole theoretical operating frequency range from 400 MHz to 3 GHz and + if it is only able to cover the required frequency band from 1.5 to 3 GHz. The radiation patterns and cross-polarisation isolation are rated in a more qualitative manner relative between the elements.

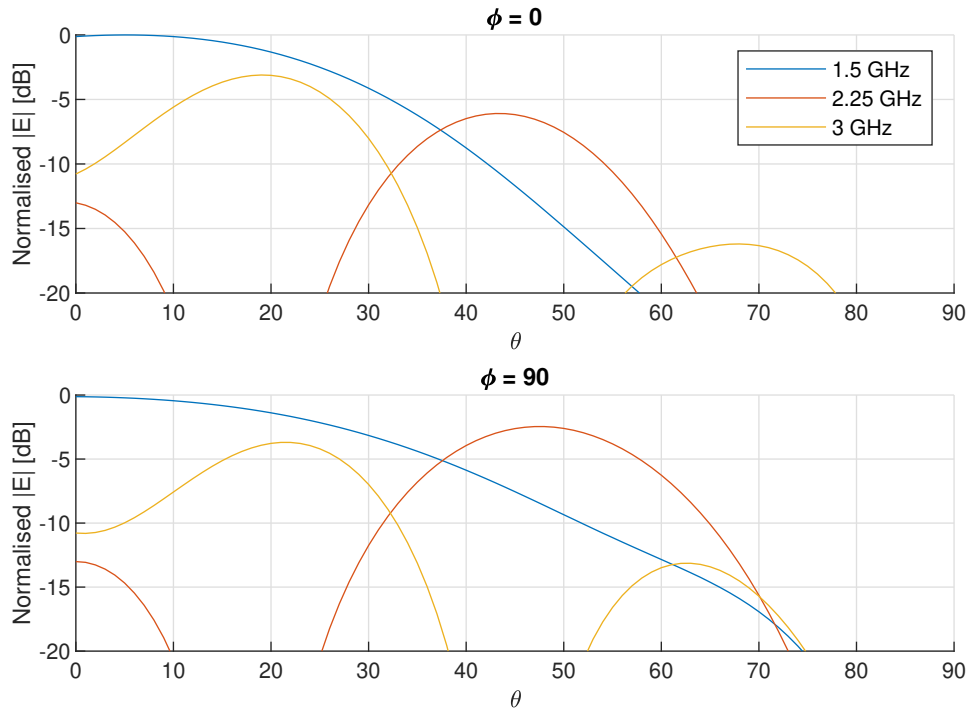

Figure 4.23: Normalised far field cuts for the ground plane backed planar log-periodic antenna at several frequencies.

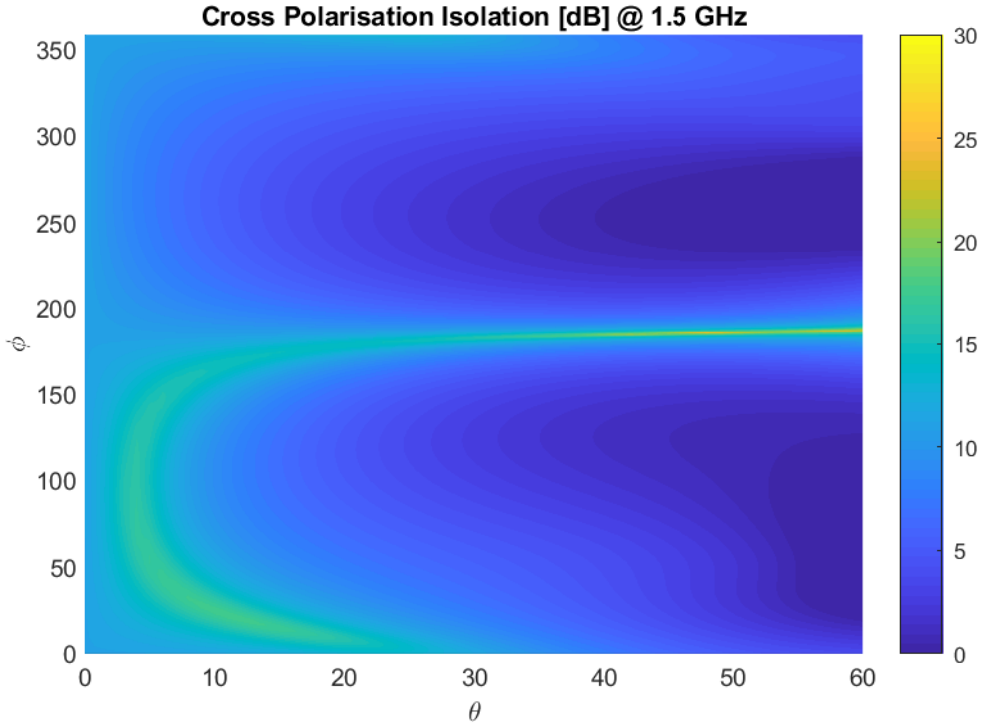

Figure 4.24: Cross-polarisation isolation in dB of the ground plane backed planar log-periodic antenna at a frequency of 1.5 GHz.

Table 4.1: Comparison of antenna properties of the antennas of interest.

Antenna	Receiver Noise Temperature	Radiation Patterns	Cross-Polarisation Isolation
Crossed Modified Bow-Tie	+	+	+
Crossed Tapered Slot	+ +	-	-
Planar Log-Periodic	+ +	- -	- -

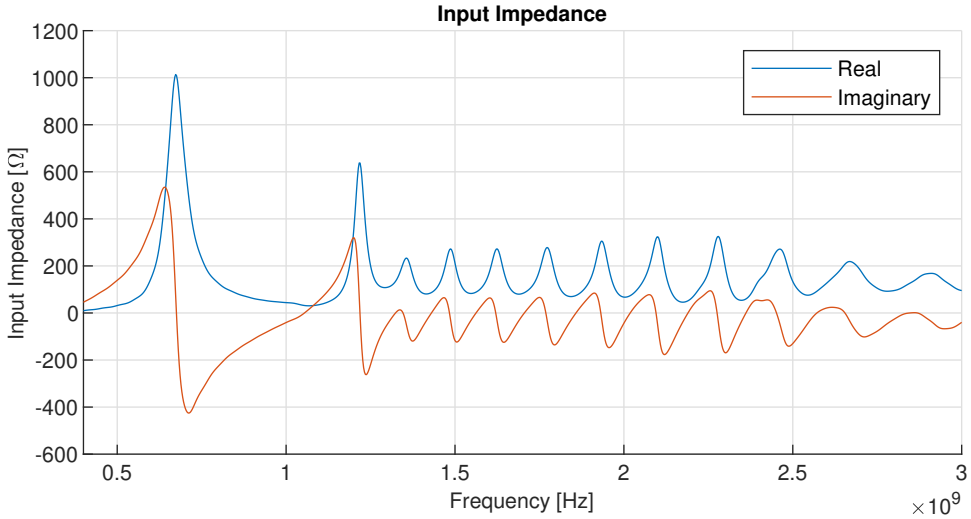

Figure 4.25: Input impedance of the ground plane backed self-complementary planar log-periodic antenna.

Ratings can vary from + +, meaning far superior to the other antenna elements, to - -, meaning far inferior.

Table 4.1 shows that the crossed TSA and the self-complementary planar log-periodic antennas are able to provide a good match to the LNA over the whole band. However, the radiation patterns at low frequencies for the crossed TSA only start to become usable from 1 GHz onward, thus the operational bandwidth is still limited.

The self-complementary planar log-periodic antenna has relatively good radiation patterns at frequencies below 1 GHz. Since the wavelength at the low frequencies is long, the electrical distance to the ground plane is smaller which results in a more typical dipole-over-ground radiation pattern. However, the impedance at the lower frequencies changes dramatically as shown in figure 4.25. Therefore, the fact that the antenna is able to meet the noise requirement is most likely made possible by the low equivalent noise resistance of the LNA at those frequencies. Therefore, simply scaling the antenna to obtain nicer radiation characteristics in the 1.5 to 3 GHz range is not easily possible since a large change in impedance would drastically increase noise as the equivalent noise resistance of the LNA is not so forgiving at higher frequencies.

In conclusion, the crossed modified bow-tie antenna seems to be the best compromise regarding receiver noise temperature, radiation patterns and cross-polarisation isolation. The lowest frequency at which the receiver noise temperature is below 100 K, is about 1.3 GHz. At this frequency, the radiation pattern of the antenna is also comparable to the patterns at the lower frequencies of the 1.5 to 3 GHz range as can be seen in figure 4.9. Considering before mentioned reasons, the crossed modified bow-tie antenna is selected for use in the full final array configuration. An artist's impression of this final quasi-spherical geodesic array is shown in figure 4.26.

4.4. Conclusion on Antenna Elements

In order to approach the theoretical performance of the geodesic quasi-spherical array designed in the previous chapter, the properties of an idealised antenna element that would obtain maximum performance is investigated. It is derived that this idealised antenna element has an isotropic radiation pattern in the region from 60° from zenith. Furthermore, it has an input impedance which is perfectly matched to the optimum noise reflection coefficient of the LNA. This leads to an ideal input impedance

as shown in figure 4.4, which in differential configuration varies roughly between 85Ω and 20Ω for both the real and imaginary parts. Also, the ideal antenna element should be sensitive to only one direction of polarisation and reject the other completely, leading to a cross-polarisation isolation of infinity.

As this idealised antenna element does not exist in reality, a practical antenna element needs to be designed to approach this idealised antenna as well as possible. Of the almost infinite number of possible practical antenna element designs, four have been investigated. These are the crossed bow-tie antenna, open-ended waveguide, crossed tapered slot antenna and the self-complementary planar log-periodic antenna.

From the investigation of these antennas, it is found that a modified version of the crossed bow-tie design is able to best approach the ideal antenna. The crossed modified-bow tie antenna has an input impedance resulting in a receiver noise temperature below 100 K from 1.3 GHz to the upper frequency of 3 GHz. Furthermore, it is found that this antenna element has of all of the considered elements the best cross-polarisation isolation and the radiation pattern that closest resembles that of the idealised element.

In the next chapter, the crossed modified bow-tie antenna is used in the novel geodesic quasi-spherical array configuration to estimate its performance in practice.

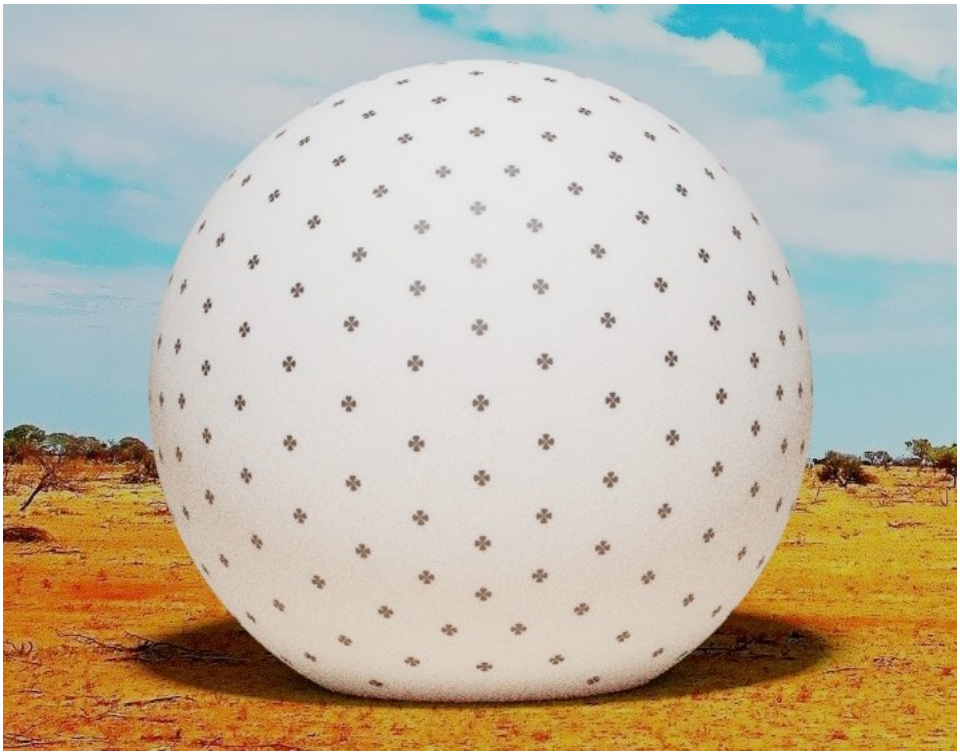

Figure 4.26: An artist's impression of the quasi-spherical geodesic conformal array antenna.

5

Conformal Array Performance

This chapter treats the subject of evaluating the performance of the selected array configuration in chapter 3 with the antenna element designed in chapter 4. Aspects of this include the effect of a spherical ground plane, the influence of mutual coupling on radiation patterns and active antenna impedance and the impact of element orientation. Subsequently, the HPBW is computed over scan angle and over frequency. Besides this, the isotropic active element assumption is revisited and checked for its validity by comparing it to the results obtained for the completed array. Lastly, this chapter also presents the comparison of the designed conformal array with a parabolic reflector antenna.

5.1. Full Wave Analysis of the Quasi-Spherical Array

Now that the conformal array configuration and antenna element have been selected, the whole array can be evaluated using a numerical solver. Instead of CST, Altair's Feko™ is used for this purpose. This is because CST mainly uses the finite element method when doing frequency domain simulation and the finite integration technique when solving in time domain. These methods have the downside that they also tend to mesh the whole computational domain, including the air around the antenna array. In the case of the quasi-spherical array, a lot of the computational domain is air and therefore the mesh may become too large resulting in a very heavy computational load.

In contrast to CST, Feko uses method of moments. With the method of moments, only the surfaces of the antenna objects are meshed. This results in significantly less mesh cells overall which should result in a reduced computational demand.

The full wave analysis using Feko is performed on a computer with two Intel® Xeon® CPU E5-2650 v2 running at 2.60 GHz and 125.7 GB of random access memory.

5.1.1. Effect of Spherical Ground Plane

The first difference with respect to the evaluation of the antenna elements in chapter 4, is the fact that the ground plane is no longer a perfect flat plane but part of a sphere instead. In order to study the effect of the ground plane shape, the radiation patterns and impedances are compared with each other. It is interesting to know this effect so it can be distinguished from the influence of mutual coupling.

The two antenna geometries are set up as follows. The antenna element designed in chapter 4 is converted to a STEP file by redrawing the element in Dassault Systèmes' SolidWorks. Subsequently, this STEP file is imported in Feko and the ports are added. For the flat ground plane scenario, an infinite ground plane is created at a distance of 3.3 centimetres below the antenna element, as designed in chapter 4.

For the spherical ground plane, the antenna element is imported in the same manner as with the planar ground plane. Since the radius of the quasi-spherical array is 1.55 metres and the distance from the element to the ground plane is 3.3 centimetres, the radius of the quasi-spherical ground plane should be 1.517 metres. Since the antenna designed in chapter 4 is about 7 centimetres, the ratio of the antenna versus ground plane is about 0.045. The quasi-spherical ground plane is then drawn in SolidWorks, exported to STEP and imported in Feko. Subsequently, the imported ground plane is translated to the correct position so that the distance between the element and the ground is 3.3

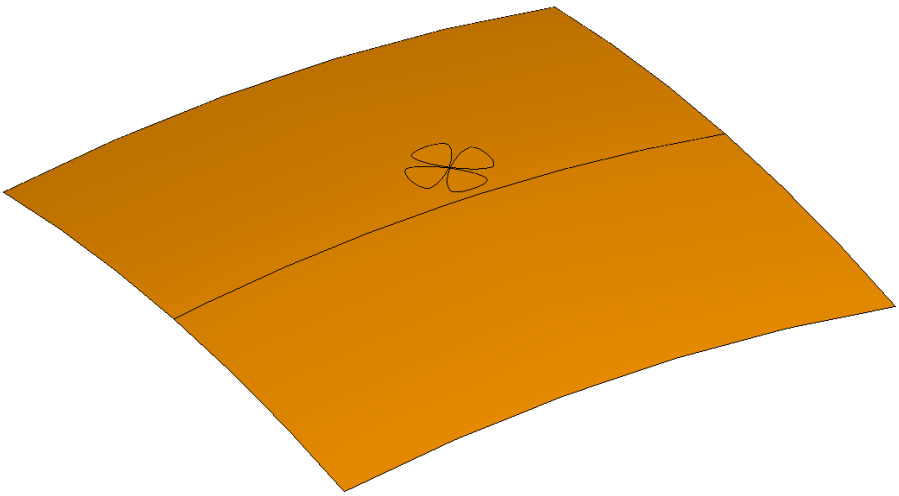

Figure 5.1: The Feko simulation set-up for a crossed modified bow-tie antenna 3.3 centimetre above a spherical ground plane.

centimetres. Lastly, since the full ground plane is very large causing an unnecessary large mesh, a cuboid is drawn of 50 by 50 centimetres and a few centimetres high which is intersected with the ground plane. This results in a plate which follows the curvature of the original sphere which measures 50 by 50 centimetres when seen from above. A picture of the finalised geometry is shown in figure 5.1.

First, the difference in impedance is considered. A comparison of the input impedances of the modified bow-tie antennas above a flat and a spherical ground plane is shown in figure 5.2. It can be seen from this figure that at the lower end of the maximum theoretical operational frequency range, the impedance of the antenna with spherical ground plane is almost identical to that of the antenna with the flat ground plane. However, at higher frequencies, the impedances of both antennas start to differ a bit. This is probably because the curvature of the spherical ground plane becomes significant in terms of wavelength at the high end of the frequency band.

Figure 5.3 shows a comparison of the far fields of both ground plane variations. This plot shows that the fields are relatively comparable for angles close to zenith. However, when looking towards the horizon, the modified bow-tie antenna with a spherical ground plane seems to radiate stronger fields. This could be explained by the fact that the spherical ground plane allows radiation for larger θ angles before the ground plane blocks the line of sight. Also, the spherical ground plane configuration shows some radiation in the nadir direction whereas the flat ground plane does not show this behaviour. This backwards radiation can be explained by the fact that the spherical ground plane is not infinite whereas the flat ground plane is. Therefore, in the flat ground plane scenario, no radiation can occur underneath the ground plane whereas electromagnetic waves are diffracted by the edges of the spherical ground plane.

Figures 5.2 and 5.3 show that the differences between the two ground plane configurations are relatively small and therefore it can be concluded that the spherical ground plane has no significant effect compared to the antenna properties as designed in chapter 4.

5.1.2. Influence of Mutual Coupling

When using antenna elements in an array configuration, the antenna elements may perform radically different than when the element is used in isolation. When considering an antenna array in transmission, one radiating element can induce a current in another element which re-radiates back to the transmitter. This re-radiated wave may subsequently interfere with the original emitted wave, thus potentially influencing input impedance and radiation patterns.

Since reciprocity must hold, mutual coupling should also occur when the antenna array is used for reception of signals. This can be explained as follows. When a wave is incident on the antenna array, current is induced on all antenna elements. Thereafter, the current that is induced will also start re-emitting waves that may in turn start interfering with the signal that is directly incident on its neighbouring elements. Therefore, this also results in mutual coupling as all elements detect a superposition of the

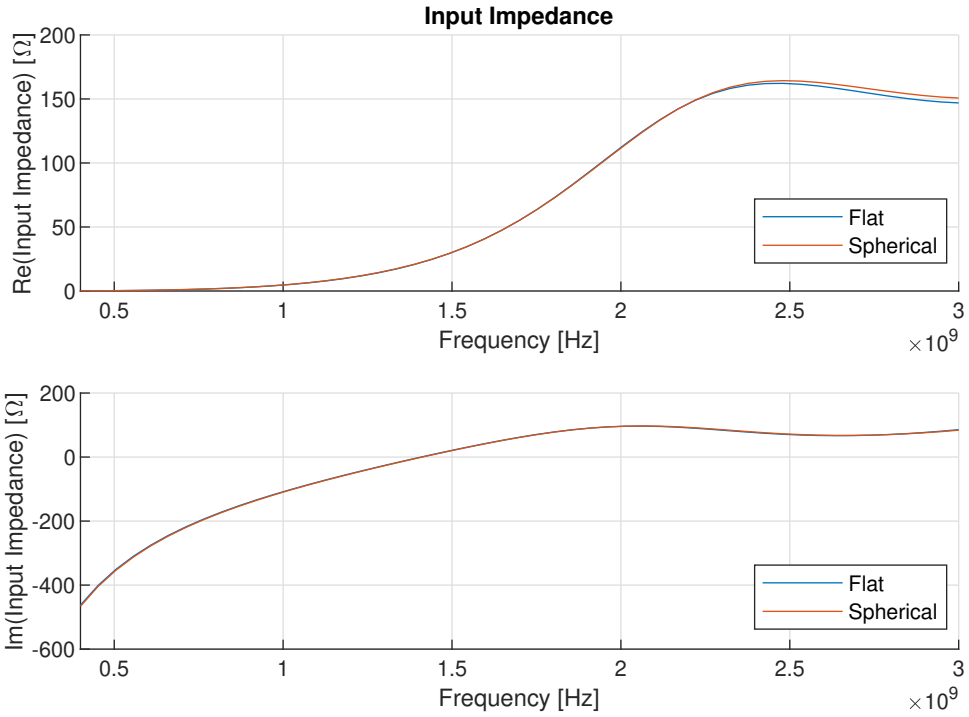

Figure 5.2: Comparison of the input impedances for the modified bow-tie antennas with flat and spherical ground planes.

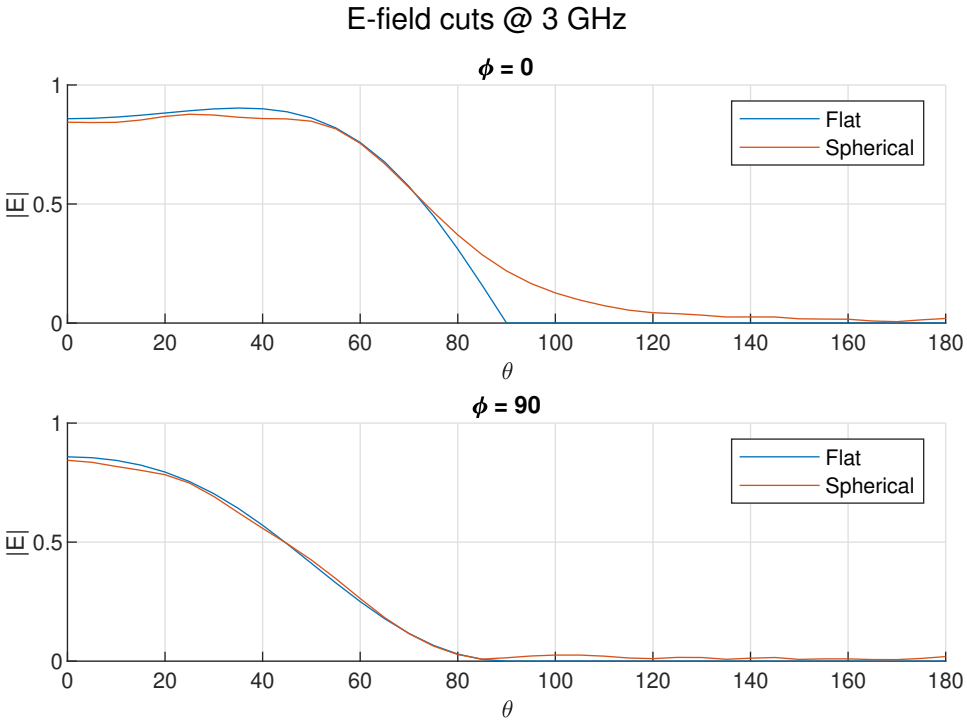

Figure 5.3: Comparison of the far fields for the modified bow-tie antennas with flat and spherical ground planes.

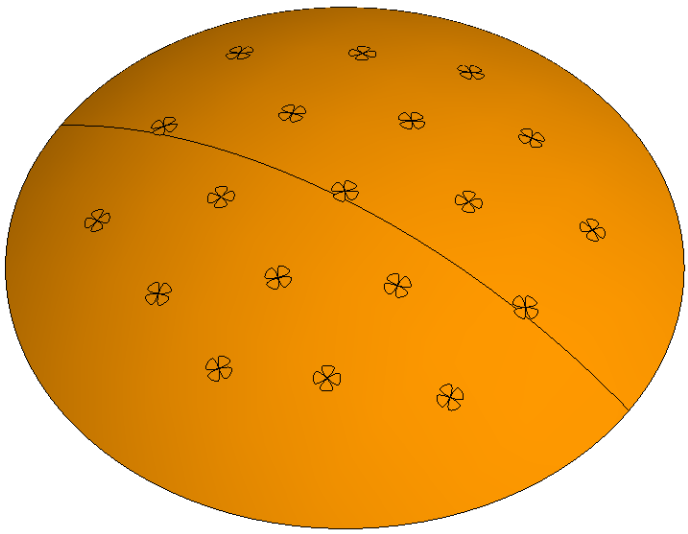

Figure 5.4: Feko set-up for the quasi-spherical array scanning to zenith, reduced to 30°.

directly incident wave plus the scattered waves from the other antenna elements.

Even though the orientation of the elements when scanning towards the horizon is almost the same, the selected array configuration is expected to have weak mutual coupling between the elements due to large inter element spacing as mentioned in chapter 3. Large distances between antenna elements reduce mutual coupling since the strength of the scattered fields is inversely proportional to the distance travelled.

In order to evaluate the effect of mutual coupling, full wave simulations are performed using Feko. To avoid the time consuming task of adding all the antenna elements manually, a script is used to import the antenna element STEP file, copy and translate the elements to the correct positions which have been generated in MATLAB. The script also adds in the quasi-spherical ground plane from the respective STEP file. Next to this, the script also makes sure that all the solution configurations are set correctly so that all embedded element patterns are calculated.

However, when importing the full geodesic quasi-spherical array, it is found that the memory requirement is too large. Therefore, only part of the quasi-spherical array is evaluated. It is found that when the configuration is discarded for θ angles beyond 40°, the memory requirement is about 100 GB. This can be handled successfully by the computer mentioned in the beginning of this section. However, it is not guaranteed that this amount of memory is available as the computer also performs other memory intensive tasks. Therefore, the array size is decreased to 30° instead of 40°. The ground plane is decreased to 35° to make sure the elements at the edge still are above sufficient ground plane. A picture of the simulation set-up for scanning to zenith is shown in figure 5.4.

In a first iteration, the antenna elements have been aligned via the $\hat{\theta}$ and $\hat{\phi}$ unit vectors. This means that on the top of the array, the difference in orientation between neighbouring elements is generally large and thus mutual coupling is reduced. However, when scanning to the horizon, the elements at the side of the array are used. These elements are almost aligned perfectly with each other and therefore stronger mutual coupling could potentially be observed. Because of this, both of these scan scenarios must be evaluated separately.

Even though the orientation of the elements when scanning towards the horizon is almost the same, the selected array configuration is expected to have weak mutual coupling between the elements due to large inter element spacing as mentioned in chapter 3. Large distances between antenna elements reduce mutual coupling since the strength of the scattered fields is inversely proportional to the distance travelled.

In order to check the impact of mutual coupling, the radiation pattern of the element positioned in the middle of the array is compared to the radiation pattern of the isolated element with a spherical ground plane. This comparison is shown in figure 5.5.

Figure 5.5 shows that the radiation patterns of the centre element in array configuration and that of the isolated element are approximately the same. Therefore, it can be concluded that at 1.5 GHz the

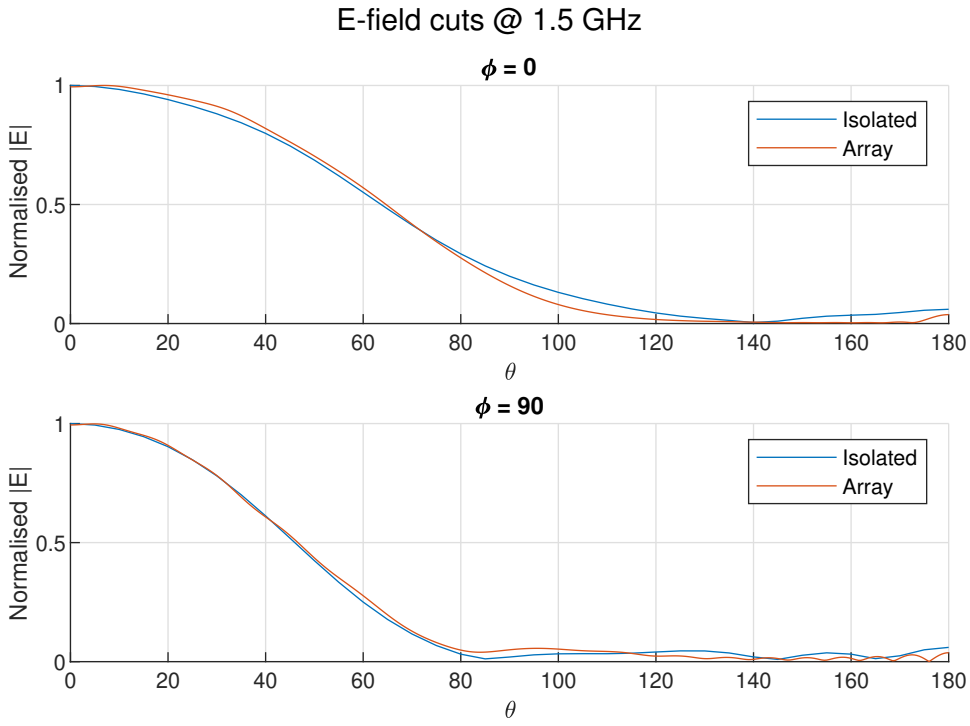

Figure 5.5: Comparison of the centre element of the configuration in figure 5.4 and the isolated element with a spherical ground plane as shown in figure 5.1.

mutual coupling is weak on the top of the array.

In order to investigate the possibility of some elements being impacted more severely by mutual coupling due to for example a more similar orientation or smaller inter-element spacing, the radiation patterns of all elements on the top of the array are compared with each other. This is shown in figure 5.6. This figure shows that all radiation patterns are approximately the same and therefore it can be concluded that the influence of mutual coupling is weak for all elements.

As mentioned earlier, the elements on the top of the array differ much in orientation compared to the elements on the sides of the array. Therefore, the mutual coupling may also be stronger. Thus, also the scenario for the array scanning to the horizon has to be taken in consideration, a picture of this configuration is shown in figure 5.7. This is done in the same fashion as for scanning to zenith by first comparing the radiation patterns and impedances for the centre element and the isolated element and subsequently comparing the radiation patterns of all elements.

Figure 5.8 and figure 5.9 shows that the element radiation patterns are not influenced significantly by mutual coupling.

The absence of severe mutual coupling leads to the fact that a useful and essential approximation can be made in order to evaluate the performance of the quasi-spherical array. Namely, since the antenna properties of all elements is approximately the same, the embedded pattern of one antenna element can be used for the other elements as well. Instead of performing full-wave analysis, this embedded element pattern can be used in the MATLAB framework to evaluate the performance of the full array. This approximation is essential as the available computational resources are not sufficient to solve a full active aperture which requires 60° from zenith instead of the maximum 40° possible.

Since the comparisons of radiation patterns in figures 5.6 and 5.9 are plotted for 1.5 GHz, it is of importance to verify that the before mentioned approximation also holds at 3 GHz. This should be the case because the electrical distance increases as the wavelength is halved with respect to a frequency of 1.5 GHz and mutual coupling should therefore be less. This is confirmed by figure 5.10 which shows a comparison of the radiation patterns for the configuration shown in figure 5.7 at 3 GHz.

Lastly, figures 5.11 and 5.12 show the active input impedance for the array configuration shown in figure 5.7 for various scan angles. Of these scan angles, the scan angle $\theta_s = 90°$ and $\phi_s = 0°$ is the

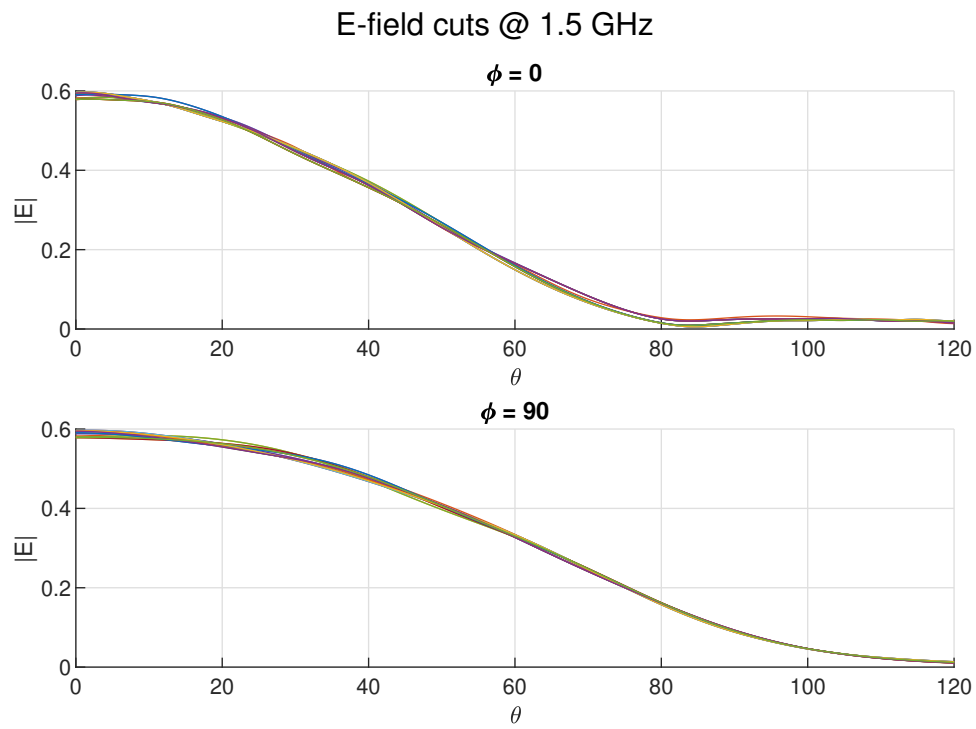

Figure 5.6: Comparison of embedded element patterns of the elements of the configuration shown in figure 5.4 at 1.5 GHz.

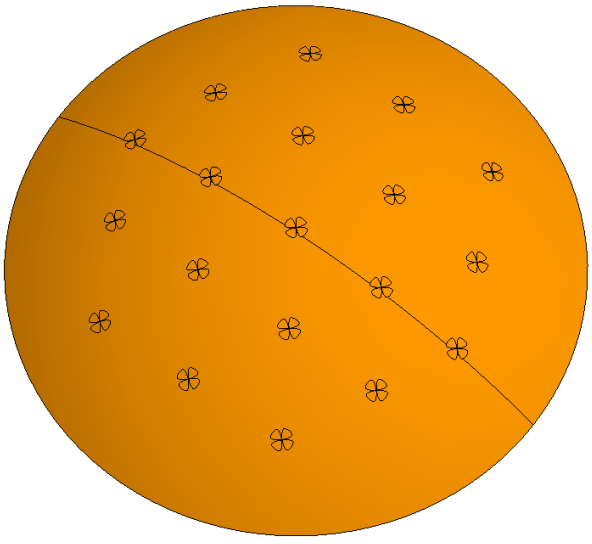

Figure 5.7: Feko set-up for the quasi-spherical array scanning to horizon at an angle ϕ of 0°.

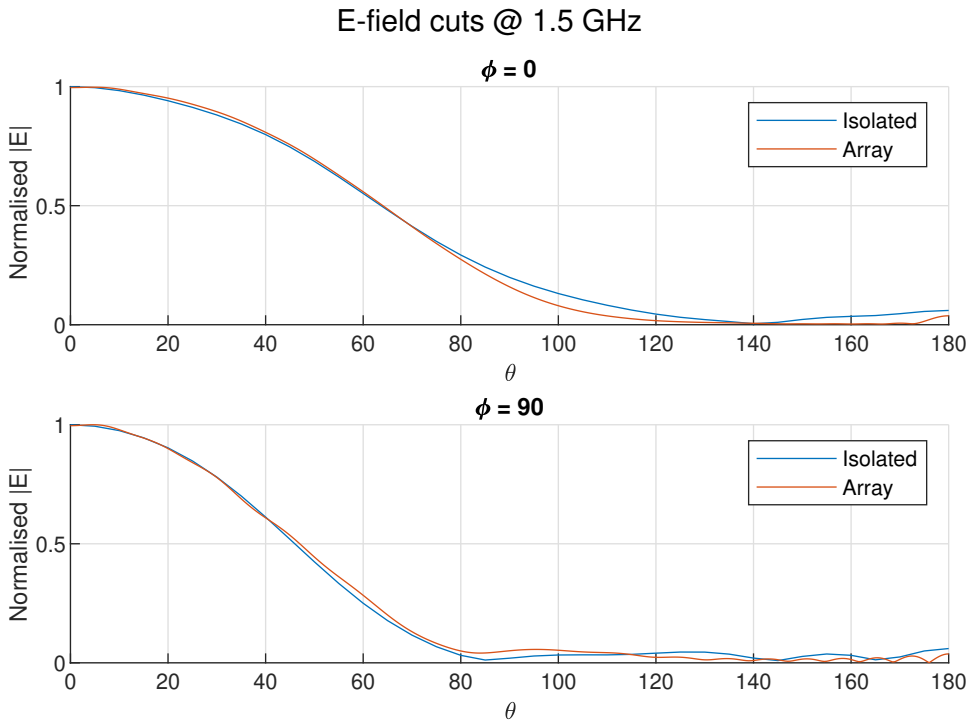

Figure 5.8: Comparison of the centre element of the configuration in figure 5.7 and the isolated element with a spherical ground plane as shown in figure 5.1.

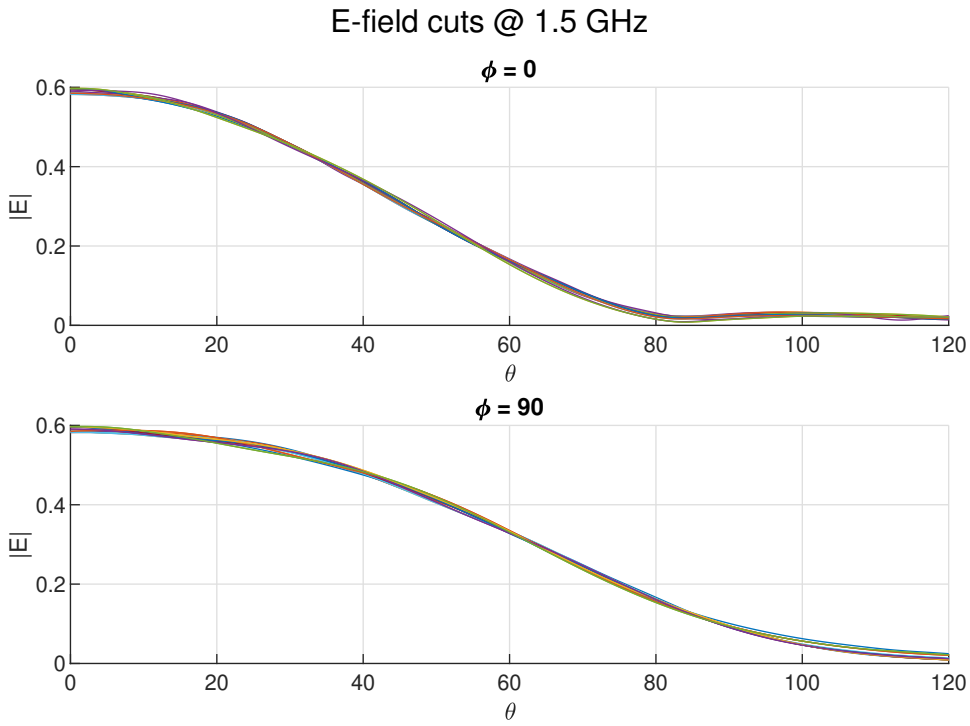

Figure 5.9: Comparison of embedded element patterns of the elements of the configuration shown in figure 5.7 at 1.5 GHz.

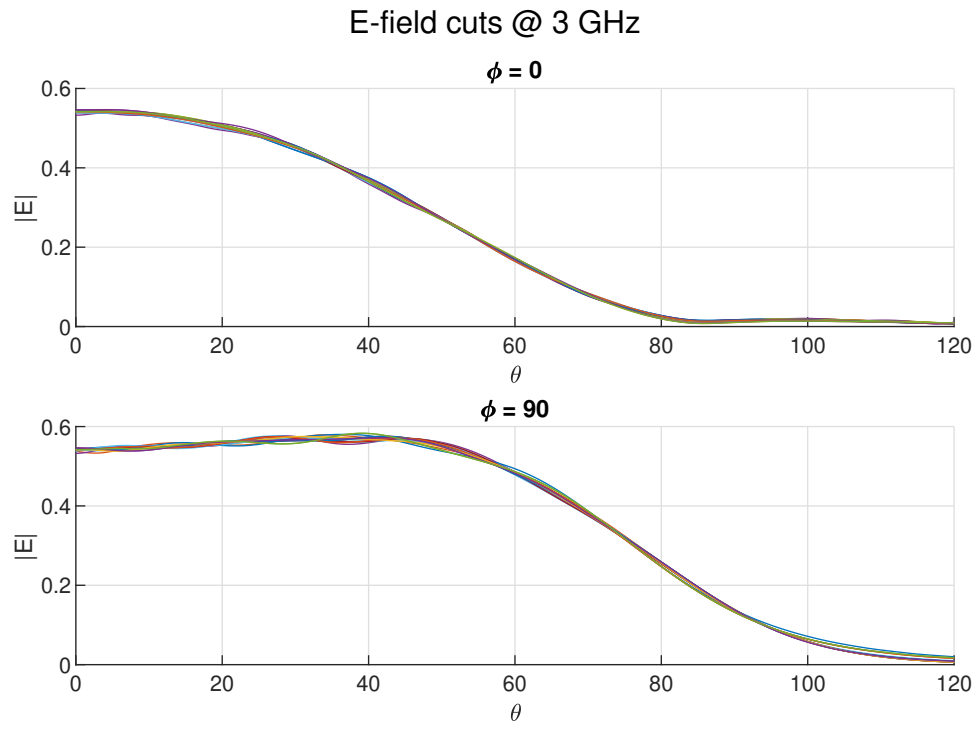

Figure 5.10: Comparison of embedded element patterns of the elements of the configuration shown in figure 5.7 at 3 GHz.

most important as the aperture changes with scan direction so that it is always normal with respect to the desired scan direction. However, to demonstrate that mutual coupling is minimal, also some other scan angles are considered for this specific array section.

Figure 5.12 shows that at 3 GHz, the active impedance is on average almost equal to the input impedance of the isolated element. Also, the deviation from the isolated element input impedance is relatively small. Therefore, the active input impedance can be approximated by the input impedance of the isolated element. Thus, the active impedance at 3 GHz also shows that the mutual coupling is weak.

Figure 5.11 shows that the effect of mutual coupling is more significant at 1.5 GHz as the imaginary part of the average active impedance differs with that of the isolated input impedance. On the other hand, the real part of the active impedance is close to the real part of the isolated input impedance. This makes that although the effect of mutual coupling is stronger at 1.5 GHz than at 3 GHz, the active impedance still can be reasonably approximated with the impedance of the isolated element. Despite the slight increase in mutual coupling at 1.5 GHz, also the equivalent noise resistance of the LNA is lower at that frequency. Therefore, the effect of the larger difference in impedance on receiver noise temperature is diminished.

5.1.3. Element Orientation

The orientation of the elements on a conformal array is of great importance. This is not only due to mutual coupling as explained in section 5.1.2. In fact, element orientation can have a much larger impact on the radiation pattern of the resulting array than mutual coupling itself.

Consider for example the configuration displayed in figure 5.4. Since all elements are oriented along $\hat{\theta}$, two opposing antenna elements, when drawing a line through the pole of the array, are rotated 180° with respect to each other. Also those elements are the same distance away from the pole due to symmetry. This results in the fact that when scanning to zenith, the radiation of these sets of two elements cancel out as they are 180° out of phase with each other at an observation angle θ of 0°. The resulting pattern is shown in figure 5.13.

For the case where the scan angle θ_s equals 0° this can be corrected without the need for elaborate mathematical means. Namely, by adding a phase shift of 180° upon the phase compensation factor

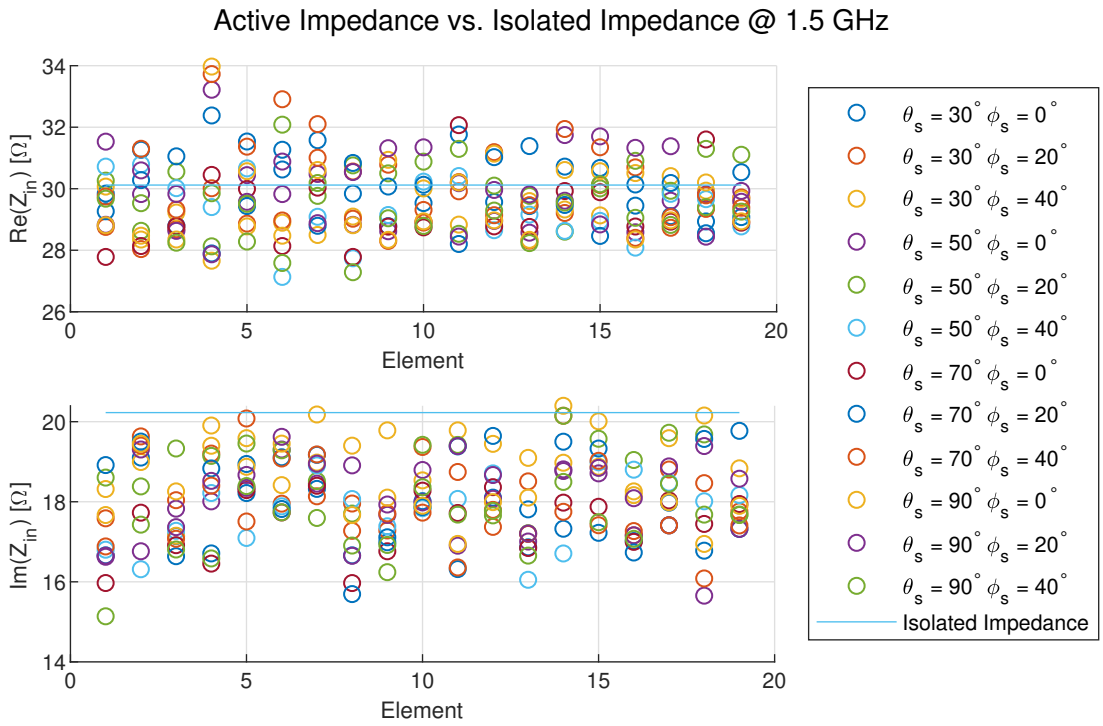

Figure 5.11: Comparison of active input impedance of the elements of the configuration shown in figure 5.7 at 1.5 GHz. The circles indicate all combinations of θ_s is 30, 50, 70 and 90 degrees and ϕ_s 0, 20 and 40 degrees, resulting in 12 circles per element. The line indicates the input impedance of the isolated crossed modified bow-tie.

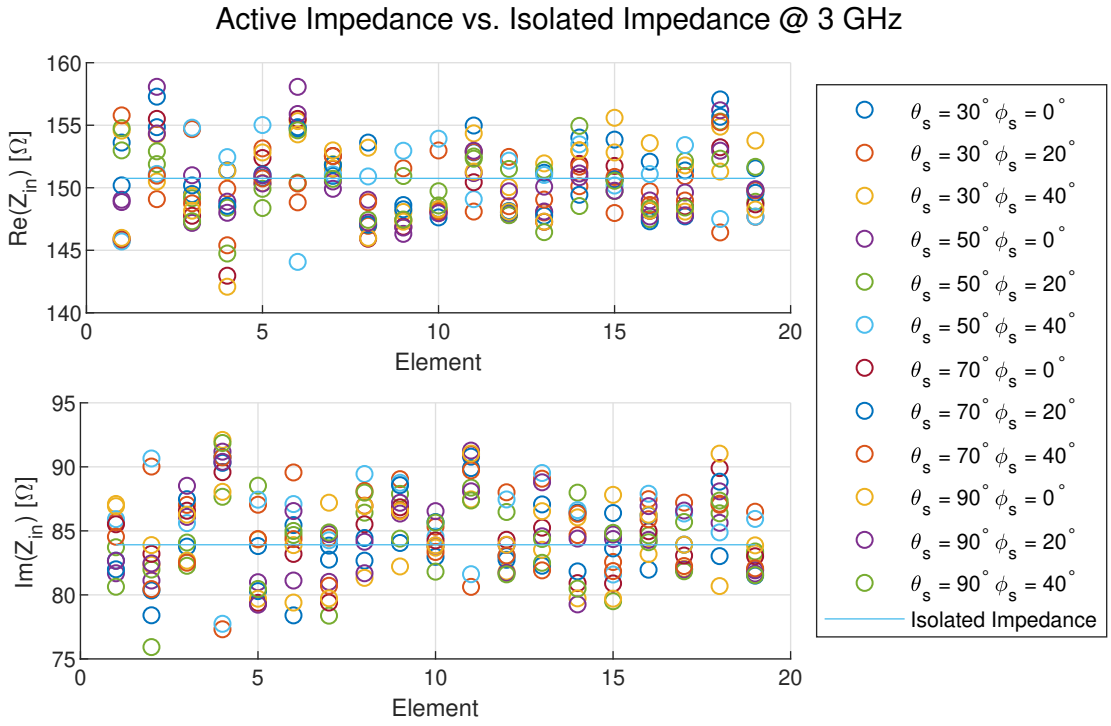

Figure 5.12: Comparison of active input impedance of the elements of the configuration shown in figure 5.7 at 3 GHz. The circles indicate all combinations of θ_s is 30, 50, 70 and 90 degrees and ϕ_s 0, 20 and 40 degrees, resulting in 12 circles per element. The line indicates the input impedance of the isolated crossed modified bow-tie.

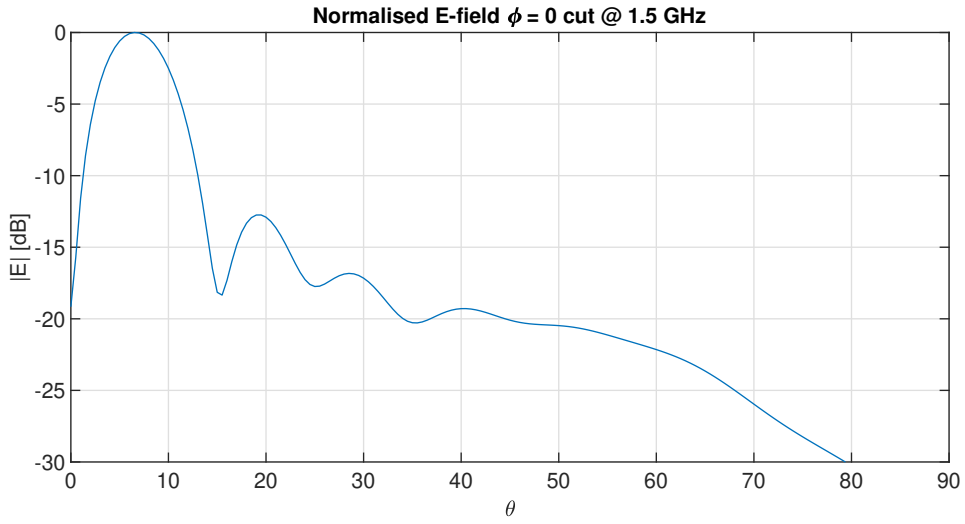

Figure 5.13: Total radiation pattern of the array configuration shown in figure 5.4 when scanning to zenith at 1.5 GHz.

β_i (equation 2.28) for one of a set of two opposing elements, the radiation is in-phase and is interfering constructively at the desired scan angle. However, it is important to make sure that the resultant radiation from a set of two elements has the same polarity as the other sets.

The phase compensation strategy used is shown in figure 5.14. Here, an additional phase shift of 180° is applied to the elements in red. The resulting far field pattern is displayed in figure 5.15.

As proven by figure 5.15, this phase correction is effective and ensures that the main lobe is directed towards zenith. Now the situation of the array scanning towards the horizon, as shown in figure 5.7, is considered. Since the elements are all aligned along the $\hat{\theta}$ unit vector, the orientation of the elements is the same. Therefore, no polarity inversion needs to be applied. However, when the scan angle θ_s is somewhere between zenith and the horizon, the aperture is not symmetrical any more. This complicates the phase correction process since it is non-trivial to conclude which elements need an additional 180° phase-shift as not every element has an opposing element any longer.

The orientation of the elements also plays a significant role regarding polarisation. For example, if the Sun is directly overhead, i.e. scanning to zenith, the sub-elements aligned with the $\hat{x}$-axis will receive an orthogonally polarised field with respect to the sub-elements aligned with the $\hat{y}$-axis. Therefore, simply summing the outputs from all elements aligned with $\hat{\theta}$ is not sufficient when the array is desired to be operated as a polarimeter as both elements may receive components of the co- and cross-polarised radiation.

This effect can be corrected for since the sub-elements of the antenna elements are orthogonally polarised with respect to each other as well. However, this correction is different for every scan angle as the projection of the antenna elements on a plane normal to the scan direction is different. This is even more complicated by the fact that the sub-elements do not have symmetrical isotropic radiation patterns and therefore, the gain of the elements also needs to be taken into account. Due to time constraints, it has been decided that the development of this correction is outside the scope of this thesis project. The orientation correction could also be combined with a beamforming algorithm that applies weights to each element which could potentially reduce side lobe level.

5.1.4. HPBW over Scan Angle

If the antenna array is to be used as a polarimeter, one would like to know the radiation pattern properties for both directions of polarisation. However, in order to find these exact patterns, a method to correct polarisation has to be implemented too. This is because, for example when scanning to zenith, the sub-elements aligned with the $\hat{x}$-axis should be active and the sub-elements aligned with the $\hat{y}$-axis should be inactive when scanning for a specific polarisation.

As no such correction is available at the time of writing, the scenario of scanning to the horizon is used to make a realistic estimation of the half-power beam width. Since the aperture size is mostly independent of the scan angle due to the quasi-spherical nature of the array, it is assumed that the

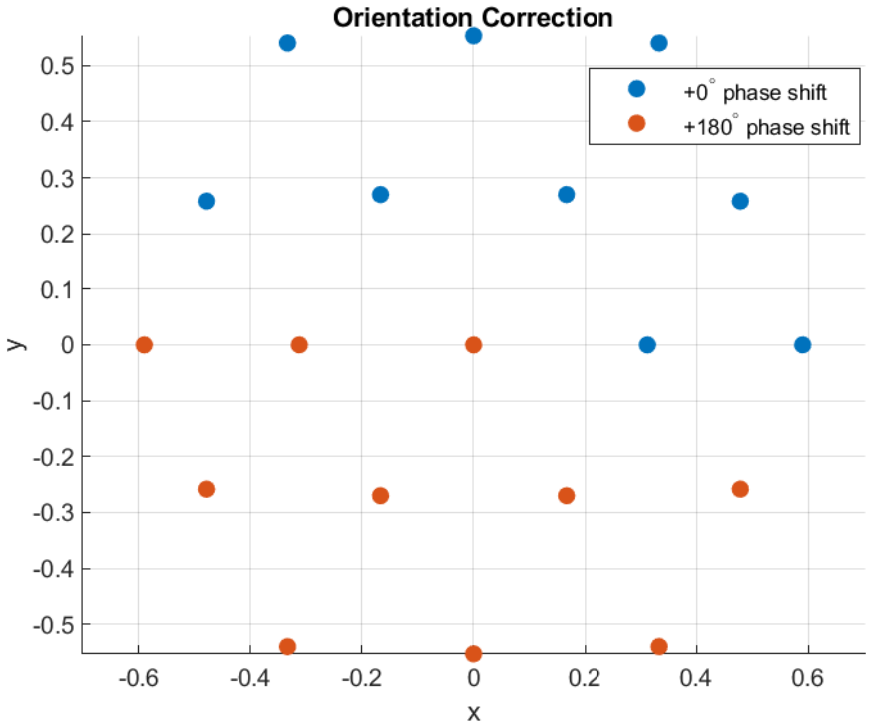

Figure 5.14: Phase compensation strategy for the geodesic quasi-spherical array antenna when scanning to zenith.

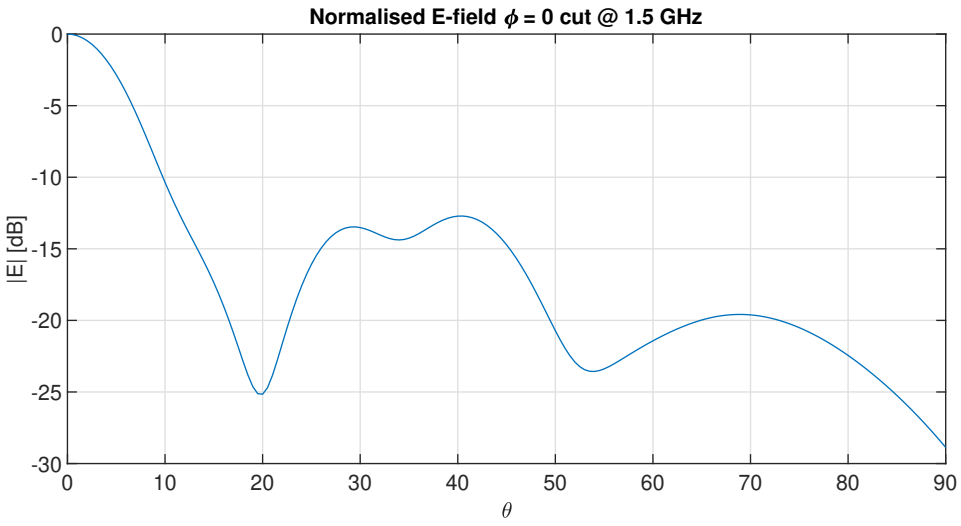

Figure 5.15: Radiation pattern of the total array shown in figure 5.4 with additional phase correction at 1.5 GHz.

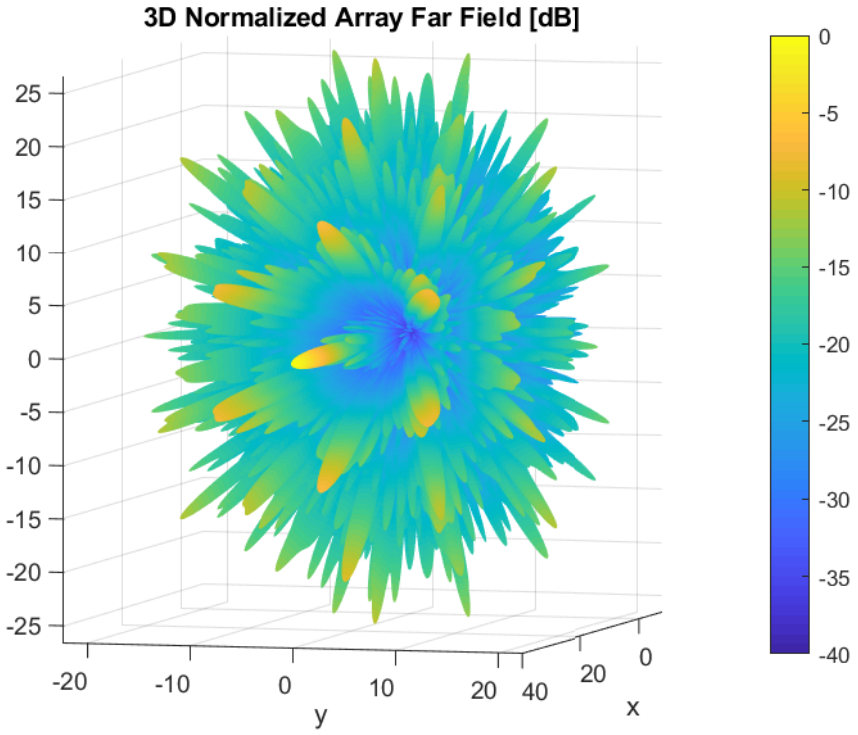

Figure 5.16: Three-dimensional radiation pattern plot of the complete geodesic quasi-spherical array at 3 GHz when scanning to the horizon with the $\hat{\theta}$-oriented sub-elements.

HPBW for scanning to horizon is approximately the same as every other scan direction if orientation correction were to be applied. It should be noted that even though most $\hat{\theta}$ sub-elements are aligned with $\hat{z}$ and the $\hat{\phi}$ sub-elements with $\hat{y}$, the elements at the edges of the aperture are rotated a bit with respect to the aligned sub-elements. This makes that the far field properties of the array when scanning to the horizon still differ a bit from a same array that is perfectly corrected for element orientation.

As mentioned in section 5.1.2, only a piece of 30° from zenith could be evaluated using full wave analysis. However, as also described in section 5.1.2, the radiation patterns of the elements are about the same and thus an approximation of the array far field pattern can be made in MATLAB by using the same radiation pattern for each element. Next to this, if the cross-polarised component is assumed to be negligible, a first order approximation of the co-polarised array radiation pattern can be made using the absolute value of the embedded radiation patterns. Figure 5.16 shows the radiation pattern of the complete geodesic quasi-spherical array when scanning to the horizon with the $\hat{\theta}$-oriented sub-elements at 3 GHz.

The minimum HPBW of the radiation pattern displayed in figure 5.16 is estimated to be 2.00 degrees and the maximum HPBW is estimated at 2.16 degrees, thus satisfying the requirements. A plot of the $\phi = 0°$ cut of the radiation patterns for $\hat{\theta}$- and $\hat{\phi}$-oriented elements is shown in figure 5.17.

5.1.5. HPBW over Frequency

The embedded radiation patterns of the antenna elements are dependent on frequency. This makes that the perfect relation between half-power beam width and frequency as described in section 3.1 is lost. With a similar procedure and assumptions as in section 5.1.4, the radiation pattern of the full quasi-spherical array scanning the $\hat{\theta}$-oriented elements to the horizon is evaluated. A three-dimensional plot of this radiation pattern at 1.5 GHz is shown in figure 5.18.

Figure 5.19 shows the $\phi = 0°$ cut of the array radiation pattern generated by the $\hat{\theta}$- and $\hat{\phi}$-oriented elements. The minimum HPBW for scanning to the horizon is found to be 4.01 degrees and the maximum HPBW is found to be 4.33 degrees.

Since the receiver noise temperature is below 100 K up to about 1.3 GHz as shown in figure 4.10, also the array pattern at 1.3 GHz is calculated. A plot of this radiation pattern is shown in figure 5.20.

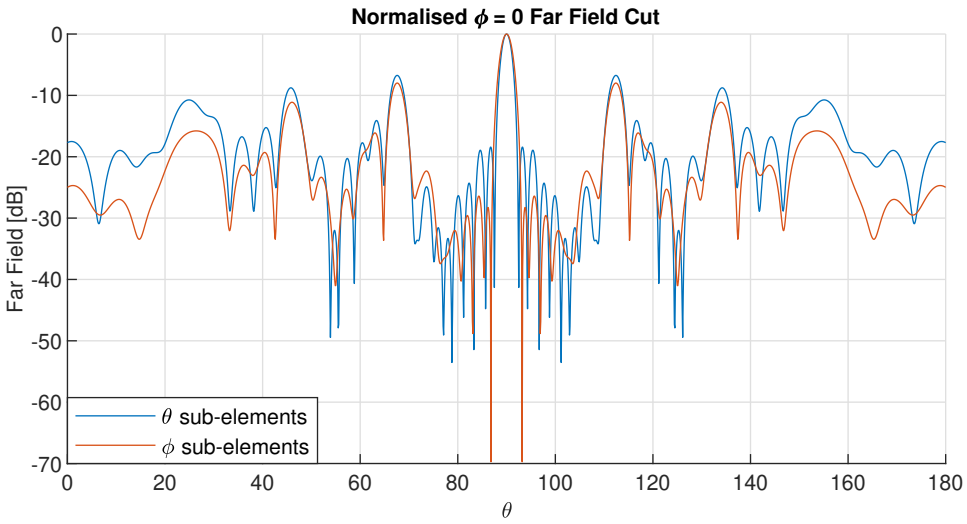

Figure 5.17: Radiation pattern cut of the complete geodesic quasi-spherical array at 3 GHz when scanning to the horizon with the $\hat{\theta}$-oriented (blue) and $\hat{\phi}$-oriented (red) sub-elements.

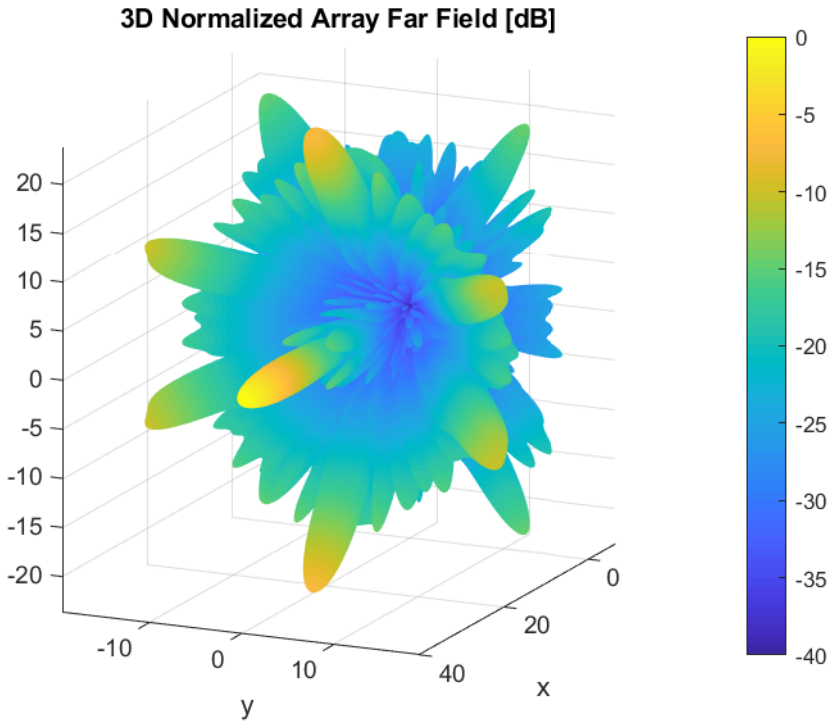

Figure 5.18: Three-dimensional radiation pattern plot of the complete geodesic quasi-spherical array at 1.5 GHz when scanning to the horizon with the $\hat{\theta}$-oriented sub-elements.

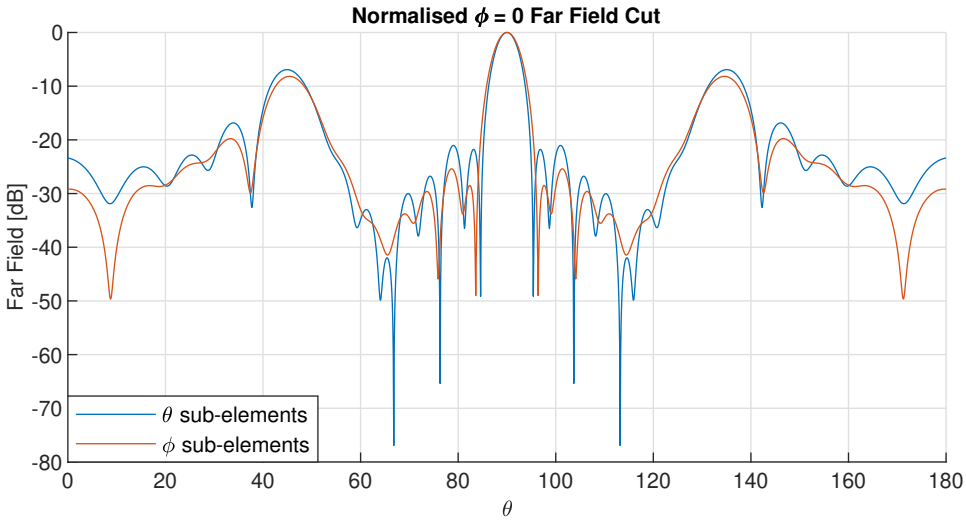

Figure 5.19: Radiation pattern cut of the complete geodesic quasi-spherical array at 1.5 GHz when scanning to the horizon with the $\hat{\theta}$-oriented (blue) and $\hat{\phi}$-oriented (red) sub-elements.

The ϕ = 0° cut of this pattern is shown in figure 5.21. The minimum HPBW at 1.3 GHz is estimated to be 4.62 degrees and the maximum HPBW is found to be 5.00 degrees.

Figures 5.16 to 5.21 show that the array successfully can cover frequencies from 1.3 GHz to 3 GHz within the specifications listed in section 1.3.1, resulting in a fractional bandwidth of 79%.

5.1.6. Comparison of Far Fields using Isotropic Elements

To reflect on the accuracy of the design method, a comparison is made between the array patterns obtained in chapter 3 using isotropic patterns and the patterns generated in section 5.1.4 and 5.1.5. These comparisons at 1.5 and 3 GHz are shown in figures 5.22 and 5.23 respectively.

These figures show that the isotropic elements approximate the final pattern reasonably well. Therefore, it can be concluded that designing arrays with isotropic patterns is a powerful method to reduce computational time while still providing reasonable results as long as the embedded element patterns are locally isotropic. However, it should be mentioned that the $\phi = 180°$ cut will look significantly different as the embedded radiation patterns show almost no radiated power toward their anti-normal directions whereas this is by definition not the case for isotropic elements.

5.2. Parabolic Reflector Performance

In order to put the performance of the conformal array in perspective, a comparison with a parabolic reflector antenna is made. First, the analysis of the far field of a parabolic reflector antenna is presented. Subsequently, the results obtained from this analysis are compared to the results of the conformal array.

5.2.1. Analysis of Parabolic Reflector

The far field of a parabolic reflector can be computed via a similar approach using Green's functions as in section 2.3. The computation is performed via the following steps.

First, it is assumed that the feed is in the far field with respect to the parabolic reflector. Using physical optics (PO), the strength and phase of the electric field after reflection from the parabolic reflector can be found at the equivalent aperture. The equivalent aperture is a circular domain which results from a projection of the dish on a plane that is parallel to the dish and passes through the focus at which the feed is located. The field at the equivalent aperture can subsequently be used to find the equivalent current distribution using the equivalence principle together with the image theorem. Finally, using the Green's functions, the far field of this equivalent current distribution can be calculated. [47]

If maximum directivity is desired, the equivalent current distribution on the equivalent aperture should be uniform [47]. The far field of such a distribution is an Airy pattern. The Airy pattern is described by equation 5.1 which is contains a first-order Bessel function, indicated by J_1 [47]. In this

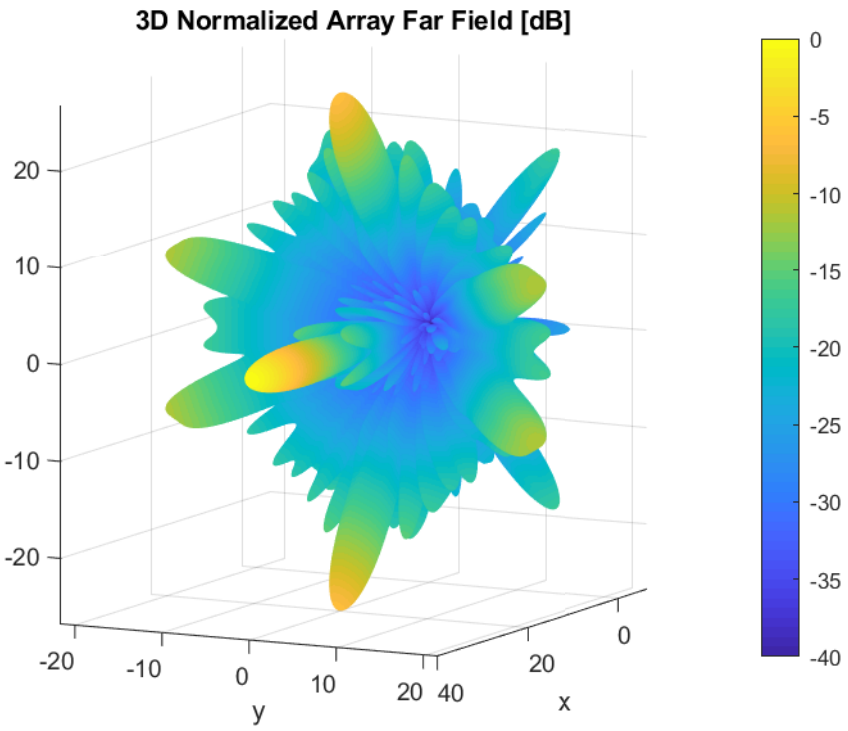

Figure 5.20: Three-dimensional radiation pattern plot of the complete geodesic quasi-spherical array at 1.3 GHz when scanning to the horizon with the $\hat{\theta}$-oriented sub-elements.

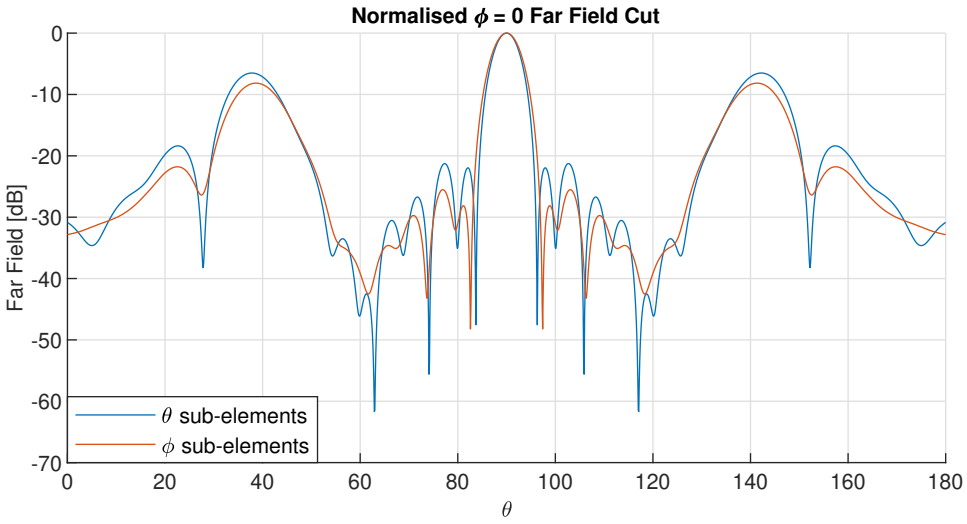

Figure 5.21: Radiation pattern cut of the complete geodesic quasi-spherical array at 1.3 GHz when scanning to the horizon with the $\hat{\theta}$-oriented (blue) and $\hat{\phi}$-oriented (red) sub-elements.

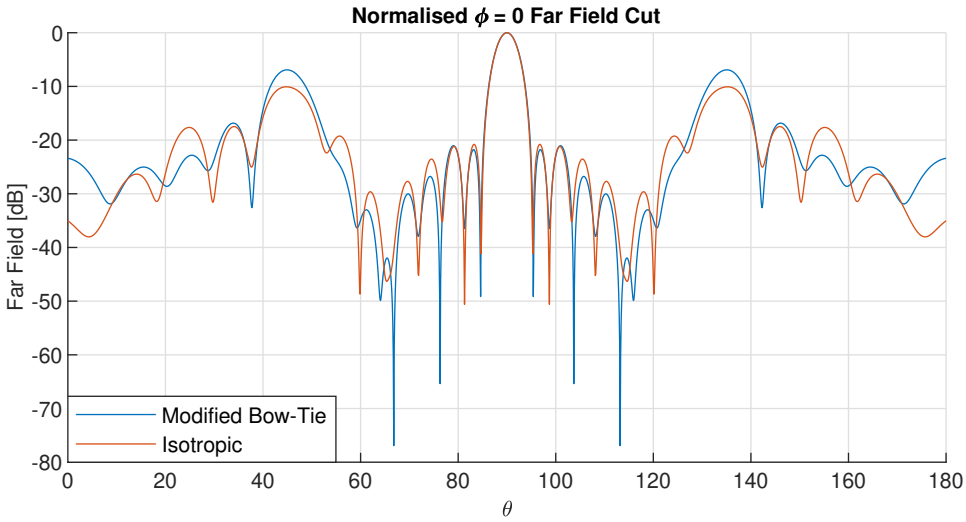

Figure 5.22: Comparison of the $\phi = 0°$ cuts of the complete geodesic quasi-spherical array at 1.5 GHz when scanning to the horizon with the $\hat{\theta}$-oriented sub-elements and the same configuration with isotropic elements.

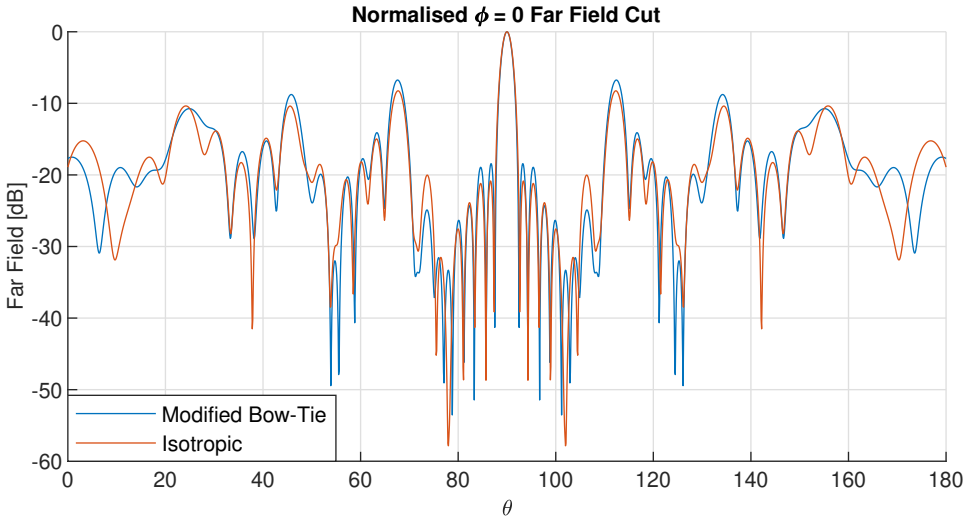

Figure 5.23: Comparison of the $\phi = 0°$ cuts of the complete geodesic quasi-spherical array at 3 GHz when scanning to the horizon with the $\hat{\theta}$-oriented sub-elements and the same configuration with isotropic elements.

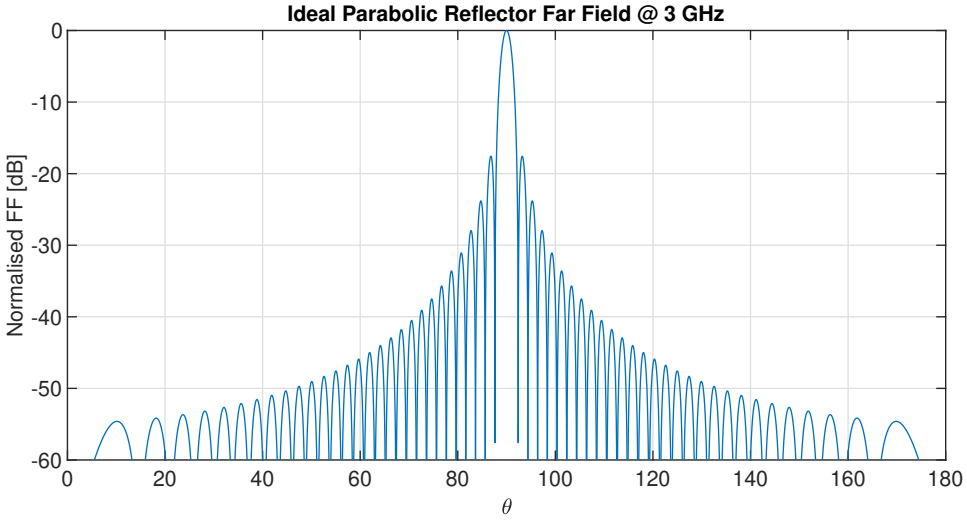

Figure 5.24: Normalised far field cut at $\phi = 0$ of an ideal parabolic reflector when pointing to the horizon at 3 GHz.

equation, M_0 is the magnitude of the equivalent magnetic current, a is the radius of the equivalent aperture, k is the wave number and $\hat{p}$ indicates the polarisation.

$$\vec{M}^{FF}(\vec{r}) = 2M_0 \frac{\pi a^2 J_1(ka\sin\theta)}{ka\sin\theta}\hat{p} \tag{5.1}$$

The half-power beam width in degrees of the far field pattern of a uniformly distributed current on a circular aperture can be found using equation 5.2 [70].

$$HPBW = 29.2\frac{\lambda}{a} \tag{5.2}$$

Using a desired HPBW of 2°, it can be found that the radius of the reflector should be equal to about 1.46 metres at 3 GHz.

Using this dish diameter, the radiation pattern of the dish antenna can be calculated. The resulting pattern is shown in figure 5.24.

5.2.2. Note on Approximations

The parabolic reflector considered in section 5.2.1 is the ideal case. In reality, it is difficult or even impossible to design a feed antenna for the reflector that is able to achieve an uniform current distribution on the equivalent aperture.

Practical reflector antennas suffer from non-perfect feed efficiency, spillover efficiency and taper efficiency. Feed efficiency is the amount of power radiated versus input power delivered to the feed. Spillover efficiency indicates how much of the radiation of the feed antenna is incident on the reflector and how much leaks past. Taper efficiency indicates how close the amplitude and phase distribution of the feed field on the reflector are to the ideal distribution, i.e. the deviation from the Airy pattern.

Unfortunately, taper and spillover efficiency are related to each other. Increasing the taper efficiency generally leads to a reduction in spillover efficiency and vice versa. For example, when the size of the reflector is increased, more of the radiation from the feed is caught thus increasing the spillover efficiency. However, the increased size of the reflector also leads to a less optimal taper efficiency as the field that is now intercepted by the reflector generally has a less ideal amplitude and phase distribution. [47]

Considering the mentioned efficiency factors, a dish with a radius of 1.46 metres will most likely have a larger beam width than 2 degrees at 3 GHz. This can however simply be compensated for by increasing the size of the dish to for example to a diameter of 3 metres.

5.2.3. Comparison of Conformal Phased Array and Reflector Antenna

Finally, the radiation patterns from the conformal geodesic quasi-spherical array and the parabolic reflector are compared. Figure 5.25 shows an overlay of the radiation patterns of the parabolic reflector

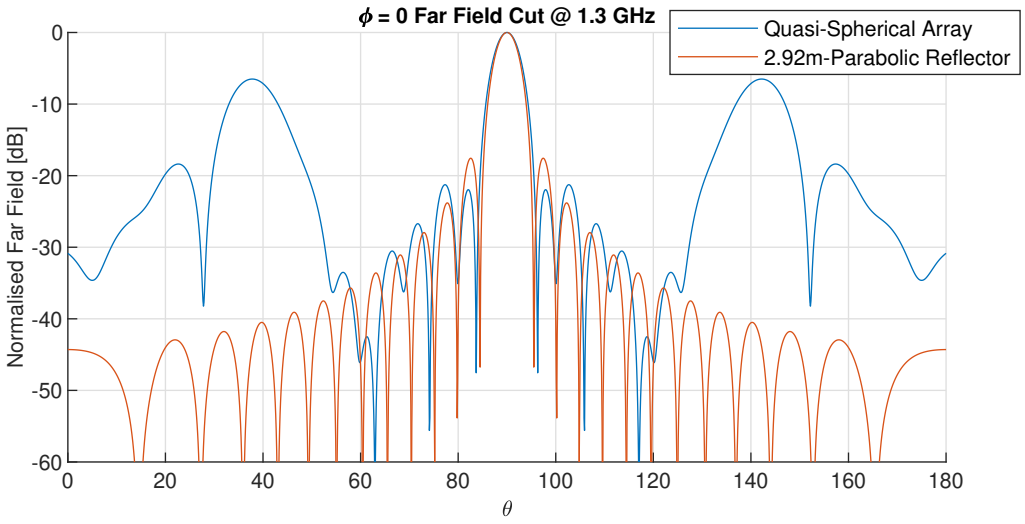

Figure 5.25: Comparison of normalised radiation patterns of the quasi-spherical array and a 2.92 metre diameter parabolic reflector at 1.3 GHz.

and quasi-spherical array which are both scanning to the horizon at 1.3 GHz and figure 5.26 shows the same comparison at 3 GHz.

From both figures, it can be seen that the side lobe level (SLL) of the conformal array is actually better in the region ± 30 degrees from θ_s at 1.3 GHz and in the region ± 10 degrees from θ_s at 3 GHz. This is probably due to the ideal nature of the Airy pattern where high directivity is achieved at the cost of a higher side lobe level. An equivalent aperture current distribution of the quasi-spherical array would likely not be uniform and thus trading HPBW for a reduced SLL.

However, the actual side lobe level of the array is higher due to the side lobes at about ± 50 degrees at 1.3 GHz and ± 20, 45 and 65 degrees at 3 GHz from θ_s which are probably related to grating lobes. Therefore, it is expected that the side lobe level of the conformal array can be made comparable or better to that of the ideal parabolic reflector if the element density is increased.

That said, the SLL of the designed geodesic quasi-spherical array could potentially already be sufficient for the DISTURB application as the source of interest is very strong, namely the Sun. Therefore, interference from weaker sources positioned at the side lobes of the array may be negligible. In addition, DISTURB will consider broadband emissions, hence the positions of these increased side lobes (grating lobes) will not coincide with local interfering sources over the entire observed frequency band.

Besides the comparison of radiation patterns of the quasi-spherical array and the parabolic reflector antenna, some other aspects need to be addressed. Unlike the parabolic reflector, the quasi-spherical array does not need any motors or other moving parts to steer the beam towards the Sun. These moving mechanical components wear out over time and therefore require maintenance. Given the fact that DISTURB should be able to monitor the Sun without interruption, a failing motor may lead to downtime during which important events may happen. Furthermore, given the fact that the DISTURB antennas may be placed at very remote locations, performing maintenance on the antennas is most likely very costly.

It should be mentioned although maintaining remote parabolic reflector antennas may be very costly, so are the upfront costs of phased array antennas. The high maintenance costs of the parabolic reflector antennas could potentially be offset by placing multiple parabolic reflector antennas for the price of one phased array antenna, thus implementing redundancy. If one parabolic reflector antenna were to fail, another parabolic reflector can be engaged quickly thus keeping downtime low. Assuming each parabolic reflector has the same time to failure on average, the lifetime of a station on average is increased by a factor of the number of redundant antennas. The ultimate trade-off between redundancy, maintenance costs and upfront costs is left to the reader.

Lastly, conformal phased array antennas may provide some other benefits that are potentially not so relevant to DISTURB but can be of importance for other applications. One such benefit is that phased arrays may steer their main beams much quicker than parabolic reflector antennas since it is done

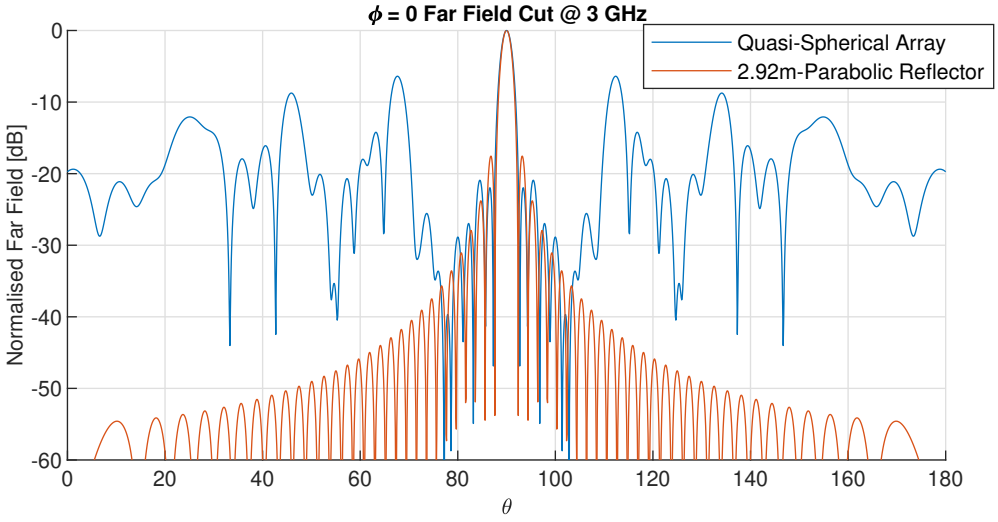

Figure 5.26: Comparison of normalised radiation patterns of the quasi-spherical array and a 2.92 metre diameter parabolic reflector at 3 GHz.

electronically instead of mechanically where the speed of redirection is limited by motors. This quick beam steering property could potentially outweigh the negatives in an application such as satellite communications with fast-moving satellites in low Earth orbit. Another application that benefits from quick beam steering as well is radar, as fast moving targets such as missiles and aircraft may need to be tracked. Also with faster beam steering, radar may be able to search a given volume more quickly. Another advantage that phased array antennas could provide is creating multiple beams allowing for the observation of multiple targets, which could be astronomical objects, satellites or aircraft. This is could be interesting for radio astronomy, satellite communications and radar respectively.

5.3. Conclusions on Array Performance

In this chapter, the performance of the conformal quasi-spherical array with the crossed modified bow-tie antenna element has been studied.

The impact of the spherical ground plane is found to have a negligible effect in comparison with the flat ground plane as used in chapter 4.

Due to the sparse nature of the selected geodesic quasi-spherical array it is found that the effect of mutual coupling is also negligible when comparing with the isolated element with respect to radiation patterns and active input impedances.

In contrast to the effect of the spherical ground plane and mutual coupling, it is shown that the effect of element orientation is very important. Namely, if antenna elements are rotated 180° with respect to each other, they can cancel each other out at certain angles. Also, from a polarimetric point of few, it is very important to compensate for orientation as at one scan angle, the $\hat{\theta}$-oriented sub-element of one modified crossed bow-tie antenna and the $\hat{\phi}$-oriented sub-element of another crossed bow-tie is aligned with the desired polarisation direction at a specific scan angle whereas this may be inverted or a combination of both sub-elements at other scan angles.

Since a full-wave analysis of the complete array is not possible due to computational limitations and the fact that effect of mutual coupling is negligible, the radiation patterns of the isolated elements were used to estimate the radiation pattern of the complete array. To eliminate the effect of element orientation, the radiation patterns of the quasi-spherical array were evaluated for scanning to the horizon which results in an active aperture where all elements are closely aligned to each other.

Using these approximations, it is concluded that the radiation pattern of the geodesic quasi-spherical array of radius 1.55 metres and 343 elements has a minimum HPBW of 2° at 3 GHz and a maximum HPBW of 5° at 1.3 GHz, thus satisfying the requirements on HPBW. Also, as the influence of mutual coupling on the active input impedance of the antenna elements is found to be negligible, also the receiver noise temperature is approximately the same as in the isolated case and thus lower than 100 K in the frequency range of 1.3 GHz to 3 GHz. This leads to the conclusion that the geodesic quasi-

spherical with crossed modified bow-tie antennas is able to achieve an operational frequency range of 1.3 GHz to 3 GHz, or a fractional bandwidth of 79%.

From a comparison of the final radiation pattern with the estimations based on isotropic active element patterns which enabled the novel comparison of many array configurations, it is shown that the estimations of chapter 3 are valid.

A comparison of the geodesic quasi-spherical array with an ideal parabolic reflector antenna with a diameter of 2.92 metres, shows that in the region of 20 degrees and 35 degrees at 1.3 and 3 GHz respectively the side lobe level of the conformal array is better. However, outside this region, the side lobe level is higher than that of the parabolic reflector due to the side lobes originating from grating lobes. However, these higher side lobes may be acceptable for the DISTURB project as the Sun is a very strong radio source.

It is concluded that although parabolic reflectors are much cheaper, it could be beneficial to select the conformal array option as maintenance costs and/or or redundant implementation of parabolic reflectors may exceed the cost of a single conformal array. However, the exact cost-benefit analysis is left up to the reader.

It is also concluded that instead of the new application of conformal arrays in radio astronomy presented in this thesis, the geodesic quasi-spherical array could be interesting in other applications. Applications of interest are for example satellite communications and radar where fast beam steering may be required at speeds which may not be easily achievable with reflector antennas.

6

Conclusions and Recommendations on Future Research

In this thesis project, a feasibility study on the application of conformal phased array antennas in DISTURB has been presented. This research covers a full circle of a conformal antenna array design to provide insight in the difficulties, trade-off's and impact of requirements involved with a novel application of conformal array antennas for radio astronomy.

The goal of this thesis project was to design a phased array antenna that has a maximum HPBW of 15 degrees and minimum HPBW of 2 degrees in the frequency band ranging from 1.5 to 3 GHz. Furthermore, the antenna elements used in the array should have a receiver noise temperature of less than 100 K in the mentioned frequency range. Next to this, the array must also be able to receive both orthogonal directions of polarisation.

Firstly, a method of analysis of conformal phased arrays is presented. This method in combination with isotropic embedded element patterns results in a significant reduction of required computational resources compared to full wave solutions. It is also shown that this method still is able to provide a relatively good approximation of the radiation pattern characteristics of a conformal array.

Using this method of analysis, for the first time, numerous conformal array configurations, comprising geometry, i.e. shape, and topology, i.e. the antenna element lattice, have been considered and compared for application to radio astronomy. This resulted in the fact that of the considered configurations, an array with a quasi-spherical geometry and a novel geodesic topology is found to best comply with the requirements for DISTURB.

Subsequently, the characteristics of an ideal antenna element for application in the geodesic quasi-spherical conformal array have been studied. This resulted in the requirement that the ideal antenna for this array has an isotropic radiation pattern in the region of 60 degrees from zenith and no radiation outside. The real part of the input impedance of the ideal antenna element is between about 90Ω and 40Ω and the imaginary part is between 80Ω and 20Ω. Furthermore, the cross polarisation isolation of the ideal antenna element is infinity.

Thereafter, a number of different antenna element designs has been investigated in order to select the design that is closest in performance to the ideal antenna element. This investigation resulted in selection of the crossed modified bow-tie antenna as it is closest in performance with respect to the ideal antenna element. This antenna element is able to provide a receiver noise match such that the receiver noise temperature is below 100 K over a frequency range of 1.3 to 3 GHz whilst providing a sufficiently good radiation pattern with respect to the ideal antenna element.

Thereafter, the crossed modified bow-tie antenna has been implemented in a partly geodesic quasi-spherical array configuration and evaluated using full wave methods. It was found that the embedded element patterns of the antenna elements are approximately the same due to low mutual coupling between the elements. Using this fact, the full array radiation pattern could be computed. It is found that the designed array is able to comply with the requirements in an operational frequency band from 1.3 to 3 GHz.

Finally, the performance of the geodesic quasi-spherical array is compared to the performance of an ideal parabolic reflector antenna. It is concluded that although an individual parabolic reflector antenna

may be cheaper whilst also having a lower side lobe level, a conformal phased array antenna may be a better option regarding maintenance costs as the DISTURB stations may be located very remotely.

The novel sparse geodesic quasi-spherical array with a radius of 1.55 metres and inter-element spacing of 0.3 metres yielding 343 elements designed in this thesis is able cover an operational frequency range from 1.3 to 3 GHz for all scan angles in the upper hemisphere. The requirements on HPBW are met as well as those on receiver noise temperature and the reception of both directions of polarisation in this band. Hence, the goal in this thesis has been achieved and even exceeded with an achieved fractional bandwidth of 79%.

Recommendations on Future Research

Considering the feasibility study nature of this project and the complexity of an end-to-end design of a conformal phased array antenna, lots of opportunities for future research remain.

Firstly, a method of compensating for element rotation needs to be developed in order to provide effective polarimetric capabilities and to provide estimations of radiation patterns for both orthogonal polarisation directions at all scan angles.

Secondly, the RF front-end needs to be designed. Most importantly, the options regarding analogue and digital beamforming and element orientation compensation need to be considered in the design of the RF front-end.

Instead of using an off-the shelf low-noise amplifier, a custom LNA could be designed providing low receiver noise temperatures over a larger bandwidth. This can be achieved by designing the LNA in such a way that its optimum noise reflection coefficient is matched to an antenna element instead of the other way around. This allows for more freedom in the antenna element design which potentially results in better receiver noise temperatures and radiation pattern characteristics over a much larger bandwidth.

Next to this, also other three-dimensional antenna designs like cones or monopoles could be considered, requiring a new approach to determining the active aperture as these elements do not have radiation towards zenith.

Another interesting research topic may be to investigate the design of conformal array geometries and/or topologies using for example evolutionary or particle swarm optimisation algorithms.

Also, the application of various digital beamforming strategies to the elements in a conformal array configuration could be investigated. Applying amplitude tapers could improve the radiation characteristics of a conformal antenna array regarding for example side lobe levels or possibly provide the capability of simultaneously observing multiple targets using multiple beams.

A

MATLAB Implementation

In order to compute and compare the performances of various conformal array configurations, the relevant formulas from section 2.3 are implemented in MATLAB. The MATLAB framework basic operation consists out a few steps, of which the first is setting-up the configuration/element locations of each array configuration. Next, it calculates which elements are active depending on scan angle. Then, the MATLAB framework computes the radiation pattern of the conformal array based on these active elements and calculates the HPBW of this radiation pattern. The calculation of the active elements, radiation patterns and HPBW is repeated for a number of scan angles to see how the HPBW behaves when scanning the entire hemisphere. A more detailed description of these steps is given in the following sections.

A.1. Setting-up Array Configuration

The first step in computing the performance of the array is by setting-up the array configuration. The configuration of an array consists out of two parts, namely the array *geometry* and the array *topology*. Throughout this thesis, array geometry refers to the three dimensional shape of the array and topology refers to the way the elements are distributed on the array geometry. For example, the geometry of an conformal array could be a hemisphere (geometry) and the antenna elements could be distributed along a spherical coordinate system (topology) or could be distributed as a rectangular grid which is projected on to the hemisphere (another topology). The combination of an array geometry and topology is referred to as an array configuration.

The MATLAB framework uses the same format for importing the locations of the antenna elements and the normal vectors of the elements, which indicate their orientations. This format is displayed in A.1. In this format, p_1^x indicates the x-coordinate of the position of the first element, p_N^y the y-coordinate of the N-th element and so on. Similarly, $\hat{n}_2^y$ represents the y-component of the normal vector of the second element, $\hat{n}_N^z$ represents the z-component of the normal vector of the N-th element and so on.

$$\vec{p} = \begin{bmatrix} p_1^x & p_2^x & \cdots & p_N^x \\ p_1^y & p_2^y & \cdots & p_N^y \\ p_1^z & p_2^z & \cdots & p_N^z \end{bmatrix} \qquad \hat{n} = \begin{bmatrix} \hat{n}_1^x & \hat{n}_2^x & \cdots & \hat{n}_N^x \\ \hat{n}_1^y & \hat{n}_2^y & \cdots & \hat{n}_N^y \\ \hat{n}_1^z & \hat{n}_2^z & \cdots & \hat{n}_N^z \end{bmatrix} \tag{A.1}$$

By using this standard format, dedicated functions can be written for generating array configurations consisting out of the element locations and element normal vectors which are the vectors normal to the surface of the array geometry at the element locations.

These functions are mostly named according to a `<geometry name>_<topology name>()` naming scheme. For instance, the array from figure 2.2 can be generated using the function `sphere_arclength(R, arclength, theta_max)`. The radius parameter `R` of this function is set to 1.5, the `arclength` parameter that determines the topology is set to 0.3 and the `theta_max` parameter is set to 1.5708, to indicate that all elements below $\theta = \frac{\pi}{2}$ should be removed and thus a hemispherical array is generated. Next to the before mentioned naming scheme, there are also the faceted shapes that follow a `<geometry name>_faced_<optional details>()` naming scheme. The optional details can for example indicate a topology or whether or not a certain facet should be populated with elements.

A.2. Active Element Computation

The next step is to compute which elements are active. From the scan angles θ_s and ϕ_s, the scan direction vector $\hat{r}_s$ can be calculated using equation A.2.

$$\hat{r}_s = \begin{bmatrix} \sin\theta_s \cos\phi_s \\ \sin\theta_s \sin\phi_s \\ \cos\theta_s \end{bmatrix} \tag{A.2}$$

Using this scan direction vector, the angle α between the element normal vector $\hat{n}_i$ can be computed using the dot product as shown in equation A.3.

$$\alpha = \arccos\left(\hat{n}_i \cdot \hat{r}_s\right) \tag{A.3}$$

When the angle α exceeds the allowed maximum local scan angle, the excitation of that element is set to 0. In the case that α is lower than the maximum allowed scan angle, the excitation is set to 1. This is implemented in MATLAB by the function `active_elements()`. This function first calculates the scan direction vector as shown in equation A.2 and expands it with copies of the scan vector so that it has the same amount of columns as element normal vectors. This is done by multiplying each of the three rows of $\hat{r}_s$ with a column vector of ones that has the same amount of columns as there are antenna elements. The angles can then be simply calculated by taking the arc cosine of the of the dot product between these two vectors. Lastly, a check is performed to see which elements have a local scan angle less than the maximum local scan angle. The function then returns only those element locations and normal vectors that have passed the check. This reduced list of elements is then used to calculate the radiation pattern of the array.

A.3. Radiation Pattern Calculation

Radiation pattern calculation is implemented in the function `FF_conformal()`. The first action this function performs is calculating the phase correction factor β_i for each element as shown in equation 2.28.

Next, the element AEPs are set-up. The MATLAB framework supports two options for this. The first option is to use isotropic patterns, this option provides the fastest calculation since the factor $\vec{E}_i^{FF}$ in equation 2.25 is always 1 independent of the scan angle.

The second option is to use non-isotropic patterns for the elements. The active element pattern of the element can be specified via the `single_element_FF` argument of the `FF_conformal()` function. However, these patterns are specified in the local coordinate system of the antenna elements and therefore these radiation patterns need to be rotated so that these local coordinate systems line up with the element normal vector $\hat{n}_i$. This rotation is performed by first calculating what the observation vectors would be in the local grid of the element. Subsequently, the active element patterns are evaluated at these apparent observation vectors and stored for later use in calculating the final radiation patterns. In case the active element is given as a table of the pattern versus θ and ϕ, the patterns are interpolated to find a value at the exact apparent observation angles. The disadvantage of this is that this interpolation is computationally demanding and slows down the overall radiation pattern calculation significantly.

The next step is to compute the actual array radiation pattern following equation 2.26. The radiation pattern calculation of conformal arrays is implemented in two different ways. The first method is an iterative method. The advantage of this method is that it requires a smaller amount of memory, but is slower in general. The second method is the matrix method. This method makes use of matrix math and since MATLAB is optimised for this, this option is generally faster. The disadvantage of this method is that it requires a large amount of memory when calculating radiation patterns for conformal arrays with a large number of elements or when a large spatial domain with high spatial resolution is required. If the memory requirement is too large, MATLAB starts writing parts of the memory to the hard disk drive of the computer which slows down the calculation significantly.

The iterative method works by first calculating the wave vectors for all observation angles. Thereafter, the variable representing $\vec{E}_{tot}^{FF}$ is set to 0. Then a loop is performed over all the elements and during every iteration of the loop, the value of the factor $A_i \vec{E}_i^{FF}(\vec{r}) e^{j\left(\vec{k}\vec{p}_i + \beta_i\right)}$ is added to the $\vec{E}_{tot}^{FF}$ variable. Therefore, this results in the same operation as in equation 2.26.

Alternatively, equation 2.26 can be implemented using matrix math. Firstly, the antenna element position matrix $\mathbf{P}$ is formed as shown in A.4 where x_i, y_i and z_i indicate the position of the i-th antenna element. Also, the phase correction factor is included in this matrix.

$$\mathbf{P} = \begin{bmatrix} x_1 & y_1 & z_1 & \beta_1 \\ x_2 & y_2 & z_2 & \beta_2 \\ \vdots & \vdots & \vdots & \vdots \\ x_N & y_N & z_N & \beta_N \end{bmatrix} \tag{A.4}$$

Secondly, the matrix with the observation wave vectors $\mathbf{K}$ is set up as shown in A.5. To this, a row of ones is added. In matrix $\mathbf{K}$, k_1^x indicates the x-component of the wave vector at the first observation angle, k_2^y is the y-component of the wave vector at the second observation angle and so on for all M observation angles.

$$\mathbf{K} = \begin{bmatrix} k_1^x & k_2^x & \cdots & k_M^x \\ k_1^y & k_2^y & \cdots & k_M^y \\ k_1^z & k_2^z & \cdots & k_M^z \\ 1 & 1 & \cdots & 1 \end{bmatrix} \tag{A.5}$$

Multiplying the matrices from A.4 and A.5 leads to equation A.6.

$$\begin{aligned} \mathbf{PK} &= \begin{bmatrix} x_1 & y_1 & z_1 & \beta_1 \\ x_2 & y_2 & z_2 & \beta_2 \\ \vdots & \vdots & \vdots & \vdots \\ x_N & y_N & z_N & \beta_N \end{bmatrix} \times \begin{bmatrix} k_1^x & k_2^x & \cdots & k_M^x \\ k_1^y & k_2^y & \cdots & k_M^y \\ k_1^z & k_2^z & \cdots & k_M^z \\ 1 & 1 & \cdots & 1 \end{bmatrix} \\ &= \begin{bmatrix} x_1k_1^x + y_1k_1^y + z_1k_1^z + \beta_1 & \cdots & x_1k_M^x + y_1k_M^y + z_1k_M^z + \beta_1 \\ \vdots & \ddots & \vdots \\ x_Nk_1^x + y_Nk_1^y + z_Nk_1^z + \beta_N & \cdots & x_Nk_M^x + y_Nk_M^y + z_Nk_M^z + \beta_N \end{bmatrix} \end{aligned} \tag{A.6}$$

Multiplying the result from A.6 with j and computing the exponential of all the entries, gives the exponent in equation 2.26. Subsequently, the resulting matrix can be point wise multiplied by the radiation patterns of the corresponding elements at the corresponding observation angles. The last step in finding the total radiated field is summing along the rows of the matrix, thus implementing equation 2.26.

A.4. Half-Power Beam Width

The last step in evaluating the performance of an conformal array configuration is computing the half-power beam width. This is implemented in the MATLAB framework by first finding the point that is closest above $\sqrt{2}$ for angles greater that the scan angle in a ϕ cut of the normalised E-pattern. Then it performs linear interpolation between this point and the next point to find the interpolated angle at which the normalised E-pattern is equal to $\sqrt{2}$. This process is then repeated for the $\sqrt{2}$ crossing at the angle less than the scan angle. The half-power beam width is subsequently found by taking the difference between these angles.

This process is well suited for finding the half-power beam width of conical beams, where the HPBW can easily determined by using the angle along $\hat{\theta}$. However, it could also be the case that the beam is oblate and widest along $\hat{\phi}$. This complicates the problem of finding the HPBW because the angles ϕ and θ cannot be compared directly. Consider a conical beam pointing towards the horizon. This beam may occupy a few degrees along $\hat{\theta}$ and the same amount of degrees along $\hat{\phi}$. However, when the conical beam is pointing to zenith, this beam may occupy only a few degrees in θ but it occupies 360° in ϕ. This is an effect of how spherical coordinates are defined.

To solve this problem and find a true value for the beam width, instead of doing involved transforms to compensate the deformation in the spherical coordinate grid, the whole conformal array is rotated so that the zenith lines up with the scan direction vector. This rotation for the element locations is done by performing $\mathbf{R}\hat{p}$ and the element normal vectors are rotated by performing $\mathbf{R}\hat{n}$ where the rotation matrix $\mathbf{R}$ is shown in equation A.7.

$$\mathbf{R} = \begin{bmatrix} 1 & 0 & 0 \\ 0 & \cos(-\theta_s) & -\sin(\theta_s) \\ 0 & \sin(-\theta_s) & \cos(-\theta_s) \end{bmatrix} \begin{bmatrix} \cos\left(-\phi_s - \frac{\pi}{2}\right) & -\sin\left(-\phi_s - \frac{\pi}{2}\right) & 0 \\ \sin\left(-\phi_s - \frac{\pi}{2}\right) & \cos\left(-\phi_s - \frac{\pi}{2}\right) & 0 \\ 0 & 0 & 1 \end{bmatrix} \tag{A.7}$$

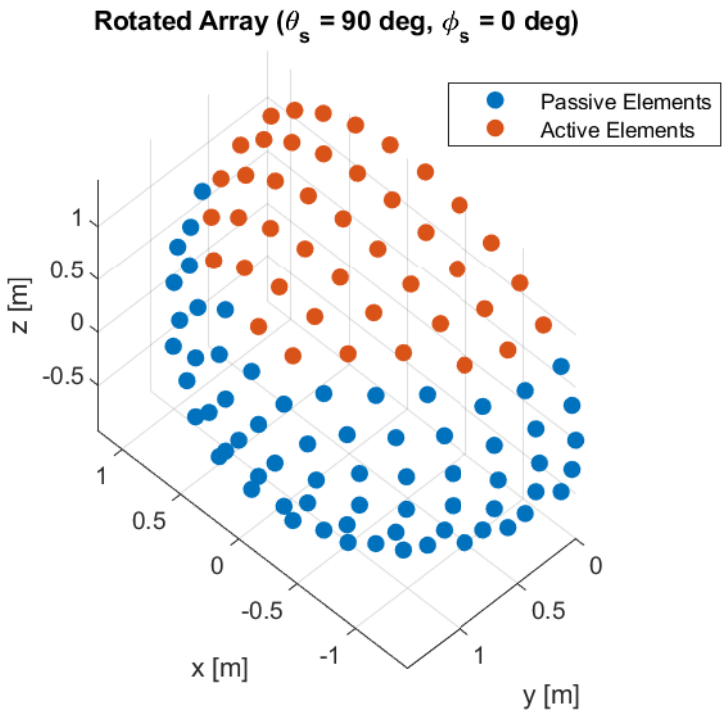

Figure A.1: Plot of a rotated hemispherical array configuration for a scan angle of $\theta_s = 90°$ and $\phi_s = 0°$.

In this way, the HPBW can reliably calculated along all ϕ-cuts to find the largest beam width. This results in a half-power beam width plot as shown in figure A.3 which corresponds to the rotated array configuration in figure A.1. A plot of the radiation pattern at this scan angle is displayed in figure A.2.

Figure A.3 can be interpreted as following. The first observation from the upper plot in figure A.3 is that the HPBW increases when scanning towards the horizon. From the lower plot in figure A.3 the limiting ϕ-cut can be seen, i.e. the cut at which the largest HPBW occurs as shown in the upper plot. For a scan angle of $\theta_s = 90°$, it can be seen that $\phi = 90°$ is limiting. This can be understood by looking at the radiation pattern computed at this scan angle in figure A.2, where it can easily be seen that the beam is widest along the V-axis, which is equal to $\phi = 90°$. This in turn can be explained by figure A.1, where it can be seen that the active aperture of the array is smallest along the y-axis. Therefore, if the HPBW needs to be decreased at a scanning angle θ_s of 90°, the size of the aperture along $\hat{y}$ is limiting and should be increased by for example increasing the height of the array.

The other observations that can be made from figure A.3 is that the behaviour of the HPBW versus θ_s is not smooth but shows small steps. This is due to the fact that elements are turning on and off depending on scan angle which result in sudden changes of the active aperture of the array. Another observation that can be made is that if the limiting ϕ-cut shows unstable behaviour, the cross-section of the beam is most likely very close to a circle.

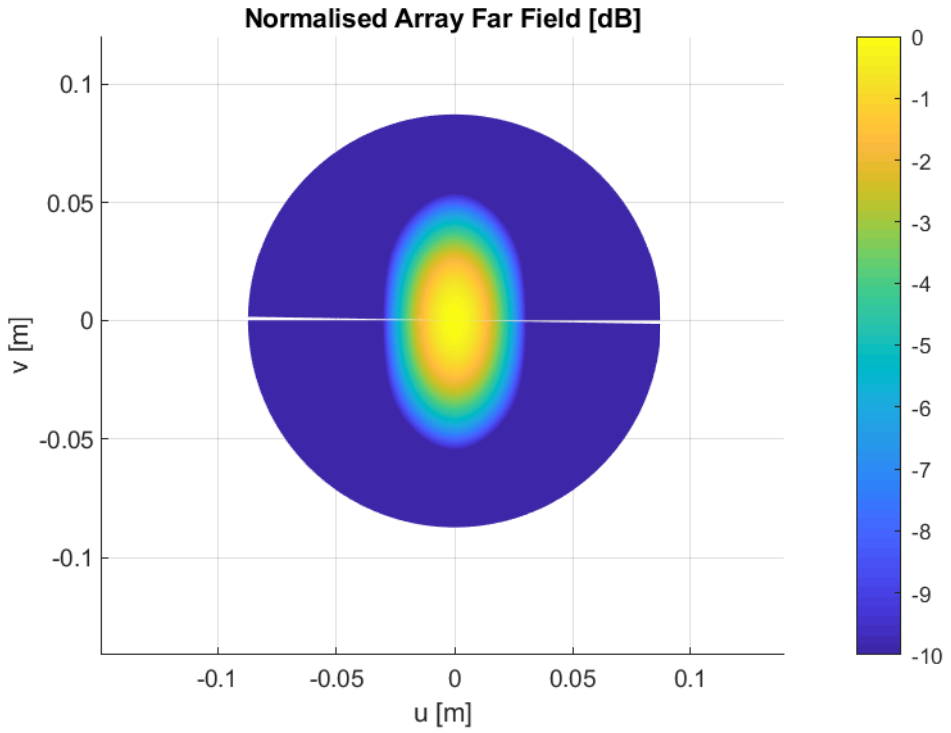

Figure A.2: UV-plot for observation angles θ ranging from -5 to 5 degrees and ϕ from 0 to 180 degrees of the normalised far field pattern for the array configuration as displayed in figure A.1.

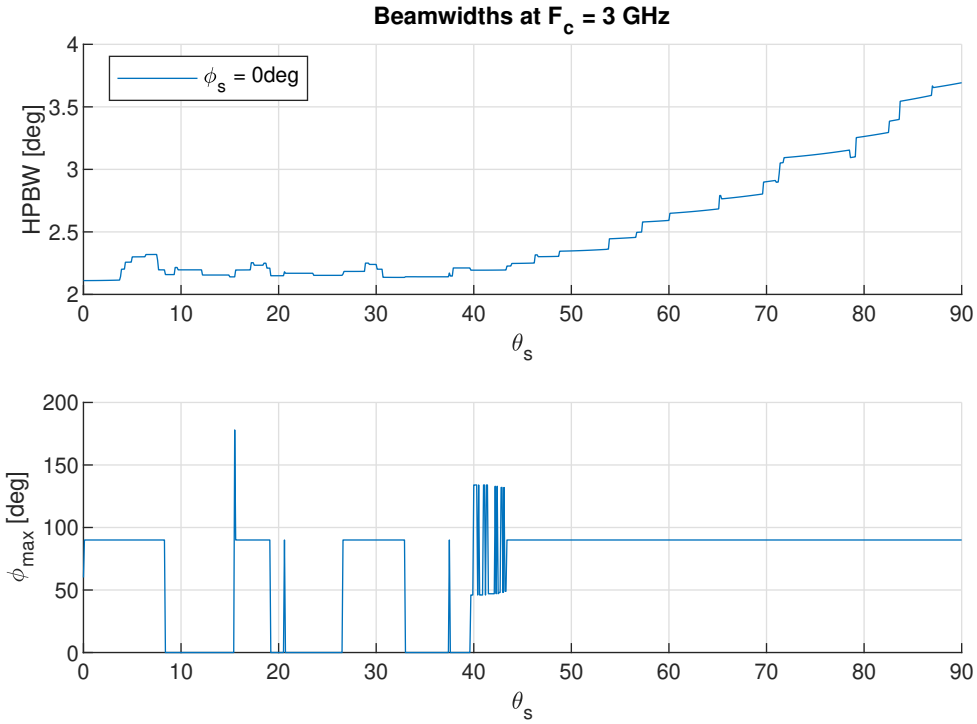

Figure A.3: Plot of the HPBW as function of the scan angle θ_s of the array configuration shown in figure A.1. The upper plot shows the value of the HPBW in degrees and the lower plot shows in which ϕ-cut this HPBW is maximum.

B

Verification of Numerical Results

Numerical solvers are a very useful tool in the evaluation of electromagnetic problems as nowadays no analytical solution exists for most problems of interest. However, the results obtained with numerical solvers are dependent on how the problem is digitised, i.e. meshed, and the employed solver algorithm. Because of this, numerical solvers should be used carefully and the obtained results should be verified and checked for physical correctness. Verification can be done by varying the mesh size to check the convergence of the results. Furthermore, different solver algorithms can be used to increase confidence in the results as this eliminates the uncertainty in the correctness or applicability of the algorithm itself.

This appendix presents the verification of the most important numerical results of this thesis. These are the results of the modified crossed bow-tie antenna and those of the section of the geodesic quasi-spherical array.

B.1. Crossed Modified Bow-Tie Antenna

To increase the accuracy of the obtained results with minimal user effort, CST Studio Suite supports adaptive meshing. With adaptive meshing, CST refines the mesh of the model and solves it for a specified number of times or when a specified convergence criterion is met. This provides a first way of verifying the convergence of the results. However, when using adaptive meshing, CST generally decreases mesh cell size at the spots at which the electromagnetic fields change most. This may lead to results that seem to have converged when in reality they may not have converged as the mesh cell sizes needed to be decreased in at other spots as well. This could for example be because the antenna edges far away from the antenna feed point could be meshed very coarsely, thus misrepresenting the geometry of the antenna.

To this end, the first step that is taken to confirm the validity of the obtained simulation results of the crossed modified bow-tie antenna is increasing the fineness of the mesh. The solver algorithm used in CST is the finite element method (FEM) which makes use of tetrahedral mesh cells. In CST's mesh settings, the maximum cell size is set to $\lambda/10$, $\lambda/20$ and $\lambda/30$ which is subsequently refined by adaptive meshing at locations where the difference in field strength is large to smaller sizes. Figure B.1 shows a comparison of the found impedances of the antenna for these mesh sizes.

This figure shows that there is a small difference in impedance, which is relatively largest for the imaginary part. As the number of mesh cells increases, the difference in impedance decreases as well. It should be said that the mesh cell size decrease from the $\lambda/20$ to $\lambda/30$ is not the same factor 2 as from $\lambda/10$ to $\lambda/20$, however, it can still be concluded that the results converge. Ideally, instead of a mesh cell size of $\lambda/30$, a mesh cell size of $\lambda/40$ should be considered but this mesh size is too computationally demanding for a regular desktop PC with 8 GB of RAM and an Intel® Core™ i5-7500 CPU at 3.40 GHz.

Figure B.2 and B.3 show the convergence of the radiated far fields of the crossed modified bow-tie antenna at 1.5 and 3 GHz respectively. These figures show that the far field is less sensitive to mesh size than the impedance. It can be concluded from these figures that the far field of the crossed modified bow-tie can be already be accurately computed with a maximum mesh cell size of $\lambda/10$.

Lastly, to confirm that the FEM solver yields good results, the same model is solved in Feko using the

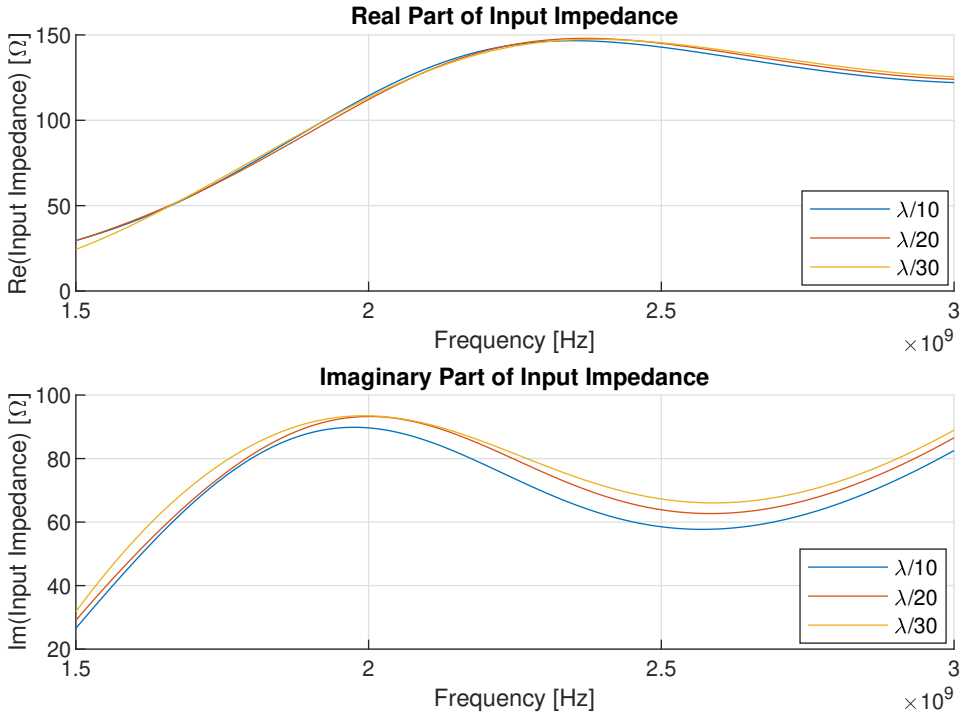

Figure B.1: Comparison of input impedance of the crossed modified bow-tie antenna for several mesh sizes.

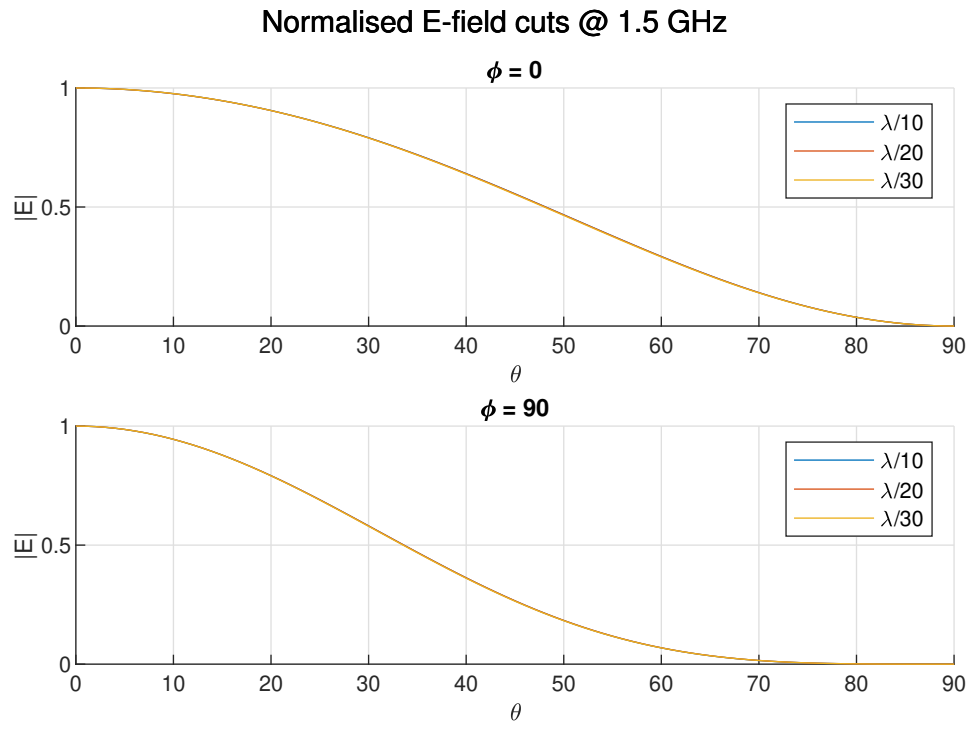

Figure B.2: Comparison of normalised far field cuts at 1.5 GHz of the crossed modified bow-tie antenna for several mesh sizes.

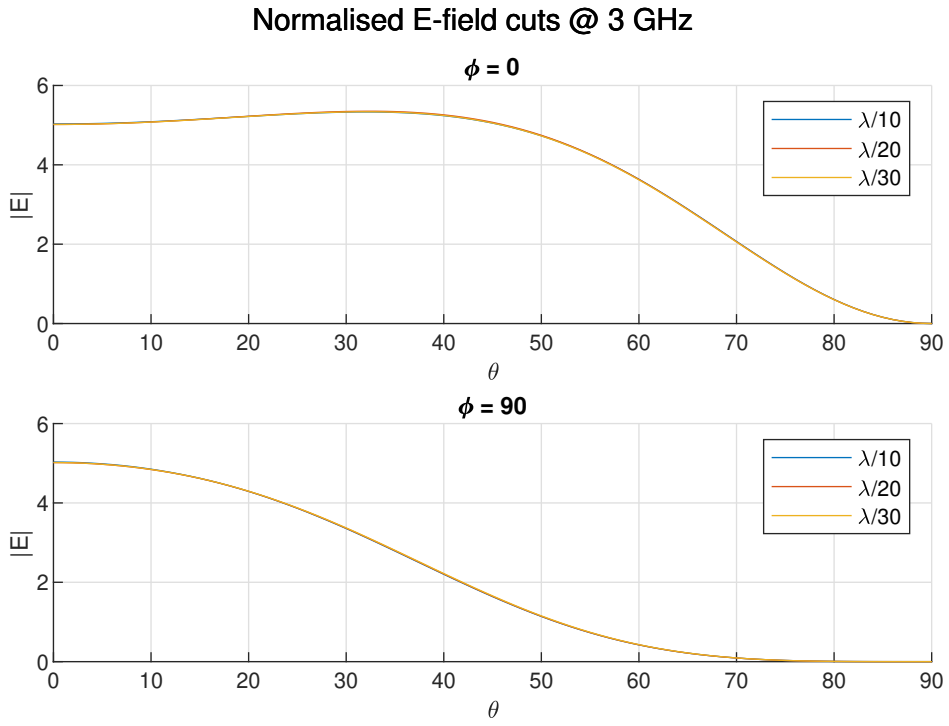

Figure B.3: Comparison of normalised far field cuts at 3 GHz of the crossed modified bow-tie antenna for several mesh sizes.

method of moments (MoM). This solver algorithm uses triangles. The maximum size of these triangles is set to $\lambda/30$. The results of the impedance are compared to those obtained with CST with a maximum cell size of $\lambda/30$ in figure B.4.

Figure B.4 shows that although the obtained impedances are not exactly equal, they follow the same behaviour. Next to the solver algorithm, further difference can be explained by the fact that mesh used by CST is generated by adaptive meshing. This results in a much more irregular mesh with smaller cells near the edges and feed point of the antenna than the mesh generated by Feko.

A comparison of the far fields obtained with Feko and CST is shown in figures B.5 and B.6. It can be seen from these figures that patterns are almost equal for values of θ below 40 degrees in the $\phi = 0$ cut at 3 GHz. At 1.5 GHz and the other cut at 3 GHz, the far field patterns are different but follow the same behaviour. For example, both solvers show a splitting of the beam occurring around 3 GHz.

In this case, it is hard to tell which far field is more correct than the other. It may be the one predicted by CST, the one predicted by Feko, somewhere in between or somewhere outside the obtained solutions. However, it is most likely safe to assume that the behaviour of the far fields is about the same as the obtained results as they are not wildly different.

B.2. Geodesic Quasi-Spherical Array

Due to the large geometry of the 30° quasi-spherical array section, the model cannot simply be meshed using the ”standard” option at 3 GHz in Feko. Namely, the mesh with ”standard” mesh cell size results in a memory requirement above 125.7 GB. This is mostly because of the fact that the spherical ground plane is a very large metal surface.

In order to still be able to evaluate a 30° quasi-spherical array section, the ground plane needs to be meshed using the ”coarse” option whilst the meshing of the antenna element can be done using the ”standard” option. However, the impact of this coarse mesh must be investigated. Since the ground plane of the 30° quasi-spherical array section cannot be meshed with standard size, the selected approach to this problem is by comparing the results of an isolated crossed modified bow-tie antenna above a ground plane meshed using both ”coarse” and ”standard” options. Figure B.7 shows a comparison of the input impedance of the coarse and standard options.

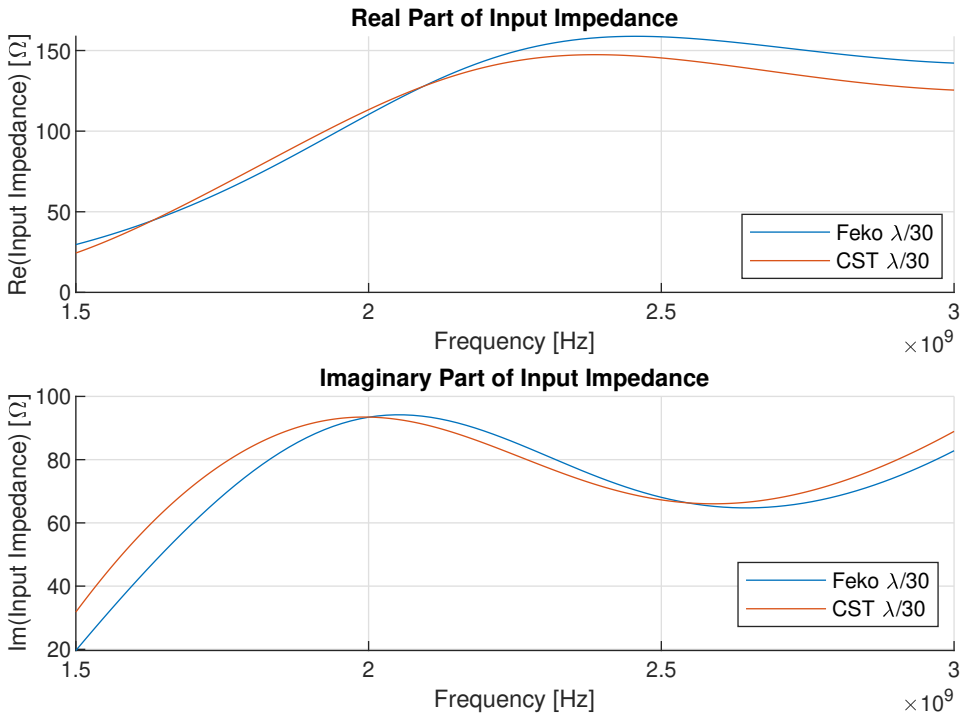

Figure B.4: Comparison of input impedances obtained with MoM using Feko and FEM using CST for a maximum mesh size of $\lambda/30$.

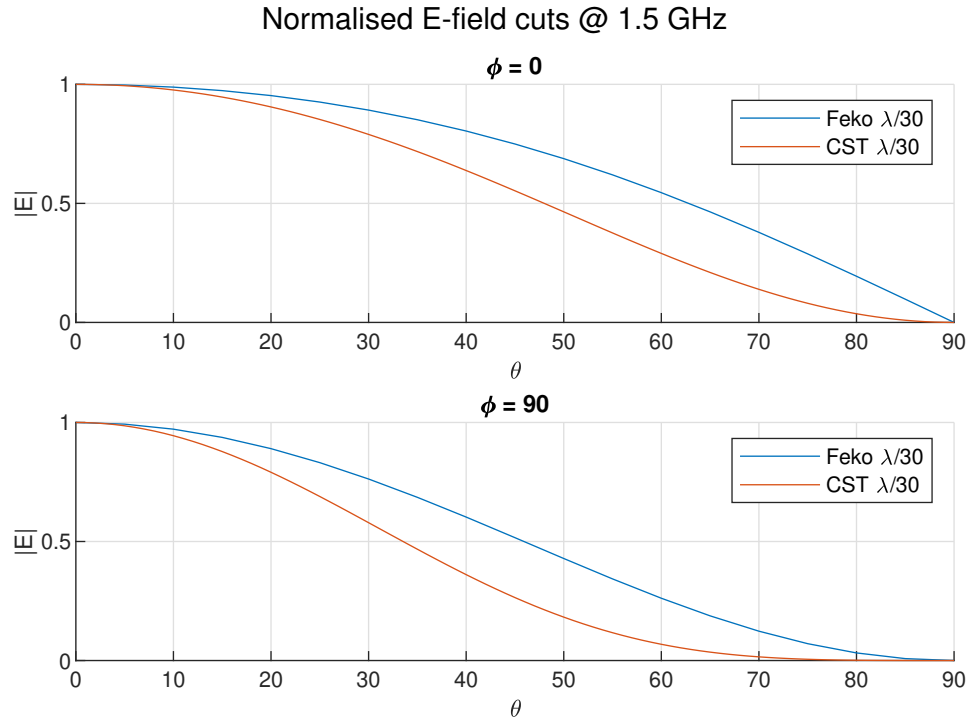

Figure B.5: Comparison of normalised far field cuts at 1.5 GHz of results obtained using Feko and CST for the crossed modified bow-tie antenna at a maximum mesh size of $\lambda/30$.

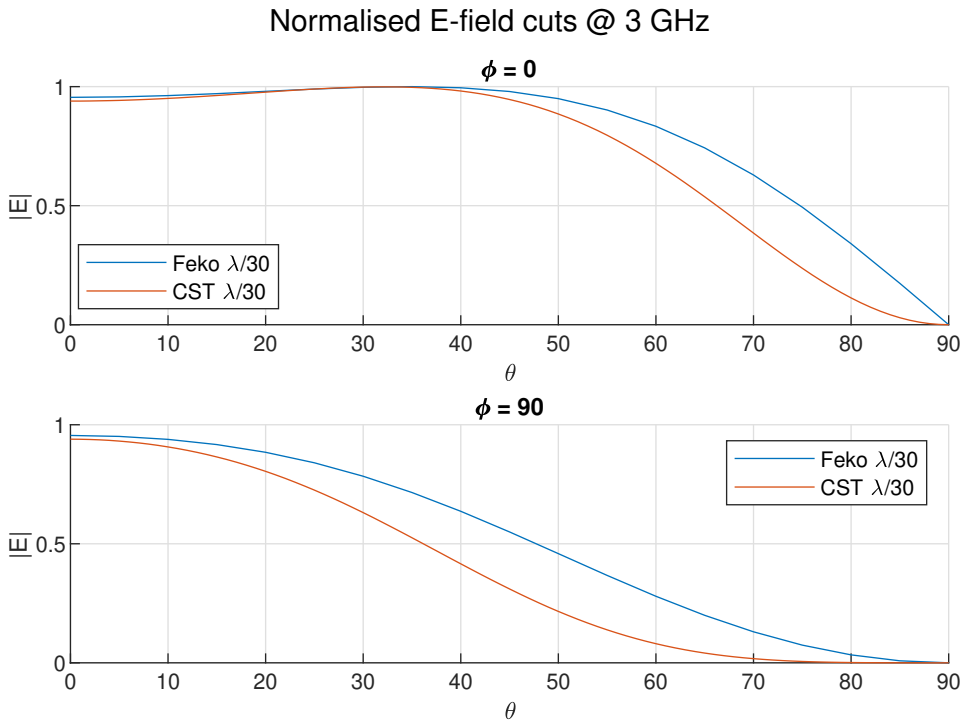

Figure B.6: Comparison of normalised far field cuts at 3 GHz of results obtained using Feko and CST for the crossed modified bow-tie antenna at a maximum mesh size of $\lambda/30$.

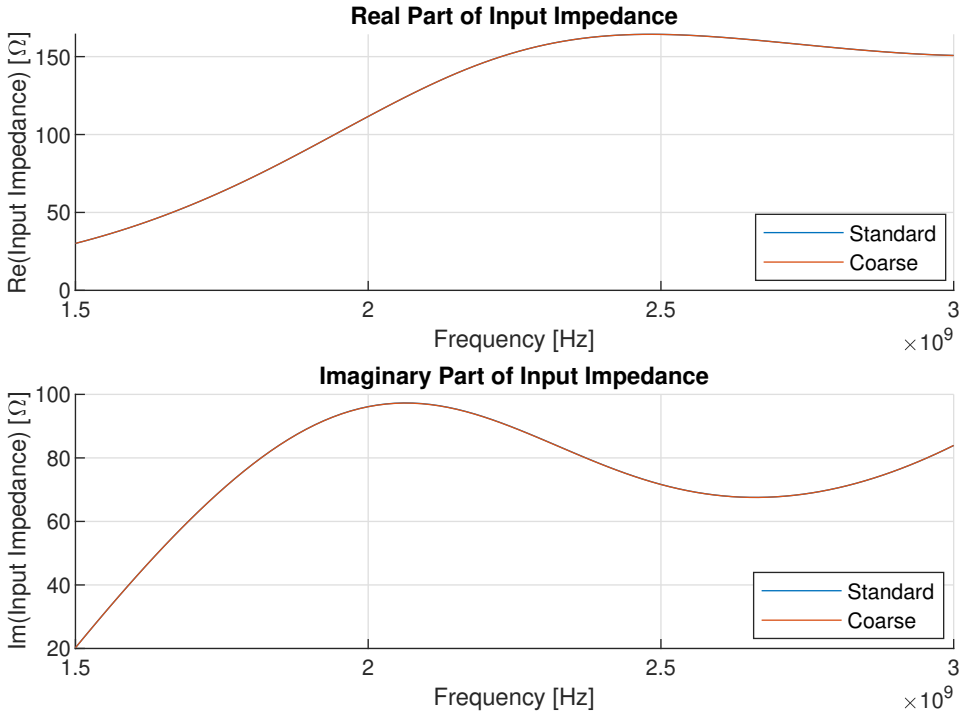

Figure B.7: Comparison of input impedances obtained with coarse and standard meshing options in Feko.

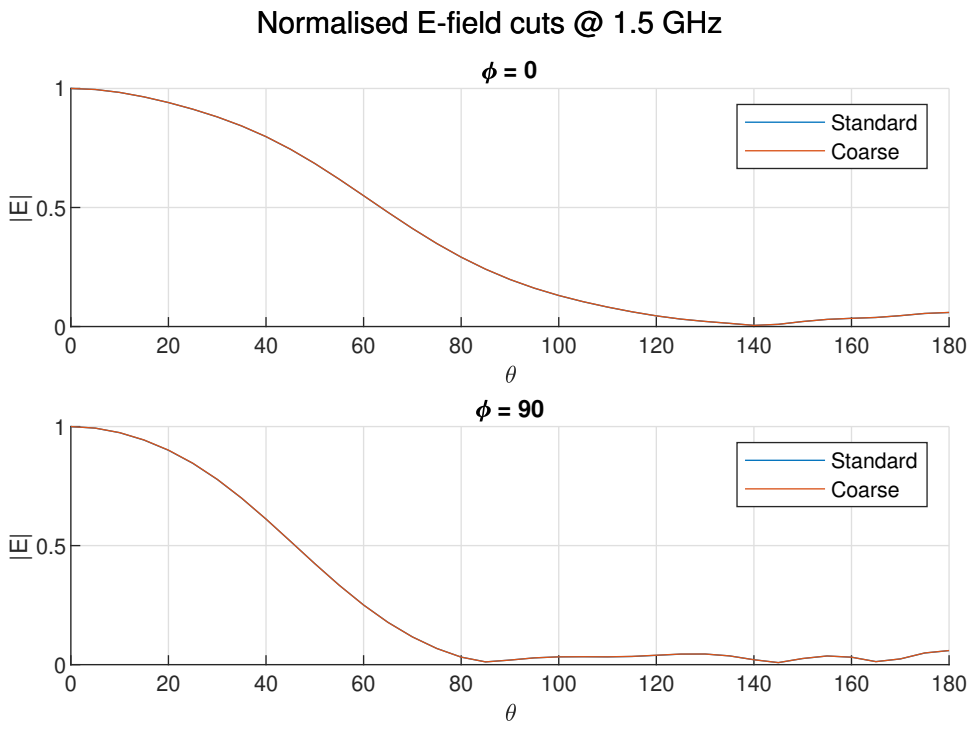

Figure B.8: Comparison of normalised far field cuts at 1.5 GHz obtained using coarse and standard meshing options for the spherical ground plane in Feko.

Figure B.7 shows that the results obtained with coarse and standard meshes are almost exactly the same. Therefore, it can be concluded from an impedance standpoint that the coarse mesh can be safely utilised.

To confirm that this is also the case with the far fields, comparisons of the $\phi = 0°$ and $\phi = 90°$ cuts of the far fields at 1.5 and 3 GHz for standard and coarse meshes are shown in figures B.8 and B.9.

These figures show that also the far fields are almost exactly the same. Thus, it can be concluded that also from a far field perspective coarse meshing can be safely applied to the spherical ground plane.

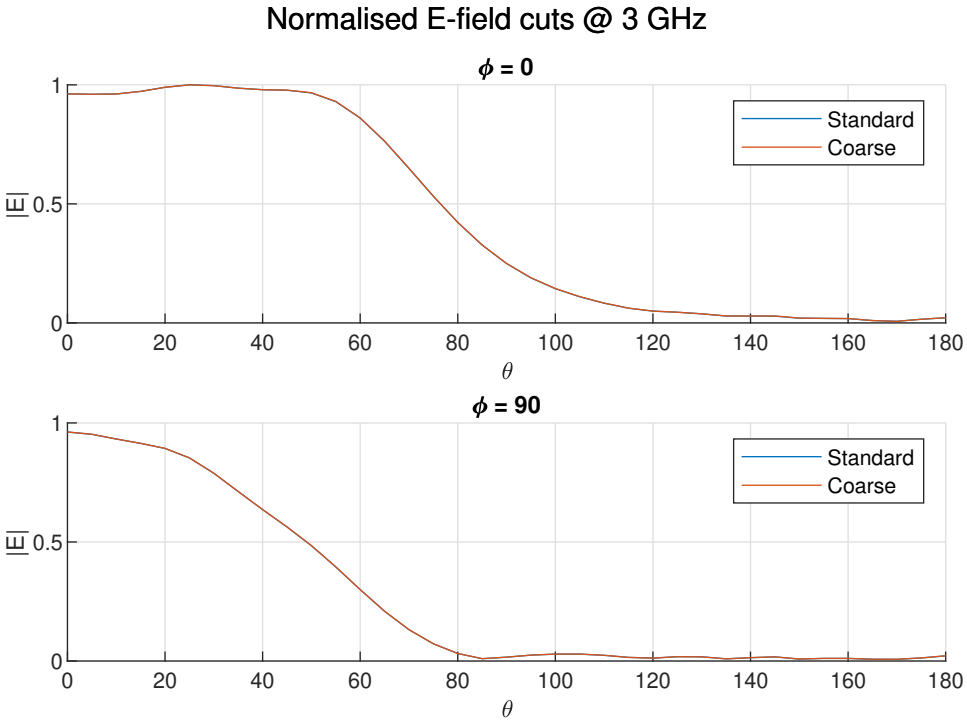

Figure B.9: Comparison of normalised far field cuts at 3 GHz obtained using coarse and standard meshing options for the spherical ground plane in Feko.

C

Computer Scripts and Codes

In order to spare the environment, the code and scripts used for this thesis project can be found at:
`https://github.com/wbouwmeester/thesis_code_base`

Bibliography

[1] S. White, “Solar radio bursts and space weather,” *Asian J. Phys.*, vol. 16, 01 2007.

[2] D. C. Ferguson, S. P. Worden, and D. E. Hastings, “The space weather threat to situational awareness, communications, and positioning systems,” *IEEE Transactions on Plasma Science*, vol. 43, no. 9, pp. 3086–3098, Sep. 2015.

[3] M. P. van Haarlem, M. W. Wise, A. W. Gunst, G. Heald, J. P. McKean *et al.*, “LOFAR: The LOw-Frequency ARray,” *A&A*, vol. 556, p. A2, 2013. [Online]. Available: https://doi.org/10.1051/0004-6361/201220873

[4] G. W. Kant, P. D. Patel, S. J. Wijnholds, M. Ruiter, and E. van der Wal, “EMBRACE: A Multi-Beam 20,000-Element Radio Astronomical Phased Array Antenna Demonstrator,” *IEEE Transactions on Antennas and Propagation*, vol. 59, no. 6, pp. 1990–2003, June 2011.

[5] L. Josefsson and P. Persson, *Conformal Array Antenna Theory and Design*. Hoboken, NJ, USA: Wiley, 2006, ch. 3, pp. 50–52.

[6] G. Knittel, “Choosing the number of faces of a phased-array antenna for hemisphere scan coverage,” *IEEE Transactions on Antennas and Propagation*, vol. 13, no. 6, pp. 878–882, November 1965.

[7] R. J. Bolt, D. Cavallo, G. Gerini, D. Deurloo, R. Grooters, A. Neto, and G. Toso, “Characterization of a dual-polarized connected-dipole array for ku-band mobile terminals,” *IEEE Transactions on Antennas and Propagation*, vol. 64, no. 2, pp. 591–598, Feb 2016.

[8] R. L. Haupt and Y. Rahmat-Samii, “Antenna array developments: A perspective on the past, present and future,” *IEEE Antennas and Propagation Magazine*, vol. 57, no. 1, pp. 86–96, Feb 2015.

[9] N. V. Larsen, “Electronically Steerable Antennas for Satellite Communications,” PhD Thesis, Technical University of Denmark, May 2007.

[10] D. Cavallo, A. Neto, G. Gerini, A. Micco, and V. Galdi, “A 3- to 5-ghz wideband array of connected dipoles with low cross polarization and wide-scan capability,” *IEEE Transactions on Antennas and Propagation*, vol. 61, no. 3, pp. 1148–1154, March 2013.

[11] R. Wang, B.-Z. Wang, C. Hu, and X. Ding, “Wide-angle scanning planar array with quasi-hemispherical-pattern elements,” *Scientific Reports*, vol. 7, 2017.

[12] W. Mavroides and R. Mailloux, “Experimental evaluation of an array technique for zenith to horizon coverage,” *IEEE Transactions on Antennas and Propagation*, vol. 26, no. 3, pp. 403–406, May 1978.

[13] Y. Bai, S. Xiao, M. Tang, Z. Ding, and B. Wang, “Wide-angle scanning phased array with pattern reconfigurable elements,” *IEEE Transactions on Antennas and Propagation*, vol. 59, no. 11, pp. 4071–4076, Nov 2011.

[14] D. S. Prinsloo, P. Meyer, R. Maaskant, and M. Ivashina, “Design of an active dual-mode antenna with near hemispherical field of view coverage,” in *2013 International Conference on Electromagnetics in Advanced Applications (ICEAA)*, Sep. 2013, pp. 1064–1067.

[15] S. N. Haider, “Antennas for Frequency Reconfigurable Phased Arrays,” PhD Thesis, TU Delft, Apr. 2015. [Online]. Available: https://doi.org/10.4233/uuid:8f0cd1af-dcab-4124-aa42-50f9240c236c

[16] Z. Peng, T. Hu, W. Cui, J. Huangfu, C. Li, and L. Ran, “Unconventional beamforming for quasi-hemispheric coverage of a phased array antenna,” *IEEE Antennas and Wireless Propagation Letters*, vol. 12, pp. 1654–1657, 2013.

[17] R. K. Luneburg, *Mathematical Theory of Optics*. Providence, RI: Brown Univ. Press., 1944.

[18] C. S. Liang, D. A. Streater, Jian-Ming Jin, E. Dunn, and T. Rozendal, “Ground-plane-backed hemispherical luneberg-lens reflector,” *IEEE Antennas and Propagation Magazine*, vol. 48, no. 1, pp. 37–49, Feb 2006.

[19] J. S. Kot, R. Donelson, N. Nikolic, D. Hayman, M. O’Shea, and G. Peeters, “A spherical lens for the ska,” *Experimental Astronomy*, vol. 17, no. 1, pp. 141–148, Jun 2004. [Online]. Available: https://doi.org/10.1007/s10686-005-0033-8

[20] J. Thornton and K. Huang, *Modern Lens Antennas for Communications Engineering*. IEEE, 2012, ch. 1, pp. 12–13. [Online]. Available: https://ieeexplore-ieee-org.tudelft.idm.oclc.org/document/6497282

[21] G. James, A. Parfitt, J. Kot, and P. Hall, “A case for the Luneburg lens as the antenna element for the square-kilometre array radio telescope,” in *Radio Science Bulletin*, vol. 293, Jun. 2000, pp. 32–37.

[22] M. C. T. Kastelijn and J. A. G. Akkermans, “Planar passive electromagnetic deflector for millimeter-wave frequencies,” *IEEE Antennas and Wireless Propagation Letters*, vol. 7, pp. 105–107, 2008.

[23] M. I. Kazim and M. H. A. J. Herben, “3d spherical passive electromagnetic deflector for the 60 ghz frequency band,” in *2014 XXXIth URSI General Assembly and Scientific Symposium (URSI GASS)*, Aug 2014, pp. 1–4.

[24] M. I. Kazim, M. H. A. J. Herben, and A. B. Smolders, “Wide angular coverage deflector: 60-ghz three-dimensional passive electromagnetic deflector achieves wide angular coverage.” *IEEE Antennas and Propagation Magazine*, vol. 58, no. 2, pp. 47–59, April 2016.

[25] L. Josefsson and P. Persson, *Conformal Array Antenna Theory and Design*. Hoboken, NJ, USA: Wiley, 2006, ch. 1, pp. 1–2.

[26] W. M. Waters, D. P. Patel, and G. V. Trunk, “Optimum number of faces of a volume-scanning active array radar,” *IEEE Transactions on Aerospace and Electronic Systems*, vol. 34, no. 3, pp. 1032–1037, July 1998.

[27] G. V. Trunk, “Optimal number of phased array faces for horizon and volume surveillance revisited,” in *IEEE International Symposium on Phased Array Systems and Technology, 2003.*, Oct 2003, pp. 124–129.

[28] I. Khalifa and R. G. Vaughan, “Geometric design and comparison of multifaceted antenna arrays for hemispherical coverage,” *IEEE Transactions on Antennas and Propagation*, vol. 57, no. 9, pp. 2608–2614, Sep. 2009.

[29] W. Wang, A. Cao, S. Ye, X. Liang, Q. Guo, W. Li, R. Jin, and J. Geng, “Design of a passive multi-faceted phased array for hemispherical coverage,” in *Proceedings of the 2012 IEEE International Symposium on Antennas and Propagation*, July 2012, pp. 1–2.

[30] P. Dianfei, B. Yanshan, and C. Naiping, “Hemispherical coverage array antenna and performance analysis,” *Wireless Personal Communications*, vol. 80, no. 3, pp. 1193–1201, Feb 2015. [Online]. Available: https://doi.org/10.1007/s11277-014-2080-9

[31] A. Villeneuve, M. Behnke, and W. Kummer, “Wide-angle scanning of linear arrays located on cones,” *IEEE Transactions on Antennas and Propagation*, vol. 22, no. 1, pp. 97–103, January 1974.

[32] G. Caille, E. Vourch, M. J. Martin, J. R. Mosig, and M. Polegre, “Conformal array antenna for observation platforms in low earth orbit,” *IEEE Antennas and Propagation Magazine*, vol. 44, no. 3, pp. 103–104, June 2002.

[33] J. R. Lambert, C. A. Balanis, and D. DeCarlo, “Spherical cap adaptive antennas for gps,” *IEEE Transactions on Antennas and Propagation*, vol. 57, no. 2, pp. 406–413, Feb 2009.

[34] K. A. Yinusa, W. Elmarissi, S. Caizzone, and A. Dreher, “A multi-band conformai antenna array for gnss applications,” in *2016 IEEE International Symposium on Antennas and Propagation (APSURSI)*, June 2016, pp. 897–898.

[35] B. Pavan Kumar, C. Kumar, V. Senthil Kumar, and V. V. Srinivasan, “Active spherical phased array design for satellite payload data transmission,” *IEEE Transactions on Antennas and Propagation*, vol. 63, no. 11, pp. 4783–4791, Nov 2015.

[36] ——, “Optimal Radiation Pattern of the Element for a Spherical Phased Array With Hemispherical Scan Capability,” *IEEE Antennas and Wireless Propagation Letters*, vol. 16, pp. 2780–2782, 2017.

[37] K. R. Subhashini and A. T. P. Kumar, “Comparative Analysis of Linear and Nonlinear Pattern Synthesis of Hemispherical Antenna Array Using Adaptive Evolutionary Techniques,” *International Journal of Antennas and Propagation*, vol. 2014, 2014.

[38] O. Franek and G. F. Pedersen, “Spherical arrays for wireless channel characterization and emulation,” in *Antennas and Propagation in Wireless Communications (APWC), 2014 IEEE-APS Topical Conference on*. IEEE Press, 8 2014, pp. 480–483.

[39] Y. Cheng, N. Song, F. Roemer, M. Haardt, H. Henniger, R. Metzig, and E. Diedrich, “Satellite ground stations with electronic beam steering,” in *2012 IEEE First AESS European Conference on Satellite Telecommunications (ESTEL)*, Oct 2012, pp. 1–7.

[40] B. Tomasic, J. Turtle, and S. Liu, “A geodesic sphere phased array antenna for satellite control and communication,” *XXVII General Assembly of the International Union of Radio Science*, 2002.

[41] E. Gschwendtner, D. Loffler, and W. Wiesbeck, “Conformal microstrip antenna array with hemispherical coverage for mobile users of future satellite systems,” in *1998 28th European Microwave Conference*, vol. 1, Oct 1998, pp. 535–539.

[42] J. Thornton and K. Huang, *Modern Lens Antennas for Communications Engineering*. IEEE, 2012, ch. 1, p. 2. [Online]. Available: https://ieeexplore-ieee-org.tudelft.idm.oclc.org/document/6497282

[43] ——, *Modern Lens Antennas for Communications Engineering*. IEEE, 2012, ch. 1, p. 6. [Online]. Available: https://ieeexplore-ieee-org.tudelft.idm.oclc.org/document/6497282

[44] L. Josefsson and P. Persson, *Conformal Array Antenna Theory and Design*. Hoboken, NJ, USA: Wiley, 2006, ch. 8, p. 319.

[45] A. B. Crawford, D. C. Hogg, and L. E. Hunt, “A horn-reflector antenna for space communication,” *The Bell System Technical Journal*, vol. 40, no. 4, pp. 1095–1116, July 1961.

[46] Andeggs, “3D Spherical,” Wikimedia Commons, 2009. [Online]. Available: https://commons.wikimedia.org/wiki/File:3D_Spherical.svg

[47] “EE4580 Quasi Optical Systems Lecture Notes - Lecture 2: Reflector Antennas,” 2019.

[48] “EE4510 Advanced Electromagnetics Lecture Notes - Lecture 4: Radiated Fields from Elementary Sources,” 2019.

[49] “EE4510 Advanced Electromagnetics Lecture Notes - Lecture 7: Distributed Sources,” 2019.

[50] C. A. Balanis, *Antenna Theory: Analysis and Design*, 4th ed. Hoboken, NJ, USA: Wiley, 2016, ch. 6, p. 349.

[51] E. W. Weisstein, “Ellipsoid,” MathWorld–A Wolfram Web Resource. [Online]. Available: http://mathworld.wolfram.com/Ellipsoid.html

[52] ——, “Prolate Spheroid,” MathWorld–A Wolfram Web Resource. [Online]. Available: http://mathworld.wolfram.com/OblateSpheroid.html

[53] ——, “Oblate Spheroid,” MathWorld–A Wolfram Web Resource. [Online]. Available: http://mathworld.wolfram.com/ProlateSpheroid.html

[54] K. M. Gorski, E. Hivon, A. J. Banday, B. D. Wandelt, F. K. Hansen, M. Reinecke, and M. Bartelmann, “HEALPix: A framework for high-resolution discretization and fast analysis of data distributed on the sphere,” *The Astrophysical Journal*, vol. 622, no. 2, pp. 759–771, apr 2005. [Online]. Available: https://doi.org/10.1086%2F427976

[55] C. P. Choi, “MEALPix (fork): Matlab package for HEALPix,” Github. [Online]. Available: https://github.com/pochoi/MEALPix

[56] K. M. Gorski, B. D. Wandelt, F. K. Hansen, E. Hivon, and A. J. Banday, “The HEALPix Primer,” 1999. [Online]. Available: https://arxiv.org/abs/astro-ph/9905275

[57] D. M. Pozar, *Microwave Engineering*, 4th ed. Hoboken, NJ, USA: Wiley, 2012, ch. 10, p. 505.

[58] Mini-Circuits, “SAV-541+.” [Online]. Available: https://www.minicircuits.com/WebStore/dashboard.html?model=SAV-541%2B

[59] Maxim Integrated Products, Inc., “Application Note 3169: Low-Noise Amplifier (LNA) Matching Techniques for Optimizing Noise Figures,” Jul. 2004. [Online]. Available: https://www.maximintegrated.com/en/design/technical-documents/app-notes/3/3169.html

[60] A. M. Niknejad, “EECS 242 Topic: Two-Port Noise.” [Online]. Available: http://rfic.eecs.berkeley.edu/~niknejad/ee242/pdf/eecs242_lect8_twoportnoise.pdf

[61] D. E. Bockelman and W. R. Eisenstadt, “Combined differential and common-mode scattering parameters: theory and simulation,” *IEEE Transactions on Microwave Theory and Techniques*, vol. 43, no. 7, pp. 1530–1539, July 1995.

[62] D. S. Prinsloo and P. Meyer, “Multi-mode noise parameters for multi-port networks,” *IET Microwaves, Antennas Propagation*, vol. 10, no. 3, pp. 333–338, 2016.

[63] H. Lin, *Solar Polarimetry: An Overview*, ser. Astronomical Society of the Pacific Conference Series. Astronomical Society of the Pacific Conference, 2005, vol. 343, p. 357.

[64] C. A. Balanis, *Antenna Theory: Analysis and Design*, 4th ed. Hoboken, NJ, USA: Wiley, 2016, ch. 9, pp. 487–496.

[65] H. G. Schantz, “Planar elliptical element ultra-wideband dipole antennas,” in *IEEE Antennas and Propagation Society International Symposium (IEEE Cat. No.02CH37313)*, vol. 3, June 2002, pp. 44–47.

[66] D. M. Pozar, *Microwave Engineering*, 4th ed. Hoboken, NJ, USA: Wiley, 2012, ch. 3, p. 113.

[67] C. A. Balanis, *Antenna Theory: Analysis and Design*, 4th ed. Hoboken, NJ, USA: Wiley, 2016, ch. 9, pp. 496–500.

[68] Y. Mushiake, “Self-complementary antennas,” *IEEE Antennas and Propagation Magazine*, vol. 34, no. 6, pp. 23–29, Dec 1992.

[69] R. Sammeta and D. S. Filipovic, “Quasi frequency-independent increased bandwidth planar log-periodic antenna,” *IEEE Transactions on Antennas and Propagation*, vol. 62, no. 4, pp. 1937–1944, April 2014.

[70] C. A. Balanis, *Antenna Theory: Analysis and Design*, 4th ed. Hoboken, NJ, USA: Wiley, 2016, ch. 12, pp. 669–673.